# The MOLLER Experiment

**M**easurement **O**f a **L**epton **L**epton **E**lectroweak **R**eaction

An Ultra-precise Measurement of the Weak Mixing Angle using Møller Scattering

# Pre-Conceptual Design Report

The MOLLER Collaboration

December 9, 2016

# The MOLLER Collaboration


J. Benesch, P. Brindza, R.D. Carlini, J-P. Chen, E. Chudakov, S. Covrig, M.M. Dalton, A. Deur, D. Gaskell, J. Gomez, D.W. Higinbotham, C. Keppel, D. Meekins, R. Michaels, B. Moffit, Y. Roblin, R. Suleiman, R. Wines, B. Wojtsekhowski
*Jefferson Lab*

G. Cates, D. Crabb, D. Day, K. Gnanvo, D. Keller, N. Liyanage, V.V. Nelyubin, H. Nguyen, B. Norum, K. Paschke, V. Sulkosky, J. Zhang, X. Zheng
*University of Virginia*

J. Birchall, P. Blunden, M.T.W. Gericke, J. Hoskins, J. Mammei, C. Match, H.S. Lee, S.A. Page, J. Pan, P. Pandey, S. Rahman, R. Spies, W.T.H. van Oers,
*University of Manitoba*

F. Araiza-Gonzalez, K. Dehmelt, C. Clarke, A. Deshpande, N. Feege, T.K. Hemmick, K.S. Kumar [Contact*], T. Kutz, R. Richards, S. Riordan, T. Ye, Y. Zhao
*Stony Brook University, SUNY*

R. Miskimen, M.J. Ramsey-Musolf
*University of Massachusetts, Amherst*

J. Bessuille, E. Ihloff, J. Kelsey, S. Kowalski, R. Silwal
*Massachusetts Institute of Technology*

G. De Cataldo, R. De Leo, D. Di Bari, L. Lagamba, E. Nappi
*INFN, Sezione di Bari and Universita' di Bari*

V. Bellini, F. Mammoliti, F. Noto, M.L. Sperduto, C.M. Sutera
*INFN Sezione di Catania and Universita' di Catania*

P. Cole, T.A. Forest, M. Khandekar, D. McNulty
*Idaho State University*

K. Aulenbacher, S. Baunack, F. Maas, V. Tioukine
*Johannes Gutenberg Universitaet Mainz*

R. Gilman, K. Myers, R. Ransome, A. Tadepalli
*Rutgers University*

R. Holmes, P. Souder
*Syracuse University*

D.S. Armstrong, T.D. Averett, W. Deconinck
*College of William & Mary*

W. Duvall, A. Lee, M. L. Pitt
*Virginia Polytechnic Institute and State University*

J.A. Dunne, D. Dutta, L. El Fassi
*Mississippi State University*

B. Jamieson, R. Mammei, J.W. Martin
*University of Winnipeg*

F. De Persio, F. Meddi, G.M. Urciuoli
*Dipartimento di Fisica dell'Universita' la Sapienza and INFN Sezione di Roma*

E. Cisbani, C. Fanelli, F. Garibaldi
*INFN Gruppo Collegato Sanita' and Istituto Superiore di Sanita'*

R. S. Beminiwattha, K. Johnston, N. Simicevic, S. Wells
*Louisiana Tech University*

P.M. King, J. Roche

*Ohio University*

J. Arrington, P.E. Reimer
*Argonne National Lab*

G. Franklin, B. Quinn
*Carnegie Mellon University*

A. Ahmidouch, S. Danagoulian
*North Carolina A&T State University*

O. Glamazdin, R. Pomatsalyuk
*NSC Kharkov Institute of Physics and Technology*

D. Jones, J. Napolitano
*Temple University*

T. Holmstrom
*Longwood University*

J. Erler
*Universidad Nacional Autónoma de México*

Yu.G. Kolomensky
*University of California, Berkeley*

K. A. Aniol
*California State U.(Los Angeles)*

W.D. Ramsay
*TRIUMF*

E. Korkmaz
*University of Northern British Columbia*

D.T. Spayde
*Hendrix College*

F. Benmokhtar
*Duquesne University*

A. Del Dotto
*INFN Sezione di Roma3*

R. Perrino
*INFN Sezione di Lecce*

S. Barkanova
*Acadia University*

A. Aleksejevs
*Memorial University, Grenfell*

J. Singh
*NSCL and Michigan State University*

*krishna.kumar@stonybrook.edu

## Executive Summary

We present the conceptual design with emphasis on technical feasibility of the MOLLER experiment, in which we propose to measure the parity-violating asymmetry $A_{PV}$ in polarized electron-electron (Møller) scattering. In the Standard Model, $A_{PV}$ is due to the interference between the electromagnetic amplitude and the weak neutral current amplitude, the latter being mediated by the $Z^0$ boson. $A_{PV}$ is predicted to be $\approx 35$ parts per billion (ppb) at our kinematics. Our goal is to measure $A_{PV}$ to an uncertainty of 0.8 ppb. The result would yield a measurement of the weak charge of the electron $Q_W^e$ to a fractional uncertainty of 2.4% at an average $Q^2$ of 0.0056 GeV$^2$.

The measurement is sensitive to the interference of the electromagnetic amplitude with new neutral current amplitudes as weak as $\sim 10^{-3} \cdot G_F$ from as yet undiscovered dynamics beyond the Standard Model. Such discovery reach is unmatched by any proposed experiment measuring a flavor- and CP-conserving process over the next decade, and results in a unique window to new physics at MeV and multi-TeV scales, complementary to direct searches at high energy colliders. Within the Standard Model, the extracted $Q_W^e$ measurement yields a determination of the weak mixing angle $\sin^2\theta_W$ with both precision and accuracy that are unmatched by any conceivable method at $Q^2 \ll M_Z^2$ in the foreseeable future, and matches the uncertainty from the single best such determination from high energy colliders.

The measurement would be carried out in Hall A at Jefferson Laboratory, where a 11 GeV longitudinally polarized electron beam would be incident on a 1.5 m liquid hydrogen target. Møller electrons (beam electrons scattering off target electrons) in the full range of the azimuth and spanning the polar angular range 5 mrad $< \theta_{lab} <$ 19 mrad, would be separated from background and brought to a ring focus $\sim 30$ m downstream of the target by a spectrometer system consisting of a pair of toroidal magnet assemblies and precision collimators. The Møller ring would be intercepted by a system of fused silica detectors; the resulting Cherenkov light would provide a relative measure of the scattered flux.

Longitudinally polarized electrons are generated via photoemission on a GaAs photocathode by circularly polarized laser light, enabling rapid polarization (helicity) reversal and suppression of spurious systematic effects. $A_{PV}$ would be extracted from the fractional difference in the integrated Cherenkov light response between helicity reversals. Additional systematic suppression to the sub-ppb level would be accomplished by periodically reversing the sign of the physics asymmetry by three independent methods.

Simultaneously with data collection, the fluctuations in the electron beam energy and trajectory and its potential systematic effects on $A_{PV}$ would be precisely monitored, active feedback loops would minimize beam helicity correlations, and detector response to beam fluctuations would be continuously calibrated. Background fractions and their helicity-correlated asymmetries would be measured by dedicated auxiliary detectors. The absolute value of $Q^2$ would be calibrated periodically using tracking detectors. The longitudinal electron beam polarization would be measured continuously by two independent polarimeter systems.

A strong collaboration with extensive experience in similar experiments is committed to the design, construction and deployment of the apparatus and to data collection and analysis. It is envisioned that construction and assembly will take three years, to be followed by three data collection periods with progressively improved statistical errors and systematic control over a subsequent three to four year period.

# Contents

# List of Figures

# List of Tables

# 1 Introduction

## 1.1 Physics Context

An important strategy to determine the full extent of validity of the electroweak theory and search for new dynamics from MeV to multi-TeV scales involves indirect probes, where ultra-precise measurements of electroweak observables at energy scales well below the scale of electroweak symmetry breaking are compared to accurate theoretical predictions. The MOLLER project [1, 2], like many of the low energy experimental measurements that have been proposed in the Fundamental Symmetries area, pursues such a strategy. MOLLER proposes to measure the parity-violating asymmetry in the scattering of longitudinally polarized electrons off unpolarized electrons, using the upgraded 11 GeV beam in Hall A at Jefferson Laboratory (JLab), to an overall fractional accuracy of 2.4%. Such a measurement would constitute more than a factor of five improvement in fractional precision over the only other measurement of the same quantity by the E158 experiment at SLAC [3].

The electron beam energy, luminosity and stability at Jefferson Laboratory are uniquely suited to carry out such a measurement. The 11 GeV JLab beam at the upgraded facility provides a compelling new opportunity to achieve a new benchmark in sensitivity. The physics motivation has two important aspects:

1. New neutral current interactions are best parameterized model-independently at low energies by effective four-fermion interactions by the quantity $\Lambda/g$, where $g$ characterizes the strength and $\Lambda$ is the scale of the new dynamics. The proposed $A_{PV}$ measurement is sensitive to interaction amplitudes as small as $1.5 \times 10^{-3}$ times the Fermi constant, $G_F$, which corresponds to a sensitivity of $\Lambda/g = 7.5$ TeV. A coupling $g$ of order one probes the TeV scale with new and unique sensitivity, while for $\Lambda \sim 100$ MeV, there is extraordinary new sensitivity approaching $10^{-3} \cdot \alpha_{_{QED}}$. This would be *the* most sensitive probe of new flavor and CP-conserving neutral current interactions in the leptonic sector until the advent of a linear collider or a neutrino factory, and would have $\pm 10\,\sigma$ discovery potential in the discovery space allowed by the existing most precise low energy measurements.

2. Within the Standard Model, weak neutral current amplitudes are functions of the weak mixing angle $\sin^2\theta_W$. The two most precise independent determinations of $\sin^2\theta_W$ differ by $3\sigma$. The world average is consistent with the theoretical prediction for the weak mixing angle assuming the 126 GeV scalar resonance observed at the LHC is the Standard Model (SM) Higgs boson. However, choosing one or the other central value ruins this consistency and implies very different new high-energy dynamics. The proposed $A_{PV}$ measurement, which would achieve a sensitivity of $\delta(\sin^2\theta_W) = \pm 0.00028$, has the same level of precision and interpretability: the best among projected sensitivies for new measurements at low $Q^2$ or colliders over the next decade.

$A_{PV}$ in Møller scattering measures the weak charge of the electron $Q_W^e$, which is proportional to the product of the electron's vector and axial-vector couplings to the $Z^0$ boson. The electroweak theory prediction at tree level in terms of the weak mixing angle is $Q_W^e = 1 - 4\sin^2\theta_W$; this is modified at the 1-loop level [4–6] and becomes dependent on the energy scale at which the measurement is carried out, *i.e.* $\sin^2\theta_W$ "runs". The prediction for $A_{PV}$ for the proposed experimental design is $\approx 35$ parts per billion (ppb) and the goal is to measure this quantity with an overall uncertainty of 0.8 ppb and thus achieve a 2.4% measurement of $Q_W^e$. Under the assumption of a SM Higgs boson mass of 126 GeV, the theoretical prediction for the MOLLER $A_{PV}$ is calculable to better than 0.2 ppb accuracy. The purely leptonic Møller PV asymmetry is a rare low energy observable whose theoretical uncertainties, especially due to hadronic effects, are well under control.

The 2007 and 2015 NSAC long range plan reports [7, 8] comprehensively described the opportunities presented by new sensitive indirect probes such as MOLLER, and how they fit into the subfield of Fundamental Symmetries. One of the overarching questions that serves to define this subfield is: "What are

the unseen forces that were present at the dawn of the universe but disappeared from view as the universe evolved?". To address this question and as part of the third principal recommendation, significant new investments, including MOLLER, are advocated. MOLLER received the highest rating from the JLab Program Advisory Committee (PAC) in January 2009. In January 2010, JLab management organized a Director's review of the experiment chaired by Charles Prescott [9]. The committee gave strong endorsement to the experiment and encouraged the collaboration and the laboratory to develop a full proposal to obtain construction funding. In January 2011, the PAC allocated MOLLER's full beamtime request of 344 PAC days. The 2012 NSAC subpanel on the implementation of the Long Range Plan (the Tribble Subcommittee) [10] strongly endorsed the MOLLER project as part of the suite of investments advocated for the subfield of Fundamental Symmetries.

In September 2014, the experiment underwent a Science Review conducted by the DOE Office of Nuclear Physics. In the review report [11], the panel strongly endorsed the goals of the MOLLER experiment and emphasized the strong potential impact of the measurement. The 2015 NSAC Long Range Plan reinforced the importance of carrying out the MOLLER measurement and highlighted the project in the Fundamental Symmetries chapter as an important new initiative for potential MIE funding over the next few years.

In this document, we describe the goals of MOLLER and provide sufficient detail to justify the technical feasablity of the proposed measurement. A strong collaboration ($\sim$ 120 collaborators from 30 institutions representing 6 countries) is carrying out pre-R&D activities under the assumption that construction funding approval will be obtained by fiscal year 2018, so that construction can be completed and installation, commissioning and first physics data could quickly follow by the end of 2020.

## 1.2 Precision Goal

Polarized electron scattering off unpolarized targets provides a clean window to study weak neutral current interactions. The leading order Feynman diagrams relevant for Møller scattering, involving both direct and exchange diagrams that interfere with each other, are shown in Fig. 1. The parity-violating asymmetry in the scattering of longitudinally polarized electrons on unpolarized target electrons $A_{PV}$, due to the interference between the photon and $Z^0$ boson exchange diagrams in Fig. 1, is given by [12]

$$A_{PV} = \frac{\sigma_R - \sigma_L}{\sigma_R + \sigma_L} = mE\frac{G_F}{\sqrt{2}\pi\alpha}\frac{4\sin^2\theta}{(3+\cos^2\theta)^2}Q_W^e = mE\frac{G_F}{\sqrt{2}\pi\alpha}\frac{2y(1-y)}{1+y^4+(1-y)^4}Q_W^e \qquad (1)$$

where $Q_W^e$ (proportional to the product of the electron's vector and axial-vector couplings to the $Z^0$ boson) is the weak charge of the electron, $\alpha$ is the fine structure constant, $E$ is the incident beam energy, $m$ is the electron mass, $\theta$ is the scattering angle in the center of mass frame, $y \equiv 1 - E'/E$ and $E'$ is the energy of one of the scattered electrons.

The electroweak theory prediction at tree level in terms of the weak mixing angle is $Q_W^e = 1 - 4\sin^2\theta_W$; this is modified at the 1-loop level [4–6] and becomes dependent on the energy scale at which the measurement is carried out, *i.e.* $\sin^2\theta_W$ "runs". It increases by approximately 3% compared to its value at the scale of the $Z^0$ boson mass, $M_Z$; this and other radiative corrections reduce $Q_W^e$ to 0.0435, a $\sim 42\%$ change of its tree level value of $\sim 0.075$ (when evaluated at $M_Z$). The dominant effect comes from the "$\gamma - Z$ mixing" diagrams depicted in Fig. 2 [5].

The prediction for $A_{PV}$ for the proposed experimental design is $\approx 35$ parts per billion (ppb) and the goal is to measure this quantity with an overall uncertainty of 0.8 ppb and thus achieve a 2.4% measurement of $Q_W^e$. The reduction in the numerical value of $Q_W^e$ due to radiative corrections leads to increased fractional accuracy in the determination of the weak mixing angle, $\sim 0.1\%$, matching the precision of the single best such determination from measurements of asymmetries in $Z^0$ decays in the $e^+e^-$ colliders LEP and SLC.

An important point to note is that, at the proposed level of measurement accuracy of $A_{PV}$, the Standard Model (SM) prediction must be carried out with full treatment of one-loop radiative corrections and leading two-loop corrections. The current error associated with radiative corrections for MOLLER is estimated to be less than 0.4 ppb, smaller than the expected 0.8 ppb overall precision. There is an ongoing effort to investigate several classes of diagrams beyond one-loop [13–15], and a plan has been formulated to evaluate the complete set of two-loop corrections at MOLLER kinematics; such corrections are estimated to be already smaller than the MOLLER statistical error. The existing work makes it clear that the theoretical uncertainties for the purely leptonic Møller PV are well under control, and the planned future work will aim to reduce the error on the $A_{PV}$ prediction, including the effects of the apparatus, to less than 0.2 ppb [16].

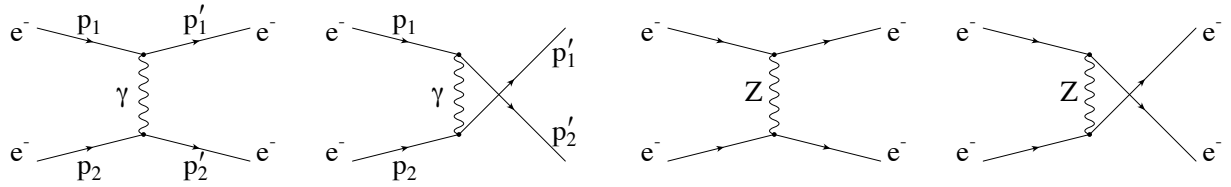


Figure 1: *Feynman diagrams for Møller scattering at tree level (reproduced from Ref. [5])*

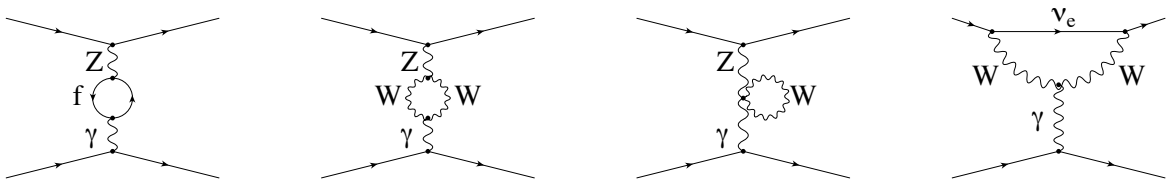


Figure 2: *Significant 1-loop radiative corrections: $\gamma - Z$ mixing diagrams and $W$-loop contribution to the anapole moment (reproduced from Ref. [5])*

The proposed MOLLER measurement will make a precision (2.4% relative) measurement of a suppressed Standard Model observable ($Q_W^e \sim 0.0435$) resulting in sensitivity to new neutral current amplitudes as weak as $\sim 10^{-3} \cdot G_F$ from as yet undiscovered dynamics beyond the Standard Model. The fact that the proposed measurement provides such a sensitive probe of TeV-scale dynamics beyond the SM (BSM) is a consequence of a very precise experimental goal ($\sim 10^{-3} \cdot G_F$), the energy scale of the reaction ($Q^2 \ll M_Z^2$), and the ability within the electroweak theory to provide quantitative predictions with negligible theoretical uncertainty. The proposed measurement is likely the only practical way, using a purely leptonic scattering amplitude at $Q^2 \ll M_Z^2$, to make discoveries in important regions of BSM space in the foreseeable future at any existing or planned facility worldwide.

## 1.3 Summary of Physics Motivation

### 1.3.1 Electroweak Physics

The **weak mixing angle** $\sin^2\theta_W$ has played a central role in the development and validation of the electroweak theory, especially testing it at the quantum loop level, which has been the central focus of precision electroweak physics over the past couple of decades. To develop the framework, one starts with three fundamental experimental inputs characterizing, respectively, the strength of electroweak interactions, the scale

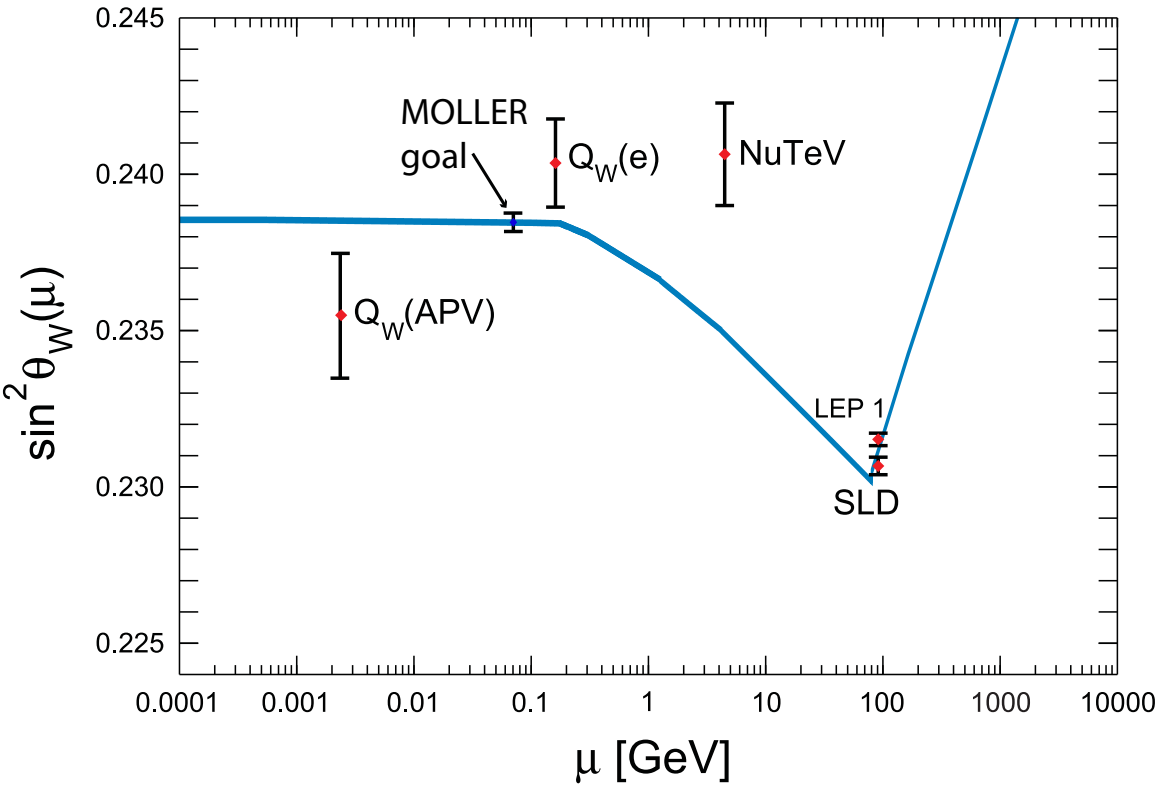


Figure 3: *The three most precise measurements of the weak mixing angle measurements vs. the energy scale $\mu$ are shown as red diamonds with error bars; the curve is reproduced from the PDG [20]. The APV result reflects the reanalysis in Ref. [18]. The $Q_W(e)$ point is the E158 result [3]. The NuTeV point is the extracted value from the original publication result [21]. The proposed MOLLER measurement is shown at the appropriate $\mu$ value and the proposed error bar but with the nominal SM prediction as the central value.*

of the weak interactions, and the level of photon-$Z^0$ boson mixing. The three fundamental inputs are chosen to be $\alpha$ (from the Rydberg constant), $G_F$ (from the muon lifetime) and $M_Z$ (from the LEP $Z^0$ line-shape). Precise theoretical predictions for other experimental observables at the quantum-loop level can be made if experimental constraints on the strong coupling constant and heavy particle masses, such as $m_H$ and the top quark mass, $m_t$, are also included.

Precision measurements of the derived parameters such as the W boson mass $M_W$, and the weak mixing angle $\sin^2\theta_W$ are then used to test the theory at the level of electroweak radiative corrections. Consistency (or lack thereof) of various precision measurements can then be used to search for indications of BSM physics. One important new development is the discovery of the scalar resonance at LHC with mass of about 126 GeV. Each individual observable used to extract values for $M_W$ and $\sin^2\theta_W$ can now be precisely predicted within the SM context.

A crucially important additional feature of MOLLER $A_{PV}$ is that the measurement will be carried out at $Q^2 \ll M_Z^2$. The two best measurements of the weak mixing angle at lower energies are those extracted from the aforementioned SLAC E158 measurement [3], and the measurement of the weak charge of $^{133}$Cs [17] via studies of table-top atomic parity violation. The interpretation of the latter measurement in terms of an extraction of the weak mixing angle has been recently updated [18]. A precise measurement of the weak charge of the proton is expected from the JLab Qweak experiment via the measurement of $A_{PV}$ in elastic electron proton scattering; the first result from the commissioning run was recently published [19].

Since $\sin^2\theta_W$ "runs" as a function of $Q^2$ due to electroweak radiative corrections, one can use $\sin^2\theta_W$ as a bookkeeping parameter to compare the consistency of the full $Q^2$ range of weak neutral current measurements, as shown in Fig. 3. The theory error in the low energy extrapolation is comparable to the width of the line in the figure [6]. MOLLER $A_{PV}$ would be the first low $Q^2$ measurement to match the precision of the single best high energy measurement at the $Z^0$ resonance. As discussed previously and also further elaborated in the following with additional examples, low energy measurements have enhanced sensitivity to new physics. MOLLER will build on the pioneering low $Q^2$ measurements shown in the figure to extend the discovery reach for new physics not only to the multi-TeV scale but also, as shown in the following, to light new degrees of freedom.

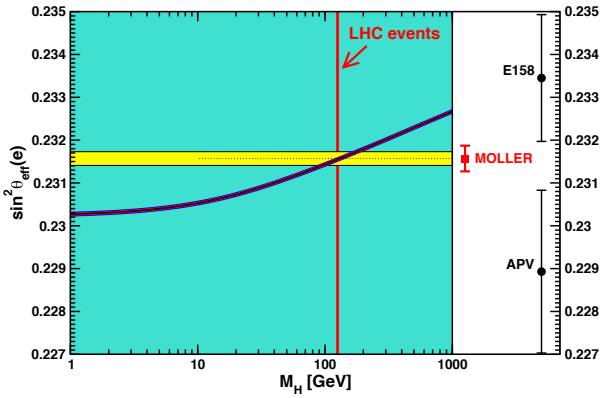


Figure 4: $\sin^2\theta_W$ *vs* $m_H$. *The yellow band is the world average. The black points are the two most precise measurements at* $Q^2 \ll M_Z^2$. *The projected MOLLER error is shown in red.*

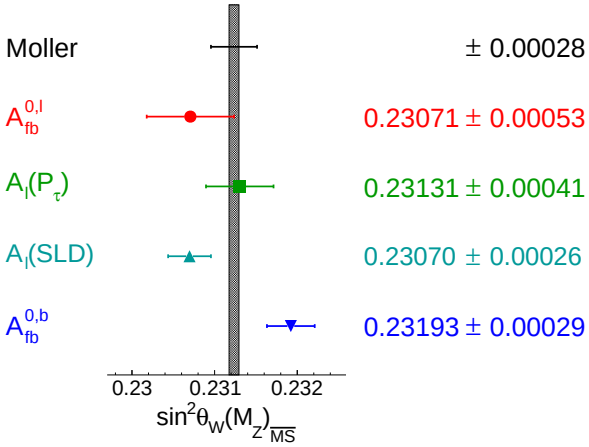


Figure 5: *The four best* $\sin^2\theta_W$ *measurements and the projected error of the MOLLER proposal. The black band represents the theoretical prediction for* $m_H = 126$ *GeV.*

Figure 4 shows the dependence of $\sin^2\theta_W$ to $m_H$ and the two best published low energy measurements (evolved to $Q \sim M_Z$) discussed above, as well as the projected $A_{PV}$ error. Remarkably, a variety of BSM dynamics, such as those discussed in previous sections, can have a significant impact on low $Q^2$ observables while having much reduced impact on corresponding measurements made at colliders. This is because interference effects are highly suppressed on top of the $Z^0$ resonance; those measurements account for the bulk of the statistical weight in high energy grand averages. Since the low energy measurements at the moment span the entire y-axis range in Fig. 4, there is a $\pm 10$ $\sigma$ discovery potential in the phase space allowed by the existing most precise low energy measurements given the proposed MOLLER $A_{PV}$ uncertainty.

Figure 5 shows the four best measurements of $\sin^2\theta_W$ from studies of $Z^0$ decays [22] and the projected uncertainty from MOLLER $A_{PV}$. Also shown is the Standard Model prediction for $m_H = 126$ GeV. The bottom two point are the constraints from the most precise single determinations of $\sin^2\theta_W$: the left-right asymmetry in $Z$ production at SLC ($A_l$(SLD)) and the forward-backward asymmetry in $Z$ decays to b-quarks ($A_{fb}^{0,b}$). Each of the two measurements taken independently implies very different BSM dynamics [23].

The proposed MOLLER $A_{PV}$ measurement would achieve a sensitivity of $\delta(\sin^2\theta_W) = \pm 0.00028$. That is the most precise anticipated weak mixing angle measurement currently proposed over the next decade at low or high energy. The most precise proposed weak charge measurement is the Mainz MESA P2 proton weak charge measurement with anticipated precision $\delta(\sin^2\theta_W) = \pm 0.00031$. Proposals for

anti-neutrino scattering, both deep-inelastic [24] and elastic [25], also fall short of the MOLLER projection. In particular, elastic anti-neutrino-electron scattering is the best direct comparison to MOLLER as a purely leptonic low $Q^2$ measurement. Reactor experiment projections have fallen short of the proposed MOLLER goal. Matching MOLLER precision and accuracy likely would require beta-beams or neutrino factories. Finally, the projected uncertainty from forward-backward asymmetries after 300 fb$^{-1}$ integrated luminosity at the LHC is a systematics limited $\delta(\sin^2\theta_W) = \pm 0.00036$, with the dominant error being from parton distribution function (pdf) uncertainties [26].

### 1.3.2 New Physics Beyond the Standard Model

The MOLLER experiment would measure a unique observable and be among the most sensitive in terms of discovery reach for flavor- and CP- conserving scattering amplitudes in the next decade; see recent reviews that situate the measurement in broader contexts [27–29]. It is very complementary to other precision low energy experiments and the energy frontier efforts at the LHC. If the LHC continues to agree with the Standard Model with high luminosity running at the full 14 TeV energy, then MOLLER will be a significant component of a global strategy to discover signatures of a variety of physics that could escape LHC detection. Examples include hidden weak scale scenarios such as compressed supersymmetry [30], lepton number violating amplitudes such as those mediated by doubly charged scalars [31], and light MeV-scale dark matter mediators such as the "dark" Z [32, 33]. If the LHC observes an anomaly, then MOLLER will have the sensitivity to be part of a few select measurements that will provide important constraints to choose among possible beyond the Standard Model (BSM) scenarios to explain the anomaly. Examples of such BSM scenarios that have been explicitly considered for MOLLER include: new particles predicted by the Minimal Supersymmetric Standard Model observed through radiative loop effects (R-parity conserving) or tree-level interactions (R-parity violating) [34, 35] and TeV-scale $Z'$s [36] which arise in many BSM theories.

A fairly general and model-independent way to quantify the energy scale of BSM high-energy dynamics (that MOLLER is sensitive to) is to express the resulting new amplitudes at low energies in terms of **contact interactions** (dimension-6 non-renormalizable operators) among leptons and quarks [37]. Specializing here to vector and axial-vector interactions between electrons and/or positrons, the interaction Lagrangian is characterized by a mass scale $\Lambda$ and coupling constants $g_{ij}$ labeled by the chirality of the leptons. For the MOLLER $A_{PV}$ measurement with 2.4% total uncertainty (and no additional theoretical uncertainty) the resulting sensitivity to new 4-electron contact interaction amplitudes can be expressed as:

$$\frac{\Lambda}{\sqrt{|g_{RR}^2 - g_{LL}^2|}} = \frac{1}{\sqrt{\sqrt{2}G_F|\Delta Q_W^e|}} \simeq \frac{246.22\text{ GeV}}{\sqrt{0.023 Q_W^e}} = 7.5\text{ TeV}. \tag{2}$$

For example, models of lepton compositeness are characterized by strong coupling dynamics. Taking $\sqrt{|g_{RR}^2 - g_{LL}^2|} = 2\pi$ shows that mass scales as large as $\Lambda = 47$ TeV can be probed, far beyond the center of mass energies of any current or planned high energy accelerator. This allows electron substructure to be studied down to the level of $4 \times 10^{-21}$ m.

The remarkable feature of the MOLLER sensitivity to four-lepton flavor-conserving contact interactions has been emphasized recently [38]. Not only does the contact interaction scale reach exceed those at LEP-200, the highest energy electron-positron collider to collect data, but there is unique sensitivity to a specific linear combination of left- and right-handed four electron operators to which all other collider measurements happen to be insensitive. Indeed, in the current global analysis, the E158 result [3] is used to break the degeneracy. The MOLLER measurement will allow the extension of the current limits for these operators from about 2 TeV to more than 7 TeV.

The MOLLER measurement is sensitive to Beyond the Standard Model (BSM) scenarios that predict observable consequences at the LHC and those that might escape detection there. If the **LHC observes an anomaly** in the next decade, then MOLLER will have the sensitivity to be part of a few select measurements that will provide important constraints to choose among possible BSM scenarios to explain the anomaly. One example of such a scenario are new, **super-massive $Z'$ bosons** with masses in the multi-TeV range, as predicted in many BSM theories. The MOLLER $A_{PV}$ measurement would see a a statistically significant deviation in many models that predict $Z'$ bosons in the 1–3 TeV mass range. Specific examples have been considered in [36] for a fairly large class of family-universal models contained in the $E_6$ gauge group.

Should a $Z'$ resonance in the 1–3 TeV range be found at the LHC, the importance of off-peak LHC data as well as low-energy precision EW data to completely disentangle all of the chiral $Z'$ couplings to SM particles has been emphasized [39], with MOLLER providing important constraints. Another important class of BSM physics that could have signatures both at the LHC and in MOLLER are new particles predicted by the **Minimal Supersymmetric Standard Model** observed through radiative loop effects (R-parity conserving) or tree-level interactions (R-parity violating) [34, 35]. The RPV and RPC models generate effects of opposite sign in the weak charge. The difference is not academic, since RPC would imply that the lightest supersymmetric particle is stable and therefore an obvious candidate for the non-baryonic dark matter which is needed to understand galactic-scale dynamics. On the other hand, RPV would imply that neutrinos are Majorana particles.

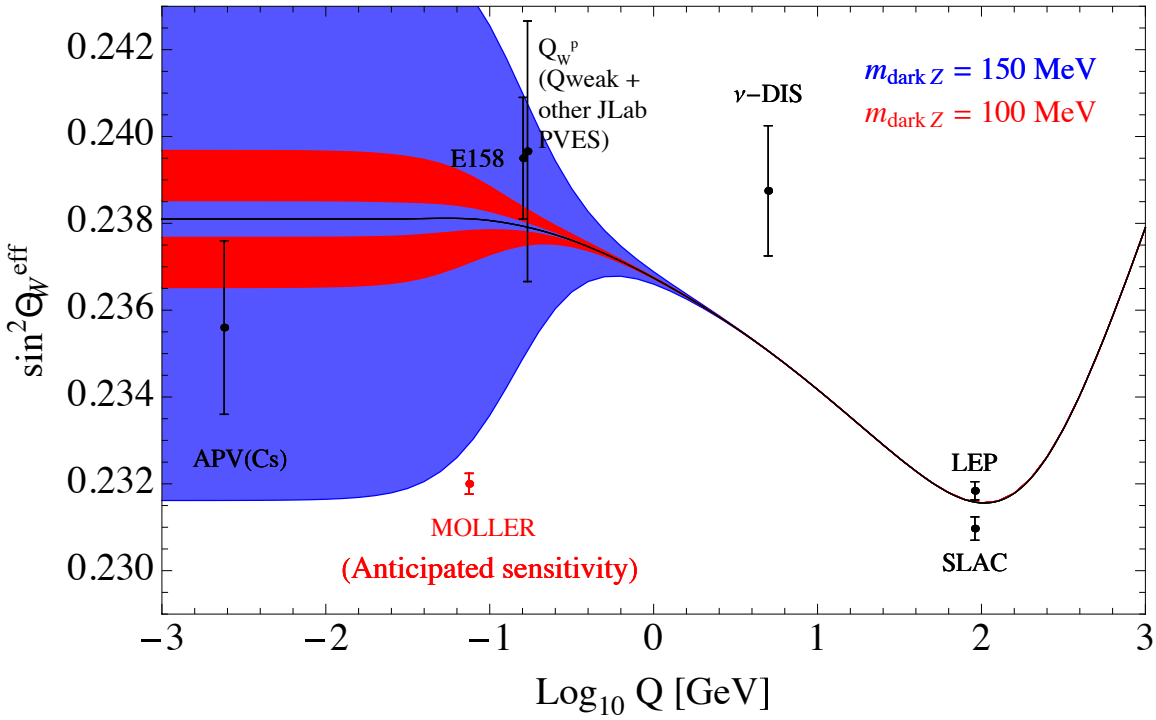


Figure 6: *The potential deviations of* $\sin^2\theta_W(Q)$ *under the scenario of small parity-violating admixture of a light* $Z_d$ *to explain the* $(g-2)_\mu$ *anomaly is shown for two different masses, taking into account rare kaon decay constraints. Also shown is the extracted* $\sin^2\theta_W$ *from the value of the weak charge of the proton* $Q_W^p$ *quoted in the recently published Qweak result from the commissioning run [19]. The proposed MOLLER measurement is shown at the appropriate Q value and the proposed error bar but with an arbitrary central value. Note: the sign of the deviation is model-dependent.*

If the **LHC continues to agree with the Standard Model** wtih high luminosity running at the full 14

TeV energy, then MOLLER will be a significant component of a global strategy to discover signatures of a variety of physics that could escape LHC detection. One example is hidden weak scale scenarios such as **compressed supersymmetry** [30]. Such a situation would occur if one of the superpartner masses is relatively light, as would be the case if the super-partner masses were nearly degenerate. In that scenario, the LHC signatures would be very challenging to disentangle from QCD backgrounds. Another example is lepton number violating amplitudes mediated by **doubly charged scalars**. The MOLLER measurement is one of the rare low $Q^2$ observables with sensitivity to such amplitudes, which naturally arise in extended Higgs sector models containing complex triplet representations of SU(2). In a left-right symmetric model, for example, the proposed MOLLER measurement would lead to the most stringent probe of the left-handed charged scalar and its coupling to electrons, with a reach of

$$\frac{M_{\delta_L}}{|h_L^{ee}|} \sim 5.3 \text{ TeV},$$

significantly above the LEP 2 constraint of about 3 TeV. Moreover, such sensitivity is complementary to other sensitive probes such as lepton-flavor violation and neutrinoless double-beta decay searches [31].

Finally, the interesting possiblity of a light MeV-scale dark matter mediator known as the **"dark" Z** [32, 33] has been recently investigated. It is denoted as $Z_d$ and of mass $m_{Z_d}$, and it stems from a spontaneously broken $U(1)_d$ gauge symmetry associated with a secluded "dark" particle sector. The $Z_d$ boson can couple to SM particles through a combination of kinetic and mass mixing with the photon and the $Z^0$-boson, with couplings $\varepsilon$ and $\varepsilon_Z = \frac{m_{Z_d}}{m_Z}\delta$ respectively. In the presence of mass mixing ($\delta \neq 0$), a new source of "dark" parity violation arises [32] such that it has negligible effect on other precision electroweak observables at high energy, but is quite discernable at low $Q^2$ through a shift in the weak mixing angle [33]. Recently, it has been pointed out [40] that the existing constraints are considerably weakened if the "dark" $Z$ decays to other dark matter particles, rendering the branching ratio $Z_d \to e^+e^- \ll 1$. In such a scenario, the only constraints on $Z_d$ masses in the range between 50 and 200 MeV would come from neutral current parity-violation measurements and rare kaon decay experiments ($K \to \pi + Z_d$, $Z_d \to$ missing energy). Figure 6 shows the range of possible deviations to $\sin^2\theta_W(Q)$ for $Z_d$ mass of 100 and 150 MeV, under the scenario that the "dark" Z explains the $(g-2)_\mu$ anomaly, but taking into account constraints from the K decay measurements. It can be seen that the proposed MOLLER $A_{PV}$ measurement has significant discovery potential under this scenario.

In summary, the discovery reach of the proposed MOLLER measurement is unmatched by any proposed experiment measuring a flavor- and CP-conserving process over the next decade. It results in a unique window to new physics at MeV and multi-TeV scales, complementary to direct searches at high energy colliders such as the Large Hadron Collider (LHC).

## 2 Experimental Design

A CAD-generated rendition of the layout of the MOLLER apparatus to be placed in Hall A at JLab is shown in Fig. 7. In this section, we provide an overview of the experimental design and discuss the main subsystems. We start by listing the main experimental parameters in Table 1. Many of the technical choices are driven by the requirement to measure a very small parity-violating asymmetry, and consequently the need to measure the scattered electron flux at an unprecedentedly high rate. The MOLLER design is grounded on the extensive experience gained by the collaboration from completed high flux integrating (as opposed to counting individual particles) parity-violation measurements such as MIT-Bates $^{12}$C [41], SAMPLE [42], HAPPEX [43] and SLAC E158 [3] as well as ongoing projects such as PREX [44] and Qweak [45].

Table 1: *Nominal design parameters for the proposed $A_{PV}$ measurement. Note that some of the design parameters will change at the few percent level as the design is further optimized.*

| Parameter | Value |
|---|---|
| $E$ [GeV] | $\approx 11.0$ |
| $E'$ [GeV] | 1.7 - 8.5 |
| $\theta_{cm}$ | 46°-127° |
| $\theta_{lab}$ | 0.23°-1.1° |
| $\langle Q^2 \rangle$ [GeV$^2$] | 0.0058 |
| Maximum Current [$\mu$A] | 85 |
| Target Length (cm) | 150 |
| $\rho_{tgt}$ [g/cm$^3$] (T= 20K, P = 35 psia) | 0.0715 |
| Max. Luminosity [cm$^{-2}$ sec$^{-1}$] | 3.4·10$^{39}$ |
| $\sigma$ [$\mu$Barn] | $\approx 40$ |
| Møller Rate @75 $\mu$A [GHz] | $\approx 137$ |
| Statistical Width(2 kHz flip) [ppm/pair] | $\approx 89$ |
| Target Raster Size [mm] | 5 x 5 |
| $\Delta A_{raw}$ [ppb] | $\approx 0.6$ |
| Background Fraction | $\approx 0.09$ |
| $P_{beam}$ | $\approx 80\%$ |
| $< A_{pv} >$ [ppb] | $\approx 35$ |
| $\Delta A_{stat} / < A_{expt} >$ | 2.1% |
| $\delta(\sin^2 \theta_W)_{stat}$ | 0.00023 |

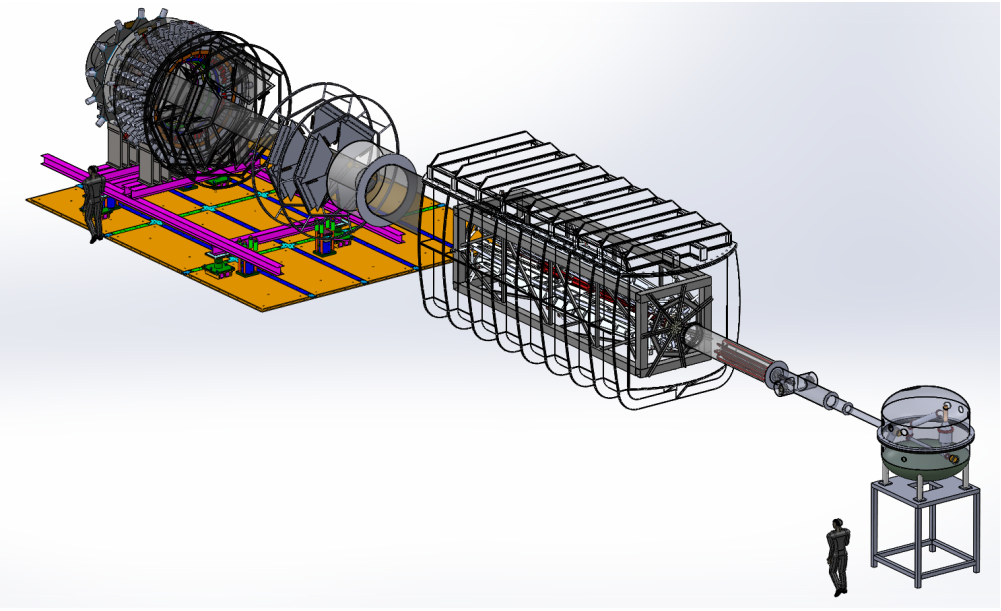

Figure 7: *Layout of the target, spectrometer and detectors. Distance between two the figures is* $\sim 28\mathrm{m}$.

## 2.1 Polarized Beam

The MOLLER apparatus is being designed to fit into Hall A, where a 11 GeV beam will be incident on a liquid hydrogen target. Fixed target Møller scattering is rather special because the QED cross-section is proportional to $1/E_{\rm beam}$, and the figure of merit for $A_{PV}$ rises linearly with beam energy. The projections for MOLLER are made assuming a 11 GeV, 75 $\mu$A electron beam with 80% polarization and with the anticipated stable beam conditions extrapolated from the extensive experience on "parity quality" beams from the 6 GeV experiments. The upgraded JLab beam is thus a unique opportunity to carry out the proposed MOLLER measurement; indeed these conditions are unavailable in any other currently running or planned accelerator facility worldwide.

The polarized electron beam is created using a technology first developed at SLAC to enable the original parity-violating electron scattering experiment [46]: laser-induced photoemission from a GaAs wafer. The circular polarization of the laser light, controlled by the polarity of the voltage across a Pockels cell [1], determines the sign of the longitudinal polarization of the emitted electron bunch, thus facilitating rapid helicity reversal of the electron beam. Time "windows" are generated in the electron bunch train at a frequency of 1.92 kHz, with the sign of the beam's longitudinal polarization in each window assigned on a pseudo-random basis (with a set pattern of 32 windows optimized to eliminate 60 Hz noise). The design of the apparatus is based on a maximum beam intensity of 85 $\mu$A.

Nearby time windows of opposite helicity form window-pairs. The time-averaged responses of beam position monitors characterize the beam trajectory and energy for each window. The monitoring instrumentation has to be precise enough so that the relative cross section (except for statistical fluctuations) is stable over nearby time windows at the level one part in $10^5$, after beam fluctuations are regressed out. Therefore, beam properties must be measured window by window with high precision and further, the variance of window pair differences must be small. Quantitatively, the beam centroid fluctuations must be tracked with precision at the level of a few microns, and should be stable to $\sim$10's of microns, at 1 kHz[2].

Averaged over the entire data collection period, the beam trajectory must remain unchanged with respect to the sign of the electron beam polarization at the sub-nanometer level in order to keep beam-related false asymmetry corrections at the 1 ppb level. It will be necessary to use a "slow reversal" of beam helicity to further cancel systematic errors to the 0.1 ppb level, from sources such as residual electronics cross-talk and higher-order effects such as potential helicity-dependent variations in the beam spot size. These considerations are discussed in the following and in Sec. 3.1.

### 2.1.1 Polarized Electron Source

Laser light illuminates a semiconducting photocathode, the surface of which has been chemically treated to produce a negative work function, referred to as a negative electron affinity (NEA) surface. The laser light wavelength is tuned to promote electrons from a specific valence band to the conduction band of the semi-conductor. The photocathode is held at a negative potential, so as the electrons from the conduction band exit the cathode they are accelerated into the injector beamline.

Through doping or other stress applied to the photocathode, the degeneracy in the spin-orbit states of the specific valence band are split, as shown in Fig. 8. For circularly polarized light, the spin-1 photon is restricted to exclusively promote electrons to a single spin state. This process produces an electron beam polarization of nearly 100%, however, some depolarization occurs in the diffusion of the liberated electrons to the photoconductor surface. The CEBAF polarized source now routinely provides close to $\sim 90\%$ polarization with nearly 200 $\mu$A beam current. Since the electron polarization is fully determined by the

[1] The Pockels cell is a birefringent crystal whose phase retardation is directly proportional to the applied potential difference; $\sim \pm 2.5$ kV is required to produce $\pm\pi/4$ retardation for a wavelength of $\sim 800$ nm.

[2] This does not include 60 Hz noise, since data will be collected in time-slots phased to 60 Hz.

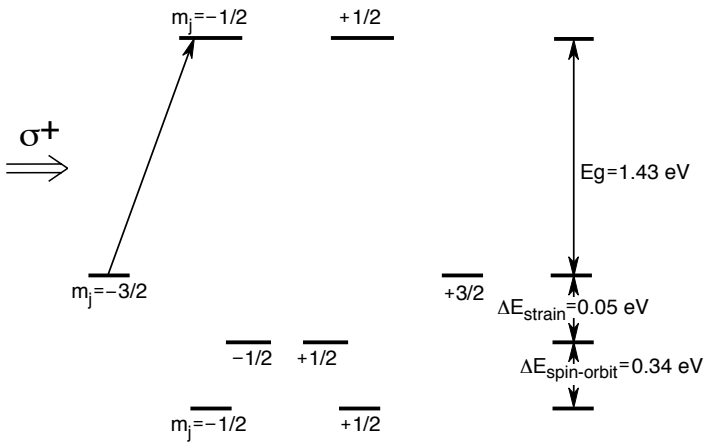


Figure 8: *Band structure of GaAs, showing how circularly polarized laser light produces polarized electrons.*

circular polarization of the incident laser light, it is possible to rapidly flip the helicity of the electron beam by changing the laser polarization. A reversal of the applied voltage on the Pockels cell reverses the circular polarization of the laser light, and thus the helicity of the electron beam. A schematic diagram of the experimental configuration is shown in Fig. 9.

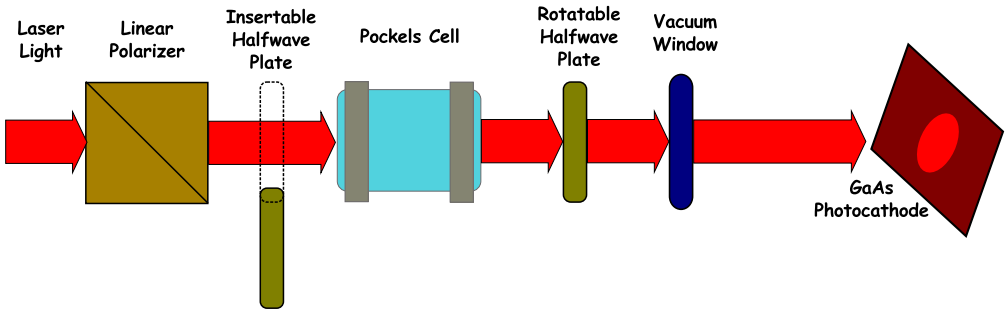


Figure 9: *Schematic of the laser transport line that allows for rapid reversal of the electron beam polarization.*

### 2.1.2 Operational Experience

There is significant operational experience in using the polarized electron source for parity-violation experiments at Jefferson Lab [58]. One challenge of these experiments is that changes in the beam properties (intensity, position, profile) will change the detected scattered flux. If the changes in the beam are correlated with the electron helicity, the result can mimic the tiny parity-violating asymmetries. While changes are typically measured and corrections are applied, the corrections are typically made with precision of around 10%. Helicity-correlated beam asymmetries (HCBAs) are therefore a potential systematic error in the measurement of small asymmetries, and a very high level of control of HCBAs is required for the precision measurement contemplated here.

A sophisticated understanding of the sources of HCBAs at JLab has been achieved. The HAPPEX-II experiment, which ran in Hall A in 2005, made use of this improved understanding to achieve run-averaged

helicity-correlated position differences, measured in the experimental hall, which were consistent with zero systematic offset with uncertainties of $< 2$ nm and $0.2$ nanoradian in angle (see Fig. 10).

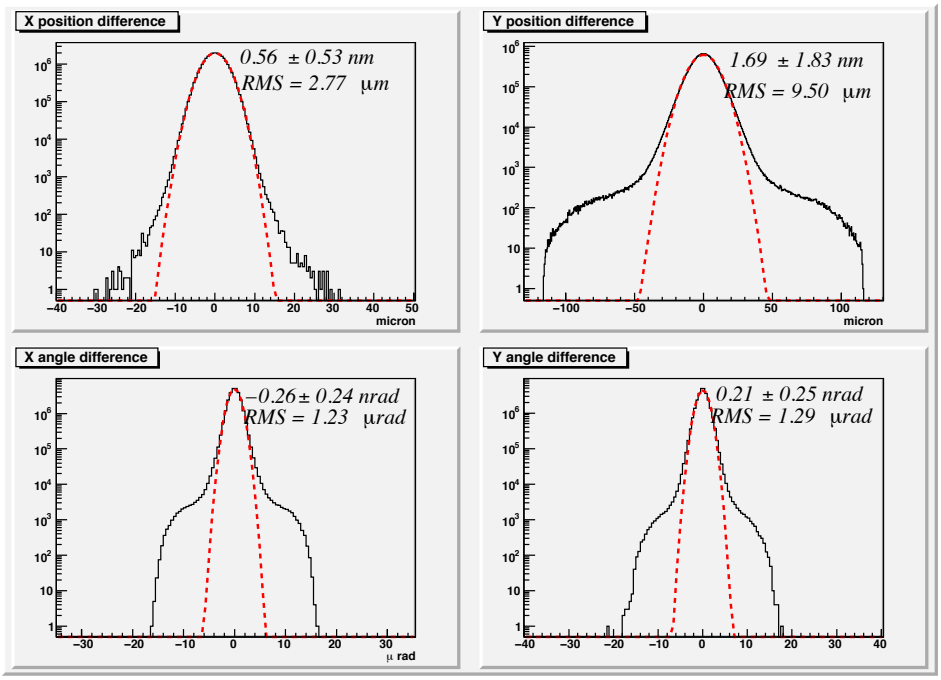


Figure 10: *Beam position and differences, plotted for all* $27 \times 10^6$ *pairs of the HAPPEX-II analysis. Arithmetic means, widths, and centroid uncertainty due to random noise are shown. The systematic correlation to helicity was measured to be consistent with zero within the random beam noise. Gaussian fits are included for reference.*

The PREX experiment, which ran in Hall A in early 2010, and the Qweak experiment, which ran in Hall C during the period October 2010 - May 2012, have statistical-precision goals that are approximately an order of magnitude better than what has been achieved previously at JLab. Regarding systematic effects, the PREX experiment ultimately aims to keep helicity correlated beam motion to $< 1$ nm (HAPPEX-II achieved $< 2$ nm) and to bound the beam spot difference to $< 10^{-4}$ of the intrinsic beam size. In the 2010 run, with only eight days of production beam, correlated beam motion was held to $< 4$ nm with no feedback, a notable achievement in such a short running time when other problems, mostly vacuum related, dominated. We note that polarized-source setup for that run, fine-tuned to reduce systematics, was likely the best ever achieved to that point. Even smaller position differences in the early injector were achieved during the polarized-source setup for the Qweak experiment; further details of that work are discussed in Sec. 3.1. Given what has been learned about source-related systematics, the goal of holding helicity-correlated beam motion to $< 0.5$ nm for MOLLER is achievable with careful planning. Between further PREx running (PREx-II is tentatively scheduled to run in 2018), and lessons learned from the completed Qweak experiment, valuable experience will have been gained toward meeting the stated MOLLER goals for controlling HCBAs.

### 2.1.3 Rapid Helicity Flip

Most previous parity-violation experiments at Jefferson Lab have used a rapid helicity reversal frequency of 30 Hz, which had the benefit of largely cancelling beam jitter and electronics noise related to 60 Hz line noise. The recently completed Qweak experiment used a faster helicity reversal frequency of 960

Hz, primarily to be above the frequency range where density fluctuations in the high-power cyrotarget are significant. To reduce the contribution of target density fluctuations even further, MOLLER is designing around a flip rate of at least 2 kHz, which implies that each helicity state is held for 500 microseconds. In order to avoid excess noise from 60 Hz line variations, a scheme for selecting helicity states will be used which will force complementary pairs at corresponding points in the 60 Hz cycle.

The goal is to flip the Pockels cell within 10 $\mu$s, which implies a dead-time of 2%. At present, a settling time of 60 $\mu$s is achievable for reversal rates of 960 Hz with KD*P Pockets cell technology. However, it has proven difficult to push the transition of the Pockels cell to be shorter than 60 $\mu$s while keeping the cell optical properties stable after the shock of the fast transitions. Additional studies of switching with the Pockels cell will explore possible improvements from both shaping the leading edge of the voltage transition and electrical or mechanical damping of oscillations. Current R&D efforts (see Sec. 5.1.1) are focussed on RTP (Rubidium Titanyl Phosphate) Pockels cells, where initial studies have demonstrated a $\sim$ 12 $\mu$sec settling time with virtually none of the ringing that is observed with KD*P.

## 2.2 Liquid Hydrogen Target

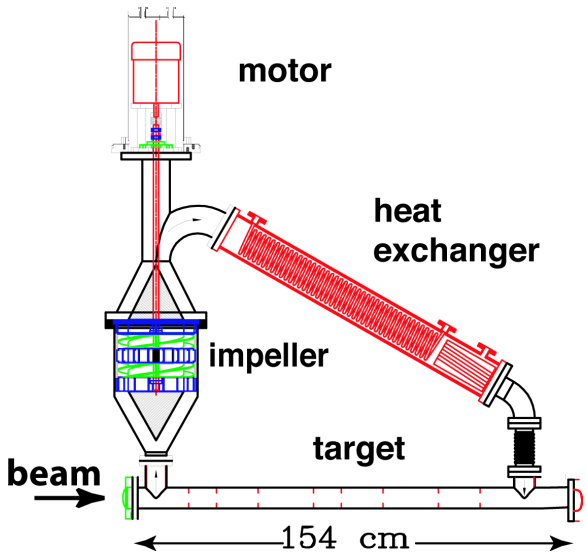


Figure 11: *The SLAC E158 target loop is shown. Liquid flows clock-wise in the picture (downstream to upstream). The liquid-gas interface is just below the motor. MOLLER proposes to use it as a prototype.*


Figure 12: *A CAD drawing of the SLAC E158 target chamber. The target loop is remotely movable 6" in the vertical direction. A table containing optics targets can be moved in and out horizontally.*

After acceleration to 11 GeV, the electron beam will impinge on a liquid hydrogen ($LH_2$) target. Hydrogen is the ideal source of target electrons for two reasons. First, it provides the greatest electron target thickness for the least radiation length. Secondly, the irreducible backgrounds are confined to radiative electron-proton elastic and inelastic scattering, which are relatively well-understood. Scattering off other nuclei would include radiative elastic scattering ($\propto Z^2$), breakup channels and scattering off neutrons, which would introduce significant systematic errors due to unknown and potentially large electroweak couplings.

In order to achieve the necessary rate, more than 10 g/cm$^2$ of $LH_2$ is needed, making the target cell about 150 cm long, which in turn requires a cryogenic target system capable of handling a heat load of $\sim$ 5 kW

from the beam. This is far larger than the typical $\sim$ 1 kW targets that are routinely in use and about twice as large as the target for the Qweak experiment. A plan for adequate target cooling at the JLab site has been formulated.

The preliminary assessment is that the E158 target cell is a good starting point for the design of the high power target required for MOLLER. Figure 11 shows the E158 target loop containing the main target cell, impeller, hydrogen motor and heat exchanger. The hydrogen flowed against the beam direction. The target loop was housed in a scattering chamber (Fig. 12) which also contained a table with auxiliary targets, with the capability to move both remotely, the main target loop vertically and the table horizontally. The target chamber also serves as a secondary containment vessel for hydrogen, which is a safety requirement. The design of the MOLLER target will make use of computational fluid dynamics (CFD), a key development which has been validated by the successful operation of the Qweak target.

The most important target design consideration is the suppression of density fluctuations at the timescale of the helicity reversal rate. Preliminary estimates based on operational experience with the Qweak target suggest that density fluctuations can be maintained at $\lesssim$ 26 ppm at 1.92 kHz, corresponding to 5% excess noise to counting statistics. In the following subsections, we discuss some of the aforementioned technical considerations.

### 2.2.1 Comparable Targets

Unpolarized $LH_2$ targets with internal heat dissipation of up to 1 kW have been successfully and safely run in the SAMPLE, HAPPEX, PVA4, G0 and E158 experiments. The $LH_2$ target for the Qweak experiment is the first target in the world that has significantly exceeded 1 kW in internal heating. It was successfully operated up to 3 kW, higher than its design power of 2.5 kW, between 2010-2012.

Although these targets could not be more different in geometry and experimental conditions, they all have as a central part a cryogenic closed re-circulation loop, made of a thin-windowed cell traversed by the beam, a heat exchanger, an in-line pump and a high power heater. The central part of the cryogenic loop is the target cell as it is the region where the interaction between the target fluid and the $e^-$ beam takes place. The rest of the loop is designed around the cell to satisfy the needs for cooling power and fluid flow.

In this respect the MOLLER target will have the same conceptual components as previous $LH_2$ targets. The design will have to satisfy the detector acceptance requirements, and, more stringently for such a high luminosity and high precision experiment, the target density fluctuations that affect the physics measurement will have to be minimized. In nominal running conditions the MOLLER target is rated for 5 kW.

The Qweak target was the first one designed with CFD at Jefferson Lab. The CFD software engines used were `FLUENT 6.3` and `FLUENT 12.0` developed by Fluent Inc. (now part of ANSYS). The Qweak target was commissioned in 2010 and its measured performance indicates that its design goals have been met. The target has been successfully operated with 3 kW of cooling power. It has been run at beam currents between 150 and 180 $\mu$A. The target boiling contribution to the asymmetry width has been measured using several techniques. In nominal running conditions, 180 $\mu$A beam current, 30 Hz $LH_2$ pump rotation, 4x4 $mm^2$ beam rastered spot on the target cell and 960 Hz helicity frequency, the measured target noise was 46 ppm. The counting statistics for the Qweak asymmetry measured in quartets of beam helicity states was estimated to be 200 ppm. In nominal running conditions the target noise increased the asymmetry width by less than 3%. The bulk density changes have also been bounded to 0.8% at 180 $\mu$A. CFD estimated a density loss of 0.8% in nominal running conditions for the Qweak target, the same as the measured upper bound. The data accumulated with the Qweak target will be used to benchmark the simulations, thus reducing technical risk.

### 2.2.2 Target Parameters

The MOLLER experiment at 11 GeV proposes using a 150 cm long liquid hydrogen target cell. The design beam intensity is 85 $\mu$A and the nominal beam raster size is 5 mm x 5 mm. The nominal running point for $LH_2$ in the thermodynamic phase space $(p, T)$ is 35 psia (2.38 atm) and 20 K, although these parameters might change slightly depending on the refrigeration solution for the target. In these conditions the liquid is 3.7 K subcooled and its density is 71.5 kg/m$^3$. The target thickness is 10.72 g/cm$^2$ and its radiation length is 17.5 %. The heating power deposited by the $e^-$ beam in the target cell is given by

$$P = I\rho L\frac{dE}{dx} \tag{3}$$

where $\rho L$ is the nominal target thickness in beam, $I$ is the beam intensity and $dE/dx$ is the average energy loss through collisions of one electron in unit target thickness. If $dE/dx = 4.97$ MeV/(g/cm$^2$) for electrons of 11 GeV in $LH_2$ then $P = 4533$ W. For an Al target cell made with beam entrance and exit windows of 0.127 mm (0.005 inches) each, the heat deposited by the beam in the windows, calculated with Eq. 3, is 6.4 W per window. The cumulative beam heating in the target cell is then 4546 W. The nominal parameters of the target and beam are in Table 2. In order to minimize target density variations, all high power $LH_2$

Table 2: *MOLLER $LH_2$ target and beam nominal parameters.*

| Target Parameters | | Beam Parameters | |
|---|---|---|---|
| cell length | 150 cm | I, E | 85 $\mu$A, 11 GeV |
| cell thickness | 10.72 g/cm$^2$ | raster | 5 mm x 5 mm |
| radiation length | 17.5 % | beam spot | 100 $\mu$m |
| p, T | 35 psia, 20 K | detected rate | 170 GHz |
| $\phi$ acceptance | 5 mrad (0.3°) | helicity flip rate | 2000 Hz |
| target power | **5000** W | beam power | **4546** W |
| $\rho$ fluctuations <26 ppm | | | |

targets run in a closed feedback loop with the high power heater, allowing a constant heat load on the target to be maintained over time. The heater needs to account for beam heating and target power losses to the environment (such as radiative and viscous losses) and to maintain a cooling power buffer for the feedback loop. Based on experience with previous such targets, the losses and the buffer account for about 10 % of the beam heating. Taking this into account the MOLLER target is rated for 5000 W of cooling power in nominal running conditions, which is a factor of 2 higher than the Qweak target rating, and by far the most powerful $LH_2$ target ever built and with the most stringent requirements on systematic effects.

The measured detector asymmetry width for the MOLLER detector is given by $\sigma_m^2 = \sigma_A^2 + \sigma_b^2$, where $\sigma_A$ is the counting statistics width and $\sigma_b$ accounts for systematic effects independent of counting statistics, which are typically dominated by the target density fluctuations (boiling) on the time scale of the electron beam helicity pair. For the current design parameters, the projected counting statistics width for the experiment is about 83 ppm. Target density fluctuations on the level of less than 26 ppm would contribute only a few % to the measured asymmetry width $\sigma_m$.

### 2.2.3 Density Variation

The MOLLER target will use $LH_2$ as the target material and it thus contributes two important systematic uncertainties to the physics measurement: density reduction and density fluctuations. The equation of state

of the target fluid in steady-state isobaric conditions is $\rho(p,T) = \rho(T)$. Density reduction is the effect of the fluid density variation with temperature caused by beam heating over the volume of the target cell illuminated by the beam. A $LH_2$ temperature increase of 1 K causes a density reduction of $\Delta\rho/\rho \approx 1.5$ %. Whenever the beam is on target, a dynamic equilibrium is established in the interaction region, where the temperature of the fluid increases locally with respect to the beam-off condition and the fluid density decreases, resulting in a net reduction of the target thickness in beam. If the target fluid density reduction is e.g. 5 % then the experiment would have to run 5 % longer to get the same statistics as expected from a fixed target density. This effect can be predicted with CFD and the target cell geometry can be designed to mitigate the $LH_2$ density loss.

Table 3: *Liquid hydrogen targets for parity violation experiments. The first group represents actual operating targets, while the last one is a target under design.*

| | p/T/$\dot{m}$<br>psia/K/kg/s | L<br>cm | P/I<br>W/$\mu$A | E<br>GeV | beam spot<br>mm | $\Delta\rho/\rho$<br>% | $\delta\rho/\rho$<br>ppm |
|---|---|---|---|---|---|---|---|
| SAMPLE | 25/20/0.6 | 40 | 700/40 | 0.2 | 2 | 1 | <1000<br>@60Hz |
| | | | | | 4.8x4.8 | | <100 |
| HAPPEX | 26/19/0.1 | 25 | 1000/100 | 3.481 | 6x3 | | @30Hz |
| PVA4 | 25/17/0.13 | 10 | 250/20 | 0.854 | 0.1 | 0.1 | 392<br>@50Hz |
| E158 | 21/20/1.8 | 150 | 700/11-12 | 45/48 | 1 | 1.5 | <65<br>@120Hz |
| G0 | 25/19/0.3 | 20 | 500/40-60 | 3 | 2x2 | 1.5 | <238<br>@30Hz |
| $Q_{weak}$ | 35/19/1 | 35 | 2500/180 | 1.165 | 4x4 | | <50<br>@240Hz |
| MOLLER | 35/20/1 | 150 | 5000/85 | 11 | 5x5 | | <26<br>@2000Hz |

In nominal running conditions a laminar fluid flow of 1 kg/s transverse to the beam axis and going through the beam volume in the MOLLER target would result in the fluid temperature increase of 0.5 K and a relative density decrease of less than 1%, which would be further decreased by turbulence effects. A summary of design parameters and target systematic effects for previous and future $LH_2$ targets used in parity violation experiments is presented in Table 3. The quoted target systematic effects for targets that have run before are the measured ones, for the MOLLER targets they are the desired ones. The two highest power $LH_2$ targets in the world have the most stringent requirements for target density fluctuation compared to previous targets.

There are three boiling regimes that can contribute to the target density fluctuation effect: nucleate, bubble and film boiling. Nucleate boiling could happen in subcooled liquids at low heat flux into the liquid, micro-bubbles could form, usually at boundaries, and recondensate as there is not enough heat to sustain

bubble growth. If the heat flux into the liquid increases the liquid reaches saturation and bubble boiling is possible. Bubble boiling starts usually at boundaries, but in forced convection flow, bubbles could break from boundaries and the flow becomes 2-phase flow. If the heat flux into the liquid increases further then neighboring bubbles on a boundary can connect with each other forming a continuous film of vapor on that boundary, called film boiling.

The target density fluctuation effect is usually dominated by the target cell windows region. The heat density deposited by the $e^-$ beam in the thin Al windows is typically one order of magnitude higher than the heat density deposited in $LH_2$. The heat deposited by the beam in the window material is dissipated through conduction in the window material and convection on only one side of the window, the $LH_2$ side, as the other side is exposed to vacuum. The target liquid boils at a window with high probability if two partially correlated effects happen simultaneously: surpassing the critical heat flux and a temperature excursion between the window and the bulk liquid greater than a few tens of degrees. Typically for these targets the heat flux from the window to $LH_2$ is much higher than the critical heat flux for boiling. The critical heat flux for $LH_2$ at a wall is on the order of 10 W/cm$^2$ [74]. The total heat flux at the windows in nominal conditions is 43 W/cm$^2$ for the G0, 78 W/cm$^2$ for the Qweak and 25.6 W/cm$^2$ for the MOLLER targets respectively. CFD simulations revealed that over the beam raster area the convective part of the total heat flux is 18 W/cm$^2$ for the G0 target and 33 W/cm$^2$ for the Qweak target. The temperature excursions determined with CFD for the G0 and the Qweak targets at the windows are on the order 30-50 K. The G0 and the Qweak targets seem likely to develop liquid boiling at the windows. Of these three targets the MOLLER target has the lowest total heat flux at the windows and careful CFD design could drop the convective part of the total heat flux below the boiling threshold.

From experience with previous $LH_2$ targets, the effect of density fluctuation is mitigated by optimizing both fluid conditions (flow, turbulence etc.) and beam conditions (raster size, intensity). The measurements done with the G0 target [75] at a helicity reversal frequency of 30 Hz indicate a drop by a factor of 2.4 in the magnitude of $LH_2$ density fluctuation when the raster size was increased from 2 mm to 3 mm at constant pump rotation, and by a factor of 3.5 when the $LH_2$ pump pressure loss was doubled at the same raster size.

The MOLLER collaboration plans to run with an electron beam helicity reversal frequency (1920 Hz) that is nearly two orders of magnitude greater than the 30 Hz that was routinely used for first generation parity experiments. More recently, the Qweak experiment successfully used a reversal rate of 960 Hz. As noted above, the counting statistics and target density fluctuation asymmetry widths add in quadrature to give the measured statistical width. The advantage of the higher helicity reversal frequency is that it is expected to reduce the relative contribution of the target density fluctuations to the measured asymmetry width. As the helicity reversal frequency is increased, the counting statistics width increases, while the expectation is that the target density fluctuation width will decrease (or at worst remain constant) with increasing frequency.

### 2.2.4 Density Fluctuation Estimate

To make an estimate of the target density fluctuation noise for the MOLLER target, we use the measured G0 target properties to extrapolate from. The G0 target cell had a longitudinal flow design similar to the E158 target cell, which we are using for prototyping a MOLLER target cell. The G0 target was run in the CW JLAB electron beam (as opposed to the pulsed beam used in the E158 experiment at SLAC). An upper limit of 238 ppm was observed for the target density fluctuation in the G0 target at 40 $\mu$A beam current. We estimate the density fluctuations in the MOLLER target by using conservative power laws for each of the parameters known to affect density fluctuations. We expect the target density fluctuations to vary inversely with the raster area, linearly with the beam power and linearly with the inverse mass flow rate; these expectations have been borne out by previous target studies. We assume a linear dependence on inverse mass flow rate, which seems to be the most conservative choice.

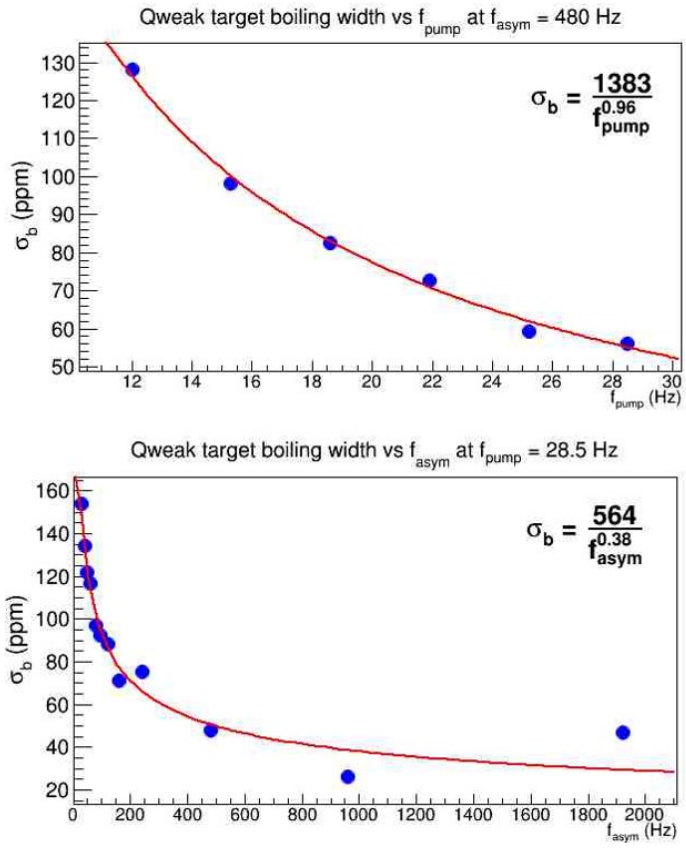


Figure 13: *Target density fluctuation noise versus $LH_2$ pump frequency (above) and versus beam helicity reversal frequency (below) from a Qweak target data analysis. In this analysis $f_{asym}$ for Qweak is 480 Hz and for MOLLER is 960 Hz, which are half the beam helicity reversal frequencies respectively.*

The extrapolation of target density fluctuation noise is expressed in Eqn. 4

$$\sigma_{b,M} = \sigma_{b,G_0} \frac{P_M}{P_{G_0}} \frac{A_{G_0}}{A_M} \frac{\dot{m_{G_0}}}{\dot{m_M}} \left( \frac{f_{G_0}}{f_M} \right)^{0.38} \tag{4}$$

where $\sigma_{b,G_0} = 238$ ppm, the MOLLER target power and beam raster area, $P_M$ and $A_M$, were taken from table 2. We assumed the same $LH_2$ mass flow rate for the MOLLER target as for the E158 target 1.8 kg/s and the dependence on the helicity reversal frequency was taken from a Qweak target data analysis showed in Fig. 13. Considering the nominal parameters for the G0 and the MOLLER targets respectively in eq. 4 the $LH_2$ density fluctuation noise of the MOLLER target is predicted to be 21 ppm or less than 5 % contribution to the parity violation asymmetry width.

The dependence of target density fluctuation noise, $\sigma_b$, on helicity reversal frequency from a Qweak target data analysis, fig. 13, was corroborated by an empirical power law measured during Qweak beam tests that were done in June 2008. Data were taken at helicity reversal frequencies of 30 Hz, 250 Hz, and 1000 Hz on both a carbon and a 20 cm hydrogen target (not the Qweak target) at a range of beam currents. The hydrogen target available for the test was not one that was optimally designed for minimization of density fluctuations, but we ran at a variety of beam currents to see if our conclusions were valid over a range of "boiling" conditions. The scattered electron rate was monitored with "luminosity" monitor detectors at small scattering angles. The data from the carbon target were used to determine the parameterization of

all sources of random noise other than the target density fluctuation effects in the hydrogen target. The result of the work was the target density fluctuation noise as a function of beam helicity reversal frequency determined at a variety of beam currents. A simple power law ($\sigma_b \propto f^{-0.4}$) describes the data well as a function of helicity reversal frequency $f$ for the beam currents of 40, 60, and 80 $\mu$A, which is almost the same as the power law from Fig. 13.

In summary, the assumed scaling arguments for estimating the target density fluctuation noise are: linear in beam power, inversely linear in beam raster area, linear in inverse mass flow rate, and $f^{-0.38}$ in beam helicity reversal frequency. The input parameters for the G0 target are an upper limit of 238 ppm target density fluctuations for a 20 cm long target, 40 $\mu$A beam current, 2 mm square raster size, 30 Hz helicity reversal rate, and 0.3 kg/s mass flow rate. The corresponding expected parameters for the MOLLER target are a target length of 150 cm, 85 $\mu$A beam current, 5 mm square raster size, 1920 Hz helicity reversal rate, and 1.8 kg/s mass flow rate.

### 2.2.5 Cell Design

A 150 cm long cell was used in the 55 liter $LH_2$ target for the E158 Møller scattering experiment at SLAC at 45 GeV and 48 GeV electron beam energies. The E158 target was rated for 700 W beam heating removal and 1000 W cooling power. The E158 target density fluctuations contributed 65 ppm [76] to a Møller detector asymmetry width of 200 ppm at a repetition rate of 120 Hz or about 5 % of the detector asymmetry.

A drawing of the target cell for the E158 experiment is in Fig. 14. The target was designed and built by a

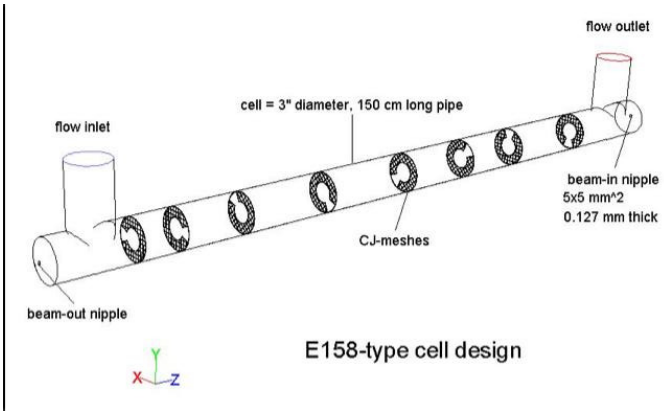


Figure 14: *E158-type target cell design. Note that the fluid flow (left to right) is opposite the electron beam direction (right to left).*

group from Caltech led Robert McKeown.

The cell is made of 3" ID pipe with a 3" inlet and outlet that are connected to the rest of the vertical cryogenic loop. Inside the target cell there are 8 wire mesh rings (see Fig. 14), with a $45^o$ cut-out and 1.5" diameter clearance in the middle. The rings are to increase fluid turbulence and mixing in the cell. This cell is a natural first candidate for a target cell for the MOLLER experiment at 11 GeV. For this reason the cell design from Fig. 14 was studied in a steady-state CFD simulation in `FLUENT` under the nominal running conditions from Table 2. The heating from the electron beam was implemented as a uniform power deposition in the volume of the cell illuminated by the rastered beam to yield 4.5 kW in this volume. The cell walls are made of Al and the beam heating in the windows was implemented also as a uniform power deposition to yield 12.5 W. Hydrogen properties are implemented as functions of temperature in isobaric conditions from the freezing point to 300 K. No boiling model was implemented for hydrogen. The mass

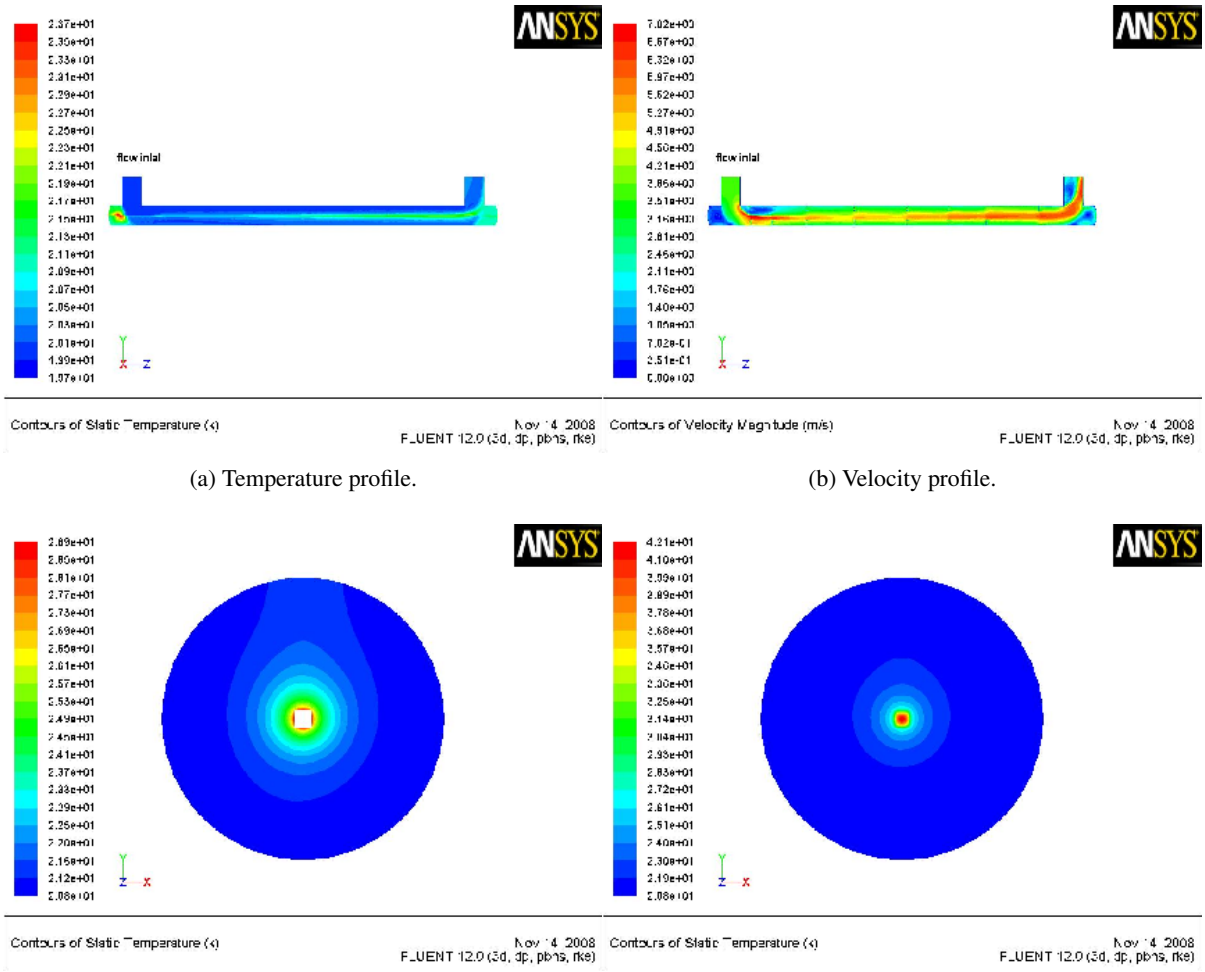


(a) Temperature profile.

(b) Velocity profile.

(c) Beam-out window without nipple.

(d) Beam-out window with nipple.

Figure 15: *CFD simulations of a E158-type cell in nominal conditions.*

rate considered was 1.2 kg/s. The cell volume is 7.8 liters. The cell was simulated both with meshes and without.

The results from Figs. 15a-15d are for the cell with internal meshes. The global temperature increase of the $LH_2$ between the inlet and the outlet to the cell is 0.37 K but the average over the beam volume is 1.23 K, which yields a $LH_2$ density reduction of 2 %. The temperature averaged over the cell windows' beam nipples is 30.1 K for the beam-in window and 34.8 K for the beam-out window. The heat flux, predicted by `FLUENT`, from the window nipples to $LH_2$ is 4 W/cm$^2$ for beam-in and 8 W/cm$^2$ for beam-out respectively, which are both less then the critical heat flux for $LH_2$. *This would indicate that there is a low probability of liquid boiling at the windows.* Although the cell is symmetrical between the inlet and outlet the flow near the end caps of the cell is not. The cap at the inlet (with the beam-out window) experiences a large vortex with very little flow in the middle, where the liquid seems to be boiling. The pressure drop over this cell at this flow rate is 0.49 psid. The cell design would have to be refined to get rid of the bulk liquid boiling, but it looks promising in the windows region.

### 2.2.6 Refrigeration

An examination was carried out to ascertain whether sufficient target cooling power will be available on the JLab site in the 12 GeV era. Such an estimate is complex since it depends on things which simply are not known today, such as the ultimate heat load of the new SRF cavities during 12 GeV operations. However, after discussion with the JLab Cryo Group, a logical and reasonable path forward has been established.

If the accelerator delivers electron beams at 12 GeV and all the new SRF cavities continue to show high heat loads, there might be little spare capacity from the new Central Helium Liquefier (CHL). However, the ESR #2 could deliver 4 kW cooling power at 4 K and could be modified to deliver more than 6 kW of cooling power at 15 K and 3 atm. A similarly novel design feature involving the reconfiguration of the existing transfer line has now been validated by Qweak, in order to simultaneously supply both 4 K coolant and 15 K coolant to the target, and in particular, to return both coolant sources on separate lines back to the ESR.

A director's review of JLab cryogenic capacity has been held recently[3]. The MOLLER experiment's 5 kW cooling power requirement figures prominently in the report. The report states that the planned ESR #2 by itself has the 5 kW capacity required for the MOLLER experiment. The ESR #2 building is currently under construction, and the refrigerator has been designed (but not yet funded). However, the first of the director's review committee's recommendations is that funding be secured for ESR #2 on a timeline that will make it available for the MOLLER experiment. Finally, the report also recommends that the Hall A 4K transfer lines be re-evaluated and upgraded for the 12 GeV era in part because they have unusually high heat loads associated with them, and in part to better meet the demands of the 12 GeV era (such as the MOLLER experiment).

## 2.3 Toroidal Spectrometer

The MOLLER Spectrometer is a system of magnets for steering the scattered electrons, and collimators for defining the angular and radial acceptance. It is an open geometry in a toroidal configuration with 7-fold symmetry that has been designed to achieve full azimuthal coverage, as explained in detail below. A set of resistive, water-cooled copper coils are used to steer and focus the scattered electrons at the detector plane. Water-cooled tungsten and copper collimators are used to localize backgrounds, define the acceptance of the experiment and shield the magnets and the rest of the experiment from radiation. The spectrometer must spatially direct the signal (scattering of electrons from the electrons in the target - Møllers) into a region where backgrounds are minimized. The largest background *rate* in this region comes from Mott-scattered electrons that elastically scatter from protons in the target (elastics) while giving up significant energy to initial- or final-state photons, while a comparable *asymmetry* background comes from electrons that inelastically scatter from protons in the target (inelastics). Special beam collimators will minimize the so-called beamline backgrounds (electromagnetic radiation and neutrons) by localizing them so they can be shielded efficiently. The target and scattering chamber will also have shielding. The downstream magnet has a quite novel design due to various constraints. The following sections describe the physical requirements of the spectrometer system as well as a summary of the engineering considerations.

**Kinematical Considerations**

The experimental configuration downstream of the target is quite novel due to some remarkable features of the Møller scattering process. The topology of interest in the 2-electron system is in the vicinity of $\theta_{COM} = 90^\circ$ where the maximum asymmetry and minimum differential cross-section, and thus the maximum figure of merit, occurs. However, the acceptance in the highly boosted laboratory frame is at extremely forward angles ($\theta_{lab}$ between 5 and 20 mrad) because the COM energy for a 11 GeV electron scattering from a target

[3]The final report is available at `http://www.jlab.org/div_dept/dir_off/ccr/`.

electron is 106 MeV. A nice feature of Møller scattering is that it is identical-particle scattering, and the electrons that are scattered to forward angles have corresponding backward angle scattered electrons. This property is exploited to achieve full azimuthal coverage of the Møller scattering process by accepting the forward and backward angle scattered electrons in opposite sectors (see drawing on the right in Fig. 16). There is a one-to-one correspondence between $\theta_{COM}$ and the laboratory frame scattered electron energy $E'_{lab}$, and between $E'_{lab}$ and $\theta_{lab}$ (see left two plots in Fig. 16). This implies that scattered electrons in the laboratory frame in the range $3 \lesssim E' \lesssim 8$ GeV must be selected - a very large fractional momentum bite - in addition to the large range of scattered angles.

The measurement requires as much rate as possible in the range of desired scattering angles ($\theta$) which is the motivation for accepting scattered electrons over the full range of the azimuthal angle $\phi$. This makes a rate of more than 140 GHz available. At this high rate, the only practical solution is to integrate the detector response of each window, eliminating dangerous dead-time systematics. This so-called flux-integration technique requires that Møller-scattered electrons be focused into a region otherwise free of background. All of the above considerations have led us to a unique solution involving two back-to-back sets of coils, one of them of conventional toroidal geometry (albeit long and quite skinny) while the other of quite novel geometry. Collimation is a very important issue in such a system and will be discussed in Sec. 2.3.2.

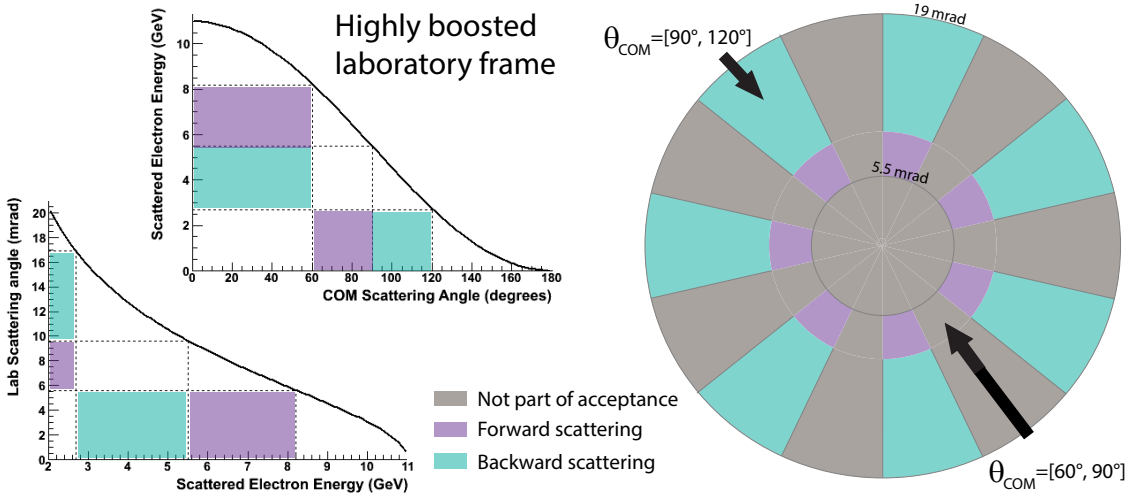


Figure 16: *$\theta_{COM}$ vs. $E'_{lab}$ for $E_{beam} = 11$ GeV, and $E'_{lab}$ vs. $\theta_{lab}$ are depicted by the two plots on the left. On the right is shown the proposed concept for the primary acceptance collimator, which is able to achieve 100% acceptance with judiciously chosen $\phi$-sectors.*

We summarize here the principal kinematic requirements of the spectrometer system:

- Full azimuthal acceptance for Møller electrons in the momentum range between ≈3 and 8 GeV.
- Clean separation from the primary background of elastic and inelastic electron-proton scattering.
- Placement of detectors out of the line-of-sight of the target.
- Clean channel for the degraded beam and the bremsstrahlung photons to the beam dump.
- Minimization of soft photon backgrounds by designing a “two-bounce” system via judiciously placed collimators.

A driving principle in the spectrometer design is to accept Møller scattering events over the full azimuth. Because the process is identical-particle scattering we are theoretically able to achieve 100% $\phi$ acceptance, for a large range of scattered electrons centered around $\theta_{COM} = 90^\circ$. The proposed design aims to accept *all* (forward and backward) Møller-scattered electrons in the range $60^\circ \lesssim \theta_{COM} \lesssim 120^\circ$, which implies that one must accept scattered electrons over a wide range of momenta. Thus, $\theta_{lab}$ and $E'_{lab}$ ranges for forward Møllers are roughly 5.5 to 9.5 mrad and 5.5 to 8.25 GeV respectively, and the corresponding ranges for backward Møllers are roughly 9.5 to 17 mrad and 2.75 to 5.5 GeV.

### 2.3.1 Conceptual Design of the Spectrometer

The spectrometer must focus the electrons in the desired angular and momentum range along with the other kinematic constraints described above, while simultaneously satisfying the additional constraints listed in more detail below. Each coil in the hybrid toroid has four current return paths, as shown in Fig. 17. The segment of the magnet closest to the target has the lowest current, with increasing current in each segment, with the fourth, most downstream part of the magnet having the maximum current. This allows the field to be tailored so that the lowest angle scattered electron tracks receive a kick to radially separate the Møller and elastic e-p scattered electrons. Further downstream, only the Møller electrons (which have a lower momentum, and are thus pushed further out radially) see the full field in the most downstream part of the magnet. The largest angle (lowest momentum) tracks must only experience field for a short distance in the magnet. This requires in a negative curvature in the most downstream part of the coil.

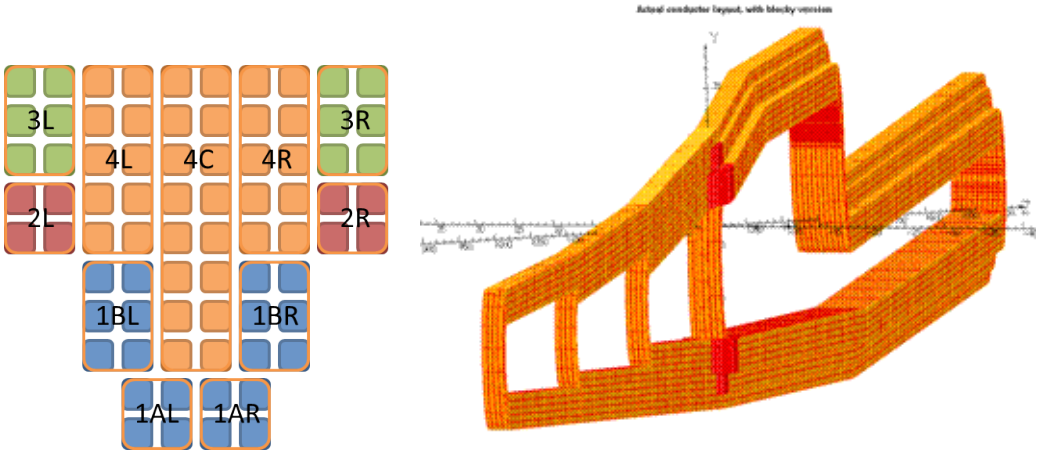


(a) (b)

Figure 17: *Conceptual model of a single hybrid coil, with the approximate currents in each return path (a). Model of the actual conductor layout in TOSCA (red) overlayed with the blocky model used for simulation and production of the maps (orange) (b).*

There are four primary features that govern the spectrometer design:

- In order to achieve sufficient total current at a realizable current density, the magnet fills nearly half the azimuth from z=10 meters to z=13 meters.
- The current in the magnet grows along z, with current returning in 4 different radial paths, spaced along the beamline by about 1 m.

- The back-end of the magnet, with the highest current, juts out to minimize the field seen by the Mott-scattered electrons, while ensuring that medium-energy Møller-scattered tracks are in high field for a longer time.
- There is a negative bend at the outer radius of each coil so that the highest-energy Møller tracks receive less $Bd\ell$.

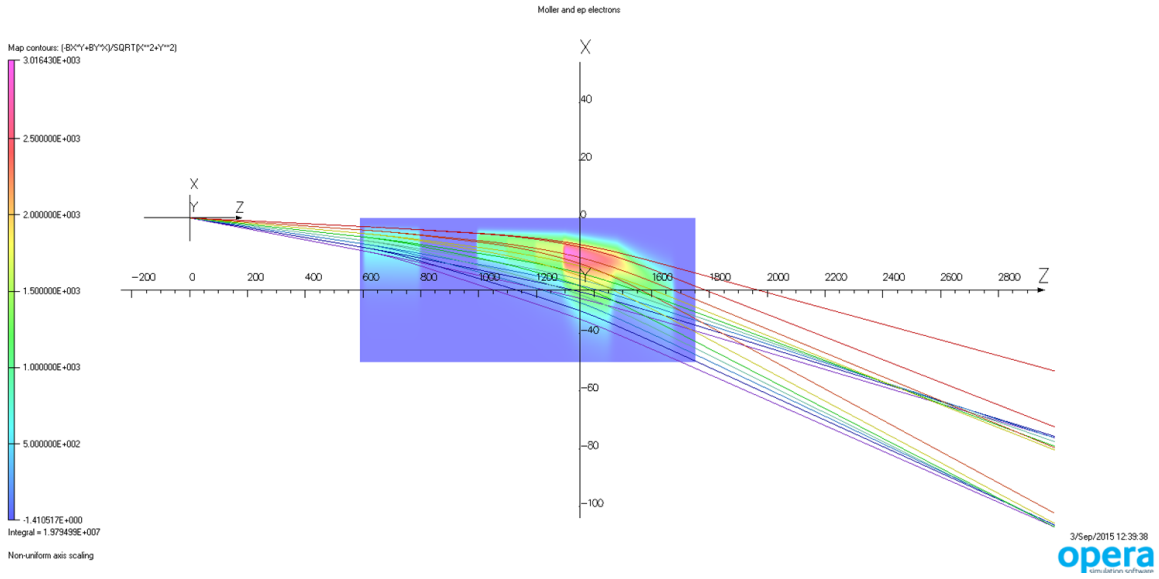


Figure 18: *Scattered Møller and elastic electron trajectories from the center of the target superimposed on a 2D plot of the $\phi$ (radially focusing) component of the magnetic field on a plane at the center of an open sector (Gauss). Line colors of the trackes represent $\theta_{lab}$ (red is lowest angle, highest rate, and purple is highest angle, lowest rate).*

A commercial software program called TOSCA, available from Vector Fields, was used to determine the conductor layout that would fit within the geometrical constraints and still achieve the required kinematic separation (see Figure 18). The shape of the hybrid toroid is designed to provide a large variation of total $Bd\ell$ experienced by electron tracks emerging at different scattering angles (see also Fig. 18). The next section will go into more detail about some of the constraints which drove this design, and Section 5.4.3 will summarize the extensive engineering pre-R&D work that has been done, including an actual conductor layout with water and electrical connections, a support structure and a vacuum box to house the hybrid magnet.

**Constraints on the design**

The biggest constraint on the coil cross-sectional area comes at the upstream end of the most downstream segment, which has the largest current. The increases in current are achieved by having an increasing number of turns in each segment, which much be arranged to fit into the available cross-sectional area at each z location, including insulation. The closest that a coil can come to the center of the beamline is $5\sigma$ of the multiple scattering angle (estimated to be 0.515 mrads) plus 1/2 inch for aluminum supports and tungsten shielding (1/4 inch each). In order to fit the conductor radially (beneath the radius of the lowest angle Møller scattered electrons) it is necessary to nearly fill the full azimuth. This results in a roughly trapezoidal cross-section.

When designing the layout, it was necessary to consider how the coils would be constructed. The diagram on the left of Figure 17 shows the scheme of how the individual double-pancakes will be put together in a cross-section at z=1300 cm. The conceptual design used in the simulation of the fields models the conductors as closed loops. Starting at z=1300 cm at the inner radius part of a coil, segment A in the picture in the left of the figure, and moving upstream toward segment Z, the conductor in pancakes 1B, 2 and 3 (left and right, or L and R) is bent inward toward the center of the coil, and continues upstream with the conductor in pancakes 1A (L and R). The conductor in pancakes 4 (L, C, and R) bends radially outward to form the current return path of segments J, I, and H. At z=1200 cm, pancakes 3 (L, R) bend radially outward to form the current return path of segments M, and L, and then at z = 1100 cm, pancakes 2 (L, R) form the current return path of segments P and O. Finally, at the upstream nose of the coil, pancakes 1A and B (L, R) bend radially outward to form the current return path of segments S, R and Q. At large radius, the conductor in the pancakes continue downstream and come together again at z=1300 cm and bend outward from the center of the coil so that they have the same cross-section as at the inner radius. The pancakes will be wound separately and then put together with the orange ones in the middle, then the green, red and blue ones fitting around them. A minimum bend radius of 5$\times$ the outer diameter of the conductor is maintained throughout the design.

As discussed earlier, the selected Møller electrons represent a significant range in lab angle and energy as well as scattering from a very long (1.5 m) target. Minimizing background rates to an acceptable level requires bringing these very different trajectories, from a large region of phase space, into a tight radial focus also separated from the majority of the principal backgrounds. The solution is a combination of two toroidal magnets which together act in a non-linear way on the charged particle trajectories. The first is a conventional toroid placed 6 m downstream of the target and the second, a novel hybrid toroid placed between 10 and 17 m downstream of the target. Each of the two toroidal magnets is constructed out of seven identical coils uniformly spaced in the azimuth.

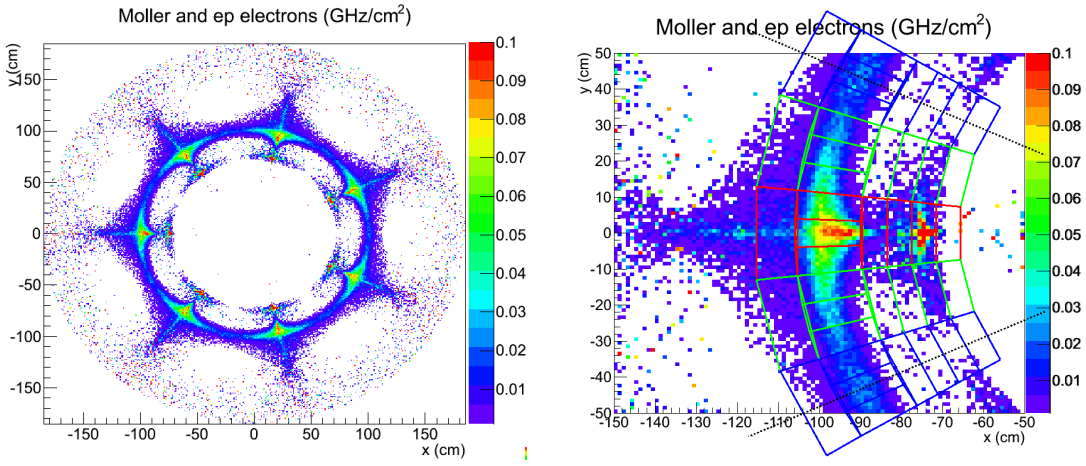


Figure 19: *Simulated, cross-section weighted, Møller and ep electron rates in 1cm$^2$ bins. The left plot shows the whole detector plane. The plot on the right zooms in to one sector and shows superimposed azimuthal and radial bins (approximate detector locations) in one toriodal sector (indicated by the dotted black lines).*

**Optical Properties of the Spectrometer**

In the radial dimension, the successful interaction of the two magnets is key. The total $B \cdot d\ell$ of the first magnet is small and thus the effect on the high-energy (≈11 GeV) elastically scattered electrons is small.

The highest energy (≈8 GeV) Møllers feel some prebending to put them at larger radius when they enter the hybrid field, and more importantly, the lowest energy (≈3 GeV), highest angle Møller electrons are bent even further away from the beamline, allowing these particles to skirt the strongest field in the second magnet. In the azimuthal dimension, the lower energy electrons are strongly defocussed by radial fields in the hybrid toroid and bend around into the regions behind the blocked portions of the primary acceptance collimator. By the time the electrons reach the detector plane 28.5 m from the target, the full range of azimuthal angles is populated by Møller electrons. The effect of this behavior is that the energy distribution of detected electrons changes along the azimuth. This azimuthal segmentation provides a variety of additional ways to understand the detector response, the modeling of the spectrometer optics and the estimates of the background dilution.

The distribution of the moller and elastic $ep$ electrons at the detector plane can be seen in Figure 19. Here we establish the color convention which will be used in future plots - red for the detector in the center of the open sector, blue for the detector in the center of the closed sector and green for the detector which straddles the open and closed sectors. For quantities that are azimuthally symmetric, the various detectors of the same "color" will have the same distribution, and for the purpose of the following plots, are combined. Figure 20 shows the E′, $\theta_{lab}$, radial and $\theta_{cm}$ distributions for Møller electrons that hit the main detectors. One can see that the "red" detector contains mostly the higher energy, forward Møllers, the "blue" detector is mostly the lower energy, backward Møllers and green has a mixture of both. The numbers relevant for estimating detector rates and predictions for asymmetries are listed in Table 1.

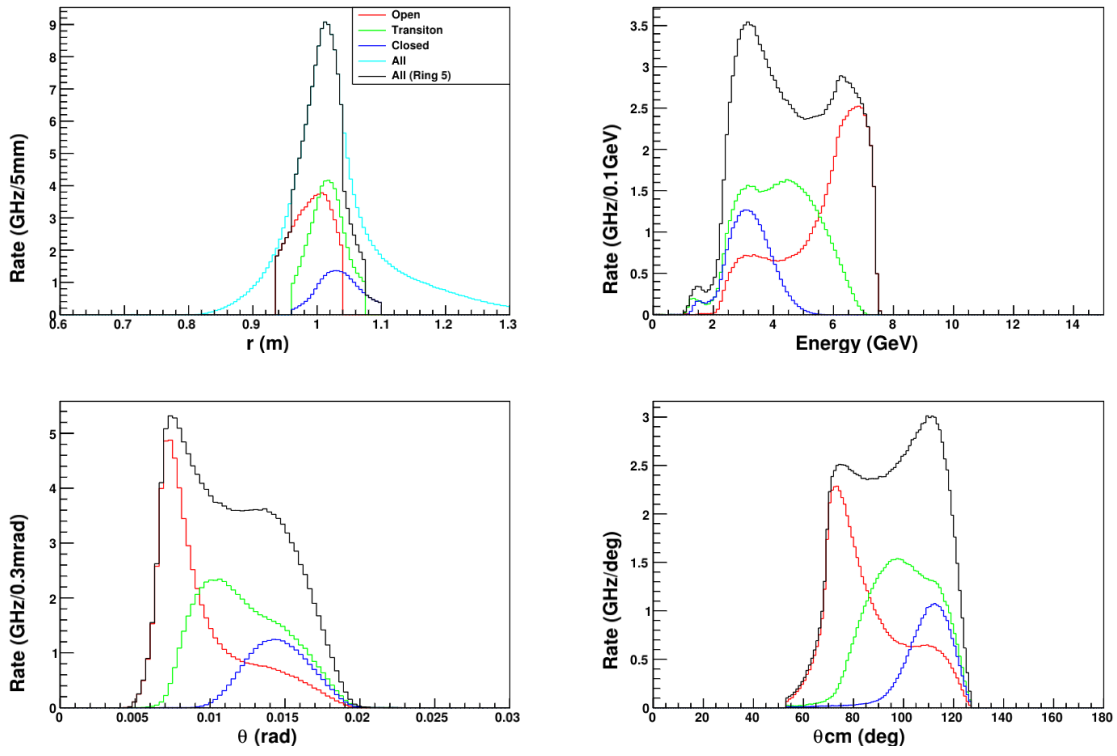


Figure 20: *Rate of Møller electrons in each of the azimuthal bins as a function of various quantities. The top left plot shows the radial distribution. The top right plot shows the distribution of $E'_{vert}$, the energy of the scattered electron immediately after the interaction. The plots on the bottom show the $\theta_{lab}$, the scattering angle in the laboratory frame (left) and $\theta_{cm}$, the scattering angle in the center of mass frame (right). Color convention from Figure 19.*

The simulation of the properties of the MOLLER spectrometer is done using the GEANT4 framework (see Sec. 2.7). The scattered electrons are propagated through the geometry which consists of collimators, coils and magnetic fields for the two toroids, and a detector plane. The detection plane was chosen to be 28.5 m downstream of the center of the target, where the Møller electrons have their tightest radial focus. At this position the $ep$ elastic (Mott) peak and the peak due to Møller electrons are separated by more than 20 cm. Field maps for the various upstream and hybrid conductor configurations are produced using TOSCA and used in various studies including optics optimization and position sensitivity studies. Optimization of the optics by adjusting the coil geometry can be done using TOSCA simulations of the Møller and Mott electrons, with the proper scattering angle/energy correlations. The rates for the default field, with 85 $\mu$A beam current, are $\sim$155 GHz, 14 GHz and 0.5 GHz for the Møller, Mott and inelastic $ep$ electrons respectively, for a background rate of $\sim$8%. It is desired that the forward and backward scattered acceptance (see Figure 20) for the Møllers be very similar, both because we want full azimuthal acceptance for the accepted range of scattering angles and because the transverse asymmetry will cancel more fully (see Section 3.3). Further optimization of the coil geometry and optimization of the collimator should be possible to improve these properties.

### 2.3.2 Collimation System and Radiation Shielding

The collimators define the acceptance of the experiment, and shield the detectors and minimize the radiation dose in the environment from backgrounds. Strategic placement of collimators will minimize soft photon backgrounds by achieving a two-bounce system. The proposed design will have a beam interception collimator to block small angle electrons upstream of the spectrometer toroids. The primary, acceptance-defining, collimator will be next along z, at the entrance of the upstream toroid. Finally, a collimator in the mid-way of the hybrid toroid will block line-of-sight photons from the detector acceptance. Additional shielding will be placed around the beam pipe to block other backgrounds. The collimation system and radiation shielding is shown in Figure 21. As described in Sec. 5.4, the conceptual design of collimation system and radiation shielding design has now been quantitatively evaluated. The same section summarizes the current status and future steps in the optimization of the designs.

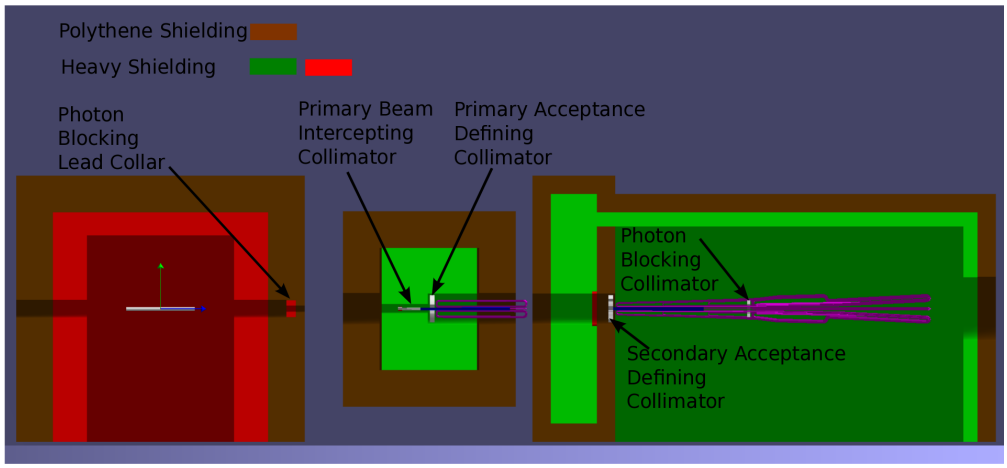


Figure 21: *Cross section view of the prototype design of MOLLER collimation and shielding. Concrete is the main heavy shielding tested in simulation and lead is used around the target region.*

## 2.4 Detectors

The MOLLER apparatus consists of a number of detector systems. A layout schematic of the main detector systems is shown in Fig. 22. The main asymmetry measurements for the Møller signal as well as the elastic and inelastic backgrounds will be performed by a large array of signal integrating (defined in Sec. 2.4.1) detectors. This array of detectors is referred to as the *main* integrating detector, which is labeled as "quartz assembly" in Fig. 22. Integrating mode detectors at very forward angle, including a set of luminosity detectors, will monitor helicity window to window fluctuations associated with the primary beam and the target. A set of tracking detectors, operating in counting mode, will be used for spectrometer calibration, electron momentum distribution and background measurements. Lead-glass detectors placed behind the main Møller ring detectors and shielding, combined with two planes of gas electron multipliers (GEMs) will measure hadronic background dilutions and asymmetries. Finally, four planes of GEM tracking detectors will be inserted periodically just upstream of the integrating detectors, at very low current, to track individual particles during calibration runs.

The following subsections provide a brief overview of the various detector systems, including basic criteria and design choices.

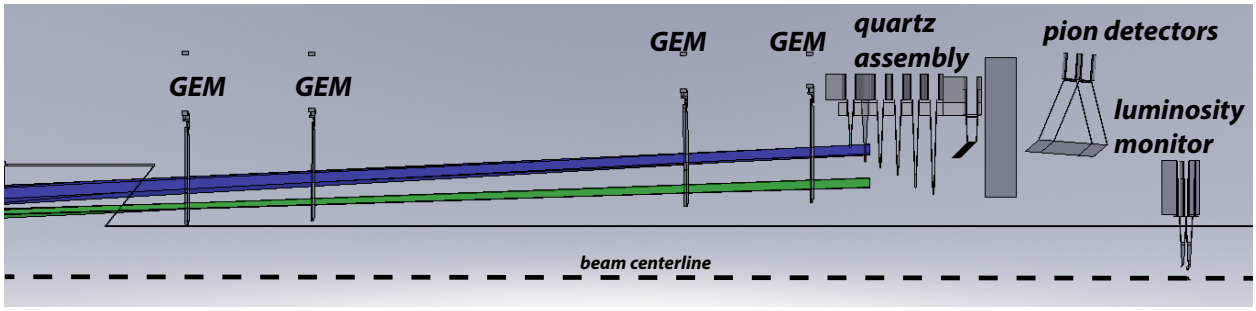


Figure 22: *Layout of the main integrating and tracking detectors. Predicted trajectories from elastically scattered electrons from target protons (green) and target electrons (blue) are also shown.*

### 2.4.1 Main Integrating Electron Detectors

The toroidal spectrometer will distribute the scattered electrons selected by the collimation system $\approx$ 28.5 m downstream of the target center in a region between a radius of 70 to 120 cm with respect to the beamline axis (see Figs. 19 and 23). This region will be populated by a series of detectors with radial and azimuthal segmentation as shown in Fig. 19, referred to as the main integrating detectors. Figure 23 shows the radial segmentation of the planned detector rings superimposed with the azimuthally averaged radial distributions. The rings are numbered 1 through 6 with the Møller electrons focused onto ring 5, with a central radius of $\approx$ 100 cm and a radial spread of $\approx$ 16 cm. The elastic e-p (electron-proton) events are distributed mainly across rings 1 through 3 and then again with a sharp rise in ring 6. The inelastic e-p events peak in ring 2 and have a very long but low rate tail extending through all rings. The main $A_{PV}$ measurement will be made from the Møller events in ring 5, but understanding the dilution from e-p events under the Møller peak requires the proposed radial segmentation. Because the tail of all radiative electron-proton elastic and inelastic processes results in an important systematic correction, the detector must be able to measure these background electrons in *several* bins, so trends in yield and asymmetry can be compared to simulations.

The primary acceptance collimator is divided into seven sectors, evenly distributed around the azimuth, covering exactly one-half of the azimuth as described in Sec. 2.3. Due to azimuthal defocusing in the magnets the Møller electrons populate the full range of the azimuth at the detector plane. However, as can be

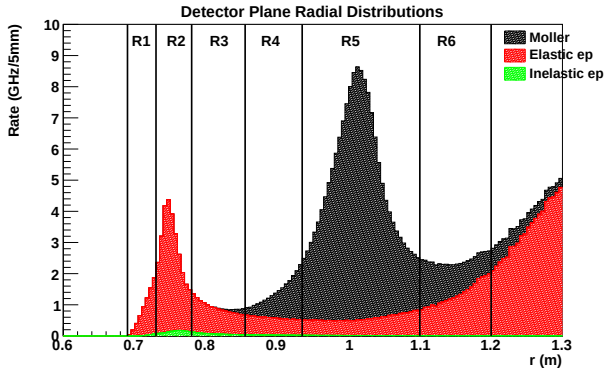


Figure 23: *Radial distribution of Møller (black), $ep$ elastic (red), and $ep$ inelastic electrons 28.5 m downstream of target. The vertical black lines delineate the proposed radial segmentation into 6 rings (R1 through R6). The principal $A_{PV}$ measurement will be carried out in ring R5.*

seen in Fig. 19 (left), the electron rate is highly non-uniform within a ring and mostly still focused on the individual seven sectors. The figure demonstrates that a detailed understanding of the signal, background fraction, and spectrometer optics requires high detector segmentation, both in the radial and azimuthal dimensions. Azimuthal segmentation is needed, since defocusing results in a correlation between azimuthal angle and $E'$. Each azimuthal sector defined by one of the toroids is further divided into 4 sub-sectors, so that there are 28 total azimuthal channels at each radial bin. The exception to this is the Møller radial bin (ring 5), which is further divided into 3 additional bins, resulting in a total of 84 channels. This arrangement is illustrated in Fig. 19 (right). Additionally, a "shower-max" quartz/tungsten sandwich detector will provide a second independent measurement of the flux in the Møller peak ring. This detector will be less sensitive to soft photon and charged hadron backgrounds. A description of the baseline design concept for the shower-max detector is given in Sec. 2.4.2. A discussion of the segmentation optimization with respect to dilution from background can be found in Sec. 3.5.

**General Detector Design:** The main detectors must operate in both integrating mode (see below) at full production current, and in event counting mode at a significantly lower beam current, during tracking runs. Being able to count single events in the main detectors, with good photoelectron resolution, during tracking runs, is necessary to verify the momentum transfer distribution across the detectors, to measure background sensitivities, and to perform periodic detector health tests, such as measurements of the photoelectron number for each detector. The following discussion focuses on the integrating mode, but most of the design considerations for that mode also apply to tracking mode operation, except for the design of the signal readout (the tracking mode front-end electronics).

At the full beam current that is required to make the proposed asymmetry measurement the detector rates vary from 10 to 100 MHz per $\mathrm{cm}^2$ in the Møller and elastic e-p rings (the high rate rings, 5 and 2). At these rates, counting individual signal pulses would require highly segmented detectors with pixel sizes at the $100\times100\ \mu\mathrm{m}^2$ level or better (since the rate is not uniformly distributed over a $\mathrm{cm}^2$). While this is something that can be done with modern semiconductor based pixel detectors, the detection efficiency, reliability, background sensitivities, and radiation hardness are major concerns. The high cost of such detectors and the associated electronics is also problematic.

The only other option is to integrate the signal, corresponding to a spatial integration of many events distributed over the exposed surface of a sufficiently large detector. The corresponding detector signal is a "steady state" current (for fixed beam and target properties), resulting from many overlapping individual

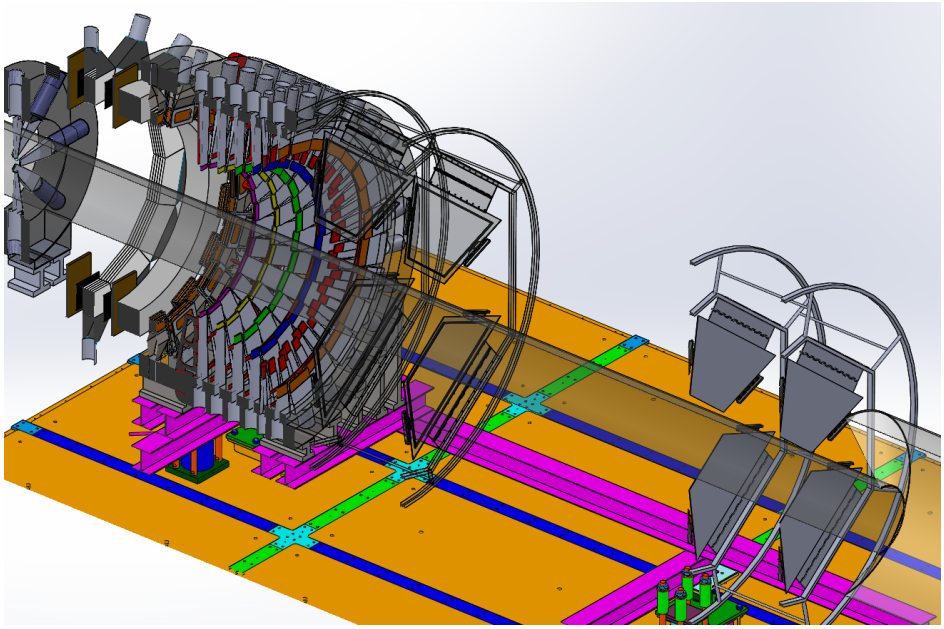

Figure 24: *A perspective view of the integrating detector assembly. The quartz tiles are shown in color, with the air-core light guides and the PMT rings in grey. Located in front of the main detector rings are the upstream GEM trackers. Located behind main detectors and a donut-shaped shield are the pion detectors and the luminosity monitors.*

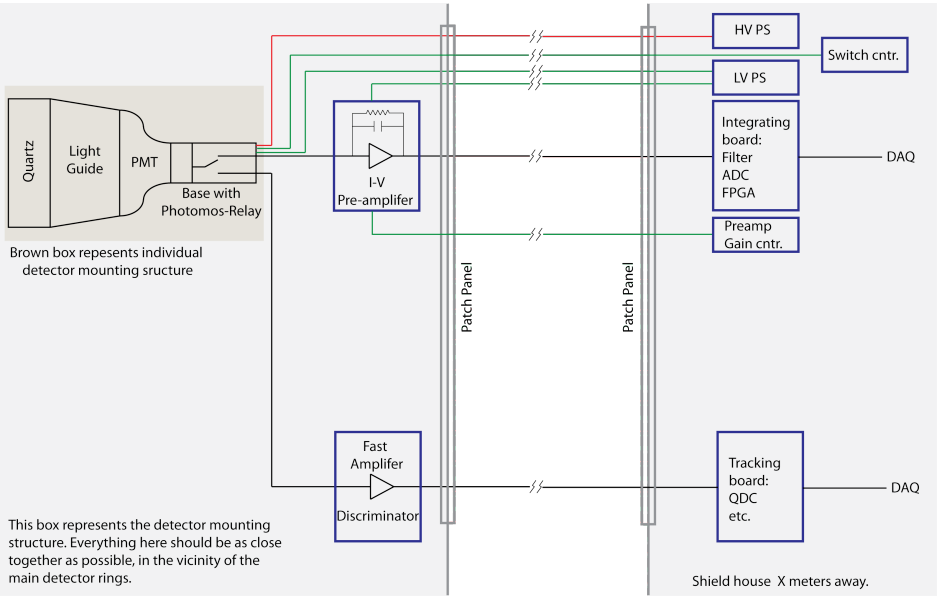


Figure 25: *Main integrating detector system layout schematic, indicating the integration mode signal chain, the tracking mode signal chain, and the PMT base control, which must be electronically switchable between the two operating modes.*

electron pulses. In the electronics the signal is then integrated in time, over a chosen sample window, which must be chosen to allow a large number of individual current samples within each helicity window to reduce non-linearities and bit noise in the ADCs (see section 5.5.3). The samples collected within a helicity window are then effectively averaged in the DAQ software to produce a mean, RMS, and minimum and maximum values of the signal within each helicity window.

The decision to operate in integration mode, with larger detectors, allows us to choose a radiation hard active material, with low background sensitivity. The ideal detector active material is artificial fused silica (henceforth "quartz"), since it is radiation-hard, and has negligible scintillation and low response to hadronic backgrounds. The best choice for the MOLLER integration running mode are therefore DIRC detectors. The integrating detectors will consist of three major parts: the active detection volume, made from quartz, the light guide, consisting of an air-core channel with walls made from a high reflectivity material, and a quartz window photomultiplier tube (PMT) with high quantum efficiency and low dark current. The integrated response of the PMT to the collected light yield is the experiment's measure of the scattered electron flux. Light guides are needed to move all PMTs away from the envelope of scattered electrons and backgrounds as much as possible while, at the same time, reducing sensitivity to background (the latter resulting in the choice for the air-core, rather than a solid material). A high level schematic of the full main detector system for a single channel is shown in Fig. 25 and a cut-away CAD view of the envisioned main detector assembly is shown in Fig. 24, with the integrating detector quartz pieces indicated by the colored tiles.

Operation in integrating mode precludes event mode cuts, based on pulse shape, and true counting statistics is not achievable. Therefore the two primary concerns for the detector design are to reduce background sensitivity as much as possible and to reduce excess noise to a level that allows the detectors to operate as close to counting statistics as possible. We define excess noise as a departure from counting statistics, such that the asymmetry error for a given detector and in the $i_{th}$ helicity pair would be

$$\sigma_{A_i} = \sqrt{1+\alpha^2}/\sqrt{2N_i}\,.$$

Where $\alpha \equiv \sigma_{PE}/n_{PE}$, $N_i$ is the number of primary electrons detected within a single helicity window, and $n_{PE}$ and $\sigma_{PE}$ are the mean photoelectron yield and standard deviation in the yield respectively. The production of showers inside the quartz, suboptimal geometry, and poor light collection efficiency typically lead to an increase in excess noise (because they produce additional variation in photoelectron count), while a higher average number of photoelectrons, per event, leads to a decrease in excess noise. These issues are intimately connected to the detector geometry, which has been optimized using bench-marked simulations. The final choice for the geometry and orientation between the quartz pieces and the light guides, as well as for the light guide material, is being studied using simulations and prototype tests with electron beams, as discussed in Sec. 5.5.2.

**Integrating Detector Signal Chain:** At the proposed maximum beam current, the event rate will vary by about an order of magnitude around the azimuth, within a given ring and by about two orders of magnitude from highest to lowest, among all of the integrating mode detectors. The highest flux in a single quartz detector will be about 5 GHz, while the lowest rate will be a few hundred MHz. In the current design, the Cherenkov light from each detector will be collected by a single 3" PMT with quartz windows. Depending on the chosen quartz thickness, the photocathode of the PMT will conservatively produce a mean of about 20 photoelectrons per track, for thin detectors (see prototype beam test results in section 5.5.2). The typical integration or current mode measurement front end signal chain is shown in Fig. 26. The light from the quartz is converted to a current using quartz glass photomultiplier tubes (PMT) with a high quantum efficiency (QE) in the UV, with a peak around 280 nm. At a nominal rate of 5 GHz and for a given detector geometry, a mean current of roughly $6.4\ \mu$A is produced at the anode of a PMT with a gain of about 400:

$$I_{anode} = 5.0\ \mathrm{GHz} \times 20\ \mathrm{pe/track} \times 400 \times 1.6 \times 10^{-19} e/C = 6.4\ \mu A.$$

This is a large signal but still below the nominal 10 $\mu$A maximum usually recommended by PMT manufacturers for good long-term stability. For the same PMT gain, the low rate detector anode signal would be only about 100 nA, which is too low. Therefore, the low rate detectors will need to have different PMT and preamplifier gains. In high precision asymmetry measurements, the PMT non-linearity is an issue and it is known that PMTs develop significant non-linearities at low gain. The largest expected asymmetry in the experiment comes from background caused by the aluminum target windows, at the ppm level. Therefore, it is necessary to establish the linearity or measure the non-linearity of the PMTs at least to the $10^{-4}$ level, which has been shown to be achievable with a suitable choice of PMT and a good base design, for low gains.

A trans-impedance preamplifier is used to convert the PMT current signal to a voltage and to provide the primary filtering stage for the signal. The preamplifier also implements a line driver to sustain the signal over the roughly 50 meter cable distance between the detectors and the ADCs. The voltage signal is then further filtered and digitized by an ADC. Several channels of the filter and ADC chain are implemented on a single board, together with an FPGA, which queries the ADCs, collects (meaning in this case integrates) the data and facilitates the readout. Details about the integrating detector electronics operational criteria and design are provided in section 5.5.3.

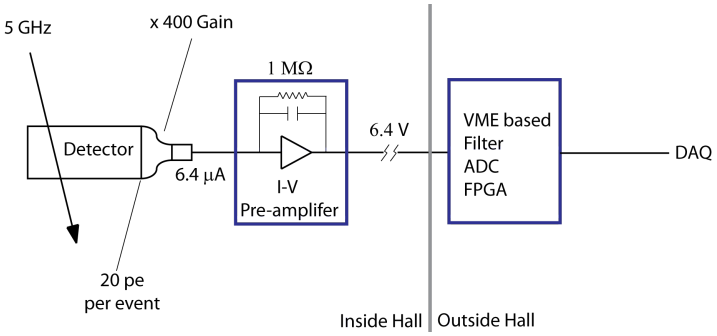


Figure 26: *Basic schematic of the frontend signal path for integration mode measurements. The event rate is order of magnitude, taken from simulations, and the photoelectron number is conservatively based on prototype tests for some of the MOLLER detector geometries. The gain of the PMT should be chosen to prevent premature aging due to the large cathode and dynode currents and to reduce PMT non-linearities.*

**Tracking-Mode Signal Magnitude:** As stated at the beginning of this section, for various studies, it is necessary to operate the detectors in single electron counting mode during tracking runs. In this mode, the main detectors must be able to resolve single events with fast timing, which typically requires a much higher gain than could be handled in integrating mode.

At a gain of $1 \times 10^7$, the average voltage pulse across a 50 $\Omega$ termination is

$$V_{signal} = I_{signal} \times R = (15pe \times 10^7 \times 1.6 \cdot 10^{-19} C/e / 10^{-8} sec) \times \ 50\Omega = 120 \text{ mV}$$

which is a robust signal. Even a single photoelectron signal of 8 mV, produced for example by Compton scattering of a few MeV gamma-ray background in the radiator, could be easily observed.

Such a gain change (from the low gain integrating mode to the high gain tracking mode) requires either a physically separate PMT base for each mode, or an electronically switchable base, with two separate anode outputs feeding into two separate DAQ chains corresponding to the parity ADCs for integrating mode (which operate like slow flash ADCs, but have a maximum time resolution of only about 1 $\mu$sec) or to flash ADCs for tracking mode (with time resolutions of nsec or better). Physically switching the PMT base on 250 or more PMTs, every time a tracking run is taken, is not a practical solution, which means that we

must develop a single base that can be operated in both high gain and low gain modes and which allows electronics switching between the two modes. A prototype for this base exists.

Both the integration-mode, and the tracking-mode PMT parameters are summarized in Table 4 and an overview signal schematic of the detector system is provided in Fig. 25.

Table 4: *Parameters for the PMT signals from the quartz detector with the largest flux.*

| **Parameter** | **Value** |
|---|---|
| Total PMTs | 252 ($6 \times 28$ and $1 \times 84$) |
| **current mode:** | |
| $I_{cathode}$ | 16 nA |
| gain | 400 |
| $I_{anode}$ | 6.4 $\mu$A |
| non-linearity (goal) | $5{\times}10^{-4}$ |
| **pulsed mode:** | |
| $I_{cathode}$ | 0.24 pA at 100 KHz |
| gain | $1{\times}10^{7}$ |
| $I_{anode}$ | 2.4 $\mu$A |
| $V_{signal}$ (no amp.) | 8 mV for 1 pe; 120 mV for 15 pe |
| non-linearity (goal) | $< 10^{-2}$ |

**Radiation Hardness** Radiation damage is in principle a concern, since Cerenkov light production occurs predominantly in the UV, which is exactly where loss in light transmission first shows up. For example, the familiar "yellowing" of lead-glass is due to the loss of transmitted light at the blue end of the spectrum. The dose to the artificial, fused-silica radiator material from the $e + e \rightarrow e + e$ events will be only 15 MRad by the end of the experiment. Given the average path length in the radiators of only a few cm, and our non-agressive short wavelength cutoff of 250 nm set by the UV glass of the PMT windows, no measurable loss is transmission is expected. This is ideal since it means that the photoelectron yield and any detector biases (e.g., with respect to $Q^2$) will be stable throughout the experiment.

All other detector construction materials in the beam envelope (such as radiator supports) must be vetted for susceptibility to damage under 15 MRad dose. Degradation by potentially elevated ozone and nitric acid levels may also be a factor in the choice of detector materials.

### 2.4.2 Shower-max Detectors

The shower-max detector ring is located just downstream of the main integrating detector rings and will intercept the same peak-electron flux as Møller ring 5 (as shown in Fig. 22). The purpose of the shower-max is to provide a supplemental, energy-weighted measurement of the Møller signal with less sensitivity to hadronic and soft backgrounds. As the name suggests, the shower-max counts electrons by inducing an electromagnetic shower which grows to a maximum before exiting the detector. The concept uses a "stack" of tungsten interleaved with quartz to produce the shower and Ĉerenkov light respectively. The light exiting the quartz is then directed to a PMT using an aluminum air-core light guide. The shower-max ring consists of 28 azimuthally segmented detectors.

The design criteria for the shower-max are essentially the same as those for the main integrating detectors (described in the previous sub-section), including the need to operate in both integrating and counting modes. Given the radiation hard requirements for the detector materials, artificial fused silica or quartz is a natural

choice for the stack's active medium, and the interleaved, high-purity tungsten sheets give the stack the necessary radiation length thickness in a compact size. One of the primary goals of the shower-max detector is to achieve better than 20% photo-electron resolution over the full range of accepted electron energies (from $\sim$ 2 - 8 GeV). A preliminary design and associated simulations are discussed in Sec. 5.5.5.

### 2.4.3 Auxiliary Integrating Detectors

In the vicinity of the Møller "peak", we anticipate a small ($\sim 0.1\%$) contamination from pions and other charged hadrons. The background could result from processes with a very tiny cross-section but with a potentially large analyzing power, as discussed in Sec. 3.5.4. It is therefore important to be able to directly measure both the dilution fraction as well as the parity-violating asymmetry of this background.

We propose to accomplish the dilution fraction and asymmetry measurements with a set of auxiliary detectors that will be placed along the primary Møller "peak" trajectory, behind shielding (see Fig. 22). The idea is to range out the Møller electrons with a thick Pb absorber, and detect the remaining minimum ionizing particles (MIPs), primarily pions (but also kaons and muons) that penetrate the shielding using a set of acrylic Cerenkov detectors. Similar detectors were used as focal plane detectors in the HAPPEX-I experiment, and are both acceptably radiation-hard and insensitive to neutrons and soft backgrounds. .

The asymmetry measurement will be carried out during production running. We will instrument the entire azimuthal acceptance for a radial acceptance that matches the main Møller electron signal, using a set of 14 acrylic detectors, 7 corresponding to "open" sectors and 7 to "closed" sectors. Each detector will be read out by integrating the signal from a single PMT. Using 45 radiation lengths of absorber, the signal will be dominated by pions, with only a modest electron contamination. The "open" and "closed" sectors will detect different pion energy ranges, so will provide information on any energy dependence of the pion asymmetry.

The dilution measurement will be carried out in an auxiliary calibration run at very low beam current ($\sim$ 1 nA). For each of one "open" and one "closed" sectors, the acrylic detectors will be supplemented with a set of additional detectors: each acrylic detector will be sandwiched between a pair of GEM detectors and a pair of trigger plastic scintillators, followed by a Pb-glass calorimeter. All signals will be read out in conventional event-counting mode. Pions will be identified by MIP signals in the acrylic detector, a track in the GEM pair, a time coincidence with a signal in the main Møller quartz detector as well as a MIP signal in the shower-max detector (Sec. 2.4.2). We may also be able to require a match with a track seen in the upstream GEM tracking system. The Pb-glass calorimeter will measure the energy spectrum of the pions as they emerge from the Pb absorber, which can then be used, with simulation, to gain information on the pion energy spectrum incident on the main Møller detectors. Of course, only a fraction of the incident pions ($\sim$ 38%) will survive the Pb absorber to be detected in the dilution measurement, and so we will rely on simulation to scale the observed pion flux to the incident pion flux at the main detectors.

Note that this scheme allows us three independent asymmetry measurements, each with a different relative contribution from electrons and pions: the main Møller detector, dominated by electrons but with a possible pion contamination, the shower-max detector, for which the pion contamination is supressed by a factor of three relative to the electron signal, and the pion detectors, wherein the pions dominate the signal. These three should provide a redundant determination of the pion background to the electron asymmetry measurement.

Another set of detectors, referred to as scattered beam monitors (SBM) will be installed at various locations to monitor potential false asymmetries in reducible background that results from the primary scattered beam interacting in downstream collimators, beampipe, and shielding. Small and large angle scattered beam monitors (SAM and LAM) - also referred to as luminosity monitors - will be located in regions where the scattered rate is estimated to be larger than the main Møller rate, but the physics asymmetry is expected to be smaller. These detectors will consist of quartz Ĉerenkov radiators and air light guides to transport the light

to photomultiplier tubes. Diffuse scattered beam monitors (DBM) will be deployed in locations where the expected scattering rate from primary target interactions is small, so the majority of the signal would come from secondary interactions. These detectors will be similar to the luminosity monitors, but they will also consist of detectors with only PMT and lightguide or only PMT to better characterize how the background interacts with the typical detector components.

The planned location for the small angle scattered beam monitors (SAM) is shown at the right edge of Fig. 22. These small angle luminosity monitors, consisting of quartz detectors that will detect the charged particle flux at extreme forward angles, have two purposes. Since they have higher statistics than the primary Møller flux, they serve as a sensitive diagnostic of target density fluctuations, beam fluctuations and electronics noise. The small scattering angle also implies that they should have a much smaller parity-violating asymmetry, so that they can also serve as a "null asymmetry monitor".

In the current spectrometer design, we have determined that the forward angle charged particle flux in the $\theta_{\rm lab}$ range between 2 and 2.5 mrad should not feel any fields. We therefore plan to instrument the region between 6.0 and 7.5 cm thirty meters downstream of the target with eight of the small angle scattered beam monitors. This arrangement is very similar to the geometry of the $Q_{weak}$ downstream luminosity monitors [49]. The scattered electron rate into the full azimuth at this location (coming equally from Møller and elastic e-p scattered electrons) is about 1300 GHz. This will yield a rate of $\sim$ 100 GHz per detector, very similar to the $Q_{weak}$ case. Assuming 10 photoelectrons per event, we would expect a photocathode current of 160 nA. Given the similarities to $Q_{weak}$, we could employ a similar photomultiplier arrangement. A multi-alkali photocathode is used and the dynodes are tied together to run it in "unity-gain" mode. The output is fed into TRIUMF current-to-voltage preamplifier with a gain of 25 M$\Omega$ to yield a voltage of 4.0 V.

The total rate in the eight detectors will be $\sim$5 times higher than the main detector, implying a two times smaller statistical error per pulse pair. Assuming the Møller and elastic e-p processes are the largest contributors to the signal in this detector, the expected physics asymmetry is $\sim$3 ppb, an order of magnitude smaller than the asymmetry in the main detector. So this would serve as a "null-asymmetry" monitor at that level and a sensitive check for any false asymmetries from backgrounds.

One technical concern with these detectors is the high radiation dose that will be received by the artificial fused silica over the course of the run. It is about 8 Grad per detector. The similar size and material $Q_{weak}$ downstream luminosity monitors showed no evidence of radiation damage up to $\sim$ 2 Grad. There is no reason to believe that there will be any degradation as one goes beyond 2 Grad, but if there were, the materials in these detectors are inexpensive enough that periodic replacements are feasible.

### 2.4.4 Tracking Detectors

In order to verify the spectrometer optics, to measure the absolute scale and the appropriately weighted mean of the kinematic factor multiplying $A_{PV}$, and to evaluate our understanding of backgrounds, a tracking system is proposed to be used at very low current ($\sim$ 100 pA). The concept is to measure particle tracks using four GEM planes downstream of the two spectrometer toroids but before the particles arrive at the main integrating quartz detectors.

It is proposed to have GEM planes configured in two pairs placed in rotatable wheel assemblies, as shown in Fig. 24. The GEM planes must be insertable to intercept the charge particle flux after they exit the vacuum window, but must be out of the way during the collection of production data. In order to reduce costs, we propose to cover four septants with a GEM stack of 4 planes and have them attached to a remotely controlled "wheel" with the ability to rotate up to one septant in either direction.

We expect that a resolution of $\sim$ 500 $\mu$m will be required to meet the calibration requirements and a flux of $\lesssim$ 200 Hz/cm$^2$ will be incident at the proposed operating beam current of 100 pA, which should not be too taxing for established readout techniques for GEMs. The ability to stably deliver such a low-current calibration beam for similar tracking measurements has been demonstrated in the Qweak experiment, which

similarly relied on using a tracking system for background and kinematics measurements, at a beam current 6 orders of magnitude lower than that used for the primary asymmetry data-taking.

Precision tracking is important for several auxiliary measurements within the MOLLER experiment. These include verifying the acceptance of the quartz detectors, understanding the optical properties of the magnetic field configuration, providing points of comparison to a simulation, and position dependent responses of the quartz detectors. The tracking requirements for this experiment are overall full azimuthal coverage (though not necessarily in a single GEM position configuration), moderate position and angle resolution, and reasonably uniform efficiency.

The challenge of measuring the acceptance and quantifying its uncertainty is important to the systematic uncertainty of the experiment and must be constrained to effectively $0.5\%$ in $A_{PV}$. This fixes the relative contributions of Møller-scattered events over the full range of acceptance, with proper weighting, to the underlying theoretical prediction. This is the kinematic-dependent term defining the "kinematic factor" or analyzing power, $\mathcal{A} \equiv A_{PV}/Q_W^e$ from Eqn. 1 in Sec. 1.2, dependent on the beam energy $E$ and the center-of-mass scattering angle $\theta$

$$\mathcal{A} \equiv \frac{mG_F}{\sqrt{2}\pi\alpha} \frac{4E\sin^2\theta}{(3+\cos^2\theta)^2}. \tag{5}$$

Because of the very broad momentum acceptance of the spectrometer and the possibility for accurate placement of acceptance-defining collimators, the problem simplifies greatly. If the momentum acceptance is uniform as a function of accepted angle, sufficiently accurate construction and placement of the acceptance-defining collimators is all that is required. The purpose of the magnetic optics reconstruction in this context is to validate the underlying assumptions. Comparison with simulation to account for effects such as internal and external brehmstrahlung and multiple scattering will be critical. In addition, a simulation provides a useful basis to explore the distributions at the detector plane to verify the acceptance.

The proposed tracking system spaced along the beam axis provides a lever arm to reconstruct both the positions and angles. These four independent variables map from the independent variables which describe the scattered particle, the lab scattering angle, the electron momentum, the lab azimuthal angle, and the reaction vertex position (we neglect the reaction coordinates transverse to the beam as these are known precisely event-by-event from the raster current and represent small perturbations in the optics mapping). A detailed description of the calibration requirements and a study of how one would evaluate the acceptance function is provided in Sec. 5.5.8

### 2.4.5 Scanner

Another useful diagnostic will be a simple, small, movable detector that can operate at both the full beam flux and at the low beam currents needed for the tracking measurements. This "focal plane scanner" would consist of a small single Cerenkov detector made of fused silica ($\sim$ 1x1 cm$^2$), read out by PMTs, mounted on an $x, y$ motion stage covering one sector of the acceptance, and located just upstream of the main detectors. Such scanners have been used in E158 [47], HAPPEx-II, Qweak [49].

This device can be used to confirm that the rate distribution as measured at low beam currents by the full tracking system is not significantly different than that seen at full luminosity. It also would allow periodic rapid monitoring of the distribution during production data-taking, to ensure stability of the effective kinematics and to any changes in backgrounds.

## 2.5 Flux Integration

The integrated response of the Cherenkov light from electrons that traverse the detector is linearly proportional to the scattered flux. The parity-violating asymmetry is measured by averaging the fractional

difference in the response of the detectors $F$ over many window-pairs:

$$A_i \equiv \left(\frac{F_R - F_L}{F_R + F_L}\right)_i \simeq \left(\frac{\Delta F}{2F}\right)_i; \quad A_{\rm raw} = \langle A_i \rangle; \quad \delta(A_{\rm raw}) = \sigma(A_i)/\sqrt{N}. \tag{6}$$

Here, $A_i$ is the asymmetry in the $i$th window-pair, made from nearby (in the time domain) windows of opposite helicity. There are several aspects of the electronics and data acquisition (DAQ) specific to parity-violation experiments that are worth emphasizing, and we discuss them in the subsequent sections. The collaboration has extensive experience in these aspects of the experimental technique.

Second generation parity violation experiments at JLab such as HAPPEX-II used a helicity reversal frequency of 30 Hz, which had the benefit of largely canceling beam jitter and electronics noise related to 60 Hz line. PREX ran successfully with 240 Hz helicity-reversal, while Qweak used 960 Hz reversal. It will be necessary for MOLLER to flip the helicity even more quickly. One reason as mentioned above in the discussion of the target, is that target density fluctuations are only expected to contribute at frequencies below a few hundred Hz.

Perhaps of equal importance is that, at the MOLLER event rate of $\sim 150$ GHz, suppression of electronics white noise at the required level is a severe challenge. At a helicity flip rate of 60 Hz, the variance $\sigma(A_i)$ would be 28 ppm. A pedestal noise level below $3 \times 10^{-6}$ would be required in order to ensure negligible contribution from white noise to $\sigma(A_i)$. We are designing around a flip rate of 1.92 kHz, such that $\sigma(A_i)$ would be 80 ppm. This requires a pedestal noise floor of $1 \times 10^{-5}$, which appears feasible. It also implies that each helicity state is held for $\sim 500\mu$s. In order to avoid excess noise from 60 Hz line variations, a scheme for selecting helicity states will be required which will force complementary pairs at corresponding points in the 60 Hz cycle.

The main scattered electronic flux detectors are not the only parameters that must be integrated over each helicity window. Even with perfect electronics, $\sigma(A_i)$ in Eqn. 6 would be dominated by fluctuations in electron beam parameters due to window-to-window fluctuations in intensity, position, angle and energy. To exploit the full available statistics one must remove the correlations of $F$ to beam intensity, position, angle and energy, thus extracting the measured raw asymmetry as follows:

$$A_i = \left(\frac{\Delta F}{2F} - \frac{\Delta I}{2I}\right)_i - \sum \left(\alpha_j (\Delta X_j)_i\right). \tag{7}$$

Here, $I$ is the time-averaged beam intensity over the duration of a helicity window, $X_j$ are corresponding average beam trajectory parameters derived from judiciously placed beam position monitors and $\alpha_j \equiv \partial F/\partial X_j$ are coefficients that depend on the kinematics of Møller scattering as well as the detailed spectrometer and detector geometry of the given experiment. The parameters $I$ and $X_j$ will be derived from monitor signals in much the same way as the relative flux $F$, by feeding voltage outputs that are proportional to beam parameters into the same ADCs. It is critical to maintain close synchronization between the integration cycles of all the ADCs.

## 2.6 Data Acquisition

As with Qweak and other parity-violating experiments, two DAQ systems will be required: 1) An integrating DAQ for the production data, and 2) A counting-mode DAQ for low-current calibrations, e.g. measurement of $Q^2$.

An overview of the integrating DAQ is shown in figure 27. The DAQ runs in the framework of CODA, the Jefferson Lab DAQ toolkit in which multiple VME or other types of crates are synchronized by a custom Trigger Supervisor board; the event fragments are gathered via a standard TCP/IP network to a workstation

where whole events are built and written to local disk and subsequently stored in the Mass Storage Tape Silo (MSS). The same diagram describes the concept of both DAQ systems, but the differences are in the trigger source and the types of frontend boards that digitize the data. The trigger source goes to the Trigger Supervisor, as well as to the frontend boards. For the main integrating DAQ, the trigger source is a Master Pulse from the helicity electronics, while for the counting-mode DAQ the source of triggers will be scintillators positioned to intercept tracks through the GEM detectors.

The integrating DAQ will run deadtime-free at the anticipated $\sim$ 2 kHz helicity flip rate and integrate signals over the helicity period (0.5 msec). The signals consist of PMTs from the detectors or few-volt voltage levels from various devices such as beam position monitors (BPM) or beam current monitors (BCM). When the ADCs integrate over the helicity pulse, the first fraction ($\sim$ 0.1 msec) of the pulse is blanked-off to remove instabilities due to the switching of HV on the Pockels cell which controls the beam polarization. The counting-mode DAQ will run at low current and the triggers can be prescaled to ensure a low deadtime; this DAQ will use standard digitization devices to record the information from the GEMs and scintillators, much of which will have already been developed for the SBS spectrometer.

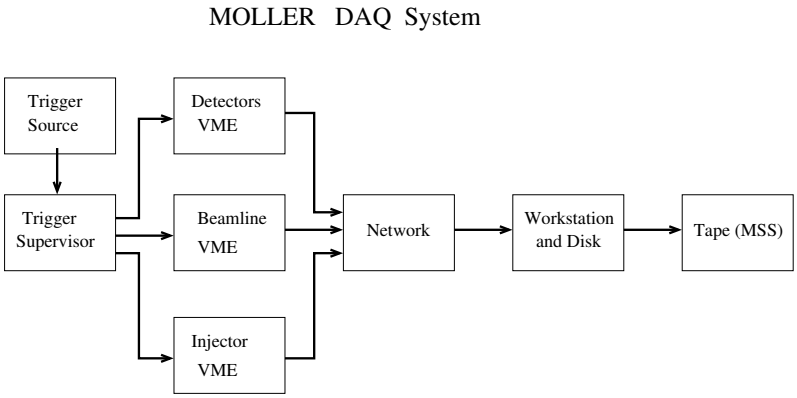


Figure 27: *Overview of the DAQ system for the MOLLER Experiment based on the standard JLab CODA system. For the integrating-mode DAQ, the trigger source is the master pulse from the helicity electronics. For the counting-mode DAQ, the triggers come from a scintillator-based tracking trigger.*

### 2.6.1 Integrating Detector Electronics

The heart of the integrating-mode DAQ will be low-noise integrating electronics similar to the ones developed for the Qweak experiment, but with enhanced capabilities matched to the higher helicity reversal frequency, larger event rate, and the need for more information read out for each helicity window. Recently, the entire electronics chain from the signal output of the PMT to the digitization process in the DAQ has been carefully studied. The same ADC design will be used to read out the beam current and beam position monitors. A collaboration has been launched with TRIUMF to review the existing electronics design and the proposed improvements given the MOLLER requirements and then design and fabricate new modules. These considerations are described in detail in Sec. 5.5.3.

### 2.6.2 Data Rates and Online Computing Needs

We anticipate needing approximately 600 of integrating ADC channels, spread across 6 VME crates. This will produce about 10 times the data rate of Qweak, hence 5 MBytes/sec per crate or 30 MBytes/sec total. This rate is comparable to the CLAS data rate and can be supported by commercial TCP/IP networks (1 GBit) and tape technology. The QWeak ADCs had a fast enough VME readout to support 2 kHz if we deploy only 10 modules per crate; a next generation of the module is likely to be faster, allowing more modules per crate.

The counting-mode DAQ will be triggered at rates between 10 kHz and 300 kHz, depending on the mode. The DAQ will consist of VME-based ADCs, FADCs, TDCs, Input/Output registers, and scalers. For the FADCs and TDCs we can use the JLab-built modules, while the others are commercial modules. We expect to need on the order of 300 channels of each (to be worked out).

We will need about 50 cpus; one as the event builder and the rest to handle various online tasks, including real-time helicity-correlated feedback on the charge asymmetry and possibly on other parameters, as well as online checks of data quality and the prompt analysis of 100% of the data with full corrections.

Given the raw data size, estimated to be between 400 and 1100 Terabytes over the course of the experiment, and that the ROOT output may be as much as four times as large, we can estimate our disk needs to be about 50 TBytes of volatile disk and 20 TBytes of disk for staging to and from the Mass Storage (MSS) tape silo.

### 2.6.3 Online Calibrations and Feedbacks

The coefficients $\alpha_j$, introduced in Eqn. 7 to describe the correlations between detector and beam parameter fluctuations, must be continuously calibrated *simultaneously* with the collection of production data, since the numerical values depend on the details not only of the apparatus but also the accelerator beam tune and the sensitivity and location of beam monitoring devices. Various ways of accomplishing this at Jefferson Laboratory have already been implemented during HAPPEX and G0 measurements, including extensive collaboration with personnel from Accelerator Operations and careful consideration of impact on other Halls.

While $\alpha_j$ can be extracted from a correlation analysis of the response of the detectors and beam monitoring devices to beam fluctuations in window-pairs, proper calibration requires deliberately dithering the beam trajectory concurrent with data-taking in a quasi-continuous fashion by an amount large enough to observe all the correlations while avoiding to add a non-statistical component to $\sigma(A_i)$. More generally, the study of the detailed noise and beam response characteristics of the monitors is a critical component of understanding the systematics.

The success of the experimental technique will also depend on careful preparation of the initial polarization states of the electron beam, which begins with a careful setup of the laser transport electronics of the polarized source. During data collection, there will be extensive electronic communication with optical and magnetic devices at the low energy end of the machine as various automated feedback loops of varying time frequencies will have to be incorporated. These systems will have to be implemented while paying careful attention to potential electronic cross-talk problems for which the proposed measurement will have sensitivity at an unprecedented level. Again, the collaboration has extensive experience on this aspect of the measurement. Details on the considerations in this subsection can be found in Sec. 3.1.

## 2.7 Simulation Framework

The simulation and analysis software for this experiment was developed internally by the collaboration and is based upon the Geant4 [77, 78] and ROOT framework. The goals of this simulation are to

- Represent the geometries and materials of the target, collimators, magnet coils, and detectors.
- Represent magnetic fields and be able to transport particles within them.
- Represent the quartz detectors and light guides, and evaluate Cerenkov optical photon generation, interaction, and detection.
- Evaluate radiative effects and multiple scattering.
- Evaluate rates and asymmetries from, but not limited to, Moller scattering, electron-proton elastic, electron-proton inelastic, target window scattering, low-energy photons, pions, and hyperons.
- Understand the radiation impact on the hall, such as from neutrons, and evaluate mitigating shielding configurations.
- Understand tracking requirements and evaluate methods for acceptance determination.
- Understand measurement sensitivities to misalignments in spectrometer components such as magnet coils and collimators.
- Optimize aspects of the experiment such as overall figure-of-merit, systematic errors, collimation, and tracking.

Geant4 provides a dependable and well supported framework for evaluating particle interactions and a variety of common processes, especially those involving low energy electromagnetic processes, hadronic and electromagnetic showering, and optical photons. In addition it provides facilities for tracking particles through detailed magnetic fields, representing geometries, and recording interactions.

### 2.7.1 Included Physics

Many commonly studied processes at Jefferson Lab kinematics, such as electron-proton interactions, deep inelastic scattering, and pion electro- and photo-production, are not included or represented sufficiently within Geant4. To study these, we have developed our own event generators, which can provide both rates and asymmetries. Of these, we have implemented

- Moller processes, with parity-violating asymmetries
- Elastic proton, with internal radiative effects and parity-violating asymmetries
- Inelastic proton based on the Christy/Bosted parameterization [79], with a simple $Q^2$ scaling parity-violating asymmetry
- Charged pion rates based on the Wiser parameterization [57] using the equivalent-photon approximation.
- Aluminum target window scattering, with parity-violating asymmetries

The framework for the generators was done in a general way so that each includes the same multiple-scattering and external radiative effects (where applicable) leading up to the primary interaction vertex. It was also done so that new generators are relatively straightforward to develop. This becomes important for future generators which will be necessary, such as self-analyzing hyperon production and decay.

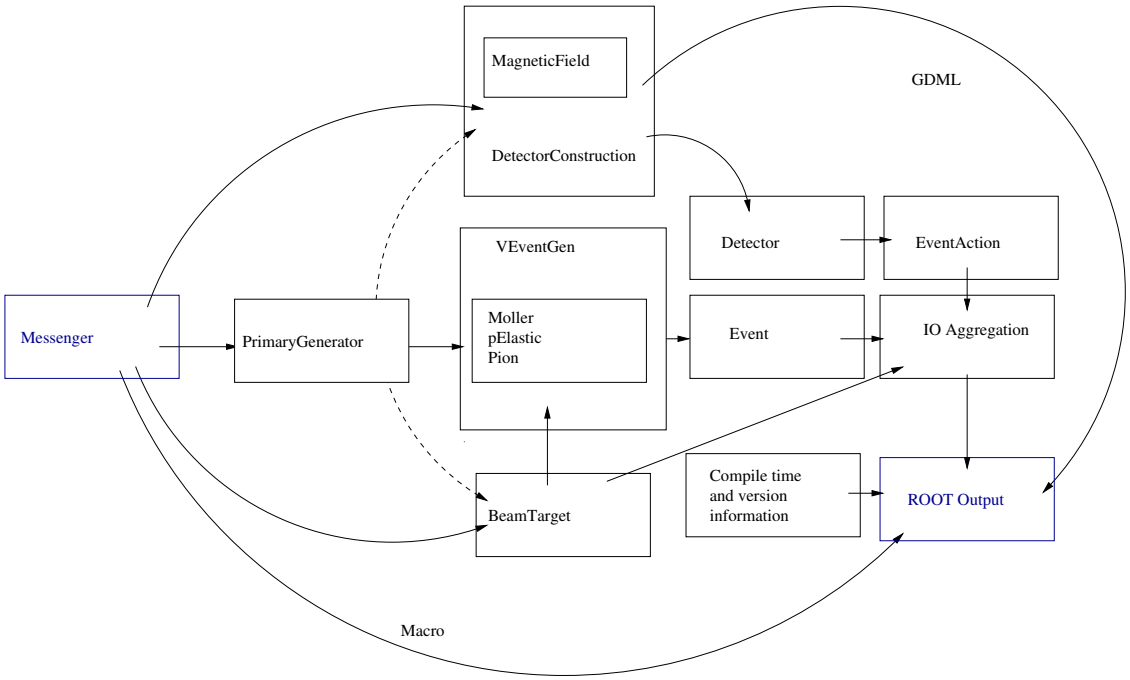


Figure 28: A schematic of the design and flow of the simulation.

### 2.7.2 Simulation Design and Infrastructure

In achieving the aforementioned goals, several design philosophies were implemented:

- A modular, object-oriented design, which is natural to such a project
- No "hard-coded" geometries to avoid recompiling while evaluating different configurations.
- No double representation of parameters, such as target position and material, which is required by both the geometry representation and event generators.
- Output directly to ROOT trees.
- Reproducible output, which involves saving run parameters directly with the output.

A schematic of the design can be found in Fig. 28.

All geometries are represented within the GDML framework provided by Geant4. This is an XML-based format which allows for full representations of detectors, materials, optical properties, and facilities for associating auxiliary data such as assigning unique identification for detectors and identifying target components. A 3D representation of this geometry can be seen in Fig. 29. With such a framework, all geometries are then saved as XML text files.

Output is saved in a ROOT tree structure which contains information on the generated events and the particle hits. In the ROOT files containing these trees, a considerable amount of information is stored in a separate object regarding the run conditions. The goal of this to be able to take the output and be able to examine the conditions on how it was produced and reproduce it. This includes the run time and date, compile time and date, Geant4 version, the full input parameters which drive the simulation, the full GDML files with comments, and the git repository information. git provides a method to reference snapshots of the source code and retrieve them later, which would allow one to run with identical source later on (provided it was checked into the repository).

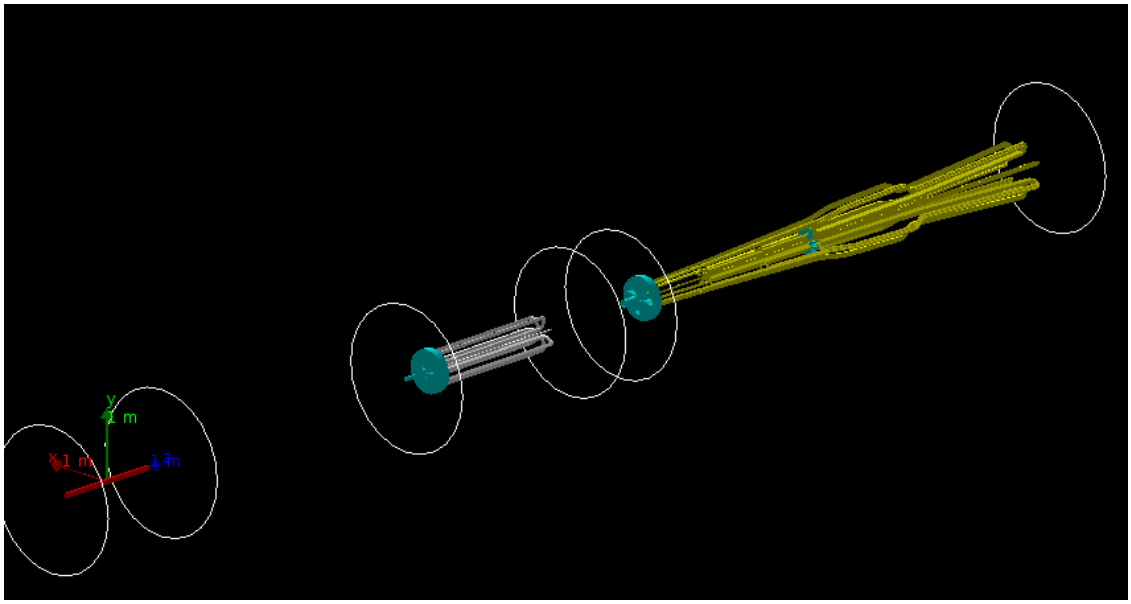


Figure 29: A representation of the spectrometer within the simulation.

## 2.8 Electron Beam Polarimetry

The longitudinal polarization of the 11 GeV electron beam is expected to be about 90%, with some variation depending on the specific details of the GaAs photocathode at the polarized electron source. The polarization will be oriented to within a degree of longitudinal to avoid an azimuthal scattering asymmetry associated with transverse polarization components (see Sec. 3.3). Since the measured parity-violating asymmetry is directly proportional to the electron beam longitudinal polarization, it is important to measure the polarization to high precision. The goal is to know the absolute polarization with robust control of systematic uncertainties to about 0.4% and to continuously monitor this polarization for significant variations. JLab experiments have accumulated extensive experience with two methods to accomplish these goals. Compton polarimetry measures asymmetric scattering from a polarized photon target. This technique is sufficiently non-invasive to be used as a continuous monitor. Møller polarimetry measures scattering from spin-polarized atomic electrons in a ferromagnetic target. In the following subsections, we describe the implementations of these polarimeters in Hall A.

### 2.8.1 Compton Polarimeter

As pictured in Fig. 30, the Hall A Compton polarimeter [80] is located in a 4-dipole vertical chicane, about 15 meters long, with the electron-photon interaction point in a horizontal segment about 21 cm below the primary (non-chicane) beamline. After passing the electron-photon interaction point, the electron beam is bent about 3.5 degrees by the third chicane magnet. The scattered electrons are separated from the primary beam and detected just before the fourth chicane magnet. Scattered photons pass through the bore of the third chicane magnet to be detected in a calorimeter.

The photon target is a 0.85 cm long Fabry-Perot cavity crossing the electron beam at an angle of 1.4°. The cavity will be operated with green (532 nm) light at a power level of about 4 kW. The laser light can be toggled between opposite polarizations of highly circularly polarized light. The cavity input beam can also be blocked, to allow measurement of backgrounds from all non-Compton scattering processes. A cycle through a laser-off period and opposing laser polarizations is typically performed with a period of 2-5

minutes. The polarization of the transmitted light from the locked cavity and the reflected light from the unlocked cavity are each monitored and can be used to characterize the laser polarization at the interaction point.

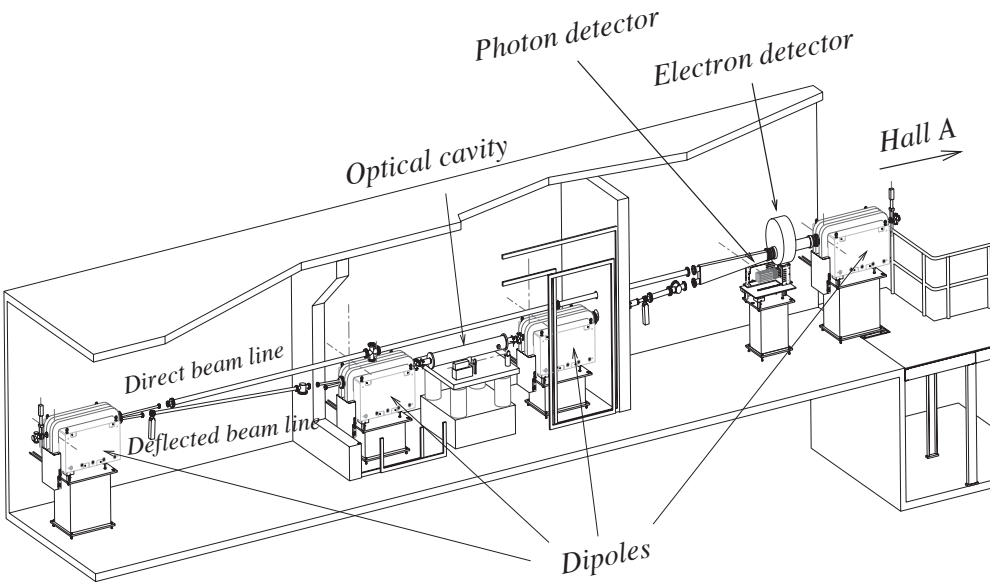


Figure 30: *Schematic of the Hall A Compton polarimeter. Figure from [80].*

The vacuum in the interaction region is at the level of few $\times 10^{-8}$ torr, implying a photon background rate due to Bremsstrahlung scattering from residual gas of around 5 Hz/$\mu$A. The dominant source of background in the photon detector is thought to be tails of the beam halo distribution interacting with the apertures in the interaction region. In contrast, for the electron detector the dominant background is thought to be dominated by energy tail or position halo of the primary beam since electrons from aperture scattering would presumably not cleanly transit the third dipole. When well-tuned, the background rates in the photon and electron detectors have been seen to be roughly similar: around $<$100 Hz/$\mu$A in recent use. At 11 GeV with a 4 kW green cavity, the Compton-scattered rates would be approximately 2 kHz/$\mu$A and the asymmetry will range from 32% to -7.6% over the energy spectrum. At 11 GeV, statistical precision of 0.4% is possible in about 5 minutes, depending on the specific detection and analysis approach which is considered.

**Laser System and Luminosity** As described above, in the current configuration of the Hall A Compton, the electron beam interacts with 4 kW green (532 nm) light in a resonant optical cavity at a crossing angle of about $1.4^{\circ}$. For 11 GeV beam energy, this corresponds to a rate of about 2 kHz/$\mu$A, which provides a large statistical power to assist with testing possible sources of systematic error.

Precision electron beam polarimetry also requires precise determination of the polarization of the photon target. Optical elements with remote actuation will be installed to allow light incident on the cavity input mirror to be prepared with an arbitrary state of polarization, and photodiodes will monitor both light back-reflected from the cavity input and light transmitted through the cavity. Analysis of the back-reflected light can be used to control the inter-cavity circular polarization with a precision not worse than 0.2% [89, 90].

**Electron Detector** In the existing polarimeter, Compton scattered electrons are detected in a set of 4 planes of silicon microstrips located just before the 4th dipole. Each microstrip plane instruments 192 strips with a pitch of 240 $\mu$m. Each silicon plane is 250 $\mu$m thick. Custom readout electronics outside the vacuum chamber pre-amplify and discriminate signals from each microstrip, implement a simple tracking algorithm to reduce non-directional backgrounds, and count hits in each strip. Presently, this system is operating at low efficiency with poor signal size for a minimum ionizing track compared to environmental noise on individual strips. The detector is also not large enough to accept the entire useful range of the scattered electron spectrum at 11 GeV. The detector will be upgraded to improve efficiency and electronics noise, and also to increase the detector size.

There are several upgrade options still under consideration. The most straightforward option would be to keep a similar detector geometry, but with a thicker (500 $\mu$m) silicon plane and a larger pitch width (240 $\mu$m) to increase the detector size. The larger signal from the thicker silicon strip would allow high detector efficiency with a higher discriminator threshold to reduce noise. Studies are presently underway to test this configuration with the existing readout electronics. Readout electronics developed for the Hall C Compton electron detector, used for the Qweak experiment, are also being evaluated for use with new silicon or diamond microstrip planes.

Another option under consideration is the use of an HVMAPS silicon pixel detector [94], in which the amplification and discimination is built into the silicon plane. These radiation-hard silicon detectors are thinner (50 $\mu$m), and provide a serial pipeline readout which is expected to be sufficient for the needs of the Compton polarimeter. Heat generated by the on-board electronics would require a heat sink, but not active cooling. The cost of such a detector, including redesigned carrier boards to match the required geometry and FPGA readout electronics, is expected to be modest. This promising technology is still under investigation.

**Photon Detector** The calorimeter for detecting scattered photons lies about 7 meters downstream of the interaction point. The strong forward boost of scattered photons leads to a tightly collimated photon beam ($<$3 mrad). For beam energies below 6 GeV, a GSO crystal scintillator of 6 cm diameter and 15 cm length, with a single photomultiplier tube, has been used. A larger calorimeter will be required for higher beam energies to better contain the shower and improve resolution. Testing has started with an lead tungstate ($PbWO_4$) array, to verify that yield and resolution is sufficient, and also to study possible phosphorescent effects.

The calorimeter signal is split between two parallel data acquisitions: one with a fast-counting, buffered ADC self-triggered on pulses from the photon detector, and the other utilizing a 250MHz flash ADC (fADC) to integrate the total signal over periods corresponding to the helicity pattern of the electron beam. The fADC system can also record a very low rate of individual pulses for calibration. Each of these dual readouts can be analyzed independently. The fast counting ADC readout and the sample pulses in the fADC system can both be triggered using the electron detector, providing an electron-photon coincidence spectrum for calibration.

### 2.8.2 Møller Polarimeter

Møller polarimetry will provide a useful cross check on beam polarization measurements performed with Compton scattering, gathering high statistics in a short amount of time and with different attendant systematic error. The principal challenge is to achieve high precision ($\sim$0.5% on the beam polarization) through careful control of the systematic effects.

We describe the plans for an upgraded Hall A Møller polarimeter, which will use a pure iron target foil held at saturation magnetization by a 5 Tesla magnetic field. A polarimeter in Hall C based on this design has already claimed control of systematic errors near the 0.5%, and the upgrades planned for the 11 GeV program at Jefferson Lab will enable that level of precision in Hall A. This upgraded polarimeter

is expected to be used for the PREX-II measurement in 2018, providing an opportunity to commission the new apparatus.

An alternative system, based on a polarized atomic hydrogen target, would be able to provide a continuous, non-invasive polarization measurement and would not require external calibration for accuracy at the few $10^{-3}$ level. The polarized atomic gas cell would be a new technology, requiring significant technical R&D. The details on this alternative system are included in Appendix A.

**Møller Target** The most common polarized electron targets are "large $\mu$" ferromagnetic alloy foils which saturate at relatively small applied magnetic fields. The electron polarization for a foil in saturation is about $8\%$. That is, roughly two electrons in the $d$-shell of each iron atom are polarized. The exact value cannot be calculated from first principles but must be inferred from calibration measurements of foil magnetization, with corrections for the expected contribution of orbital angular momentum. The magnetization may vary as a function of position on the foil, varying with thickness and perhaps also with thermal or mechanical annealing history. The accuracy of this determination is the fundamental limitation to precision polarimetry with this type of target. The best techniques have produced relative target polarization accuracy approaching $2\%$.

A significant improvement has been achieved by using pure iron foils in a strong longitudinal field approaching 4T to achieve full saturation of the magnetization. Experimental determination of the spontaneous magnetization of bulk iron at zero applied field and temperature, along with data constraining the evolution of magnetization with temperature and applied field, are used to determine the magnetization in operating conditions. An additional correction of $\approx 4\%$, based on measurements of the magneto-mechanical factor, is needed to subtract the contribution from orbital angular momentum. Accounting for these corrections, an accuracy of 0.25% in the determination of the electron spin polarization in a "saturated" iron foil is claimed [50] for the Møller polarimeter in Hall C at JLab.

The Hall A system is being upgraded from a low-field target system based on a ferromagnetic alloy, to the high-field, pure iron target modeled on the system used in Hall C. Such an upgrade was already attempted, but the target actuator assembly proved unwieldy for regular use. It was also very heavy, and required mechanical stabilization through a connection to the dewar for the cryogens. Furthermore, the magnet itself required problematic external connection to the helium supply. The redesign includes a new 5T magnet with self-contained cryogenic system, coupled to a vacuum chamber, and a target actuator system that relies on precision construction with fewer adjustable degrees of freedom. The new target actuator will allow precise rotation of the target with respect to the electron beam, to confirm our understanding of the saturation phenomenon. Figure 31 includes a photograph of the high-field foil target cryostat and target ladder, as was tested in 2016. The first prototype for the new actuator was insufficiently stable, and a new design is under construction to be tested in 2017.

**Møller Spectrometer** The Møller scattering spectrometer needs to have a well defined acceptance in the neighborhood of maximum analyzing power at $\theta_{CM} = 90^\circ$, so the average analyzing power can be determined to sufficient precision. One also needs to understand uncertainties due to the Levchuk effect [112, 113], which results from the most deeply bound (and unpolarized) atomic electrons having a very different momentum distribution. When the accepted scattering angle is closely tied to the electron momentum, the Levchuk effect can be quite large, as the momentum $p_e$ of K-shell electrons in iron is $\sim 100$ keV/c and the effect goes like $p_e/m$.

The Hall C spectrometer design [53] is based on a simple two-quadrupole approach, where Q1 focusses in the horizontal plane and Q2 defocusses. Between these two elements is a straightforward collimator system. This approach has worked well, but affords little ability thoroughly analyze the final state electrons,

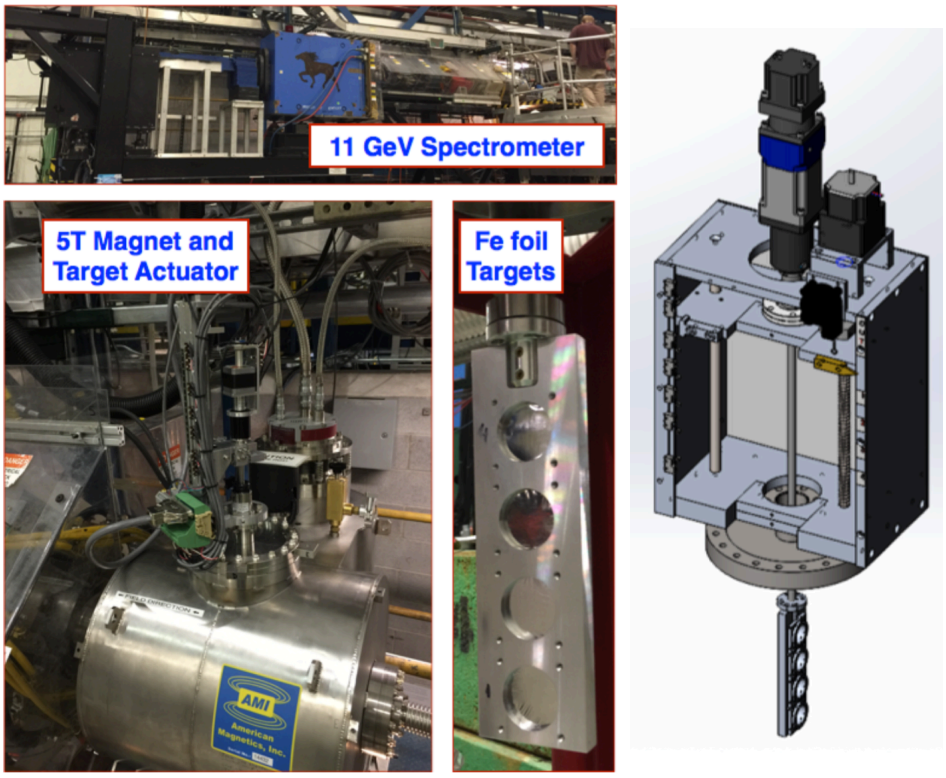


Figure 31: The high-field Møller polarimeter spectrometer and target, installed in Hall A at JLab. The beam enters from the left into the spectrometer, now a QQQQD lattice, upgraded with an additional quadrupole for 11 GeV operation. Bottom left shows the newly purchased 5T magnet from American Magnetics, Inc. (AMI), with the first prototype target arm inserted, connected to the actuator assembly, emerging vertically from the magnet bore. For scale, the cylindrical magnet cryostat is 18 inches in diameter. Bottom middle shows the target ladder which holds four one-inch diameter foil targets, generally of different thicknesses. The new design for the target actuator is shown on the right.

and the size of the Levchuk effect is calculated to be $\approx 3\%$. Furthermore, limitation in the magnetic field strength would require significant reworking to operate at beam energies of 11 GeV.

We will continue to use the existing Hall A Møller spectrometer system [55, 100], in which the Levchuk corrections are somewhat smaller, estimated to be $\sim 2\%$ [55]. Originally a QQQD magnetic array, a fourth quadrupole has been added to optimize operation up to 11 GeV. The dipole magnet will remain as is, but the detector position will be adjusted for higher energy operation. The detectors are segmented to better identify the correlations with scattering angle and energy, and an upgraded data acquisition system has been put in place for high rate operation. Studies of the event distributions in energy and angle, including measurements as a function of rate, are important for determining backgrounds and dead-time corrections.

## 2.9 Hall A Infrastructure

The apparatus depicted in Fig. 7 and related shielding is being designed so that MOLLER runs can be interleaved with other experimental programs in Hall A. A first-order check of the experiment layout in Hall A has been done and minor obstructions from various fixtures in the Hall are being addressed. A layout with both Hall A High Resolution Spectrometers (HRSs) parked at 90° to the beam line has been considered. An alternate layout with both spectrometers located beam left is also being evaluated. Such a layout would

| Error Source | Fractional Error (%) |
|---|---|
| Statistical | **2.1** |
| Absolute Normalization of the Kinematic Factor | 0.5 |
| Beam (second order) | 0.4 |
| Beam polarization | 0.4 |
| $e + p(+\gamma) \rightarrow e + X(+\gamma)$ | 0.4 |
| Beam (position, angle, energy) | 0.4 |
| Beam (intensity) | 0.3 |
| $e + p(+\gamma) \rightarrow e + p(+\gamma)$ | 0.3 |
| $\gamma^{(*)} + p \rightarrow (\pi, \mu, K) + X$ | 0.3 |
| Transverse polarization | 0.2 |
| Neutral background (soft photons, neutrons) | 0.1 |
| Total systematic | **1.1** |

Table 5: *Summary of projected fractional statistical and systematic errors.*

facilitate installation (open access to the hall truck ramp) but requires more effort to move one spectrometer to the opposite side of the beam line. Moving from the beam entrance along the beam line towards the dump, one would encounter the cryogenic target approximately 6 m upstream of the nominal pivot, the first spectrometer toroid at the HRS nominal target pivot, followed shortly thereafter by the hybrid toroid and, with the detectors approximately 20 m downstream of the pivot. Møller events and the degraded beam travel under vacuum all the way to the detectors and beam dump, respectively.

Cooling of the collimators and room temperature spectrometer toroids will be done using a closed low conductivity water (LCW) circuit to contain the beam activated water in the hall. The LCW distribution system in the hall is being upgraded to handle the additional volume required by this and other experiments. A heat exchanger will transfer the heat from the closed system to the JLab wide LCW system. An additional 2 MVA electrical transformer would be added to handle the load brought by the spectrometer toroids.

For the purpose of estimating the experiment cost, we have taken a first look at the shielding required around just donwstream of the target and primary small angle collimator. As the details of the experimental apparatus improve, simulations are being carried out to optimize the shielding configuration and specific locations. Once simulations and conceptual engineering designs are completed, the best strategies will be devised to handle the disassembly and storage of activated parts for multiple years (with other experiments taking place in between MOLLER runs) in consultation with JLab's Radiation Control group. With the target significantly upstream of the HRS pivot, the incoming hall beam line also needs to be rearranged. A detailed plan for configuring the upstream magnetic and beam diagnostic elements has been formulated.

# 3 Systematic Control

The proposed $A_{PV}$ measurement in some sense constitutes a fourth generation parity-violation experiment at Jefferson Laboratory. Apart from the obvious challenge of measuring a raw asymmetry with a statistical error less than 1 ppb, an equally challenging task is to calibrate and monitor the absolute normalization $A_{PV}$ at the sub-1% level. The collaboration continues to gain extensive experience on all aspects of such measurements as work continues on executing and analyzing the third generation experiments PREX [44] and Qweak [45].

We tabulate our estimates of the most important systematic errors in decreasing order of importance in Table 5. It is instructive to recall that the raw asymmetry is about 32 ppb and that the raw statistical

error is 0.6 ppb or about 2%. In the following subsections, we describe some of the principal challenges of controlling systematic errors in the proposed measurement and provide justification for the projected errors in the table.

## 3.1 Beam Fluctuations

As described in Secs. 2.1 and 2.6.1, the scattered flux would be integrated over the duration ($\sim$ 500 $\mu$s) of each helicity window. Equation 7 shows how one then extracts a signal proportional to the raw cross-section asymmetry by removing beam correlations. In this section, we summarize the upper limits for the random and helicity-correlated fluctuations in order to achieve the systematic error goals in Table 5. Apart from active techniques to control helicity correlations in the laser beam as well as in the low energy electron beam, one also gains additional suppression due to so-called "adiabatic damping" and with the use of several methods of "slow helicity reversal", as we elaborate below.

Numerical estimates for $\alpha_j$ were made using Monte Carlo simulation, with results which are similar to expectations based on scaling the beam-motion sensitivities measured in HAPPEX-II. They are listed in Table 6. Using these numbers, the required monitoring resolution to achieve counting statistics for 1 kHz window pairs is $\lesssim$ 3 $\mu$m in position, and 10 ppm in intensity. The position monitor resolution will be straightforward to achieve based on previous experience in HAPPEX-II, PREX and Qweak. On the other hand, achieving 10 ppm resolution in beam intensity will require significant R&D, which the collaboration has flagged for further study and effort.

### 3.1.1 Adiabatic Damping

The impact of helicity-correlated spatial variation in the beam can be greatly reduced in the accelerated beam impinging on the target due to the process of adiabatic damping. A simple consequence of relativistic mechanics is that the available phase space for a beam which has been adiabatically accelerated to a momentum $p$ from a momentum $p_0$ is reduced by a factor of $\sqrt{p/p_0}$. For the 3 GeV beam energy of the HAPPEX-II experiment, this corresponds to a reduction in beam motion in each dimension by a factor of $\sim$ 95, compared to motion of the 100 keV injector beam.

The benefits of this effect are typically not fully realized; getting close to the theoretical limit requires detailed understanding of accelerator beam optics, tuning and diagnostics. The collaboration typically works closely with accelerator physicists to produce the best results and maintain them over the duration of data collection. The best performance from the HAPPEX-II experiment suggested that helicity-correlated variations were suppressed by factors up to $\sim$ 30. When combined with careful setup of the laser optics and helicity-defining Pockels cell on the polarized injector laser table that led to $\sim$ 400 nm helicity-correlated position differences in the 100 keV region of the injector, this resulted in small position differences in the experimental hall.

The benefits from adiabatic damping have lagged behind the theoretical maximum in part due to difficulties in configuring the 100 keV injector region. Additional diagnostics and optics in that portion of the injector would presumably allow greater benefits to be realized. Such work, in addition to other, already implemented, additions to diagnostics and control, should make it possible to realize a significant fraction of the theoretically maximum suppression factor of 180 for the case of a 11 GeV beam.

The importance of focussing effort on adiabatic damping is illustrated in Figure 32, which illustrates the recent experience of the Qweak experiment. Even better polarized source laser optics setup was achieved, resulting in helciity-correlated position differences $< 50$ nm in the 100 keV region of the injector. However, adequate time was not spent to properly match the accelerator tune resulting in a lack of adiabatic damping. The result as position differences in the experimental hall of $\sim 100$ nm, actually greater than in the polarized injector region.

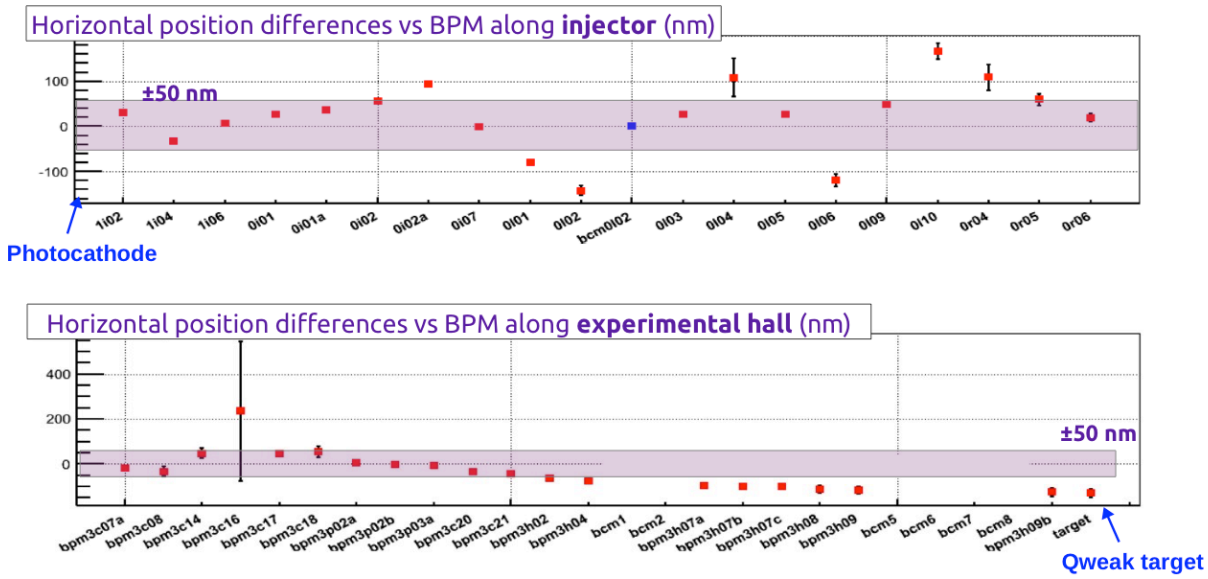


Figure 32: *Helicity-correlated position differences in the horizontal direction at various places in the beamline during Qweak. The pink band in each figure represents* $\pm 50$ *nm about zero. The upper figure shows the position differences in the polarized injector region, where careful laser optics setup resulted in position differences* $< 50$ *nm in the 100 keV region. The accelerator tune was not well matched, resulting in a lack of adiabatic damping that led to increased position differences* $\sim 100$ *nm in the experimental hall.*

Apart from the obvious benefits for helicity-correlated beam fluctuations from adiabatic damping, there are also advantages for random fluctuations in the beam trajectory on target. In order to ensure that one attains the goals for systematic corrections, random fluctuations in beam parameters at 1 kHz must be less than those specified in Table 6. Experience during Qweak has indicated that these goals for random fluctuations should be straightforward to achieve.

| Beam Property | Assumed Sensitivity | Accuracy of Correction | Required 1 kHz random fluctuations | Required cumulative helicity-correlation | Systematic contribution |
|---|---|---|---|---|---|
| Intensity | 1 ppb / ppb | $\sim$1% | $< 1000$ ppm | $< 10$ ppb | $\sim 0.1$ ppb |
| Energy | -1.4 ppb / ppb | $\sim$10% | $< 108$ ppm | $< 0.7$ ppb | $\sim 0.05$ ppb |
| Position | 0.85 ppb / nm | $\sim$10% | $< 47$ $\mu$m | $< 1.2$ nm | $\sim 0.05$ ppb |
| Angle | 8.5 ppb / nrad | $\sim$10% | $< 4.7$ $\mu$rad | $< 0.12$ nrad | $\sim 0.05$ ppb |

Table 6: *Goals for first order corrections from electron beam helicity correlations*

### 3.1.2 Helicity-Correlated Beam Fluctuations

If one averages over the instantaneous pulse-pair asymmetry $A_i$ (see Eqn. 7 in Sec. 2.5) and considers the cumulative experimental asymmetry $A_{raw}$ over many window pairs $i$, one can write

$$\begin{aligned} A_{\rm raw} \equiv \langle A_i \rangle &= \left\langle \left( \frac{\Delta F}{2F} \right)_i \right\rangle - \left\langle \left( \frac{\Delta I}{2I} \right)_i \right\rangle - \sum \alpha_j \left\langle (\Delta X_j)_i \right\rangle \\ &= A_F - A_I - \sum_j A_{Mj}. \end{aligned} \tag{8}$$

In a well-designed and well-executed high flux parity experiment, the helicity-correlated beam asymmetries (HCBAs) $A_I$ and $\Delta X_i$ will be small enough so that $\langle A_{raw} \rangle \simeq \langle A_F \rangle$, even though $\sigma(A_F)_i$ will be significantly larger than $\sigma(A_{raw})_i$ for window-pairs.

The first goal is to ensure that each correction $A_{Mj}$ is of the order of, or smaller than the projected raw statistical error of about 0.6 ppb, and that the slopes $\alpha_j$ are known to better than 10%, so that the systematic error contributions from these corrections are small. This can in turn be transformed under reasonable assumptions to goals for the grand average $\Delta X_j$. These considerations are summarized in Table 6. These are realistic goals, as we elaborate briefly in the following. During the relatively short HAPPEX-II experiment, position differences were kept to less than 2 nm and angle differences to less than 0.2 nrad; only a modest improvement over these goals is required. The more recent experience with the PREXI experiment has been similarly good, and further results and experience will come from the full Qweak dataset currently being analyzed and the future PREXII data-taking. Table 7 summarizes the experience of recent, ongoing and future parity experiments on the measured HCBAs.

| Selected parity experiments and their measured or projected demands on suppression of helicity-correlated beam-parameter differences | | | | | | |
|---|---|---|---|---|---|---|
| Experiment (*) actual (†) projected | physics asymmetry | stat. error | sys. error due to beam | limits on position differences | limits on angle differences | limits on diameter differences |
| *HAPPEX I | -15,050 ppb | 980 ppb | $\pm 20$ ppb | $< 12$ nm | | |
| *SLAC E158 | -131 ppb | 14 ppb | $\pm 3$ ppb | $< 12$ nm | 0.4 nrad | $< 10^{-5}$ |
| *HAPPEX II-p | -1,580 ppb | 120 ppb | $\pm 17$ ppb | $< 1.7$ nm | 0.2 nrad | |
| *HAPPEX III | -22,100 ppb | 550 | $\pm 66$ ppb | $< 40$ nm | | |
| *PREX-I | 657 ppb | 60 ppb | $\pm 7.2$ ppb | $< 4.0$ nm | | $< 10^{-4}$ |
| Upcoming or ongoing parity experiments | | | | | | |
| †PREX-II | 500 ppb | 15 ppb | $\pm 3.0$ ppb | $< 1.0$ nm | | $< 10^{-4}$ |
| †Qweak | -288 ppb | 5 ppb | $\pm 1.4$ ppb | $< 2$ nm | 30 nrad | $< 7 \times 10^{-3}$ |
| † 12 GeV Møller | 36 ppb | 0.6 ppb | $\pm 0.05$ ppb | $\sim 0.5$ nm | 0.05 nrad | $< 10^{-5}$ |

Table 7: *Shown are various parameters for several parity experiments, including HAPPEX I, E158, and HAPPEX II-p, that are published, HAPPEX III and PREx, the results of which are available, and QWeak, currently being analyzed. Also shown are PREx-II, recently approved, and MOLLER. The second and third columns show the actual measured or projected asymmetries and statistical errors. The fourth column shows the actual or projected error associated with corrections for helicity-correlated beam-parameters. The remaining columns indicate actual or projected limits on helicity-correlated beam parameter differences.*

Extensive tools for tightly controlling $A_I$ have been developed in previous experiments. The nonlinearity between the detectors and beam current monitors is typically controlled at the 0.5% level. Given the goal of 0.1 ppb contributed error from intensity corrections, this implies that the grand average $A_I$ must be smaller than 10 ppb. Intensity feedback will be employed to assure convergence within that bound.

A large degree of cancellation for the slopes $\alpha_j$ is expected when considering the full azimuthal symmetry of the detector. A conservative estimate of a factor 10 reduction in sensitivity is taken to account for detector alignment tolerances. After applying corrections for small position and angle differences, an uncertainty of approximately 10% is likely to remain. This leads to the specifications for the run-averaged $\Delta X_j$ in order to keep the contributed uncertainty to less than 0.05 ppb each, as listed in Table 6.

### 3.1.3 Beam Spot Size Differences

In all the discussion above on beam-related systematic effects, it has been assumed that the dominant component in the scattered flux response to fluctuating parameters is linear. In practice, it is possible that certain second-order effects might be helicity-correlated and thus lead to systematic shifts. The stability of the CEBAF beam makes it highly unlikely that there are large effects, and none have been seen in experiments to date. Typically, second-order effects tend to scale as a fraction of the first-order effects, providing additional incentive to control the first-order effects as tightly as possible. Furthermore, the $g-2$ and "double-wien" slow reversals discussed below will be powerful cross-checks of this assumption.

One common manifestation of a second-order effect is a helicity-correlated difference in the beam spot-size $\sigma$. We have simulated the effect for the proposed spectrometer/collimator geometry, finding it to be at the level of (12 ppm)$\times\Delta\sigma/\sigma$. Work on the laser table should be able to bound the laser spot size asymmetry to be less than $10^{-4}$, in which case the potential effect would be as large as 1 ppb. We assume a factor of 10 suppression from cancellation due to the proposed periodic slow helicity reversals, so that the net contribution will be limited to 0.1 ppb.

### 3.1.4 Slow reversals

The technique of "slow helicity reversal" generally refers to the introduction of an additional helicity flip, which changes the sign of the helicity relative to some sources of HCBA. An example would be the introduction of an additional half-cycle $g-2$ rotation, which would reverse the electron beam helicity with respect to the helicity of the beam created in the polarized source. The statistical consistency of data sets taken in different states of the reversal can be used to demonstrate the absence of large, unknown systematic errors, and the combination of data sets (appropriately sign-corrected) provides a method for further canceling possible unmeasured or poorly-corrected HCBA effects.

Until quite recently, only one slow-reversal has been commonly employed at CEBAF. A half-wave plate is inserted into the laser path to reverse the sign of laser polarization, relative to the voltage applied to the Pockels cell (see Fig. 9). This slow-reversal is particulary effective for cancelling two types of effects. First, any false asymmetries related to electronic signals, either from the logic or Pockels cell high voltage, will be completely unaffected by the insertion of a half-wave plate. Thus, such false asymmetries will not change sign while the physics asymmetry does change sign. Second, it is well established that when a Pockels cell is pulsed, it can steer or even focus the beam in a fully helicity-correlated fashion that is unrelated to polarization effects. Presumably this is due to the piezoelectric properties of the crystal or simple mechanical stress. Such steering and focussing will be unaffected by the half-wave plate, again insuring the false asymmetries will not change sign when the physics asymmetry does. Many HCBA's, however, are explicitly related to helicity-dependent residual linear polarization. Most of these effects will change sign with the insertion of the half-wave plate just at the physics asymmetry does, and hence are not cancelled. For this reason, other methods of slow-helicity reversal are desirable.

At 11 GeV, the total number of $g-2$ spin rotations will be large, on the order of $120\pi$. It will be possible to change the orientation of spin, while maintaining very similar beam optics properties, by changing the energy of the accelerator by about 100 MeV. This interval is small enough to not require invasive reconfiguration of the experiment: backgrounds, spectrometer optics, etc. should remain very similar. This would

be a very effective slow reversal, in that all HCBAs from the source should influence the final measurement with the opposite sign. Since this is disruptive to other halls, this method might be used a few times over the duration of the entire run.

A similarly effective slow reversal that can be used much more often can be created using spin manipulation in the injector. Spin manipulation (using a "Wien rotator") is necessary in the CEBAF source to align the electron polarization into the horizontal plane, and then to set the in-plane launch angle to optimize longitudinal polarization at the experimental target. In principle, it is possible to apply a half-cycle spin rotation without changing the optics of the beam. In practice, this requires a more complicated spin manipulation in the CEBAF injector. The "Double-Wien" filter (shown schematically in Fig. 33) uses a second Wien rotator and a solenoid, which allows a helicity slow reversal using only solenoidal spin manipulation without changes to the Wien rotator setpoints. This system was commissioned prior to the PREX run in 2010, and it was used routinely during both the PREX and the Qweak runs to achieve a slow spin flip with relatively minor changes to the front end beam optics.

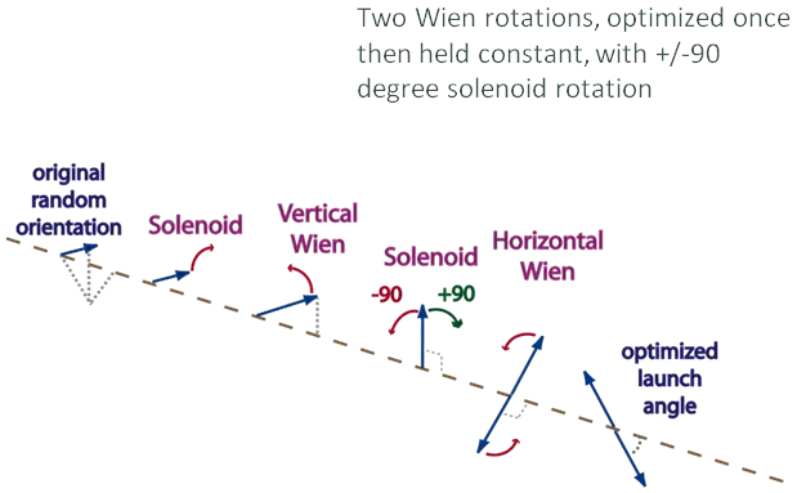


Figure 33: *Schematic of the concept of the "Double-Wien" filter, which allows a full "slow" flip of the electron beam polarization with minimal disruption to the front end electron beam optics. The flip is accomplished by adjusting the second solenoid, without changing the settings of the two Wien rotators.*

### 3.1.5 Measurement and Control of HCBAs

Monte Carlo simulation was used to estimate the sensitivity of the apparatus to beam motion. With the minimum acceptance angle defined by collimators placed 10 meters downstream of the target center, the detected flux in one azimuthal segment is expected to change by approximately 8.5 ppb for a 1 nm shift in the beam centroid. This result is consistent with simple scaling arguments applied to sensitivities measured during HAPPEX-II. This suggests the approximate sensitivity to changes in the beam angle, as well: 85 ppb/nanoradian. The ratio of these sensitivities roughly matches the accelerator which, as a rule of thumb, has a characteristic length of about 10 meters.

A reasonable goal for any measurement of a small asymmetry is to keep the cumulative correction averaged over the entire run due to random or helicity-correlated beam motion to be no larger than the grand statistical error, and to believe the correction to 10% of itself. An important (but not sufficient) step toward

achieving this goal is to further insist that beam-related corrections for an individual pulse pair are no larger than the statistical error for that pulse pair, which in our case is 78 ppm for our 1 kHz pairs. The detector for the MOLLER experiment has seven segments and a high degree of azimuthal symmetry. A goal that greatly facilitates a number of diagnostic techniques is to insist that *the beam-related corrections for each of the detector's segments are no larger than the statistical width of that individual segment, a width that will be around 200 ppm*. It is this goal (together with the caveat that we only assume that we understand our corrections at the 10% level) that guides us in most of our specifications for both beam jitter and monitor resolutions.

It is quite possible to successfully correct for HCBAs on a pulse-to-pulse basis, but still accumulate large HCBAs over the course of the entire run. This could happen, for example, if for whatever reason the corrections were always in a particular direction (with respect to the physics asymmetry). Such a problem might not become apparent until quite late in the run, since the precision of our knowledge of beam parameters during MOLLER will typically only be sufficient to keep corrections small compared to statistics. There are at least two ways out of this conundrum. One is to have significantly improved monitoring of beam parameters, something that would require improved technology beyond what we have demonstrated. The other is to employ feedback. Luckily, we have demonstrated effective feedback for both beam position and intensity at the required level. Of interest here are the sensitivities of the measured asymmetries to the HCBAs, which we will conservatively assume to be ten times better than those quoted above for individual segments.

With all the aforementioned requirements in mind, we find the following specifications for MOLLER:

- The beam centroid must be measured at two locations 10 m apart just upstream of the target with a resolution of a few microns for 1 kHz window pairs.
- The beam centroid and angle jitter must less than $\sim 50$ microns and $\sim 5$ microradians respectively at 1 kHz.
- If the beam jitter is significantly larger than quoted above, active position feedback on the electron beam at 1 kHz frequency will be necessary.
- The grand-average helicity-correlated position difference over the duration of the entire run must be less than 1.2 nm and the angle difference should be less than 0.12 nrad.

We elaborate on these issues below. The experience of HAPPEX-II, which found position (angle) differences of around 1 nm (0.2 nrad) suggests that these specifications should be achievable.

### 3.1.6 Beam jitter and monitor resolution

This section compares the MOLLER specifications for beam jitter and beam monitor resolution to the existing performance. This primarily comes from experience during the Qweak experiment in 2010-2012 and some follow-up studies. Only the results are summarized here; further details of the studies can be found in Section 5.1.2.

**Beam position monitor resolution:** The most stringent requirement on beam position monitor resolution comes from requiring that the additional random noise contribution from beam jitter (after regression) be no larger than 10% of the counting statistics width for a single azimuthal element of the detector. This leads to a more stringent requirement than applying the same criterion to the average over all detectors. This is important for two reasons. It allows for high precision comparison among selected combinations of the azimuthal detector elements to study the behavior of the linear regression corrections. It also insures the precision necessary to measure the azimuthal dependence of the raw detector asymmetries for the "manual" feedback loop to control transverse polarization described in Sec. 3.3. Applying this criterion leads to a

| Beam Property | MOLLER Specification | Qweak Observed |
|---|---|---|
| Intensity | $< 1000$ ppm | 500 ppm |
| Energy | $< 108$ ppm | 6.5 ppm |
| Position | $< 47$ $\mu$m | 48 $\mu$m |
| Angle | $< 4.7$ $\mu$rad | 1.4 $\mu$rad |

Table 8: *Summary of comparison of MOLLER specifications on random beam property fluctuations to scaled Qweak measurements. See text for further details.*

requirement on the beam position monitor measurement resolution of 3 $\mu$m for 1 kHz pairs. Scaling from measured Qweak resolution values for 960 Hz quartets for the Jefferson Lab standard "stripline" beam position monitors results in an estimated **2.4 $\mu$m resolution for 1 kHz pairs for MOLLER, which achieves the MOLLER goal of 3 $\mu$m**. It is also planned that redundant beam position measurements with a similar resolution will be performed with radio frequency microwave cavity monitors that are installed in the Hall A beamline. These have not been used extensively except during parity experiments running in Hall A where performance comparable to stripline monitors has been demonstrated.

**Beam position jitter:** The goal for the accuracy of beam corrections also imposes requirements on the "jitter" (random noise) in the beam properties. Typically, the beam parameter correction sensitivities (the $\alpha_j$ coefficients in Eq. 7) are determined with no better than $\sim 10\%$ precision. For single azimuthal sectors, this implies that the beam property jitter can be no larger than 200 ppm for a single sector (to insure that the resulting random noise contribution after regression is no larger than 10% of the counting statistics width). This leads to these requirements on the maximum allowed jitter (see Table 6): $< 47$ $\mu$m (position), $< 4.7$ $\mu$rad (angle), and $< 108$ ppm (energy) for 1 kHz window pairs. Expectations for jitter for MOLLER running with 1 kHz pairs can be scaled from Qweak experience with 480 Hz window pairs. The summary comparison in Table 8 shows that all of the jitter requirements appear achievable, assuming that the beam jitter properties are similar for the 12 GeV upgraded machine. Some recent initial experience with 11 GeV beam in Hall A suggests that the beam jitter properties for 15 Hz window pairs are similar to the 6 GeV machine.

**Beam intensity jitter:** As with past parity experiments, we will normalize our detector signals to beam intensity on a pulse-to-pulse basis. Here it is critical that the beam charge monitors (BCMs) and detector electronics chain are highly linear, something we expect will be true at the level of 1% or better. In our error budget (Table 5) we have allowed ourselves a 0.3% relative error associated with the BCM linearity, something that corresponds to about 11 ppm for an individual 1 kHz pulse pair when averaged over the entire detector. To be conservative, we have thus set a goal of 10 ppm for the BCM resolution associated with an individual pulse pair. Using this resolution, can can also put a limit on allowable jitter in the beam intensity. With a 10 ppm BCM resolution and 1% linearity we can tolerate beam intensity jitter of 1000 ppm (0.1%) before the jitter itself begins to add to the pulse-to-pulse statistical width. Scaling from the Qweak experience with 480 Hz window-pairs to 1 kHz window-pairs for MOLLER predicts $\sim 500$ ppm for 1 kHz pairs, so the goal of 1000 ppm seems easily achievable. Finally, we note that random noise at the 10 ppm level from the BCMs, when added in quadrature to the roughly 80 ppm 1 kHz pulse-pair statistical width will result in less than a 1% increase in the statistical width.

**Beam charge monitor resolution:** As mentioned above, the MOLLER goal is 10 ppm resolution for relative beam intensity measurement for 1 kHz window-pairs. The best measured results for beam charge monitor (BCM) resolution at Jefferson Lab come from the recently completed Qweak experiment. scaling from those measurements implies a resolution of 62 ppm for MOLLER for 1 kHz window-pairs. **The**

**Qweak scaled value of 62 ppm is above the MOLLER goal of 10 ppm.** Improving this is a subject of current R&D efforts involving both the collaboration and the lab (see Section 5.1.2).

### 3.1.7 Position Feedback

A more significant problem might be the slow convergence of the random beam jitter. Even with no systematic helicity-correlated offset, beam jitter of 5 micron would converge to zero with a $1\sigma$ range of 0.8 nm.

A systematic non-zero helicity-correlated position difference could be diagnosed more quickly, and the potential loss of statistical precision could be mitigated, by forcing the random jitter to converge through feedback. This feedback would necessarily be helicity-correlated, and operate with a time-scale between a few minutes and a few hours. The optimized feedback time-scale will depend on the safe dynamic range of the feedback system, the time scale of any slow-reversal or other significant beam disturbance, and the magnitude of the jitter, among other factors.

The goal of any such feedback would be to improve on the statistical rate of convergence for the beam position jitter by a relatively small amount. Under optimal feedback, the centroid would converge to zero as $1/N$, where $N$ is the number of integration periods of the feedback cycle, compared to $1/\sqrt{N}$ for the case without feedback. A balance will need to be found between keeping the average feedback correction small, while still operating on a time scale that drives convergence to zero position difference. Updating feedback every hour, for instance would improve convergence by a factor of $\sqrt{8}$ on an ideal shift, while implying that the size of the correction would be around $4 \times 10^{-3}$ of the beam jitter.

It is important not to mask serious configuration problems in the polarized source with the use of intensity and position feedback systems. For this reason, the average position correction will be monitored for significant non-zero average corrections which indicate the need for re-tuning of the polarized source. It is also crucial that any position dependent feedback does not change intensity asymmetries in a way which reduces the rate of convergence of the crucial intensity feedback.

There are several mechanisms which could be used for position feedback. The commonly employed technique at Jefferson Lab, successfully employed by the G0 collaboration, uses a piezoelectric actuated mirror in the source optics to deflect the laser beam. Similar techniques were employed or tested by the E158 collaboration at SLAC and the SAMPLE collaboration at Bates.

Since the dominant source of position differences is a non-zero first moment in the helicity-dependent residual linear polarization distribution of the laser spot, a superior feedback mechanism might involve a birefringent element with a variable, linear variation of birefringence across the beamspot. Such a device could be conceptually similar to the continuously variable birefringent system, such as the Babinet-Soleil compensator.

There are several disadvantages to position feedback mechanisms which operate on the source laser. The most important is that the photocathode changes significantly on the time-scale of days. Ion back-bombardment damages the photo-cathode, creating a quantum efficiency "hole" at the laser spot and along a path to the electrical center of the cathode. Motion of the beamspot on the cathode can interact significantly with these strong QE gradients, changing the effective slope of the correction and creating significant coupling with electron beam intensity.

These complications can be avoided by using magnetic deflection of the electron beam. A system of 4 air-core magnets has been constructed in the injector, with a fully isolated power and control system. These were constructed by the Electron Gun Group as a potential feedback mechanism. As expected, this system avoids the significant coupling to beam intensity which complicates use of the piezoelectric mirror. Further testing would be required to qualify this system at the required level of precision, and at the 2 kHz reversal frequency.

### 3.1.8 Beam spot-size asymmetry

Geometric arguments predict that the sensivity to a spot size asymmetry $\delta\sigma/\sigma$ is approximately (12 ppm)$\delta\sigma/\sigma$. An upper bound on the spot size asymmetry should be possible from measurements on the laser table of $\frac{\delta\sigma}{\sigma} < 1 \times 10^{-4}$, which would imply a net false asymmetry of about twice the statistical error bar over the course of the run. Spin precision spin flips, including both the $g-2$ and spin-manipulator slow reversals, will both serve to flip the helicity without changing the spot size asymmetry, and should provide a high degree of cancellation. Assuming roughly equal statistics are collected in each reversal state, the average effect from spot size should be reduced by a factor of 10.

### 3.1.9 Strategy for control of HCBA

As described above, modest improvements on the state-of-the-art are necessary to achieve sufficent control on the run-averaged helicity-correlated beam asymmetries. A summary of the strategy is presented here.

The intensity asymmetry requires control at the level of $< 10$ ppb. As with previous experiments, an automated helicity-correlated feedback on beam intensity will be required to achieve this small value. There does not appear to be any fundamental reason why the conventional asymmetry feedback scheme should not converge to this level. While this is approximately an order of magnitude beyond what will be required for the PREX and Qweak experiments, those runs will provide an opportunity to demonstrate feedback effiency at the required level.

Control of position differences will require careful configuration of the source optics. As is currently done, the optics system will be qualified first with diagnostics on the laser table, and then with measurements of HCBA in the electron beam in the low-energy injector. It is estimated that improvements in the injector measurements are feasible which would enable precision scans of important configuration parameters leading to the verification of injector position differences approaching $\sim$ 20nm. As is required for the PREX experiment, the potential spot size asymmetry will also be bounded in laser table studies at the level of $10^{-4}$, which limits the potential effect on the measurement at the level of 1 ppb.

Good optical transport throughout the injector and accelerator is crucial to realizing the benefits of the adiabatic phase space damping. It should be possible to achieve a damping factor approaching 100 (about half of the theoretical maximum) if further improvements in injector diagnostics are made. In combination with a source configuation giving position differences in the injector at the level of 20 nm, the average systematic helicity-correlated offset would lie in the 0.2 nm (0.02 nrad) range, sufficient for this measurement.

If the careful beam preparation succeeds at this level, the dominant source of helicity-correlated beam position difference would be the slow convergence of the random (non-helicity-correlated) beam motion. For this reason, it may be necessary to employ feedback on position differences. The feedback integration period would be long enough to allow small corrections to position differences, which are not likely to interfere with other aspects of beam preparation or delivery. The magnitude of feedback corrections will be monitored for signs of a required reconfiguration of the polarized source.

Several slow reversals will be employed. The insertable halfwave-plate in the source optics will be used frequently, possibly changed at 4-12 hour intervals. A frequent spin-manipulation slow reversal is required to cancel spot size asymmetries, so the injector solenoid slow reversal should be used on a period of approximately 1 week. The $g-2$ energy change spin flip, should be used at least once, dividing the full data set in two. Although it is potentially more disruptive, it is also expected to be the most effective of the slow reversals, and the experiment would benefit from using it as often as once per month.

## 3.2 Longitudinal Beam Polarization

The experiment requires a relative accuracy of the electron beam polarization measurement at the level of 0.4%. The electron beam polarization is expected to be about 90%, with some variation depending on

specific photocathode material and other factors. The beam polarization might vary at the 2% level over the duration of a specific photocathode's lifetime. Systematic control at 0.4% will be achieved both with high-precision cross-checks between redundant techniques and with continuous monitoring of the beam polarization during data collection.

It is worth noting that a comparable level of accuracy was achieved by the SLD collaboration [92, 93] using a Compton polarimeter with a 46 GeV pulsed beam at SLAC. JLab has accumulated extensive experience with polarimetry at or below 6 GeV. Recently completed and ongoing experiments in the JLab "6 GeV" parity-violation program, in both Halls A and C (PREX, HAPPEXIII, PVDIS and Qweak), have developed polarimeters with precisions of about 0.7–1%. The most precise comparison has recently been made in Hall C, where results from the Compton and Møller polarimeters were compatible within their quoted relative normalization uncertainty of 0.7% over the length of the Qweak experimental run [89]. While this is an encouraging step forward, there has never been a cross-check of independent polarimeters which has reached the level of 0.4%, nor has any experiment at Jefferson Lab yet required this level of precision.

In order to reach a robust 0.4% precision, a Compton polarimeter will be used continuously during data collection. Independent analysis of scattered photons and electrons provides a pair of measurements with a high degree of independence in systematic uncertainties. This polarimeter will be cross checked against periodic measurements with a Møller polarimeter using ferromagnetic foil targets. An upgrade to the Hall A Møller polarimeter, presently underway, will support improvements and studies that should ultimately lead to a systematic accuracy near 0.4%. An alternative second-stage upgrade would incorporate a polarized atomic hydrogen gas target in the Møller polarimeter, which would provide for continuous operation of a polarimeter with systematic uncertainties completely independent of the Compton-scattered photon or electron measurements. This option is described in Appendix A.

### 3.2.1 Compton Polarimetry

Compton polarimetry is a very attractive technique for high precision polarimetry with high energy electron beams. When electrons scatter off circularly polarized laser photons, the associated Compton cross-section depends on both the electron and photon polarizations. Beam interactions with a photon target are non-disruptive, so Compton polarimetry can be employed at high currents as a continuous polarization monitor. The photon target polarization can be measured and monitored with a very high precision, and the scattering between a real photon and free electron has negligible theoretical uncertainty, without atomic or nuclear effects which can complicate other measurements. Radiative corrections to the scattering process are at the level of 0.1% and are very precisely known. The SLD result of 0.5% polarimetry demonstrates the feasibility of very high accuracy Compton polarimetry [93].

JLab Compton polarimeters employ a 4-dipole vertical chicane, just below the primary beamline. The interaction point is between the second and third dipoles, where the electron beam is parallel to the primary beamline but at a lower height. A Fabry-Perot cavity serves as the photon target. The scattered electrons lose energy and are separated by the third and fourth dipoles from the primary beam and are intercepted by position-sensitive detectors such as silicon microstrips. The scattered photons are detected by a calorimeter downstream of the third dipole. The electron polarization can be extracted independently by measuring the helicity-dependent rate of the electrons or the photons, and important systematics studies can be carried out by studying electron-photon coincidences.

Table 9 summarizes the goals for various contributions to systematic uncertainty, based on the collaboration's experience with Compton polarimetry from the recent, high-precision experiments PREX and Qweak. The first four rows list sources of uncertainty which are highly or completely correlated between the electron and photon analyses. Other potential systematic uncertainties arise in detector readout or calibration and are mostly or entirely decorrelated between the analyses. Each of these separate categories of poten-

| Relative error (%) | electron | photon |
|---|---|---|
| Position asymmetries* | - | - |
| $E_{Beam}$ and $\lambda_{Laser}$* | 0.03 | 0.03 |
| Radiative Corrections* | 0.05 | 0.05 |
| Laser polarization* | 0.20 | 0.20 |
| Background / Deadtime / Pileup | 0.20 | 0.20 |
| Analyzing power<br>Calibration / Detector Linearity | 0.25 | 0.35 |
| Total: | 0.38 | 0.45 |

Table 9: *Goals for systematic uncertainties for the Hall A Compton polarimeter at 11 GeV. Topics marked * are a common systematic uncertainty between the photon and electron analyses, while the other are largely independent between the detector systems.*

tial systematic uncertainty: correlated, electron-only, and photon-only, will be discussed in the following sections.

**Sources of Correlated Uncertainty** Uncertainties associated with the Compton scattering process will be a common source of systematic uncertainty between the electron- and photon-detector analyses. One example lies in the energy normalization of the scattering process. The photon wavelength will be determined to better than 0.1 nm and the electron energy to 0.05%, which leads to an uncertainty in the analyzing power at the level of 0.03%. A similarly small uncertainty will come from radiative corrections, which are calculable [87] with high precision and will contribute at the level of $10^{-3}$.

Helicity-correlated changes in luminosity of the laser/electron interaction point can introduce a false asymmetry. Various causes of luminosity variation must be considered, such as electron beam intensity, beam motion or spot-size variation. Another possible source of false asymmetry would be electronics pickup of the helicity signal. For all of these effects, the demands of the primary experiment (for isolation of the helicity signal, and control of helicity-correlated beam asymmetries) exceed the requirements for precision polarimetry by several orders of magnitude. In addition, the laser polarization reversal provides an additional cancellation for asymmetries correlated to the electron beam helicity. For these reasons, these classes of helicity-correlated asymmetries are expected to be a negligible source of uncertainty in polarimetry.

The limits of knowledge of the laser beam polarization is likely to be the most significant source of uncertainty common to all measurements of Compton scattering. An improved technique to control the laser polarization uncertainty has been used in Hall C [90] and will be implemented in Hall A. The polarization of light arriving at the cavity entrance can be inferred from light reflected back from the cavity and analyzed with the same apparatus used to create the initial polarization state, measuring a single power level [82]. This technique was employed in Hall C to maximize the circular polarization of light injected in the cavity and to monitor the polarization during the run [89]. It was verified to work by two methods. In the first, with the cavity under vacuum in running conditions, a scan over a broad range of initial polarization states was performed, and the recorded analyzed reflected power was shown to be well described by the simple hypothesis of optical reversibility. A more direct verification was made with the cavity opened, directly measuring the polarization of the injected light in the cavity and correlating this with the analysis of the reflected light. This correlation is shown over the full range of the scan, and zoomed in for measurements at maximum circular polarization, in Fig. 34. In operation, the Hall C Compton polarimeter ran with the reflected light very near minimum, with an implied uncertainty on the circular polarization within the cavity of $0.1\%$.

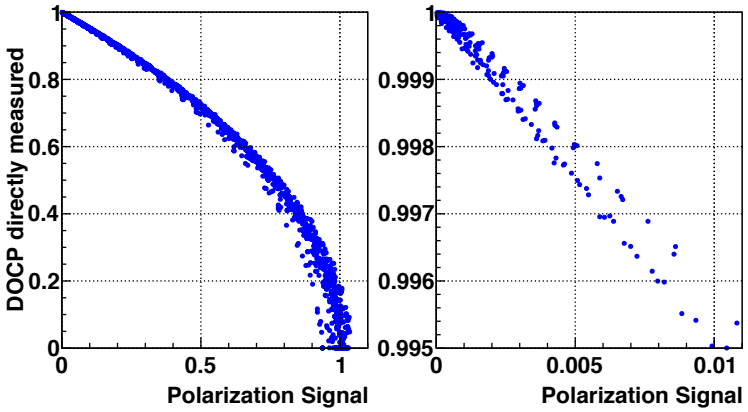


Figure 34: *Measured degree of circular polarization in the Hall C Compton laser cavity vs. the polarization-analyzed reflected light, measured over a broad scan of initial polarization states. The figure on the right is zoomed in the region of maximum circular polarization. From [89].*

**Systematic Uncertainties for the Electron Detector** The electron detector is composed of 4 planes of silicon microstrips normal to the electron beam trajectory and positioned on the low-energy side of the beam trajectory in the dispersive chicane. Electrons which have given up energy to a scattering process are separated from the primary beam by the third chicane dipole, and the energy of a detected electron is implied by the distance of the track from the primary beam with a dispersion of about 0.45% of the beam energy per millimeter. Models of the chicane magnets are used to calculate the electron energy as a function of position in the detector. The absolute normalization of the energy of the electron detected in each strip is sensitive to details of the magnetic chicane and beam position, and is the key challenge in normalizing the measured asymmetry spectrum.

The effects of electronics noise and non-directional backgrounds are reduced by triggering on tracks which are restricted to very small angles relative to the beam. The trigger can be adjusted for the range of track angles and number of planes used in the track, including a single plane trigger. The efficiency of individual strips can also be measured using data from the multiple planes. Deadtime and pileup in the DAQ system must also be understood. The fast-counting DAQ can take very high rates with low deadtime, and deterministic deadtime intervals are enforced in readout and acquisition electronics stages. While the total data rates may as high as 200 kHz, rates in individual strips will be reduced by segmentation to $<$2 kHz. However, details of the triggering and DAQ algorithms can be important, especially in the case of non-uniform detector asymmetry or significant backgrounds.

Backgrounds are studied with the laser cavity unlocked, allowing both the background rate and asymmetry to be well determined. However, high backgrounds could impact the systematic uncertainty due to deadtime or pile-up corrections. There is also the possibility of backgrounds from Compton-scattered electrons, which can produce delta rays when scattering in the detector or in its shielding. These tracks can themselves be sufficiently forward-going to pass the trigger, thus changing the analyzing power as a function of energy. Simulations, along with studies of track distributions and electron-tagged photon energy spectra, will be used to identify and correct for such effects in the data.

The cross-section and asymmetry as a function of Compton scattered photon energy is plotted in Figure 35 for 11 GeV electron beam. The Compton edge (the kinematic endpoint of the Compton energy spectrum) is observed in the electron detector and used to calibrate the distance of the detector from the primary beam. In addition, the asymmetry as a function of photon energy $k$ exhibits a zero crossing. Deter-

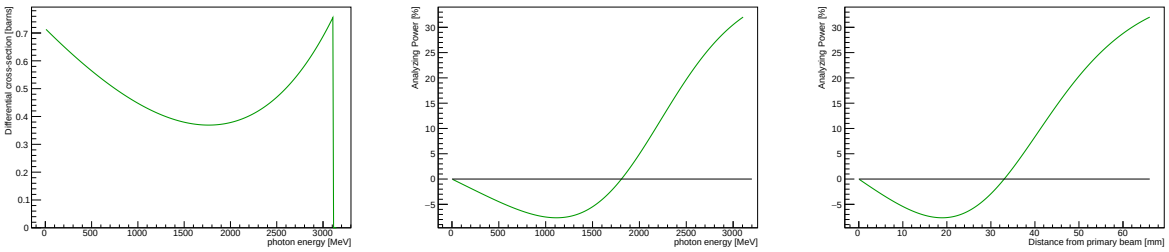


Figure 35: *The cross-section and asymmetry plotted versus Compton scattered photon energy, and the asymmetry versus distance from the primary beam at the electron detector, are shown for the Hall A polarimeter at 11 GeV.*

mining the location of this asymmetry zero crossing (0xing) provides a second absolute energy calibration point, so together the Compton edge and 0xing can be used to calibrate two parameters: the detector location relative to the beam and the strength of the magnetic field in dipole 3. In this way, survey results and magnetic field maps serve as a cross-check to a beam-based self-calibration of the Compton energy spectrum. The precision of this calibration is limited by delta-ray production in the microstrips, which distorts the measured spectrum. The precise determination of the Compton edge from the rate spectrum is also complicated by efficiency variations between the microstrips.

The recent analysis of the Hall C Compton polarimeter for the Qweak experiment provides the best example of the potential of this technique [89]. The chicane had been optimized to low energies, and with a large bend angle and 532 nm light, the 0xing was 8.5 mm from the primary beam. At this distance, backgrounds were reasonably low, and the diamond microstrip detector could be positioned close enough to the primary beam to accept well beyond the zero-crossing. While the microstrip detector exhibited significant efficiency variations from between strips, the asymmetry distribution was not distorted by this effect. The rate and asymmetry distribution are shown in Fig. 36. The shape of the asymmetry spectrum over microstrip position, which is slightly non-linear in electron momentum, was calculated in Monte Carlo simulation of the Compton spectrometer using magnetic models of the chicane magnets. This shape template was fit to the asymmetry distribution, returning a scale factor corresponding to the spectrometer dispersion, the location of the Compton edge, and the polarization of the electron beam. The fit results were stable and robust, with no observable, systematic deviations in the residuals of the fit to the asymmetry spectrum shape. Simulation was used to demonstrate that the results were very insensitive to a broad range of possible systematic errors, including uncertainties in magnet $Bdl$ or field map, detector noise, detector alignment, or the effect of triggering algorithms. Delta-ray production from the electron interacting in the detector was also seen to be important, so that results from the later detector planes had to be significantly corrected due to distortions in the asymmetry spectrum from the multiple tracks; the correction in the first plane of the detector was negligible. The most significant systematic error contributions, about 0.4%, were a result of dead-time in the fast-triggering DAQ algorithms, which could be complicated by noisy or inefficient strips. Over the run, the electron detector normalization in this analysis was estimated to be known to 0.56%. It was also clear that improvements in the DAQ algorithms would be able to further improve on this precision.

In the Hall A system at 11 GeV, the 0xing will be around 33 mm from the primary beam, which should allow for robust operation. Improvements in the DAQ system suggested by the Hall C experience should lead to a reduction of the rate-dependent DAQ inefficiencies that were the largest source of systematic uncertainty. The high statistical power of the measurement will also be important; for example, high precision studies can be performed to benchmark models of the readout system against changes the laser power or the parameters of the triggering (preamp levels, logical gate lengths, coincidence levels, etc). Based on the

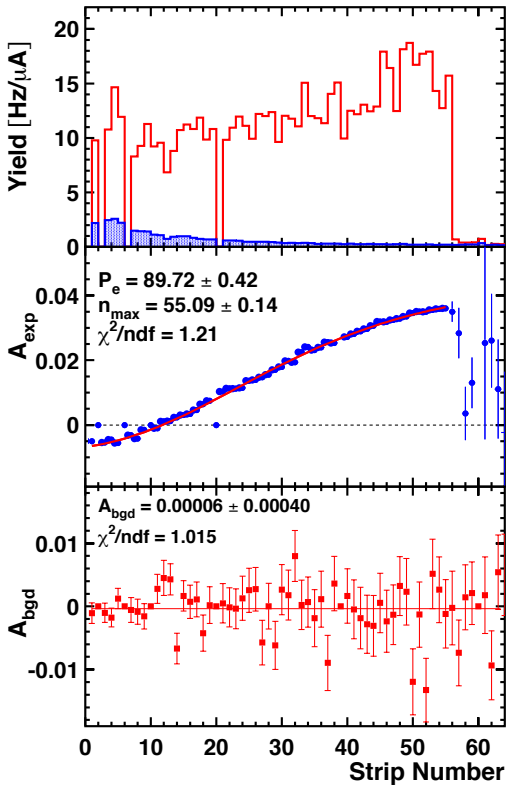


Figure 36: *The measured rate and asymmetry spectrum in the Hall C Compton polarimeter measured in the first plane of the electron detector, as a function of microstrip number from the detector edge which is about 6 mm from the primary beam. top: measured rate with laser on (red) and off (blue); middle: background-subtracted asymmetry spectrum, fit to expected shape with free parameters for spectrometer calibration and polarization; bottom: measured background asymmetry, uniform and consistent with zero.*

Qweak experience at the 1 GeV beam energy, it is expected that the electron detector analysis at high energy will be normalizable to a level better than 0.4%.

The large statistical power also enables alternative analyses with significantly different systematic uncertainties. Using only the last, single silicon strip at the Compton edge will be capable of 0.4% statistical precision on time-scales of around one hour. The rate of change of the asymmetry in this region is only 0.5% / mm. locating this strip, relative to Compton edge, to a little better than half its own width should provide a robust accuracy on the analyzing power better than 0.4%. This technique would be sensitive to determination of the location of the Compton edge, but otherwise very insensitive to other calibration parameters.

Similarly, the asymmetry minimum, which lies about 19 mm from the primary beam, could be used. The statistical power is much lower in this region, with a single strip requiring 30 hours to achieve 0.4% statistical precision on the polarization (assuming signal-noise ratio of 10:1). However, here the asymmetry is not changing with position, so there is minimal calibration error in selecting a strip in this minimum. Beam position and angle may vary the location of the asymmetry minimum on the detector over hundreds of microns during this time span, but such changes can be tracked using beam position monitors or the Compton

edge. The analyzing power varies by only about 0.4% of itself over a range of $\pm 1.6$ mm, suggesting minimal corrections will be necessary .

Cross-checks between calibrations and techniques should provide convincing evidence that the system is well understood. Given these considerations, it seems likely that the calibration of the electron detector will be understood at the level of 0.3% or better.

**Systematic Errors for the Photon Detector** The precise determination of the analyzing power as a function of energy is more difficult for the photon calorimeter than for the electron detector due to the width and shape of the detector response function. In order to fit the asymmetry as a function of detected photon energy, the analyzing power must be calculated as a convolution of the response function with the theoretical analyzing power curve. In general, determining the effect of a low-energy threshold on the analyzing power depends sensitively on the shape of the response function; at low energies this is a major source of uncertainty. At high energies, the improved resolution and consistency of the response function shape over the range of interest should significantly reduce this problem.

The $PbWO_3$ detector presently being used for high energy operation is expected to have a response function that scales reasonably linearly over a broad range of energy. The response function shape and energy calibration can be simulated, and studied using the photon tagging through coincidence triggers with the electron detector. Characterization of the phototube response as a function of both rate and pulse-size will also be important.

The pulse-counting analysis in the photon detector is also sensitive to pile-up, which distorts the asymmetry distribution. Background and rate distributions will serve as inputs to simulation for corrections to the analyzing power. In the current Hall A analysis, pile-up corrections are estimated at the level of 1%, and the effect can be controlled at a level better than 10% of itself. Deadtime corrections, which can vary significantly with background conditions, will also represent a potential systematic uncertainty.

Uncertainties related to the threshold, response function shape, absolute energy calibration, deadtime and pile-up can also be eliminated by integrating the photon calorimeter signal, without threshold [88]. These previous problems are then replaced with a requirement on the linearity of the average response to the photon energy. Because the analyzing power integral is energy-weighted, the statistical figure-of-merit in not badly degraded by the negative asymmetry region at low photon energies.

The PREX experiment, with a beam energy near 1 GeV, relied on the integrating photon method for polarimetry at the level of 1% precision. Simulations of the photon response function were sufficient to control the analyzing power uncertainties for those measurements. The dominant uncertainty in the asymmetry measurement arises from variation in the photomultiplier response with changes in average rate which introduces a systematic error through background subtraction.

At high energies, with the ability to study response function with the electron-detector-tagged photon beam over a large fraction of the energy range, the photon detector analyzing power normalization uncertainty in the range of 0.3% should be achievable.

**Summary of Compton Polarimetry** The prospects for $0.4\%$ Compton polarimetry are excellent. This ambitious goal will require vigorous and dedicated efforts to reduce sources of systematic uncertainty. At lower beam energies, precision has reached 1% (PREX at 1 GeV), 0.8% (HAPPEX-3 at 3 GeV) and, most recently, 0.7% (Qweak at 1 GeV). It is worth noting that, in each case, the systematic uncertainty of polarimetry exceeded the demands of the experiment.

In each of these measurements, the dominant systematic uncertainty lay in the determination of the analyzing power or in laser polarization. New techniques developed during Qweak provide control on laser polarization to 0.2% or better. Lower beam energies imply a reduced energy range of the Compton-scattered spectrum and smaller scattering asymmetries, both of which can complicate the calibration of the analyzing

power. With the new techniques for controlling laser polarization and at higher beam energies, the required improvement to 0.4% should be possible.

In the case of the electron detector, the "self-calibration" was successfully employed in the Hall C Compton polarimeter at 1 GeV. The fit to the shape of the asymmetry spectrum proved to be remarkably resilient to calibration errors, with an estimated uncertainty in the analyzing power normalization of 0.56%. With the increase in the scattered energy spectrum at the higher 11 GeV beam energy, it is expected that the electron detector analysis will be precise at level much better than 0.4%.

For the photon detector, the integration readout method has been successfully used in the HAPPEX-3 and PREX experiments, with the primary limitations being the characterization of the phototube response over the range of signal levels. At 11 GeV, coincidence measurements between the photon and electron detectors will also provide a significant cross-check to the response function and energy calibrations, enabling a counting measurement which is far more precise than what has been possible in previous runs at low beam energies.

It is expected that some significant fraction of data production time wil be used for studies of the Compton polarimeter system which are not disruptive to the experiment, for example, scans of detector positions, laser power and polarization, and data acquisition parameters. The scattering asymmetry at 11 GeV is relatively large which, for some analysis approaches, will provide statistical precision at the level of $\sim$0.5% in a few minutes of data collection. This rapid access to high statistical power, which is so powerful for cross-checking potential sources of systematic uncertainty, has never before been available for Compton polarimetry at JLab. Given this high statistical power, beam-based studies will be an effective method for constraining many of the possible experimental systematic uncertainties.

As described above, recent improvements in available laser power, analysis techniques, laser polarization measurements, and the favorable kinematics of the higher electron beam energy have opened the door to robust 0.4% precision Compton polarimetry for the MOLLER program.

### 3.2.2 Møller Polarimetry

Møller polarimeters exploit the helicity dependence of polarized Møller scattering $\vec{e^-} + \vec{e^-} \rightarrow e^- + e^-$ to extract the beam polarization by using a polarized electron target of known polarization. Møller scattering has a very high analyzing power, with a maximum of 7/9 for $90^\circ$ scattering in the center of mass, a very large cross section, and the two electrons with high energies in the final state make it easy to detect their coincidence and reduce background to negligible values. Such polarimeters have been in use for more than three decades and many potential systematic effects are now controlled at a level below 1%.

Inserting foils into the beam is a "destructive" measurement requiring periodic measurements at a beam current of a few to tens of $\mu$A, thus precluding continuous polarization monitoring at high beam current. Consequently, Møller polarimetry with foil targets will be used as a cross check on measurements with the Compton polarimeter, verifying that there is no common systematic error in the measurement of Compton-scattered electron and photons that leads to a beam polarization error of larger than 0.4%.

An alternative strategy to avoid the limitations of conventional Møller polarimetry is to use polarized atomic hydrogen gas, stored in an ultra-cold magnetic trap, as the electron target. Such a target has an electron polarization of practically 100%, removing the target polarization uncertainty associated with the ferromagnetic targets. Other errors can be strongly suppressed. Furthermore, such a target is thin enough to be used continuously with the experiment, providing a continuous polarization measurement which is entirely independent of the Compton polarimeter. With this system, a 1% statistical accuracy could be achieved in less than 30 minutes of running [51, 52]. The details of this alternative are given in Appendix A.

Table 10 shows the current and projected list of systematic errors for Møller polarimeters at Jefferson Lab.

| Variable | Hall C | Hall A: Foil | | Alternate: |
|---|---|---|---|---|
| | | Tilted | High Field | Hydrogen |
| Target polarization | 0.25% | 1.50% | 0.25% | 0.01% |
| Target angle | ‡ | 0.50% | ‡ | ⋆ |
| Analyzing power | 0.24% | 0.30% | 0.20% | 0.10% |
| Levchuk effect | 0.30% | 0.20% | 0.20% | ⋆ |
| Target temperature | 0.05% | ‡ | 0.05% | ⋆ |
| Dead time | ‡ | 0.30% | 0.10% | 0.10% |
| Background | ‡ | 0.30% | 0.10% | 0.10% |
| Others | 0.10% | 0.50% | 0.10% | 0.30% |
| Total | 0.47% | 1.8% | 0.42% | 0.35% |

⋆: Not applicable ‡: Not Estimated

Table 10: *Systematic error summary for Møller polarimeters at JLab, including anticipated uncertainties for future prospects. The Hall C polarimeter [53] uses a high field pure iron target [50, 54] with a simple two-quadrupole spectrometer. The existing Hall A device [55] uses a tilted ferromagnetic alloy target, and a spectrometer with a dipole magnet following three quadrupoles. A high-field pure iron target upgrade is underway, with an additional quadrupole in the spectrometer for high energy operation. Research and development for the alternative hydrogen gas target [51, 52] provides the basis for a second continuously-running high precision polarimeter to complement the Compton apparatus.*

**Ferromagnetic Foil Targets** Nearly all high energy Møller polarimeters operated to date [55, 100–106] make use of tilted ferromagnetic foil targets. High permeability alloys coupled with ∼few hundred Gauss magnetic fields preferentially polarize in the plane of the foil, so tilting the foil at a moderate angle gives a substantial longitudinal target polarization. Calculating the effective polarization, however, is typically the limiting systematic error, and such devices cannot ultimately do better than several percent precision. A different approach [53], implemented in Hall C at Jefferson Lab, using a high magnetic field perpendicular to the foil plane [50,54], has reported 0.5% precision on the beam polarization. It is this target design which will be implemented in Hall A.

Materials respond to external magnetic fields because atomic electrons, with spin and orbital angular momentum, align themselves to an applied field. However, with a Bohr magneton equal to $5.8 \times 10^{-5}$ eV/Tesla, the magnetic energy at several Tesla is still much smaller than the thermal energy at room temperature, so the effects of magnetic fields in most materials ("diamagnetism" and "paramagnetism") are quite small.

Ferromagnetism, on the other hand, is a quantum mechanical phenomenon in which a subset of atomic electrons in some elements and alloys spontaneously align. These alignments happen in localized domains, which themselves are randomly oriented. However, the application of relatively small magnetic fields cause the domains themselves to line up, leading to large induced magnetic fields.

Figure 37 shows magnetization data for pure iron. At several tens of Gauss of "applied" field $H$, the magnetic field $B$ saturates at $\sim$ 1.5 Tesla because the domains are aligned. The resulting magnetization corresponds to $\sim$ 2 Bohr magnetons per iron atom, that is, roughly two electrons worth of magnetic dipole moment in *each* iron atom. As $H$ reaches and exceeds several Tesla, the magnetization field simply adds directly to the applied field.

Measurements in *pure* iron or nickelpoint to very precise knowledge of their magnetization parameters [108, 109]. The approach used by the Basel/Hall C group [50,53,54], and to be followed in Hall A, is to polarize pure iron foil targets with a very high (several Tesla) field, provided by superconducting coils. The magnetiziation of the foils, while not directly measuremed, is taken to be implied by published data on the

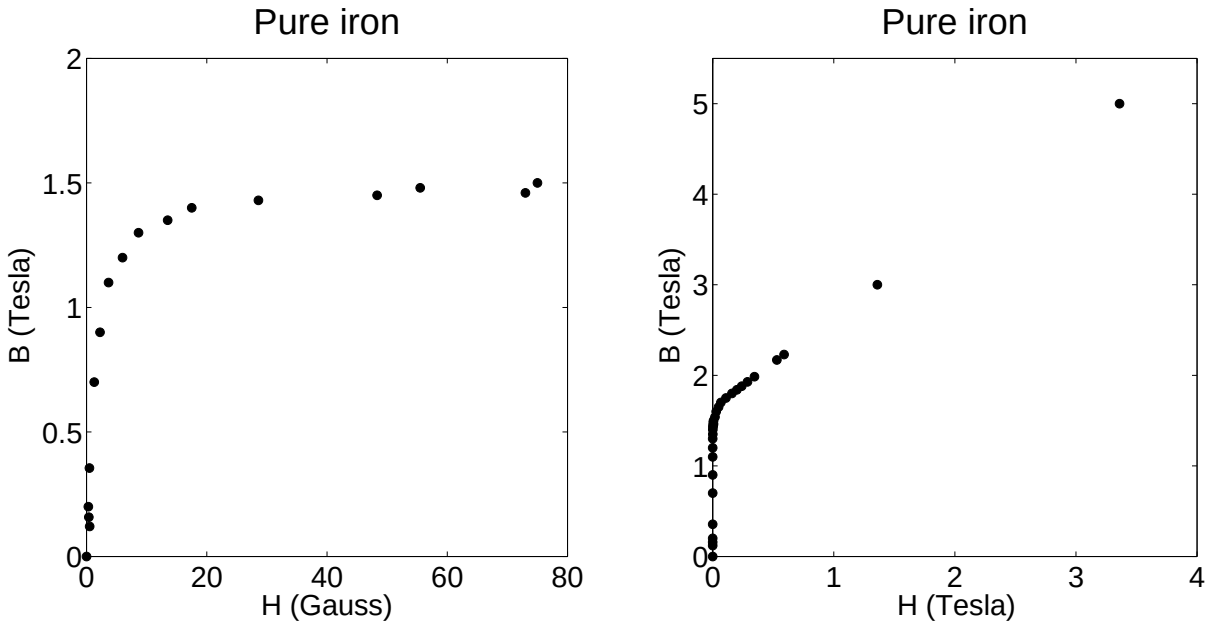


Figure 37: Magnetization curves for pure iron, from http://www.fieldp.com/magneticproperties.html. We use CGS units, so both $B$ and $H$ are properly measured in Gauss, but 1 Tesla$= 10^4$ Gauss. Both plots are of the same data set, but the horizontal scale is much expanded on the right.

properties of bulk iron, which claims an accuracy of $\sim 0.1\%$. The orbital contributions to this magnetization of about 5% can be evaluated and subtracted using the magneto-mechanical factor, measured by other dedicated experiments [110]. With strong external fields of 3-4 T several additional corrections summing to about 0.5% have to be made. These corrections are temperature dependent. It will be important to carefully evaluate the literature on these measurements and their interpretation to verify that the uncertainty is not larger than a few $10^{-3}$. For example, it is apparent that the anomolous magnetic moment of the electron has not been accounted for in recent publications, amounting to a correction of more than 0.2% to the target electron spin polarization.

Calculations of the longitudinal magnetization of a foil placed pependicularly (or nearly so) to an applied field, are quite difficult. Figure 38, taken from [50, 54], shows the magnetization (relative to its maximum value) of a pure iron foil as a function of applied magnetic field, for different angles between the field and

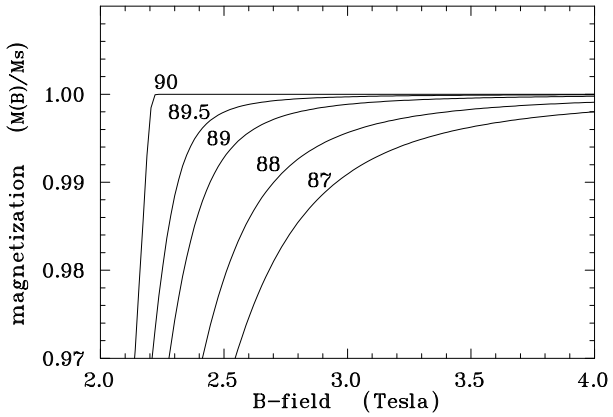


Figure 38: *Simulations of foil magnetization for angles between the foil plane and the B-field direction close to 90 degrees. Errors due to imperfect alignment or a slight warp of the foil could produce such a result. Taken from [50, 54], which uses a calculation [111] of magnetization curves for uniformly magnetized prolate ellipsoidal domans.*

the normal to the foil. To be sure, this calculation is in fact of a model of non-interacting prolate ellipsoidal domains [111], and the extent to which it applies to a pure iron foil is not clear.

### 3.3 Transverse Beam Polarization

If there is any transverse polarization component to the beam on target, the apparent $A_{PV}$ as a function of the azimuthal angle would show a modulation due to the vector analyzing power $A_T$ in Møller scattering, a QED effect involving the interference between the tree-level amplitudes and the two-photon exchange amplitudes. The relevant parameter for $A_T$ is the energy of each electron in COM frame, which is 53 MeV; the electron's boost factor is therefore rather modest. The magnitude of $A_T$ is such that even a few percent transverse polarization can result in an azimuthal modulation of the measured polarization asymmetry that is an order of magnitude larger than $A_{PV}$. While this effect should cancel if one averages data over the full range of the azimuth, imperfect cancellation could lead to a significant systematic error.

Some interesting features of $A_T$ facilitate a strategy that would allow us to keep this potential systematic error under control. If one looks at $A_T$ as a function of the COM scattering angle, or equivalently $y \equiv 1 - E'/E$, one finds that $A_T$ must vanish at $y = 1/2$, which corresponds to 90° scattering in the COM frame, due to CP symmetry. Thus, the maximum $A_T$ is around 15 ppm, and occurs at $|y - 0.5| \approx 0.2$, at the very edges of the momentum acceptance and more importantly, $A_T$ is of opposite sign at these two extremes. This leads to an order of magnitude suppression in the effective $A_T$ averaged over all detectors.

It is possible by passive setup procedures to limit the transverse component of the beam polarization at the target to be less than 1°. One can measure the $\phi$ modulation to very high precision during production data collection within the first few hours, by studying the azimuthal dependence of the raw detector asymmetry, since different azimuthal detectors have very different acceptances as a function of $y$. Thus, it should be possible to devise a "manual" feedback loop that would make small tweaks to the launch angle of the electron beam polarization at the low energy end of the machine based on the measured $A_T$'s. This technique is designed to converge to zero transverse polarization. In practice, the suppression should go like $1/N$, where $N$ is the number of adjustments. In principle, we should gain a factor of about 25 below the setup accuracy of 1° in a week. We will assume this factor for the duration of the entire data collection period for the estimate of the systematic error.

If one now further conservatively assumes only a factor of 10 suppression in the grand average of $A_{PV}$ over the full range of detectors, then the total systematic error from the correction to $A_{PV}$ is less than 0.07 ppb. If this level of suppression is difficult to achieve in practice, some of it can be recovered by a slightly different reweighting of the data from the various different azimuthal detectors with only a small loss in the statistical error in the extracted $A_{PV}$.

### 3.4 Absolute Normalization of the Kinematic Factor

For low energy scattering with a fixed beam energy, $E \ll M_Z$, $A_{PV}$ at tree level is dependent on a single variable, e.g. scattering angle or final energy. For Møller scattering, there is an additional kinematic dependence on both the scattering angle and accepted energy range of scattered electrons in the effective value of the kinematic factor given in Eqn. 1 in Sec. 1.2. The uncertainty in the overall kinematic factor therefore contributes directly to the ultimate uncertainty on $Q_W^e$. Our goal is to determine the overall kinematic factor for our apparatus to a fractional accuracy of 0.5%. We will rely on the extensive experience that was developed to measure $Q^2$ for Qweak. Also, sub-1% accuracy has been achieved in the HAPPEx measurements.

The average kinematic factor can be determined from data using comparisons to a detailed Monte Carlo which includes the full radiative treatment of the Møller process. By taking measurements at fixed angle and energy points and the known radiative $e+e \to e+e$ cross section, the acceptance function can be accurately

reconstructed. In the approximation where radiation in the target is neglected, the kinematic factor can be largely determined from surveyed, precisely-machined collimator apertures and the absolute beam energy calibration tools in the Hall A beam line. Additionally, the use of a moveable sieve is planned, allowing for the reconstruction of fixed angles to be calibrated with a set of carbon target foils (to suppress radiative effects and fix vertex position) at several beam energies, as discussed in Sec. 5.5.8.

With the beam going through a 10.5 gm/cm$^2$ target however, the distribution of trajectories and energies are significantly modified. This requires not only a detailed Monte Carlo simulation but also validation by direct measurement of individual tracks in calibration runs at low current. This is one of the primary motivations for the tracking system presented in Sec. 2.4.4. The large amount of multiple scattering, $dE/dx$ and radiative losses due to the thick target, coupled with the large kinematic acceptance, and the rapid variation of the asymmetry with scattering angle, means that the Monte Carlo simulation of the effective kinematic factor seen by each detector segment needs to be validated carefully.

Additionally, a reweighting of the kinematic factor would be required due to any variation in the analog response of the integrating detectors. The tracking system can evaluate this effect by measuring the variation in response as a function of position in the quartz using single Møller electron tracks at low beam currents. If the integrating quartz detectors cover the full acceptance of the events passing through the collimators, a precise survey of the collimators would in principle provide an accurate measurement of the kinematic factor.

The contributions from positioning uncertainties by the target, collimator, or magnetic field are all negligible compared to the upstream collimator inner radius, which is defined by a machining tolerance. Given a tolerance of $200\ \mu\mathrm{m}$ on machining and an $1\ \mathrm{mm}$ tolerance on uncorrelated positioning between systems, this gives a systematic uncertainty of no more than $0.03$ ppb, or $0.1\%$ in the measured asymmetry. The quantitive analysis of these studies are discussed in Sec. 5.5.7. The acceptance at fixed angles can be determined with a sieve allowing events at fixed angles and normalizing to the relative cross section. Based on acceptance fitting discussed in Sec. 5.5.8, systematic control on the average analyzing power of less than $0.5\%$ can be achieved through several methods such as a simple 6-point spline interpolation.

## 3.5 Backgrounds

This section describes the backgrounds anticipated in the MOLLER experiment, the approach taken in the design of the apparatus to reduce backgrounds and maintain the ability to make small and robust corrections, and our analysis approach to measure the principal components of the irreducible electron background. The MOLLER apparatus is designed to direct the collimated Møller electrons to a region otherwise free of background so that the scattered flux can be integrated to measure the parity-violating asymmetry. As shown in Figure 23, the Møller signal is fashioned into a "peak" in the radial direction by the spectrometer at the detector plane approximately 30 m downstream of the target. The primary Møller detectors must measure the flux that traverses a relatively thin annular ring (width $\sim 5$ cm) of approximately 95 cm radius. A ring of 84 quartz tiles covering this ring form the primary Møller detectors. The Cherenkov light from the quartz is directed radially outwards by air lightguides onto photomultiplier tubes (PMTs) that are enclosed in shielding in an annulus that is approximately 1.5 m in radius. The background at the PMTs can be broken into three broad categories:

1. Irredudicible electrons that originate from beam electrons (and associated bremßtrahlung) scattering off target material other than target electrons: specifically protons and Al nuclei in the target windows
2. Cherenkov light generated by other charged and neutral particles impinging on the detector quartz
3. Light and charged particles generated in the lightguides by electrons and other background radiation.

The dominant background components are from the first category and are discussed in this section. As discussed in Sections 5.4.2 and 5.5.2, pre-R&D and simulations are under way to improve our estimates and systematic errors from the subdominant second and third categories as well.

The MOLLER apparatus is designed to unfold the various background components and facilitate a robust background subtraction. The key design constraint that enables this is instrumenting a sufficiently wide annulus at the detector plane, with significant radial and azimuthal segmentation, to measure variations of fluxes as well as parity-violating asymmetries. In particular, the poorly known and difficult to calculate behaviour of the inelastic electron-proton weak neutral current vector coupling as a function of inelasticity will be directly measured in auxiliary quartz detectors adjacent to the main Møller ring. The parity-violating asymmetries in the scattered electron flux will be monitored in 18 different categories of tiles depending on their relative placement at the detector plane as a function of the radial distance from the beamline, and their azimuthal orientation with respect to the mid-planes of the spectrometer azimuthal sectors. There are large variations in the rates and parity-violating asymmetries in these tiles depending on the relative contributions from Møller, elastic e-p, inelastic e-p and elastic e-Al scattering. This enables our approach, described in detail below in Section 3.5.6, to extract both the signal and background asymmetries. First, we subtract out asymmetry and dilution components which are smaller or comparable to the ultimate statistical error i.e. of the order of 3% or less. These will include all subdominant components (second and third background categories in the PMTs described above). Then we carry out a simultaneous fit of the remaining components using dilutions determined from Monte Carlo simulations and extract independent parity-violating couplings for the chosen $e - X$ scattering processes. This procedure results in acceptably small systematic errors associated with correcting for the irreducible electron background asymmetries.

In the sections below, we provide brief summaries of the principal backgrounds followed by a description of the simultaneous fit procedure and its results. A more complete description of all these topics can be found in the backgrounds report [61] prepared by the collaboration in response to a recommendation from the DOE 2014 Science Review of MOLLER [62].

### 3.5.1 Elastic $ep$ Scattering

The principal irreducible background under the Møller "peak" (see Fig. 23) is radiative elastic electron-proton ($ep$) scattering, which constitutes 8.9% of the signal. The background can be easily modeled and then verified explicitly with auxiliary tracking measurements of the radial profile of the scattered flux. The theoretical prediction for the parity-violating asymmetry is also well known for this process. Recently, the $\gamma - Z$ box radiative correction was calculated at 11 GeV [56]; this significantly impacts the effective value of $Q_W$ but does not add significantly to the projected error in the correction. In addition, the Qweak measurement of the weak charge of the proton $Q_W^p$ can be used to directly cross-check the predicted background asymmetry. After the modeling has been fine-tuned with calibration data, the $Q^2$ distribution of the background under the Møller peak can be estimated from the Monte Carlo simulation. The average $Q^2$ is 0.004 GeV$^2$.

### 3.5.2 Inelastic $ep$ Scattering

A more challenging background correction is due to the smaller dilution from inelastic $ep$ scattering, as well as that same process from the Al target windows. Even though the contribution from the background to the detected rate is expected to be small, $\lesssim 0.5\%$, the asymmetry correction can be significantly larger due to the fact that the estimated coupling to the Z boson is more than an order of magnitude larger than $Q_W^e$. There are only a few data points on the asymmetries for $\Delta$ and resonance region production, and none at higher $W$ ( [63–65]). Cross sections are also less well known than for the elastic processes.

The world data on parity-violating asymmetries in inelastic scattering from the nucleon are summarized

| Experiment | $Q^2$ (GeV$^2$) | $W$ (GeV) | $A/Q^2$ (ppm) |
|---|---|---|---|
| G0 [63] | 0.24 | 1.18 | $-98 \pm 22$ |
| PVDIS [64] | 0.95 | 1.26 | $-72 \pm 10$ |
| " | 0.83 | 1.59 | $-89 \pm 9$ |
| " | 0.76 | 1.86 | $-82 \pm 7$ |
| " | 1.47 | 1.98 | $-81 \pm 12$ |
| " [65] | 1.28 | 2.03 | $-61 \pm 19$ |
| " | 1.08 | 2.07 | $-84 \pm 4$ |
| " | 1.91 | 2.33 | $-84 \pm 4$ |

Table 11: *World data on parity-violating asymmetries in inelastic scattering from the nucleon.*

in Table 11. Note that the data are consistent with a simple scaling: $A_{\rm inel} = -85$ ppm/(GeV)$^2 \times$ Q$^2$ , without radical $W$-dependence. One additional datum is from E158 [3], where they extracted the asymmetry from a combination of proton elastic and inelastic scattering, and obtained a result consistent with the standard model proton weak charge and the above scaling at about 20% accuracy. The $W$-dependence is key for us: the range of accepted $W$s for the experiment spans 1 to 5 GeV, and the inelastic background underneath the Møller signal in the main Møller detector ring represents a different mix of $W$'s than the inelastic events measured in the other detector rings. Therefore, if there is a significant variation of the asymmetry with $W$, then we will need to extract asymmetries for the appropriate regions in $W$ from the simultaneous fit.

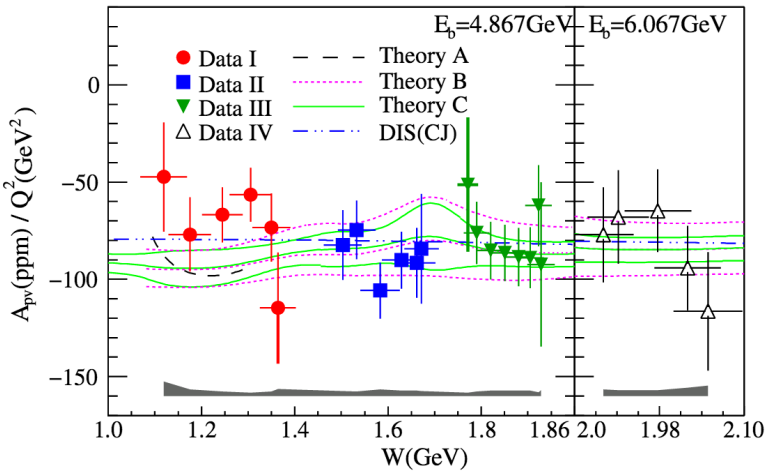


Figure 39: *Inelastic asymmetry from the 6 GeV PVDIS experiment [64] compared to model calculations: Theory A: Matsui* et al. *[66], Theory B: Gorchtein* et al. *[67], Theory C: AJM group [68], as well as a duality-based prediction, DIS(CJ).*

Theory does give us some guidance here. Several groups have provided calculations of the inelastic ep asymmetries. These have been mainly motivated by the desire to benchmark calculations of the $\gamma Z$ box diagram contributions for Qweak [70]. Results from Matsui, Sato and Lee [66], Gorchtein, Horowitz and Ramsey-Musolf [67], and the Adelaide-JLab-Manitoba (AJM) collaboration [68] are compared with the 6 GeV PVDIS data in Fig. 39. All the calculations are in good agreement with the data, and suggest at most

a modest $W$ evolution in the resonance region. Indeed, the models are in good agreement with the simple $A_{\rm inel} = -85\ {\rm ppm}/({\rm GeV})^2 \times {\rm Q}^2$ scaling in this $W$ region, at the 20% level.

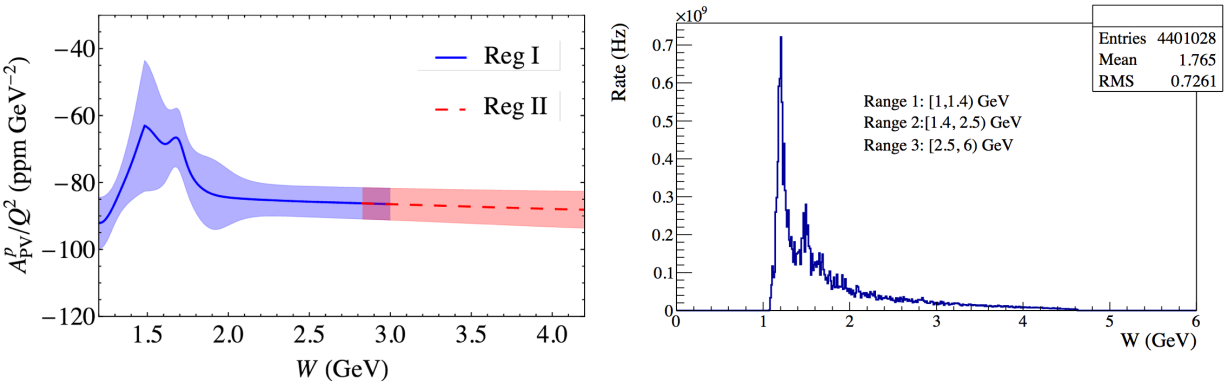


Figure 40: *Left: AJM collaboration [56] calculation of ep inelastic asymmetry for MOLLER kinematics, with theoretical uncertainty band indicated. Right: Simulated rate from ep inelastic scattering vs. $W$. The ranges for the three bins in $W$ for our asymmetry ansatz are indicated.*

The AJM group have extended their calculation to the MOLLER kinematic range [56] ($Q^2 \sim 0.004\,{\rm GeV}^2$). The results are shown in Fig. 40. In a more recent publication [69], they have further explored the dependence of the asymmetry on the scale at which they match the high-$Q^2$ and low-$Q^2$ region. Assuming a very conservative (100%) uncertainty on the key parameter (the continuum $\gamma - \gamma$ to $\gamma - Z$ rotation parameter) for all $Q^2 < 1\ {\rm GeV}^2$, the relative uncertainty in their Region I kinematics increases from $\sim 8.6\%$ (as shown in Fig. 40) to $\sim 12\%$.

The modest $W$-dependence shown motivates our ansatz for treating the inelastic asymmetry: we break the kinematics for inelastics into three bins in $W$: (i) the $\Delta$ region, $1 < W < 1.4$ GeV (ii) the "resonance region", $1.4 < W < 2.5$ GeV, and the "continuum" $2.5 < W < 6$ GeV. We use the Christy-Bosted global fit [71] for the cross sections. Figure 40 shows the simulated rate as a function of $W$ in our acceptance. We then model the inelastic asymmetry in these three bins using $A_{\rm inel} = Kf(W)Q^2$ where $K$ contains electroweak couplings, and $f(W)$ is assumed to be constant in each of the three bins in $W$. We then treat the three $f(W)$ as free parameters to be extracted from our data via the simultaneous fit to the asymmetries in all bins in (radius, $\phi$) described in Section 3.5.6. We thus minimize uncertainty due to theoretical input on the inelastic asymmetries; we rely *on our data* to extract the inelastic contributions.

### 3.5.3 Aluminum Target Windows

The 150 cm long MOLLER hydrogen target will have $\sim 100$ $\mu$m thick entrance and exit windows made of aluminum. The dilution and asymmetry from electron scattering off Al nuclei represents one of the irreducible background corrections. The aluminum end window correction in the Qweak experiment [19] led to a $\sim$28% correction to the parity-violating e-p asymmetry that Qweak measured. The correction for the MOLLER experiment will be much smaller (about 1.5%). Below, we briefly describe the Qweak correction and provide a simplified estimate of why it will be significantly smaller in MOLLER before moving on to the detailed simulations in Section 3.5.6.

For the kinematics of the Qweak experiment (E = 1155 MeV, $\theta_{lab} \sim 7.9°$, $Q^2 = 0.025$ (Gev/$c$)$^2$), the contribution of the aluminum windows to the rate is about $\sim 3.2\%$ (about 76% of which is e-Al elastic nuclear scattering). A detailed calculation of the e-$^{27}$Al parity-violating asymmetry has been performed by

Horowitz [72]. At the average momentum transfer of the Qweak experiment, the asymmetry is $\sim$2200 ppb, significantly larger than the e-p asymmetry of $\sim -240$ ppb. So, despite the relatively small rate contribution of 3.2%, the $2200/240 = 9$ times larger asymmetry leads to a 28% contribution to the measured asymmetry in the Qweak experiment. Qweak ultimately anticipates knowing this correction to better than 10% of itself.

This contribution will be significantly smaller in the MOLLER experiment for two main reasons. The ratio of aluminum to hydrogen is about a factor of four ($35/150$, the ratio of hydrogen target lengths) smaller in the MOLLER experiment. Most importantly, in Qweak the full elastic e-Al peak was detected along with the e-p elastic peak. In contrast, for MOLLER, the e-Al elastic peak is well separated spatially from the main Møller peak (see Fig.41 in Section 3.5.6). It is only its radiative tail (about 12% of the peak rate) that gets detected.

Including some other less significant factors leads to the conclusion that the correction is about 0.5 ppb, which is 1.5% of the anticipated Møller asymmetry of $\sim$34 ppb. The other contributions from scattering on aluminum are smaller. Thus we do an estimate of their asymmetry and a direct subtraction prior to the simultaneous fit described in Section 3.5.6. These processes include quasi-elastic scattering, inelastic excitations of the aluminum nucleus, and scattering off of impurities in the alloy planned for the target windows. More details of how these processes are treated are available in the full backgrounds report [61].

### 3.5.4 Hadrons and Muons

There is the possibility of negatively charged pions, heavier mesons and muons to contribute at a small level to the signal in the Møller detectors. The dilution from such a background is likely to be negligibly small, but the parity-violating asymmetry of this background will depend on the processes that create them. The dominant source is from pions produced by real and virtual photoproduction off protons in the target. We have run Monte Carlo simulations with representations of the MOLLER magnetic fields and collimation using a pion generator based on the Wiser parameterization [57] for direct photoproduction and using the equivalent photon approximation for electroproduction. We find the rate in the Møller ring to be of the order of 0.06%. The parity-violating asymmetry in real photoproduction should be of the order of the hadronic parity-violation parameter $f_\pi$, which is experimentally known to be less than $10^{-7}$.

We estimate that the rate above is 60% of the total pion rate, with the rest coming from electroproduction. We estimate that the average $Q^2$ for the latter process is 0.04 GeV$^2$ and that therefore the parity-violating asymmetry for these pions will be of the order of 4 ppm. Combining all these factors, one can see that the correction in the Møller ring will be of the order of 1 ppb or about 3%. This is the basis for the pion contributions assumed in Table 12 of Section 3.5.6.

For comparison, this background was studied for the E158 configuration and the dilution factor was explicitly measured to be 0.12% in the Møller detector. The parity-violating asymmetry, measured in dedicated pion detectors sensitive to the hadronic leakage behind the Møller detector and shielding, was found to be $\sim 0.5$ ppm.

Decays of hyperons produced in the hydrogen target require special treatment. Estimates show that the acceptance in the Møller ring is a fractional rate below $10^{-9}$. Nevertheless, the analyzing power (polarization transfer from the primary beam electron) could be very significant, and we are in the process of carrying out more careful calculations. More importantly, this is the primary reason why we plan to directly measure the pion asymmetry during physics data collection by monitoring the flux of charged particles downstream of the Møller ring and shielding. We have a preliminary concept to accomplish this with dedicated "pion" detectors described in Sec. 2.4.3. Using realistic assumptions for the efficiency of measuring the parity-violating asymmetry by integrating the detector response over the full duration of data-taking, the projected statistical error is $\sim 105$ ppb. This projects to a systematic error of the order of 0.14 ppb on the correction to the Møller $A_{PV}$ in the thin quartz detectors or about 0.5%. The correction and thus the systematic error will be smaller by a factor of 3 for the "shower-max" quartz/tungsten sandwich detectors. Given the redundancy

and the different weights to the corrections in the two kinds of detectors, we assign a systematic error of 0.3%. Additional Monte Carlo studies of the kinematic acceptances of pions from weak decays are being planned as input to further refine the conceptual design of the "pion" detectors.

### 3.5.5 Photons and Neutrons

In a forward spectrometer of the type being discussed, it is very challenging to suppress neutral background from soft photons and neutrons. We will follow a strategy similar to E158, where neutron background was heavily suppressed by burying the photodetectors in a lead shield and we will follow a similar strategy here. As described in Section 5.4, a collimation system has been designed to achieve a near-perfect "two-bounce" collimation system. There will be at most one or two edges from which photons could reach one of the primary detectors after undergoing only one bounce from the target. The flux at these edges will be rather modest compared to the signal flux.

Further suppression will be achieved for the auxiliary Møller detector made of alternating plates of quartz and tungsten i.e. a "shower max" detector. Based on previous experience and simulation, we anticipate suppressing this background at the level of a fraction of a percent and expect to make the correction with an error less than 0.1%. These backgrounds can be measured with special runs, such as by "blinding" the Cherenkov photodetectors and looking for the residual beam-correlated response, as well as runs with the spectrometer magnets turned off. Such backgrounds are not expected to have any polarization asymmetry.

### 3.5.6 Simultaneous Fit Strategy and Results

Here we describe our strategy for making use of the radial and azimuthal segmentation of the detector to do a simultaneous fit to separate the signal and background components. Electron distributions at the detector plane are shown in Fig. 41 from a full GEANT 4 [78] simulation of interactions in the long liquid hydrogen target with the approriate collimation and 3-D magnetic field map for the two toroid assemblies. Events were generated in the target from Møller scattering from electrons in hydrogen, elastic and inelastic scattering from protons in hydrogen, and elastic, quasielastic, and inelastic scattering from the Al entrance and exit windows of the target, using appropriate cross sections and material thicknesses. The plots show the detected electron rates *vs.* radial location at the z-location of the MOLLER detector, as well as the dilution-weighted asymmetries $f_i A_i$. The dilution for a given process is defined as

$$f_i = \frac{N_i}{\sum_j N_j},$$

where $N_i$ is the rate of detected events from process $i$. The rates and asymmetries shown are summed over the full detected azimuth $\phi$, and correspond to the maximum beam current of 85 $\mu$A and beam polarization of 80%.

These distributions represent what the experiment will see, after we have subtracted out the small backgrounds from particles other than scattered electrons which generate light in the quartz detectors. These small asymmetry and dilution components (the second and third background categories listed in the introduction to this section) are each smaller or comparable to our statistical error *i.e.* of the order of 3% or less, and are not discussed further here.

These plots make our strategy clear for dealing with the remaining irreducible backgrounds (*i.e.* from scattered electrons in the detectors from processes other than the Moller-scattering signal). The division of the detector into six radial rings will allow us to measure the asymmetries in rings where the signal completely dominates, *i.e.* ring 5 (0.92 to 1.1 m), where the signal will be about 85% of the measured asymmetry, but also to measure the asymmetries in rings where the various different backgrounds contribute differing fractions to the asymmetry. A simultaneous fit to all these asymmetries, constrained by the various

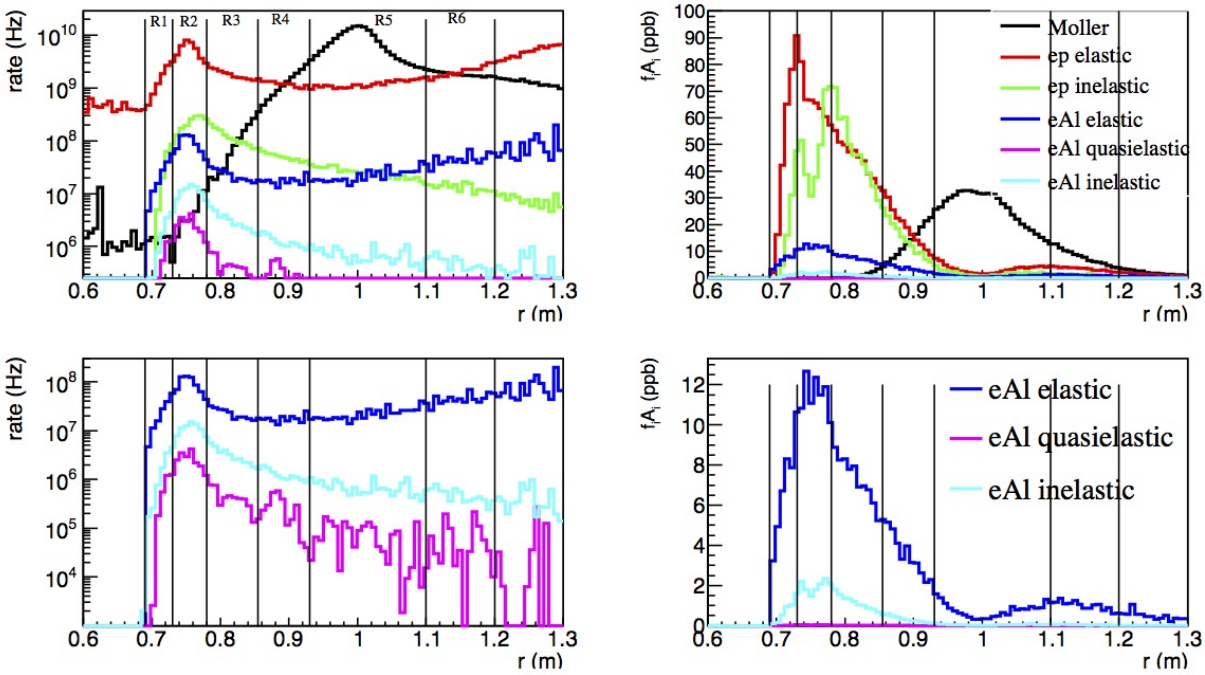


Figure 41: *Simulated signal and background vs. radial location of detected electron at the MOLLER detector ring. In all figures: the Moller electron signal is in black, background from elastic scattering on the proton is red, inelastic scattering from the proton in green, and elastic, quasielastic, and inelastic scattering from the Al target windows in blue, magenta and cyan, respectively. Upper left: rates, in Hz. Lower left: rates for just the Al contributions. Upper right: contribution to the total measured asymmetry, in ppb, for all processes ($f_i A_i$, where $f_i$ is the dilution for the individual process). Lower right: as above, for Al contributions only. Note: the figures on the left have a log scale, while those on the right are linear scale. The boundaries of the 6 detector rings are indicated by vertical black lines.*

dilution factors for each process, will allow us to extract the Møller asymmetry with high precision, and, along the way, determine the asymmetries of the various background processes as by-products.

Note that these figures actually hide an additional degree of freedom that will be very useful in the fitting process: the azimuthal ($\phi$) dependence of the various dilutions and asymmetries. Each detector ring is divided into three $\phi$ sectors (see Fig. 19). Due to the spectrometer optics, the different $\phi$ sectors of a given ring will accept a different kinematic range and so each will see different fractions of the various backgrounds. This gives us additional leverage to extract each asymmetry contribution independently, as discussed below.

For this fitting process we clearly need to know (1) the cross sections and kinematics (and thus the dilution $f_i$) in each detector bin (radius,$\phi$) for each process and (2) a model for how the asymmetry $A_i$ varies with kinematics ($Q^2$ and $W$) over the detector acceptance (radius,$\phi$) bin.

Knowledge of the $f_i$ is not problematic; the relevant form factors and differential cross sections are well-known, so in combination with simulation of the well-determined spectrometer optics we will have the $f_i$ available for each detector element. We can validate these using high-granularity measurements of the total detected electron rates as a function of (radius,$\phi$) using our tracking system, which will also extract the central kinematics of the experiment. We might even envision using the rate distributions from the tracking system as an additional input constraint to the fitting method.

Table 12 shows the total predicted asymmetry in each radial ring, $A_m$, and its statistical precision $\sigma_A/A$ along with the fractional contributions to the measured asymmetries from each relevant process. One can see from this table the strategy of the simultaneous fit. Ring 5 is dominated by the Moller signal. Rings 1 and 2 have very different contributes from ep-elastics and ep-inelastics, allowing these asymmetries to be disentangled. Ring 6 has a large relative contribution from e-Al elastics compared to other rings, *etc.*. Note also that the background fraction from Al elastic scattering in ring 5 is 1.47%, in agreement with the 1.5% scaling estimate from Qweak given above in Section 3.5.3. The azimuthal $\phi$ degree of freedom also has some striking differences in the variation of the processes which are useful; more details can be found in the full backgrounds report [61].

| ring # | $\frac{\sigma_A}{A}$ (%) | $A_m$ (ppb) | Møller | e-p elastic | e-p inelastic | e-Al elastic | e-Al quasielastic | e-Al inelastic | pions |
|---|---|---|---|---|---|---|---|---|---|
| | | | $f_iA_i(\%)$ | $f_iA_i(\%)$ | $f_iA_i(\%)$ | $f_iA_i(\%)$ | $f_iA_i(\%)$ | $f_iA_i(\%)$ | $f_iA_i(\%)$ |
| 1 | 3.05 | -78.69 | 0 | 79.9 | 28.6 | -9.66 | 0 | 1.12 | 0 |
| 2 | 1.09 | -103.1 | 0 | 65.3 | 44.1 | -11.3 | 0 | 1.83 | 0.05 |
| 3 | 1.68 | -91.15 | 1.12 | 50.3 | 54.3 | -8.25 | 0 | 1.34 | 1.13 |
| 4 | 3.06 | -44.73 | 33.5 | 37.8 | 28.3 | -7.33 | 0 | 0.63 | 7.04 |
| 5 | 1.61 | -34.26 | 88.2 | 6.61 | 3.56 | -1.47 | 0 | 0.09 | 2.98 |
| 6 | 7.24 | -13.28 | 57.5 | 25.3 | 8.40 | -7.47 | 0 | 0.30 | 15.9 |

Table 12: *Asymmetries from various contributions for the 6 rings. A contribution of less than* $0.05\%$ *is listed as* $0$*.*

**Simultaneous Fit Results:** The 18 asymmetries (6 radial rings, each with 3 $\phi$ sectors) produced in the full simulation, with statistics corresponding to the full beam time request of 344 days, were simultaneously fitted. The fit had 6 free parameters: the asymmetries for Møller, ep-elastic, e-Al elastic and e-p inelastic (3 $W$ bins) scattering with appropriate $Q^2$ evolution for each. The $f_i$ dilutions were taken from the simulation. The small contributions from quasielastic scattering and inelastic scattering from the Al windows were subtracted before the simultaneous fit.

| Processes | Expected A (ppb) | $\sigma_A$ (ppb) | $\frac{\sigma_A}{\lvert A\rvert}$ (%) |
|---|---|---|---|
| Moller | -35.20 | 0.64 | 1.8 |
| ep-elastic | -19.67 | 1.82 | 9.2 |
| ep-inelastic (1) | -439.94 | 80.6 | 18.3 |
| ep-inelastic (2) | -433.96 | 38.3 | 8.8 |
| ep-inelastic (3) | -384.59 | 91.5 | 23.8 |
| eAl-elastic | 297.27 | 83.01 | 27.9 |

Table 13: *Results of the simultaneous fit to the 18 quartz tile asymmetries. The asymmetries ($A_i$) in ring 5 and their fitting errors in ppb and in % are shown.*

The results of the fit are shown in Table 13. We see that the desired precision (1.8%) in the Moller asymmetry is achieved. Very similar results are found with a 4-parameter fit (where the ep-inelastics were assumed to have single asymmetry that scales as $Q^2$, independent of $W$), with again a 1.8% precision on the Møller asymmetry. The extracted uncertainties are degraded in all the background couplings in the 6-parameter fit due to correlations. We choose this fit as our final result as a very conservative estimate of the systematic errors due to Al and inelastic backgrounds. Table 14 shows the size of each correction as well

as systematic error (due to the statistical uncertainties including correlations in the extracted couplings from the fit in Table 13).

| Process | Correction (%) | Systematic Error (%) |
|---|---|---|
| e-p elastic | -6.61 | 0.38* |
| e-p inelastic ($W < 1.4$ GeV) | -1.03 | 0.22 |
| e-p inelastic ($1.4 < W < 2.5$ GeV) | -1.22 | 0.13 |
| e-p inelastic ($W > 2.5$ GeV) | -1.31 | 0.36 |
| e-Al elastic | +1.47 | 0.15* |
| e-Al other | $< 0.10$ | $< 0.10$ |

Table 14: *The fractional correction to the Møller asymmetry in Ring 5 and the associated systematic errors due to the extracted fit uncertainties shown in Table 13 are listed. The statistical error in the Møller asymmetry is 1.88%. The rows marked with a * are assumed to have additional external input. The systematic error on the e-p elastic contribution is assigned a fractional error of 5%. The systematic error on the e-Al elastic contribution is assigned as a fractional error of* $10\%$ *as discussed in the full backgrounds report [61]. The "e-Al other" contributions include quasi-elastic scattering and inelastic scattering from discrete nuclear excited states and the giant dipole resonance.*

The important takeaway message is this: **the radial and azimuthal segmentation of the detector, combined with the toroidal spectrometer optics and the kinematics of the various background processes, will allow us to untangle the Moller asymmetry from those of the dominant background processes, without recourse to other data or theoretical predictions for those background asymmetries**. All that we require are the cross sections and simple expectations on the leading $Q^2$ (and, for inelastics, $W$) dependence of the asymmetries.

Given the individual systematic errors in each correction in Table 14, we have done a preliminary exploration of the correlations between the corrections. We find that the systematic error on the sum of the corrections from the error matrix is of the order of 0.3%, significantly smaller than several of the individual systematic errors. This essentially indicates that the linear combinations of the various components in the corrections in Ring 5 (the main Møller signal) are well constrained in other tiles. Since this requires further study, we just state here that the total systematic error from the corrections due to inelastic scattering are bounded at 0.7% (linear sum of the three components), but that they are likely to be reduced by about a factor of two after further study.

In summary, a simultaneous fit of measured asymmetries making use of the radial and azimuthal segmentation of the detector determines the background asymmetry contributions to the needed precision. It also provides asymmetry measurements for these additional processes.

# 4 Beam Time Request and Run Goals

While the MOLLER apparatus is being designed for a beam current of 85 $\mu$A at 11 GeV, we have assumed a beam current of 75 $\mu$A and a beam polarization of 80% to formulate the beam time request. If higher beam current and/or higher beam polarization are considered routine, the request can correspondingly be reduced using the appropriate $P^2I$ factor. In order to ensure the technical success of this challenging measurement, we are proposing to take data in three separate run periods. These run periods have been optimized so that not only important technical milestones are met, but also that each run will provide publishable results and will significantly add to our knowledge of electroweak physics to date.

| Run Period | 1kHz Width (ppm) | % Stat. Error | Stat. Error (ppb) | PAC Days (Prod.) | Eff. % | Calendar Weeks (Prod.) | Comm. Weeks | Total Weeks |
|---|---|---|---|---|---|---|---|---|
| I | 100 | 11.4 | 2.93 | 14 | 40 | 5 | 6 | 11 |
| II | 94 | 4.1 | 1.06 | 95 | 50 | 27 | 3 | 30 |
| III | 89 | 2.5 | 0.64 | 235 | 60 | 56 | 4 | 60 |
| | | 2.1 | 0.54 | **344** | | | **13** | 101 |

Table 15: *Summary of the Estimated Beam Time (75 $\mu$A, $P_e = 80\%$ ).*

One important criterion for gauging the amount of running time required is to estimate how close one can approach counting statistics in the instantaneous raw asymmetry measurement (see the discussion in Sec. 2.1.3). From our Monte Carlo simulation, we estimate that the counting-statistics-limited $\sigma(A_i)$ for a 0.96 kHz pulse-pair is 81 ppm. Considering the various sources of additional fluctuations such as target density and electronics noise, an aggressive but realistic goal for final production running is $\sigma(A_i) = 89$ ppm. However, it will be challenging to achieve the final goal for $\sigma(A_i)$ in early running, so we will assume 100, 94 and 89 ppm respectively for the three running periods.

Another important criterion is overall efficiency. Generally, once parity experiments have been properly commissioned, the up-time should be 90% for the experimental apparatus, since stable run conditions are required over extended periods of time. Coupled with an accelerator efficiency of 70%, the final running should yield an effective efficiency greater than 60%. Again however, we are unlikely to achieve this in early on. So, we have assumed total efficiencies of 40, 50 and 60% respectively for the three running periods.

We summarize our estimated beam time in Table 15. The total request is for 344 PAC days for production running and 13 commissioning weeks over the three running periods. In the following, we summarize the goals of each run and then discuss special considerations that must be part of the discussion with both the scheduling committee and accelerator operations before final beam time allocation.

## 4.1 The Three Runs

### 4.1.1 Run I

The primary goal of the first run will be to commission the principal subsystems of the apparatus. The focus will be on validating the target design, the spectrometer optics, rejection of background and the demonstration that detector fluctuations are dominated by statistics. Once this is established, a reasonable goal would be to achieve a statistical error better than or equal to the E158 result, which we conservatively estimate can be done in 5 calendar weeks. The duration of production running also allows enough sensitivity to demonstrate that there are no anomalously large background asymmetries from charged current processes.

### 4.1.2 Run II

The primary goal of the second run is to get more than 25% of the proposed statistics so that one is able to achieve $\delta(\sin^2\theta_W) \sim 0.0005$. This would be the single-best such measurement at $Q^2 \ll M_Z^2$, which could already potentially have a major impact on TeV-scale physics depending on the status of LHC data anomalies. The control of beam helicity correlations must be fully commissioned to achieve $\delta(A_{raw}) \sim 1$ ppb. The fractional statistical error of 4% will require modest but not the ultimate systematic control of absolute normalization errors such as the beam polarization. We have assigned 3 weeks for recommissioning of the apparatus. We will also strive to achieve better than 50% overall efficiency for data collection.

### 4.1.3 Run III

This run must have all aspects of the apparatus to be working to their full scope. We must also have enough diagnostics in place and sufficient trained personnel within the collaboration so that high quality data can be collected with the best possible efficiency. We are targeting 60% total efficiency. The full control of normalization errors such as the absolute value of $Q^2$ and the beam polarization at the level of 0.4-0.5% must be achievable. The long duration of this run likely means that it must be split between two fiscal running cycles, and we have assigned 2 weeks of commissioning for each period.

## 4.2 Special Beam Considerations

Systematic control is one of the most important considerations that must govern various decisions on the design as well as running conditions for the experiment. Two important aspects of this are the methods of "slow helicity reversals" (passive sign flips of the raw asymmetry), and controlled changes to the degree of transverse beam polarization.

### 4.2.1 Transverse Polarization Running

The large vector analyzing power $A_T$ for Møller scattering (ranging from 5 to 15 ppm at our kinematics) presents a unique opportunity to test the complete apparatus and its capability for absolute normalization at the fraction of a percent level, including detector acceptance, background corrections, azimuthal imperfections, radiative corrections, absolute value of $Q^2$ and the longitudinal beam polarization. This is because $A_T$ is known theoretically at the 0.1% level. The MOLLER apparatus is capable of measuring $A_T$ with a fractional statistical error of $\sim 0.2\%$ in a matter of 8 hours at full luminosity. We are therefore planning to request several periods, each lasting 2 to 3 shifts, of 100% transverse polarization in Hall A for a sensitive test of systematics. The periods can likely be synchronized with a change of beam energy that we also plan to request (see Sec. 4.2.4 below).

### 4.2.2 Wien Angle "Tweaks"

The large $A_T$ value also represents a challenge in terms of systematic control. As discussed in Sec 3.3, in order to ensure a negligible systematic error at the fraction of a ppb level due to a coupling between residual transverse components of the electron beam polarization with azimuthal imperfections in the apparatus, it will be required to make periodic corrections to the polarization launch angle at the polarized source. We estimate that changes at the level of $1^\circ$ to the launch angle might be requested once a day during production running. Assuming the launch angle was set correctly given the sensitivity of the available diagnostics, over many days the total change to the launch angle should average out to zero to high precision. We expect that these changes will be small enough to have no impact on the average longitudinal polarization that will be seen in any of the Halls that happen to be running at the same time.

### 4.2.3 The Double-Wien

The "Double-Wien" filter at the front end of CEBAF was commissioned during the PREX run. The system accomplishes a full flip of the beam polarization direction with a aid of two Wien filters and a solenoid lens. The method is very effective because the flip is achieved with a relatively minor change to the beam optics at the front end of the machine. This is a very powerful and crucial way to cancel subtle systematic errors. It would be good to get 50 to 100 flips by this method over the duration of the full set of runs. This might require a configuration change once every 5 to 7 days during production running.

#### 4.2.4 Beam Energy

Over the next two years, as the detailed design of the MOLLER apparatus evolves and depending on discussions with the Accelerator Division, the exact beam energy for MOLLER (somewhere in the range of 10.5 to 11 GeV) will be chosen and used to fix the geometry of the spectrometer and the associate collimation. Once this energy is chosen, we will immediately investigate what minimum configuration change would accomplish a beam polarization sign flip either by slightly reducing the total energy of the machine or moving from symmetric to slightly asymmetric energies in each of the two linacs.

For a symmetric linac configuration change, the beam energy change needed is $\sim$ 93 MeV. This is a small enough fractional change in the total beam energy that the MOLLER apparatus can be designed to accommodate both energies for production running with no other changes. Of course, if an asymmetric linac configuration can be found that will maintain the total energy to be the same while accomplishing a polarization sign flip, that would be desirable. However, we do not believe this is a necessary constraint, especially if it complicates other aspects of beam quality.

Over the duration of all the production running, a total of 10 energy flips would be desirable, with at least one such flip during run I, 3 to 4 flips in run II and 6 to 8 flips in run III, or effectively a configuration change every 6 to 10 weeks during production running. The exact frequency and the nature of the configuration change would be chosen after detailed consultation with the Accelerator and Physics Divisions. Since the requested frequency for the configuration change is similar to that required for transverse running, it might well be optimal to schedule the required 100% transverse running in the period in which an energy configuration change is being made.

# 5 Pre-R&D and Evolutionary Design Topics

It is hoped that the MOLLER project can obtain funding approval in the near future and that proper planning would ensure construction can be completed and assembly of the apparatus in the Hall to commence by the end of 2020. In anticipation of this schedule, the collaboration has been executing a pre-R&D plan over the past few years. We discuss these activities in this section. While some of the topics are being carried out in collaborating institutions with partial graduate student and postdoc efforts from ongoing user grant funds, a significant portion of further activities will require technical manpower from national laboratories. There has been a small amount of seed funding provided for these activities by the JLab Physics Division. Based on further discussions within the collaboration and with JLab management, the prioritization of the various activities will be continuously updated given the amount of available funding.

## 5.1 Polarized Beam

### 5.1.1 Polarized Laser Light

In collaboration with the Polarized Electron Gun Group at JLab, research has started on methods for achieving the fast helicity flip goal of stable polarization in $10\mu$s. The ringing of the Pockels cell is thought to be related to piezoelectric shock on the voltage transition, and the resistance to completing the transition quickly may be related to other mechanical relaxation effects. A liquid-filled Kerr cell would presumably not suffer from either effect, and is expected to be capable of very fast transitions. Kerr cells are inconvenient compared to Pockels cells, but are none-the-less a very promising route to meeting the needs for MOLLER.

As a more convenient alternative, current efforts are focussed on RTP (Rubidium Titanyl Phosphate) Pockels cells made of two RTP crystals operating with a transverse electric field (in contrast to the longitudinal field used in KD*P cells). This material is promising due to its apparent lack of piezoelectric

resonances to very high frequencies. In initial work with commercially available RTP cells a $\sim$ 12 $\mu$sec settling time was observed with virtually none of the ringing that is observed with KD*P.

However, these cells performed worse in terms of the helicity-correlated intensity gradients across the face of the crystal; this is a critical parameter because it can lead to large helicity-correlated position differences after interaction of the laser light with the photocathode. Recent work with a custom designed RTP cell that provides independent positioning control of the two crystals has led to asymmetry gradients that are comparable to KD*P, while preserving the short settling time. Work continues, but this technology shows great promise for satisfying the needs of MOLLER with a technology that is as convenient to use as the existing KD*P cells.

### 5.1.2 Beamline Instrumentation and Beam Properties

Section 3.1.6 compares the MOLLER specifications for beam jitter and monitor resolution to the existing performance. The latter numbers primarily come from experience during the Qweak experiment in 2010-2012 and some follow-up studies. In this section, we describe the Qweak measurements in more detail and discuss ongoing and upcoming pre-R&D work in this area.

**Beam position monitor (BPM) resolution:** The MOLLER specification for beam position monitor resolution is $< 3$ $\mu$m for 1 kHz window-pairs. Qweak has measured the beam position monitor resolution for 960 Hz quartets for the Jefferson Lab standard "stripline" beam position monitors (BPM). The study was done by using two beam position monitors in a drift region of the Hall C beamline to project to a third. The RMS of the difference in helicity-correlated differences between the measured and projected beam position at the third BPM gives its resolution. The study [59] was done versus beam current and the results are shown in Figure 42. For MOLLER beam currents, typical resolutions of $\sim$ 1.2 $\mu$m are found. Taking the conservative assumption that the monitor noise is dominated by white noise, the scaling from quartets to pairs and the scaling from 480 Hz pairs to 1 kHz pairs can be estimated as two factors of $\sqrt{2}$. **This results in an estimated 2.4 $\mu$m resolution for 1 kHz pairs for MOLLER, which achieves the MOLLER goal of 3 $\mu$m**. It is also planned that redundant beam position measurements with a similar resolution will be performed with radio frequency microwave cavity monitors that are installed in the Hall A beamline. These have not been used extensively except during parity experiments running in Hall A where performance comparable to stripline monitors has been demonstrated. Recently, a third microwave cavity monitor assembly has been installed on the Hall A beam instrumentation girder, so definitive resolution measurements using the three BPM technique can be carried out in the near future.

**Beam position jitter:** As discussed in Section 3.1.6, the MOLLER specifications for beam parameter "jitter" (random noise) are these values for the maximum allowed jitter (see Table 6): $< 47$ $\mu$m (position), $< 4.7$ $\mu$rad (angle), and $< 108$ ppm (energy) for 1 kHz window pairs. Typical numbers for the jitter for 480 Hz window pairs from the Qweak experiment are shown in Figs. 43 and 44. To project to what to expect for 1 kHz pairs, we assume a white noise assumption and multiply by $\sqrt{2}$ to obtain projected jitter values of: $\sim$ 48 $\mu$m (position), $\sim$ 1.4 $\mu$rad (angle), and $\sim$ 6.5 ppm (energy). Thus, all of the jitter requirements appear achievable, assuming the jitter behavior is similar after the 12 GeV accelerator upgrade. A summary comparison is shown in Table 8. Some recent initial experience with 11 GeV beam in Hall A suggests that the beam jitter properties for 15 Hz window pairs are similar to the 6 GeV machine. Studies of this type at higher window pair rates will be carried out in the near future in Hall A when 11 GeV beam is in use.

**Beam intensity jitter:** The MOLLER specification for beam intensity jitter for 1 kHz window pairs is $< 1000$ ppm. Qweak data on intensity jitter at 480 Hz is shown in Figure 44. Applying the standard $\sqrt{2}$ "white-noise" scaling factor predicts $\sim$ 500 ppm for 1 kHz pairs, so the goal of 1000 ppm seems easily achievable.

**Beam charge monitor resolution:** The MOLLER specification is 10 ppm resolution for relative beam intensity measurement for 1 kHz window pairs. Here, we report on the best values achieved to date and the

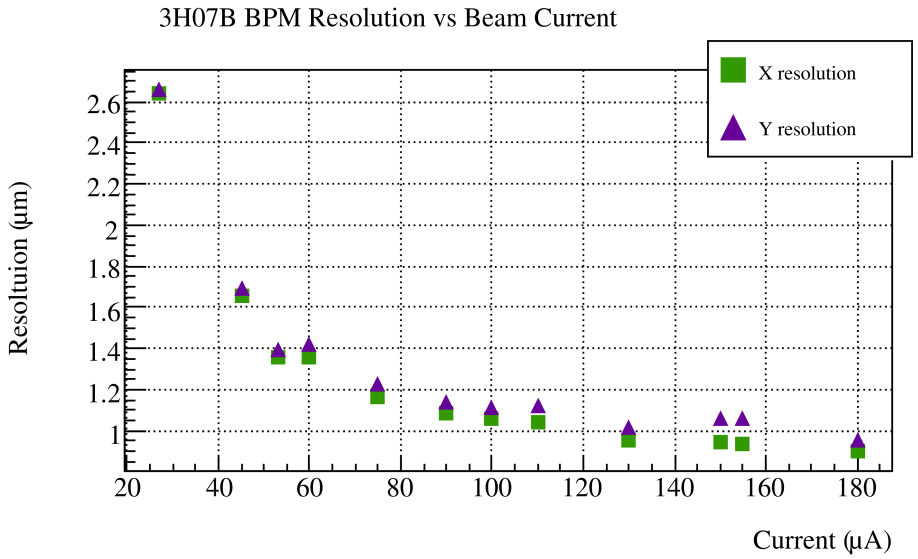


Figure 42: *Measurements of beam position monitor resolution as a function of beam current during the Qweak experiment. See text for further details.*

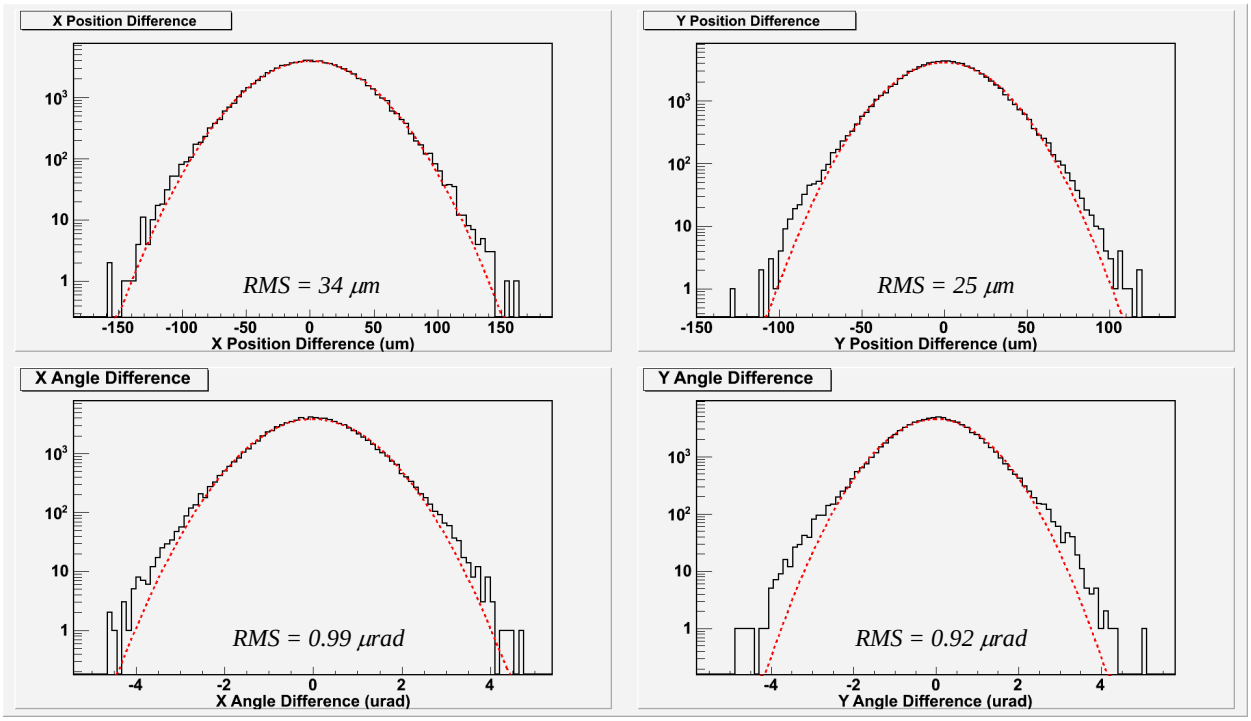


Figure 43: *Typical X and Y position and angle difference distributions for 480 Hz window pairs from the Qweak experiment at 160 μA beam current. The RMS values from the Gaussian fits are the random beam noise ("jitter") in these parameters.*

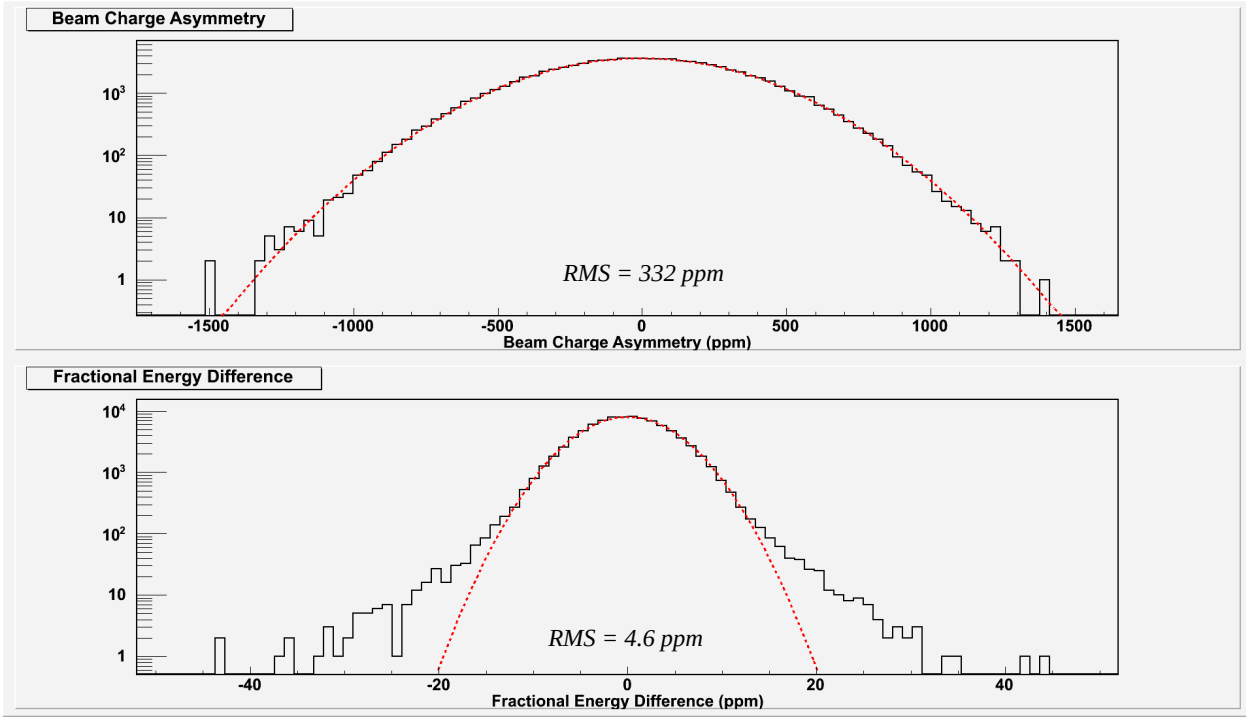


Figure 44: *Typical intensity asymmetry and energy difference distributions for 480 Hz window pairs from the Qweak experiment at 160 $\mu$A beam current. The RMS values from the Gaussian fits are the random beam noise ("jitter") in these parameters.*

work in progress by the collaboration and lab to achieve this goal. In particular, we report on the results from the recently completed Qweak experiment. Qweak measured beam intensity with beam charge monitors (BCM) consisting of the standard JLab hardware of resonant microwave cavities operating in the $TM_{010}$ mode. The best results we obtained with an all-digital receiver electronics designed by Jefferson Lab staff member John Musson [60]. The random noise in the beam charge measurement was determined by forming the double-difference, which is the difference between the helicity-correlated charge asymmetry for two BCMs. The RMS of this distribution determines the uncorrelated random noise of the charge measurement, referred to as the resolution. A typical measurement at the nominal Qweak beam current of 180 $\mu$A is shown in Figure 45. The resulting resolution for a single monitor is $\sim 62/\sqrt{2} = 44$ ppm for effective 480 kHz pairs. From the behavior versus beam current, this appears to be a noise floor, so it is also the appropriate value for the MOLLER current of 80 $\mu$A. Using the white noise scaling argument from above, the scaled Qweak value for 1 kHz pulse-pairs is 62 ppm. **Thus, the Qweak scaled value of 62 ppm for BCM resolution is above the MOLLER goal of 10 ppm; the collaboration and lab have efforts underway to improve this.**

To facilitate improvements, dedicated bench tests have been set up using a Qweak data acquisition test stand. The first goal was to show that the behavior of the Qweak digital test receivers with beam could be reproduced with the beam signal coming from the microwave cavity monitor replaced with a radio-frequency source signal. As Figure 45 shows, the results with beam and rf source are very similar, with a similar noise floor in each case. Since there is a noise floor that is independent of beam current, one hypothesis is that the noise floor in the charge measurement is limited by phase and amplitude noise in the 1.5 GHz local oscillator that is mixed with the incoming signal in the receiver electronics. To test that hypothesis, the bench study shown in Figure 46 was done. Here, a single receiver with the signal going into the two available inputs was used. Each signals electronics path is independent with the exception of the local oscillator that is shared

between the two. In this case the noise floor is reduced to $\sim$ 18 ppm. This is consistent with the local oscillator being responsible for the 62 ppm noise floor. Further studies are in progress to confirm this and improve the situation if it is confirmed to be the cause.

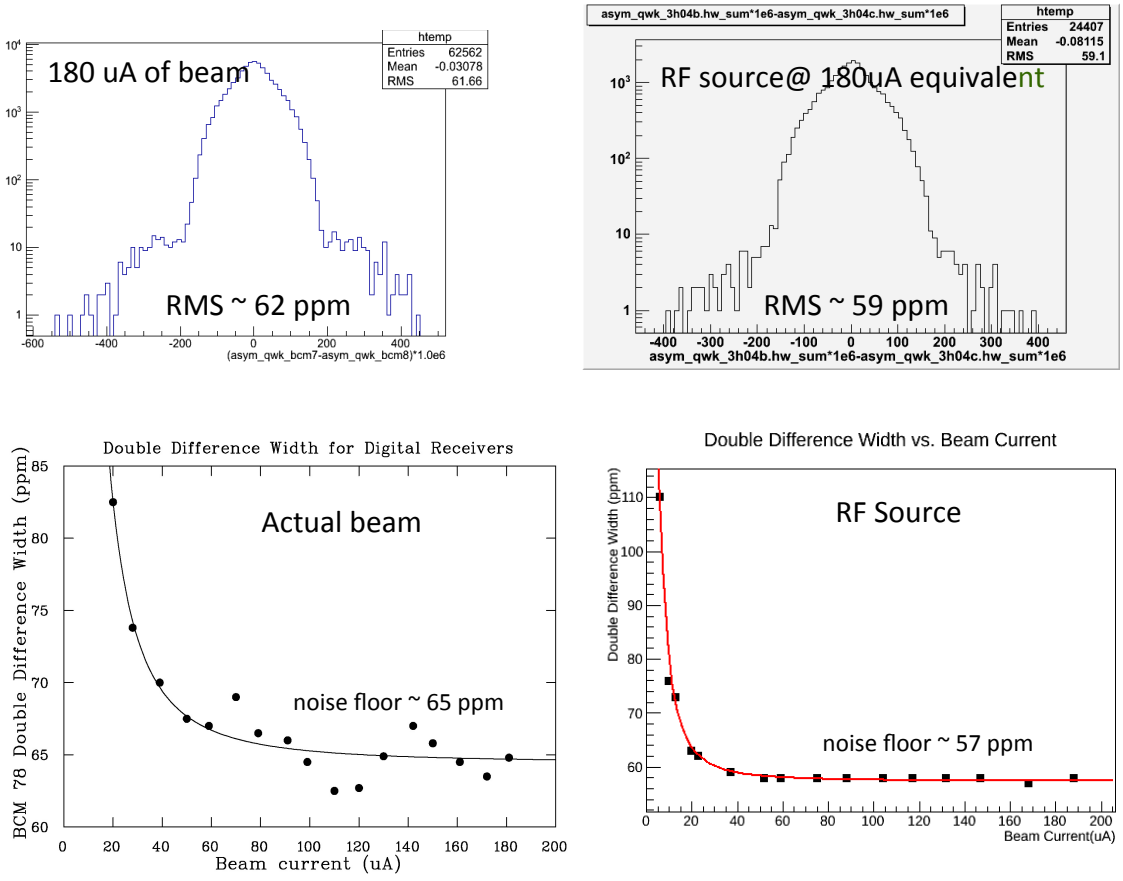


Figure 45: *Qweak measurements of beam charge monitor (BCM) resolution. The left panels show the distribution of the double-difference between the helicity-correlated charge asymmetry of two BCMs at 180 $\mu$A and versus beam current, respectively. The right two panels show the results of bench studies with the same digital receiver electronics used during Qweak, but the input signal is replaced with a radio-frequency source of the appropriate amplitude for that beam current.*

### 5.1.3 Beam Transport

Compared to 6 GeV, at 11 GeV the CEBAF beam will have a much larger emittance due to synchrotron radiation in the recirculation arcs. The effect of this emittance growth will be complicated by skew focusing fields in the RF accelerating cavities and in other optical elements. Accelerator Division has initiated simulation studies of beam properties to predict the increase in beam halo associated with this effect and known non-linearities in machine optics. These studies will also be used to refine procedures for maximizing the benefits of adiabatic damping of helicity-correlated beam asymmetries. The collaboration will encourage

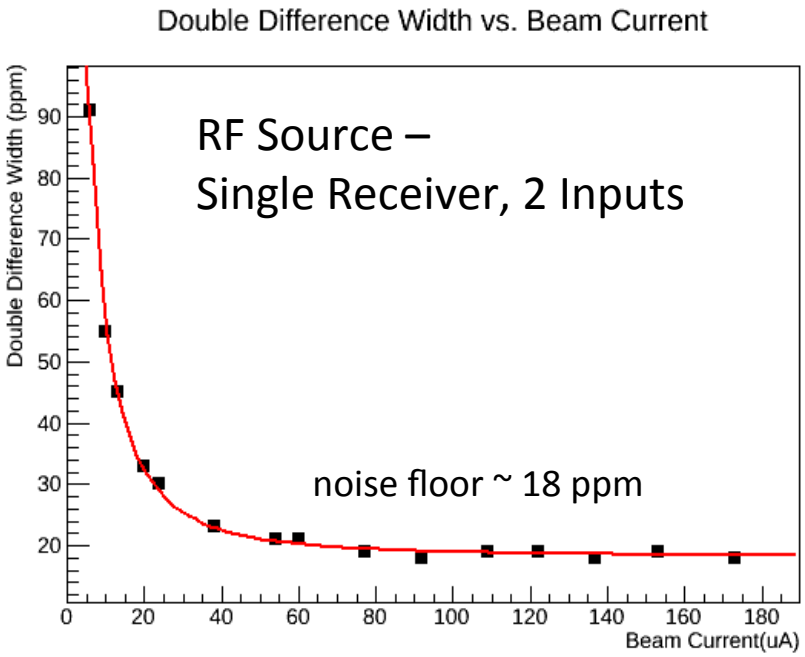


Figure 46: *BCM resolution results from a bench study with a rf source and with a single receiver with two inputs and shared local oscillator.*

and assist this program of studies, including supplementing these studies with beam-based measurements after the energy upgrade.

## 5.2 Target Design

Prototyping the MOLLER target is part of the scope of a DOE Early Career grant awarded in 2012 to Silviu Covrig Dusa. Silviu has set up a CFD Facility (CFDFAC) at Jefferson Lab. CFDFAC uses ANSYS-CFD on high power computing (HPC). CFDFAC develops new technologies to design low noise targets for scattering experiments. CFDFAC has made low noise, high performance designs for the stardard $LH_2$ targets in Halls A and C up to 30 cm in length. One such target design has been used by the DVCS/Gmp experiments that ran in Hall A after the 12 GeV upgrade of the CEBAF machine. The DVCS/Gmp target density reduction was almost an order of magnitude better than similar targets that ran during the 6 GeV era at Jefferson Lab.

### 5.2.1 Qweak Target Experience and Expected MOLLER Performance

The design of the MOLLER target, as described in the proposal, is predicated on several novel ideas which were to be tested for the first time with the Qweak target. The Qweak target, we argued in the proposal, is really the prototype for the MOLLER target. This section reviews what has been learned from the Qweak experience in order to see whether those Qweak ideas and design aspects crucial to the Moller LH2 target hold any water.

The most crucial aspect of the MOLLER target design which needs to be validated is the novel use of CFD as a design tool. CFD was used in almost all aspects of the design of the Qweak target. It was used

to tailor the cell design in order to optimize the flow, temperature and density profiles across the beam axis in the hydrogen volume as well as at the cell windows. These simulations were used to fix the mass flow required of the target, one of the most crucial design parameters. The pressure head represented by the complicated cell shape was derived by CFD. Analytic calculations for the Qweak target's heater and some aspects of the heat exchanger were checked with CFD simulations. CFD simulations fixed the raster size required for the target and helped us design strategies for various off-normal events. In many respects the novel design which emerged was considered a bit of a gamble, given that CFD was not a proven tool for target design.

The 35 cm long, high power Qweak target has met its ambitious design goals. The target has been successfully operated with 3 kW of cooling power, significantly greater than any target previously built. It has been run up to 180 $\mu$A of 1.165 GeV electrons. The target boiling contribution to the asymmetry widths in the experiment has been measured at a raster size of 3.5x3.5 mm$^2$ in the beam current range from 50 to 170 $\mu$A (Figure 47). The measured performance is in excellent agreement with the expectation estimated from scaling the performance of the G0 target with the CFD model. The bulk density changes have also been bounded to less than 0.8% at 180 $\mu$A. This should be compared to the performance of the standard pivot 15 cm machined cells, for which the density variation at 100 $\mu$A has been measured to be at the level of 20%. Although the design raster size for the Qweak target was 4x4 mm$^2$, the target's performance is so good that it was operated routinely at 150 $\mu$A with a raster size of only 3.0x3.0 mm$^2$.

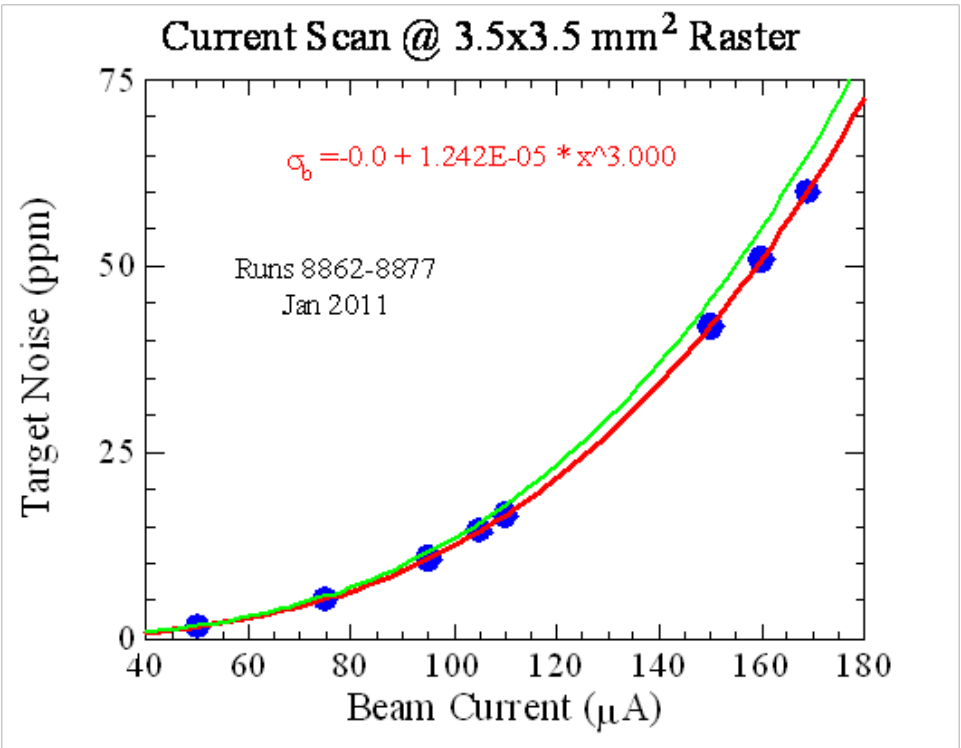


Figure 47: *Qweak target performance: density fluctuation widths versus beam current from Qweak measurements. The blue points are measured data, the red curve is a fit to the data, the green curve is another fit, providing a measure of the uncertainties.*

The fact that the Qweak target has achieved all of its design goals validates the use of CFD as a design tool. Predicting the MOLLER target density fluctuations with eq. 4 from the Qweak target data yields a

density fluctuation noise for the MOLLER target of about 30 ppm on the same level (21 ppm) extrapolated from the G0 target data.

Since the density fluctuation caused by boiling at the aluminum windows is often the dominating factor, a study was carried out with the CFD calculations for the MOLLER target in comparison with the two Hall C parity experiments (G0 and Qweak). Figure 48 shows the heat flux for the three experiments, both the convective part, which is responsible for film boiling at the windows, and the total. Also shown is the threshold for film boiling. It is interesting to notice that the MOLLER situation is just below the threshold. A careful design of the target cell may actually eliminate the film boiling.

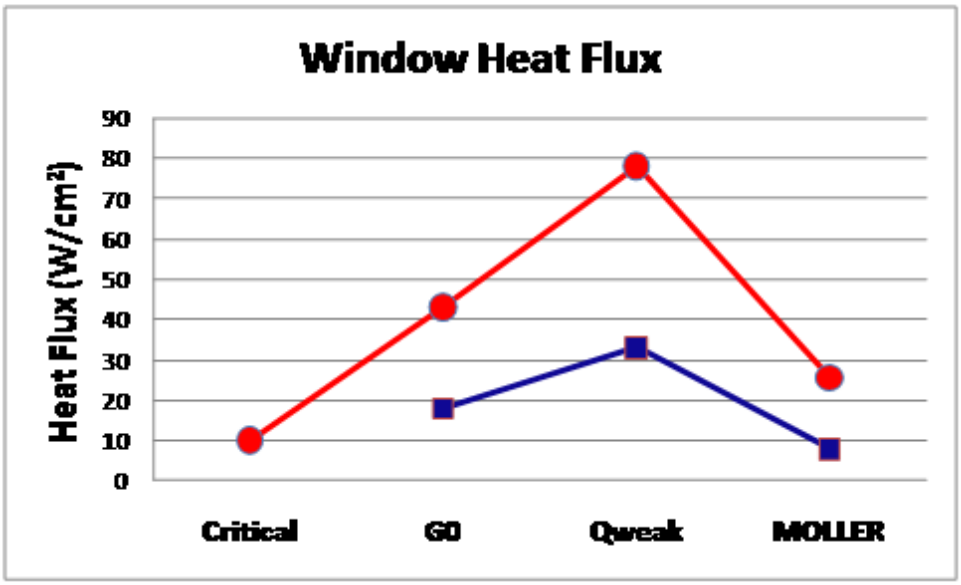


Figure 48: *CFD study of boiling at the aluminum windows: window heat flux for three experiments (G0, Qweak and MOLLER). The blue points are the convective part of the heat flux, which is mainly responsible for boiling at the windows. The red points are the total heat flux. The first (red) data point shows the threshold for film boiling.*

We note that the matrix of 24 solid targets that were part of the Qweak experiment were also designed with CFD. The relationship between temperatures at the center of each target to thermometry scattered around the solid targets frame was assessed with CFD. Knowing how high these thermometers can safely go, by virtue of the CFD calculations, has made it possible to put more beam current on our solid targets than has ever been done before at JLab.

It also shows that the heat exchanger design process used for the Qweak target was correct. Note that the Qweak heat exchanger is a completely novel design which combines a 4 K and a 15 K heat exchangers using overlapping heat exchanger coils in the same shell. The heat exchanger geometry has been assessed with CFD to insure that $LH_2$, which freezes at 13.8 K, does not freeze in its coils at the nominal flow rate.

It also shows that the high power heater design and fabrication process was correct. The 3 kW heater performance is unmatched. When beam trips occur, or beam is restored to full current, the typical temperature excursions in the target loop thermometers are less than 0.1 K. The high power heater was designed with CFD to insure that $LH_2$ does not boil at the surface of its wires.

The pressure head predicted for the Qweak target at the design mass flow of 1.1 kg/s was 1.2 psi. The head measured with the Qweak target at this massflow is 1.1 psi, in amazingly good agreement with the

prediction considering how very difficult it is to calculate this ahead of time. Note that head and massflow are the two most crucial design parameters for most of the target's components.

The fact that the required massflow and pressure head were achieved for the Qweak target also validates the pump design. Problems have been encountered with the Qweak pump bearings, which have led to some down time during the first data aquisition period. However the basic deliverables of the pump (head and massflow) have been achieved at the required values.

Qweak initiated the use of faster helicity reversal as a tool to mitigate the effects of target noise on the experiment. Fast Fourier transforms acquired under a wide variety of conditions during the Qweak experiment's commissioning phase show that this is an important and effective tool for reaching the goals of the experiment, and its effectiveness for the MOLLER experiment is now also validated.

Qweak also pioneered the use of a recovery heat exchanger at the ESR in order to boost the effectiveness of the ESR by making use of the enthalpy of the returning 4 K coolant. The ESR recovery heat exchanger (designed by Rao Ganni for Qweak) has been used for both the HAPPEX-III/PVDIS experiments in Hall A and for Qweak in Hall C. It has been proven to be enormously successful that it boosted the 15 K cooling power the ESR can deliver by about a factor of two.

Another novel design feature now validated by Qweak is the re-configuration of the existing transfer line infrastructure in order to simultaneously supply both 4 K coolant and 15 K coolant to the target, and in particular, to return both coolant sources on separate lines back to the ESR. This required using the LN2 supply shield as a 20 K helium return. A small superconducting polarimeter magnet in the Qweak experiment is also fed and successfully operated with this highly unusual configuration.

To summarize: the Qweak target employed a large number of novel and highly unusual ideas to meet its goals. We now know that every single one of these new ideas has worked. This greatly reduces the risk associated with the extensions needed for the MOLLER target. The expected performance in terms of the density fluctuation should meet the MOLLER requirements. The cooling power needed for the experiment has been carefully considered by the lab and solutions are already under way that will insure that the experiment's requirements can be met. CFDFAC has assumed responsibility for designing the MOLLER target. CFDFAC has delivered high performance designs for the standard $LH_2$ targets in Halls A and C. The $LH_2$ density reduction of such a cell design has been measured to be an order of magnitude better than similar cells used during the 6 GeV era at Jefferson Lab. CFDFAC is developing state of the art time-dependent simulations that would capture a target's noise on the time scale of the beam helicity reversal.

## 5.3 Simulations and Software

The collaboration has chosen to use GEANT4 to develop an application for designing the acceptance and studying the backgrounds for the experiment. Field maps are produced using the "coils only" capability of TOSCA (which was used to design the actual conductor layout for the coils of the magnets) and then read into the GEANT4 simulation. The basic framework of the simulation package for MOLLER is described in App. 2.7.

The geometry used in the simulation will continue to grow in complexity. The simulation group is in the process of designing and verifying a "2-bounce" collimation system for photon background. Additional physics generators are being added for backgrounds from pion production, electrons which scatter from the aluminum in the target cell, and weak decays with large analyzing power, to test the conceptual design of auxiliary detectors, and to gauge the radiation levels in the Hall from neutron production. The simulation will also be used to determine the expected energy deposited in the collimators and the coils of the spectrometer, and to optimize the dimensions of the radial and azimuthal segmentations of the primary quartz detectors, and design the air light-guides.

The analysis software and software tools needed for MOLLER will be related to those used by previous parity violation measurements at JLab, such as Qweak and PREX. The higher event rate and larger number

of detector channels lead to a data rate that would be a challenge for the software to provide rapid diagnostic and analysis results. The development of the analysis software and online tools can progress in parallel with the continuing development of simulation, allowing exploration of different software choices before the electronics and data acquisition designs are fully developed.

## 5.4 Spectrometer Design

In summer 2010, a Magnet Advisory Group was formed to provide advice to the MOLLER project regarding the design of the spectrometer magnets. The group consists of engineers and physicists who have extensive experience with high power warm magnet designs. The current external group members are: Vladimir Kashikhin (Fermilab), Dieter Walz (SLAC) and Steve Williamson (UIUC). Their initial input was used to prioritize the design efforts over the past couple of years and also used to optimize the design to avoid potential technical problems. In the following subsections, we describe some of the engineering and simulation work on the collimation, shielding and toroid design.

### 5.4.1 Collimators

Table 16: *Power deposited in the various MOLLER collimators broken down by particle type.*

| Collimator | $e^-$ Power (W) | $e^+$ Power (W) | $\gamma$ Power (W) | Total Power (W) |
|---|---|---|---|---|
| Beam interceptor | 3836 | 1811 | 171 | 5821 |
| Primary | 476 | 191 | 24 | 692 |
| Cleanup | 110 | 48 | 5 | 163 |
| Photon blocker | 21 | 10 | 1 | 32 |

All of the collimators will be made of a copper-tungsten ($5\% - 95\%$ alloy CW95). The power deposited in the various collimators is summarized in the Table 16. The beam intercepting collimator will block incident angles from $0.1569^{\circ}$ to $0.351^{\circ}$. About $85\%$ of the total power intercepted by the collimators will deposited into this collimator, for a total of approximately $6\ \mathrm{kW}$. This collimator therefore requires careful consideration of its geometry and water cooling. It is designed to have energy deposited over a length of about 50 cm to optimize the outer surface water cooling of the collimator as shown in Figures 49 and 50. The collimater is essentially a series of $10\ \mathrm{cm}$ collimators that absorb about $1 - 2\ \mathrm{kW}$ each.

A realistic water cooling model was tested; the maximum temperature with water cooling is about $105\ ^{\circ}\mathrm{C}$ and temperature contours are shown in the Figure 51. Cooling water will be fed from secondary chiller loop (also used for the spectrometer coils). Further studies are needed to ensure that the collimator will maintain temperature compatible with vacuum in the beamline, and that its shape will be maintained over extended periods. This collimator will also need to be surveyed with positioning requirements on the order of $\pm$ 0.5 mm with respect to the primary beam.

The primary, or acceptance defining, collimator (just upstream of the upstream torus) and the cleanup collimator (just upstream of the hybrid torus) have a similar design (see Figure 52, left). They are disks with trapezoidal openings, and clearance for the primary beam which goes to the dump. In the primary collimator the trapezoidal openings define scattered electron acceptance. The cleanup collimator is sculpted to allow full acceptance for the Møller electrons while shielding the hybrid torus. The collimator within the hybrid toroid is designed to shield the downstream part of the hybrid from any photons with line-of-sight to the target.

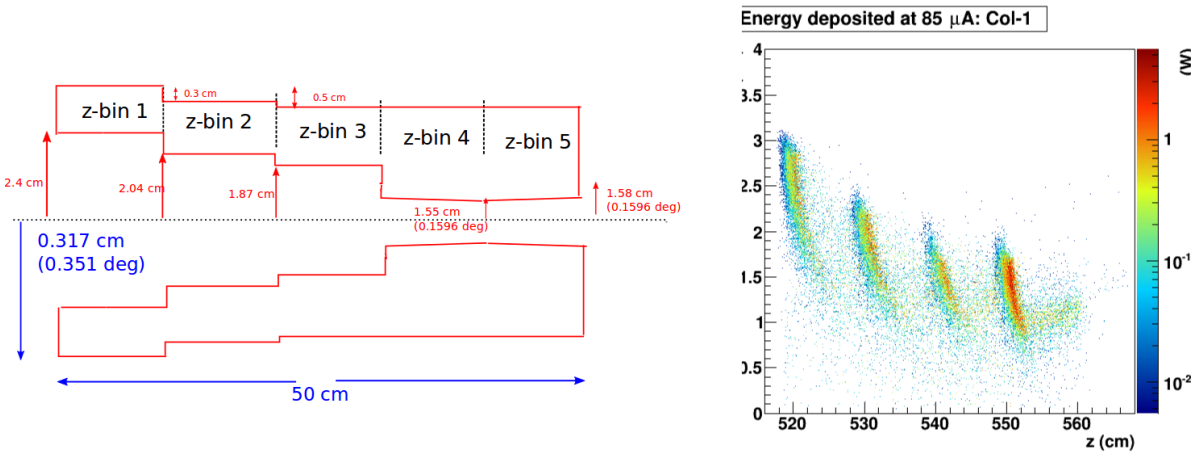


Figure 49: *Beam intercepting collimator prototype design (left) and energy deposited map along the longitudinal direction (right).*

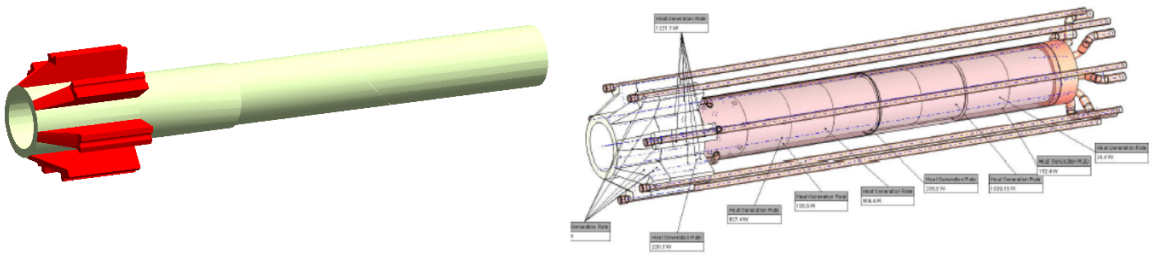

Figure 50: *Beam intercepting collimator prototype design in Geant4 (left) and CAD design with water cooling lines added (right).*

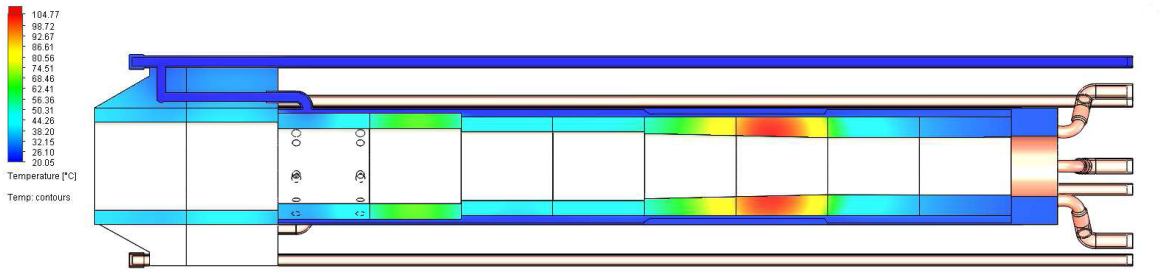


Figure 51: Temperature contours in the beam intercepting collimator when the collimator is cooled using 20 C water at 2.5 $\mathrm{ms}^{-1}$.

### 5.4.2 Radiation Shielding

Electrons from small angle scattering of 11 GeV electrons in the target, interacting with the beam intercepting collimator, and to a lesser extent the primary acceptance defining collimator, will become sources of

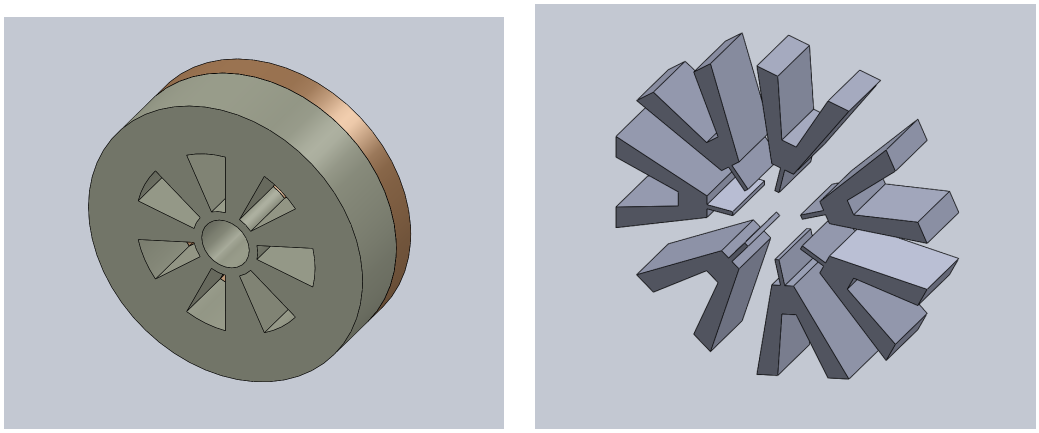

Figure 52: *The primary, acceptance-defining collimator (left) and the photon collimator (right).*

neutrons. The same is true of the downstream end of the target enclosure. These locations will also produce secondary electromagnetic radiation that will act as further neutron sources when interacting with materials in the hall. Therefore these regions will require aggressive shielding to slow down and/or stop high energy neutrons. The remaining low energy neutrons will be shielded by additional polyethylene shielding located at outermost regions of heavy shielding.

The radiation levels to the experimental hall under PREX-I and PREX-II experiments are used as the Geant4 simulation benchmarks for estimating radiation to the hall infrastructure for the MOLLER design. Initial benchmark studies done with the MCNPX neutron generator at $1\ \mathrm{GeV}$ electron beam agreed with Geant4 neutron estimates. Neutron radiation in the hall was observed during PREX-I experiment and comparison with Geant4 simulation showed that simulation overestimated the radiation dose by about a factor of 2. The neutron energy spectrum scales in intensity when going from $1\ \mathrm{GeV}$ to $11\ \mathrm{GeV}$ electron beam which suggests Geant4 uses same physics models for neutron production at these energy ranges. Simulation studies have shown that part of the downstream wall as well as the top of the target must be made of high Z material to absorb the electromagnetic power. The proof of concept shielding design is shown in the Figure 21.

The collimation and shielding systems are also designed to reduce the photon background at the main detector region. While the neutron radiation flux due to collimators and shielding are negligible at the detector area after optimization, the photon background with the current collimation system and shielding design is shown in the Figure 53. High energy photons above $10\ \mathrm{MeV}$ are about factor of 5 below the Møller signal peak. Since low energy background photon to detector signal conversion active detector (thin fused silica plates) are estimated to be below $1\%$, the total photon background should be well below $1\%$. The next phase of shielding optimization will be to further reduce the photon background at the detectors and ensure that the PMTs are also well-shielded.

The remaining radiation to the hall infrastructure is estimated by calculating the integrated power and flux on the hall enclosure. The goal was to reach radiation levels less than or equal to those expected by the PREX-II experiment. Steps are underway to further minimize the electromagnetic radiation coming from the beamline collimator. The current proof-of-concept shielding design mainly concentrated on the target and the beam interceptor collimator to shield against neutrons in energies $10 - 100\ \mathrm{MeV}$. Current estimates project instantaneous electromagnetic radiation is below our set limit based on the PREX-II experiment. The high energy neutron flux above $10\ \mathrm{MeV}$ is well below this goal. The low energy neutrons below $10\ \mathrm{MeV}$ are less than a factor of 2 larger than our goal (see Table 17). The next step will be to tweak the high density,

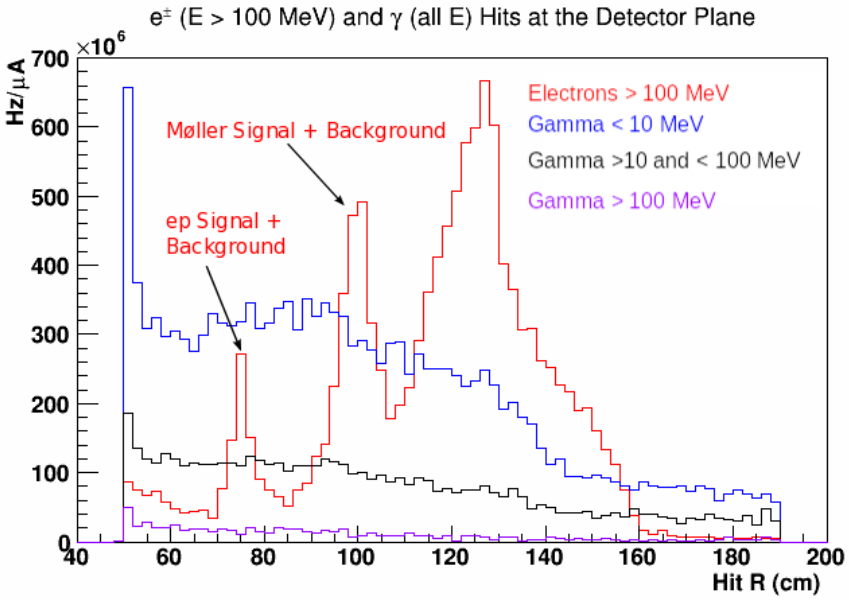


Figure 53: *Photon background compared to the electron signal at the MOLLER detector plane*

high Z material to polyethylene ratio while accommodating restrictions due to other structures in the hall. A dialog with JLab engineering staff as well as more detailed CAD design of the entire experiment enclosure has been launched to complete the optimization of the shielding design.

### 5.4.3 Spectrometer Engineering

The baseline coil design has been slightly modified from a 5.8 mm conductor to a 6.0 mm one (Outokumpu #8204, now Luvata), with a 4.5 mm cooling hole. This optimization was determined by limiting the number of total cooling channels, while keeping the correct NI in all locations. A great deal of modeling and work has gone into figuring out how to properly wind the coils such that they are manufacturable, and allow access to the external connections and inter-connections in the assembly. A separate cooling loop with heat exchanger to the Jefferson Lab main cooling will be necessary to meet radiation, pressure and flow requirements. Water flow rate of approximately 85-100 GPM at 250 psi would be needed to extract

Table 17: *Comparison of simulated radiation flux to hall enclosure in MOLLER to PREX I and II. We already have met the design goal to be less than the PREX II values for all but the low energy (< 10 MeV) neutrons, which will require further optimization.*

| Particle Type | E range (MeV) | Flux ($\times 10^9$ Hz/uA) | | |
|---|---|---|---|---|
| | | PREX I | PREX II | MOLLER |
| $e^{\pm}$ | E < 10 | 345 | 20.5 | 3.43 |
| | E > 10 | 210 | 9.42 | 1.00 |
| photons | E < 10 | 5490 | 641 | 62.9 |
| | E > 10 | 343 | 19.3 | 4.55 |
| neutrons | E < 10 | 16.2 | 1.79 | 2.99 |
| | E > 10 | 0.393 | 0.134 | 0.0374 |

the 761 kW of heat generated in the full hybrid toroid. In addition to the 6.0 mm conductor, a separate design is being investigated utilizing an 11.7 mm conductor that would require 4 separate power supplies. The advantage to this concept is that it would require even fewer cooling connections and produce less heat overall due to a greater copper proportion in the cross section. This design is referred to as MkII (or "mark 2".) The 4-power supply configuration will also be investigated for the baseline/MkI variant. Extensive FEA studies have been done to analyze loading to the coils package from stresses induced by coil forces, gravity, thermal stresses and a realistic coil carrier has been presented that addresses these loads. We have incorporated manufacturers suggestions along with extensive experience at Bates to determine the appropriate coil manufacturing process. The coils will be wound around an internal mandrel and double wrapped with fiberglass insulation to achieve the final configuration. The wrapped coil will then be placed in a vacuum mold for impregnation with epoxy. We are designing the coils for a high radiation environment (108 grays) and thus have picked appropriate materials. This is a process we have used for other large coils on several projects with excellent results.

Table 18: Summary of the optimization of the conductor and water-cooling hole size. Values are for individual coils unless otherwise noted.

| | | Proposal | 2015 MkI | 2015 MkII | Unit |
|---|---|---|---|---|---|
| Conductor | | 5.8 sq | 6.0 sq | 11.7 sq | mm |
| Cooling Hole | | 3.125 | 4.5 | 6.5 | mm Ø |
| Number of Turns | | 78 | 78 | 20 | - |
| Current Density | | 1553 | 1965 | 1960 (max) | A/cm$^2$ |
| Power Supply Voltage (7 coils) | | 1600 | 2000 | 60-180 | V |
| Power | | 86 | 109 | 94.6 | kW |
| Pressure Drop | 1A | 196 | 201 | 243 | psi |
| | 1B | 192 | 246 | | psi |
| | 2 | 227 | 175 | 48 | psi |
| | 3 | 227 | | 80 | psi |
| | 4 | 126 | 78 | 150 | psi |
| | 4C | 128 | 237 | | psi |
| Water Flow | | 17.3 | 11.9 | 13.0 | GPM |
| Water Channels | | 24 | 14 | 8 | - |

**Coil Services**

The water cooling requirement for the Hybrid Toroid will be met by the design of a stand-alone self-contained water cooling system. The requirements for this water system are to supply $>1$ M$\Omega$-cm deionized (DI) water with a total cooling capacity of less than 2 MW (570 tons) at a maximum pressure up to 250 psig. The Jefferson Laboratory water cooling system supplies 500 GPM through 8" diameter cooling lines at a supply temperature of 85°F and return temperature up to 110°F. This gives a $\Delta$T of 25°C at 13.8°C which results in 1.8 MW of cooling. The Hall A water supply will be used to cool the compressors of a condenser-less chiller that is both skid-mounted and uses multiple compressors to allow for redundancy and efficient reduced load operations. This chiller will supply water that is 10°C. City water will be run through a DI filter tank with a flow rate of less than 5 GPM to initially fill the system. Then, the closed-loop water systems will be designed to allow approximately 1-2% of the system flow to be continuously polished by both DI and deoxygenated resins. Many years of experience with accelerator water systems at MIT-Bates and SLAC [ref-SLAC blue book chapter 24] show that it is easy to maintain $>1$ M$\Omega$-cm deionized water using this

amount of bypass water through the resins. In addition, the entire flow will be mechanically filtered using cartridge filters with temperature and resistivity monitoring. It is expected that the cooling lines will require insulation to limit condensation within Hall A.

A variable frequency drive controller will be used to control the main pump flowrate and to fine tune the system. Overall system pressure will be controlled by a bypass control regulator valve and then individual supplies to equipment will be supplied with water pressure regulators to set and limit the required pressure if it is less than the overall system pressure. The entire system will have individual flow meters to remotely monitor the flow to all circuits in the loop. In addition, flow limit switches will be installed in each loop to interface with the hardware interlock system. Because the Chiller will be located within Hall A, special options will be selected to minimize vibration and ambient noise. The water connections to the chiller and manifolding within Hall A will be rigid stainless steel pipe with Victaulic type fitting which will allow for simplified disassembly of the water system during time that Moller is removed from the beamline. In summary, the water cooling system of the Moller experiment is crucial to the success and long term reliability of the experiment. The engineers for the experiment plan to design a stand-alone cooling system that will be specific to Moller toroid operation. The design of the water cooling system needs to be closely coordinated with Jefferson Lab Hall engineers and the site Facility engineers.

The two possible configurations for the hybrid coils use four separate power supplies that each power a given section for each of the seven coils. This configuration allows for fine tuning of the magnetic field to match experiment requirements. The power supplies are high constant current supplies that supply up to 800 kW of power, combined. The highest currents used in the baseline configuration are 384 A, in the MkII, we will see up to 2000 A. The input AC will be 480 V, 3 phase. While not a COTS (commercial off the shelf) device, this type of supply is common in accelerator systems. It is envisioned that the power supply will monitor the delivered current by using a current monitor with approximately 0.01% accuracy at the nominal full current. Physics requirement will have to be studied closely to define the correct current stability requirements prior to power supply selection. The power supplies will be selected in conjunction with the DC Power Group at Jefferson Lab.

**Support Structures**

A conceptual design of the MOLLER coil supports and frame has been completed. During the design process, several concepts were considered including placing the magnet in atmosphere with a 7-segment beam pipe and placing the magnet in a helium bag. Ultimately, the decision was made to place the entire magnet in a large vacuum chamber. The design of this chamber is discussed in the last paragraph of this section. The magnet consists of 7 racetrack-type coils. These coils are each connected to a strong, rigid "strong-back", or coil carrier, which provides the additional stiffness required to accurately hold the coils in place against gravity and magnetic forces. Each coil must be independently adjustable in position with six degrees of freedom to achieve the desired magnetic field uniformity. To achieve this, the coil and carrier assemblies are connected to the support frame via six adjustable struts each, arranged such that adjustment in all six degrees of freedom is possible, while minimizing coupling between adjustments in different dimensions. Struts are oriented with three tangential, two radial, and one longitudinal degree of freedom. The coil support concept analysis shows very little coil deflection due to internal "rounding" forces ($< 0.20$ mm). Further analysis will consider failure modes unique to composite structures. However, approximation using homogeneous material showed very low stresses in the coils.

The coil supports were designed based on experience with the Qweak and BLAST toroids. In contrast to those projects, MOLLER requires a much smaller radial range for particle tracks passing between the coils, so very little space is available there to add structural material. The bulk of the coil carriers must exist radially outwards from, rather than between, the coils. Increasing the overall radius of the magnet

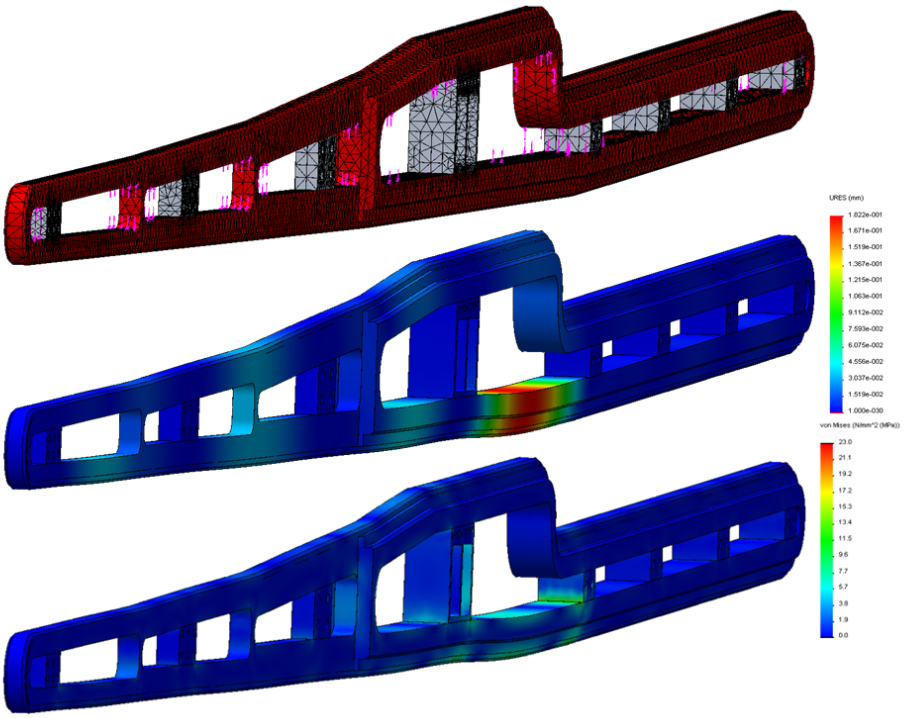


Figure 54: Structural Analysis of Coils subjected to magnetic "rounding" forces. Deflections are less than 0.2 mm and stresses less than 23.0 MPa. However, the stresses assume a homogeneous material and thus only serve as a general guide. Further analysis will incorporate composite material properties.

increases the force due to atmospheric pressure and thus structural requirements and cost of the vacuum chamber. Therefore, much effort was placed into optimizing the shape of the carriers to minimize deflection while limiting the overall size of the assembly. The carriers are designed for maximum stiffness to minimize deflection of the coils, while still staying outside the envelope of scattered Moller and ep electrons. The carriers will be made of large, machined aluminum strongback which serve as a spine for loads and coil services. They will bolt to each coil through a number (likely 4-6 per side) of removable side plates, attached with silicon-bronze bolts. The connections to the coils will be such that radial and tangential motion is completely constrained, while in the longitudinal direction, only one pair of side plates will provide constraint, with the others allowing slight change in length as the coil temperature changes. This length change is expected to be less than 4.5 mm (over 7 m of coil length) at operating temperature. Struts are connected to the carrier by small clevis assemblies and titanium pins. The loads experienced by the carriers are due to the weight of the coil ($\approx$ kgf) and the magnetic centering forces ($\approx$3000 lbf). Additionally, they may be subjected to tangential loads due to an unbalanced coil. Analysis of our current design predicts deflections on the order of 1.0-1.5 mm due to the coil carriers alone; further deflection due to frame and strut loading is to be expected. Stresses in the carrier are also low, roughly 40 MPa near the pre-loaded bolts.

The MOLLER Hybrid toroid support frame is an open, space-frame type design, possessing 42 connection points for the coil struts, as well as 4 connection points for hanging the frame inside the vacuum enclosure. It is made of commercially available 6061-T6 aluminum extrusions and bare plates, formed into three box sections (upstream, middle, and downstream) oriented perpendicular to the beamline, with trusses on either side connecting the three sections. The majority of connections are welded. Bolted connections will employ silicon-bronze fasteners which are as strong as grade 5 steel bolts but are non-magnetic. A sin-

gle removable section of the frame allows all coils to be installed from above using the Hall A crane. Due to the large range of adjustment of the struts, dimensional tolerances between sub-weldments (and even within sub-weldments) may be fairly generous (on the order of 0.25"). The approximate mass of the frame is 1400 kg. The frame will be designed to support the cleanup collimator as well as the photon collimator within the hybrid torus. Mounting hardware and cooling connections will be oriented in phi to be in the sectors occluded by the coils. The primary and beam intercepting collimators will likely be mounted together and movable as a unit as part of the upstream magnet support structure.

The magnet will be placed in vacuum and therefore care is being taken to minimize the amount of surface area and trapped gas volumes within the frame. Several iterations have been analyzed in an attempt to minimize deflections, size, and complexity. The most recent analysis, which includes the coil carriers, strut supports, and all weight and gravity loads, predicts about 3 mm deflection (maximum) of the carriers. Stresses in the frame are on the order of 20 MPa. This small magnitude of stress is to be expected from a deflection-driven design. The design of the hybrid magnet along with physics considerations has presented challenges for the vacuum system design. Several solutions were considered to minimize scattering in this region. One solution included vacuum chambers between the magnets with the appropriate windows. This was considered too complicated and also difficult to implement without compromising the physics. Another solution that is still an alternative is to use helium bags in this region. This still has the potential to compromise the physics due to scattering issues. The baseline we are pursuing is a large vacuum chamber that encloses the entire hybrid toroid that then connects to the rest of the vacuum system for the experiment. This eliminates any scattering issues and maximizes the acceptance between the coils.

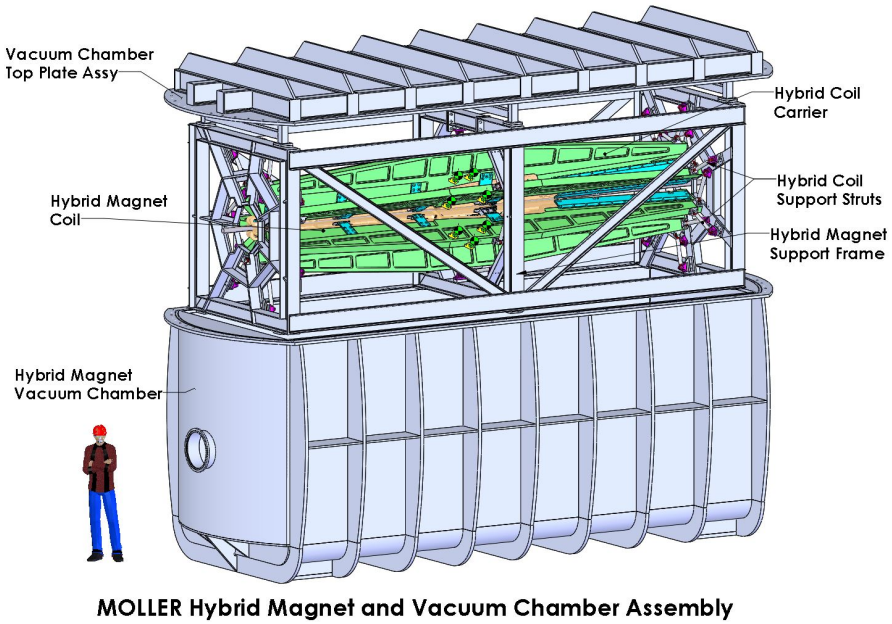


Figure 55: CAD drawing of the vacuum assembly for the hybrid toroid, with the lid pulled up. The hybrid assembly (coils, frames and support structure) are shown as attached to the lid.

The vacuum chamber for the hybrid magnet is designed to allow the coil frame assembly to be supported from the top lid of the chamber. This configuration allows for several advantages. The coil and support package can be assembled and aligned outside of the chamber to the fiducials in the top flange so that global alignment can use the top flange for a reference. This configuration also includes the ability to have

electrical and water services for the coils connect through top flange. This allows all connections to be made before inserting the coils into the vacuum chamber. These connections will have manifolds in the chamber to reduce the hose and cabling services routed to the coil package in the facility hall. Finally for maintenance and repair purposes the coil package can be conveniently removed and re-inserted without having to disturb the beam line. The design of the vacuum chamber has gone through several iterations. The initial design required an extensive gusseting system to get stresses to an acceptable level. The feature of everything being supported from the top lid also imposes a deflection constraint so that the top lid requires a higher stiffness. This is to ensure that we can maintain alignment of the coils after pumping down the system. Due to the amount of welding required, the stress limit had to be sensitive to the aluminum having reduced yield strength near the weld. The chamber is currently designed using 6061-T6 aluminum. The yield stress limit is 240 MPa and 105 MPa across welds. Results from finite element analysis indicate maximum stress levels of 120 MPa in the bulk and 60 MPa near the welded sections. Global deflections of the vacuum chamber walls are on the order of 3 mm. Deflections at the support points of the coil package on the top flange are sub-millimeter.

In meetings with vendors who have extensive experience with chambers of this size, we were advised to eliminate stainless steel as an option. This was due to the cost of the raw materials in this size range, hence aluminum is the material of choice. The vendor also had advice about chamber geometry (curved sections where possible) and gusseting. These were all incorporated in the latest design. Below is an exploded view of the chamber and coil package. The vacuum system will consist of cryogenic panels (LN2) incorporated into the chamber walls with supplemental turbo and roughing pumps to achieve appropriate vacuum levels ($10^{-7}$ torr). This will necessitate periodic regeneration of the cryogenic system. The design also includes a double o-ring seal for the top flange for redundancy as well as robustness. These seals will be replaced during annual maintenance periods. All supplemental pumps will be "dry" to minimize contamination. In conclusion, the vacuum chamber design is at a point where the stress and deflections are well understood and controlled. Due to the size and forces involved and the evolving design of the coil and collimator package there have been several iterations of the design so far. At this point the design is mature enough to obtain budgetary bids, to date the quotes we have range from $600,000 to $1,600,000. Due to the size of this chamber there are limited shops that can do the fabrication. Given the initial bid range we are consulting with other manufacturers for budgetary bids.

**Assembly and Alignment**

The positions of the detectors and magnet coils will be set based on the scattered particle envelopes. The envelopes are defined by the positions of the collimators. Therefore, it is paramount that the position of the collimators with respect to the beamline, target, and each other is established and known to a high level of accuracy. Positioning of the coils will then be such that they are completely within the shadow defined by the collimators. Further adjustment of the coils to optimize the magnetic field can only occur within this small range. Studies show that the tightest position constraint is the radial position, followed by roll, at 2.9 and 6.3 mm, respectively (based on an allowed asymmetry uncertainty of $\delta$A = 0.1 ppb). Allowable errors for other orientations are much higher, therefore, a baseline requirement of 2.9 mm positional and stability accuracy will be enforced. To measure the position and orientation of the coils, fiducial marks will be installed such that they can be seen during all phases of assembly. The alignment will be continuously checked throughout the assembly process in collaboration with the JLab survey & alignment group. This includes surveying the vacuum chamber to the hall, the coils to the chamber lid, and finally checking the chamber lid to hall. The position of fiducials on the coils will be monitored as the frame is being populated, after installation into the vacuum chamber, and after pump down of the chamber. We plan to deliver a carefully designed and tested lifting fixture for manipulating coils with the Hall A frame. We also expect to provide stands that will allow safe and easy staging of the coil + carrier assemblies prior to installation in the frame.

Table 19: *Position sensitivities given in cm for various offsets of a single coil asuming an asymmetry uncertainty of $\delta A$ = 0.1 ppb. The $\phi$ and roll offsets are over half the radius of the coil, and the yaw and pitch are over half the length. The most sensitive is the radial offset, which gives a 2.9 mm limit on coil offset.*

| Direction (cm) | Large Range (higher order fit) | Small Range (linear fit) |
|---|---|---|
| z | -9.73 | -8.89 |
| R | 0.28 | 0.29 |
| $\phi$ | -6.37 | 19.11 |
| Roll | 0.63 | -1.37 |
| Yaw | 9.73 | 2.9 |
| Pitch | -4.46 | -3.29 |

Table 20: *Engineering specifications for the hybrid magnet.*

| Parameter | Value | Unit | Notes |
|---|---|---|---|
| Vacuum Chamber Lid Mass | 10,500 | lbs | |
| Vacuum Chamber Base Mass | 27,800 | lbs | |
| Vacuum Chamber Assy. Mass | 38,300 | lbs | |
| Magnet Support Frame Mass | 3,400 | lbs | |
| Coil Mass | 177 | lbs | Each ($\times$7) |
| Coil + Carrier Assy. Mass | 1,575 | lbs | Each ($\times$7) |
| Hybrid Toroid Magnet Assy. Mass | 14,700 | lbs | |
| Hybrid Toroid Complete Assy. Mass | 53,000 | lbs | Coils + vacuum chamber |
| Water per Coil | 12 | GPM | Hybrid only |
| Total Water for Hybrid System | 120 | GPM | Estimate inc. upstream toroid and collimators |
| Water System Pressure | 250 | PSIG | |
| Power per Coil | 109 | kW | |
| Total Power for Hybrid Magnet | 761 | kW | |

## 5.5 Detector Design

Figures 22 and 24 in Sec. 2 show the layout of the main detector elements. The conceptual design is a natural evolution of the experience gained from the performance of the Qweak and PREX detector designs. Ongoing efforts are focused on fleshing out the detector concept and reaffirming the technology choices that were made based on this experience.

### 5.5.1 Quartz and Light Guide

Thin quartz detectors were the technology of choice for the PREX and Qweak experiments. The shape, dimensions and surface quality of the quartz all play critical roles in determining how many photo-electrons will reach the detector. After emission of the Ĉerenkov light from the quartz, the amount of light hitting the cathode is a strong function of the reflective properties of the light guide surfaces, as well as the length of the light guide. The orientation of the light guide with respect to the quartz and the shape of the light

guide largely determine the number of reflections the Ĉerenkov light undergoes, before hitting the PMT cathode. Each reflection reduces the probability for detection at the cathode. The orientation of the quartz tiles and the light guides relative to each other and with respect to the scattered electrons must be optimized, such that the collection of the Ĉerenkov photons from each quartz piece is maximized, while the detection of light *created by events in the light guide itself* (accidentals) should be minimized. Figure 56 illustrates two possible setups for the detector module assembly, with straight or angled light guides, with respect to the quartz. Figure 57 shows a single simulated electron event in a piece of quartz with a single 45 degree cut at one end and illustrates how total internal reflection is broken to allow the light to exit into the light guide. The detector must also minimize cross-talk between adjacent radial bins, with widely differing asymmetries, and minimize electron hit location and electron incident angle dependent biases. The latter point, again, primarily places restrictions on the individual detector active material geometry.

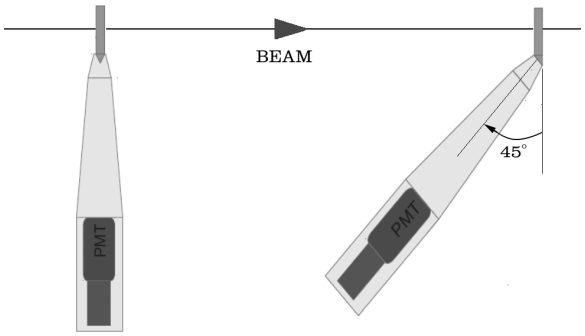


Figure 56: *Schematic of the two prototype detector assembly types that were tested with an 855 MeV electron beam, at MAMI. Both the Møller ring and the super-elastic ring detectors were tested with both straight and angled light guides. All quartz pieces had a 45 degree angle cut at the edge where the light exists the quartz and enters the light guide.*

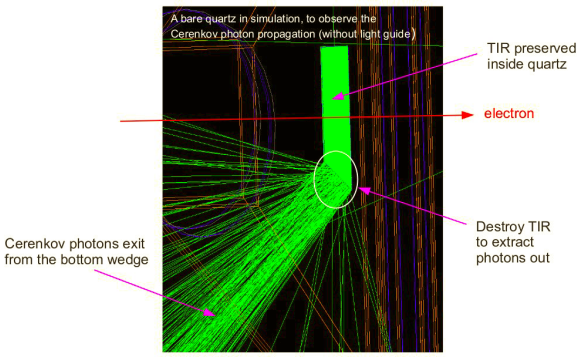


Figure 57: *Simulated event in a single MOLLER main detector. The Ĉerenkov light produced by the passage of a minimum ionizing electron that hits the detector at normal incidence is totally internally reflected until the light hits a surface at nearly normal incidence and can escape to be detected by a photosensitive device.*

### 5.5.2 Integrating Detector Development Status

Over the past three years, significant progress has been made in the design and prototype testing of the integrating detectors. The first step was to develop a small set of viable detector configurations (geometry and material combinations between quartz and light guide), using detailed simulations. These were then implemented as prototype detectors and tested with minimum ionizing cosmic rays and beam electrons.

A complete detector design has been implemented in the full MOLLER simulation and many single detector simulation studies were performed to optimize geometry material and background rejection. An example of a single detector simulation study is shown in Fig. 57. A complete angle study was carried out, to study the effects of the quartz orientation with respect to the incident electrons and to study the effects of the light guide orientation with respect to the quartz. Simulations also included variations of quartz geometry, including trapezoidal and rectangular chapes, thickness and flat or 45 degree angle cuts along the edge that interfaces with the light guides (see Figs 57 and 56). Light guide geometry (length, flare, size) were also studied using simulations. The primary results that were obtained for each configuration include photoelectron yield and signal RMS width. The simulations were checked against cosmic ray data, however, to get a definitive value for the number of photoelectrons, to benchmark the simulations against, and to carry out a realistic study of light yield variation as a function of reflective material properties in the

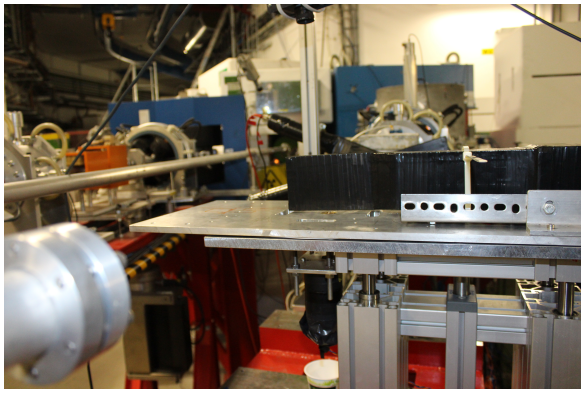

Figure 58: *Møller detector geometry prototype test setup with an 855 MeV electron beam at the MAMI facility in Mainz, Germany.*

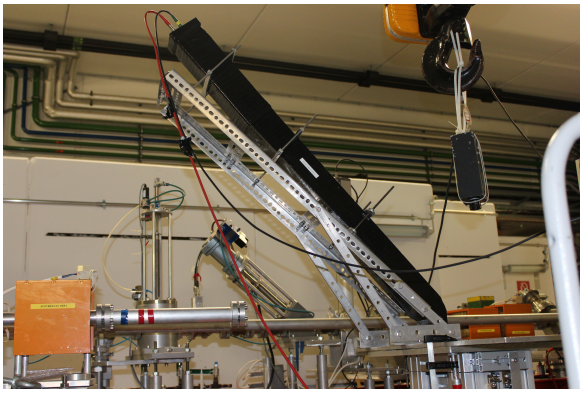

Figure 59: *Super-elastic detector geometry prototype test setup with an 855 MeV electron beam at the MAMI facility in Mainz, Germany.*

light guide (which is very difficult to simulate accurately), dedicated prototype tests needed to be performed with minimum ionizing beam electrons.

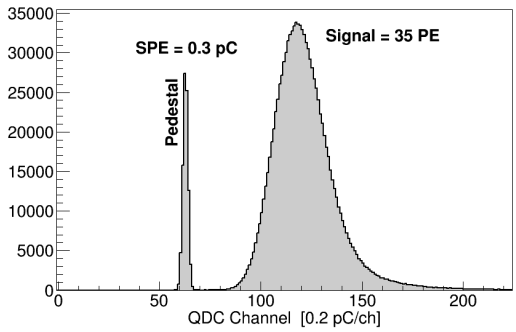


Figure 60: *Measured photoelectron yield from 855 MeV electrons incident on a 1 cm thick polished quartz attached to a 25 cm air-core light guide with Miro-Silver reflectors and a 3 inch high gain PMT.*

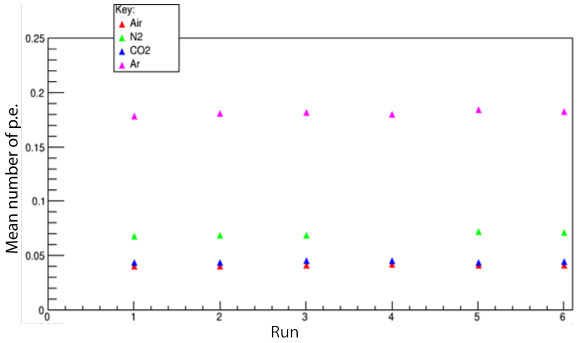


Figure 61: *Photoelectron yield from electrons traversing the light guides with various gases. The test results demonstrate that the photoelectron yield from the light guide will be very low compared to the light yield from the quartz.*

Since October 2013, the detector working group has carried out many tests with prototype detectors at the MAMI facility in Mainz, using 855 MeV electrons during five separate test beam periods. Measurements were carried out to verify the single event photoelectron yield for the simulated quartz and light guide geometries as well as for a variety of light guide reflective materials. Overall five different light guide lengths were tested (80 cm, 60 cm, 56 cm, 35 cm, and 25 cm), corresponding to the guides needed for different rings and assemblies, with two different angles between the quartz and the light guide, as seen in Fig. 56. In addition, a variety of different reflective materials for the light guides were tested. The guides were coupled to various different quartz geometries, including 1 cm, 1.5 cm, and 2.5 cm, thick quartz pieces for the Møller and super-elastic geometries. The super-elastic detector geometry is expected to have the poorest photoelectron yield, since it has the longest light guide and the least optimal quartz geometry of all the detectors. Consequently, achieving sufficient light yield in that detector means that we can expect the designs for the other detector rings to work as well or better. The lateral dimensions of the quartz pieces were $8.4 \times 16\ \mathrm{cm}^2$ for the Møller ring and $17.1 \times 4\ \mathrm{cm}^2$ for the super-elastic ring. The beam tests were done

with 3 inch photomultipliers with quartz windows and bialkali cathodes, manufactured by Electron Tubes Inc. Figure 56 also illustrates the two detector assemblies that were tested and Fig. 60 shows the result for the photoelectron spectrum for the Møller ring detector prototype. In addition, several tests were carried out to determine the signal magnitude from events going through the light guide, to study the relative signal dilution when events traverse the light guides, as opposed to the quartz. The results are now being used to benchmark our optical simulations. The most recent beam tests were performed in May 2016 and included a repeat of the light yield measurements for the Møller ring and the super-elastic ring detector geometries with new light guide designs, as well as more precise tests for light yield from the light guide only, when filled with a variety of gases (aside from air). The results of the light guide study are shown in Fig. 61. Two of the prototypes tested at the MAMI facility are shown in Figs. 58 and 59. The results from the beam tests show the important result of the relative signal yield (in photo-electrons) produced by MIP electrons in the quartz and in the light guides. These results can now be folded into our simulations to verify our assumption, that the background, caused by electrons traversing the light guide, is negligible. Table 21 summarizes the main tests that were done up to now, and the general results obtained. Additional beam tests are planned for December 2016, with a tagged photon beam, at the MAMI A2 beam line, to test our assumptions made about the detector signal yield for incident photons, particularly up to energies of $\sim 100$ MeV. High beam current integrating mode measurements with the prototypes are planned for 2017.

Table 21: *Most Important Prototype Tests Performed at MAMI*

| | **Description** | **General Results** |
|---|---|---|
| 1 | Light yield from 1.0 cm thick highly polished quartz, 25 cm Miro-Silver guide) | A minimum of 25 photoelectrons per event, with 4% excess noise. |
| 2 | Light yield from 1.5 cm thick highly polished quartz, 25 cm Miro-Silver guide) | A minimum of 35 photoelectrons per event, with 4% excess noise. |
| 3 | Light yield from 2.5 cm thick hand polished quartz, 25 cm Miro-Silver guide) | A minimum of 55 photoelectrons per event, with 5% excess noise |
| 4 | Comparison of various common Light guide reflective materials, including UVS, Miro-Silver, Alanod, and mylar. | Data with Kapton blacked-out guide shows that a small portion of the light is from direct shine and most of it is reflected into the PMTs from the guide walls. Relative light yields for the tested materials are all within 90% of each other. |
| 5 | Light guide length comparison for 2.5 cm thick quartz between 60 cm and 25 cm Miro-Silver guide | 60 cm, corresponding to longest guide in current design, looses 32% of the light relative to the 25 cm guide. |
| 6 | Comparison of different quartz wrapping materials: No wrapping, mylar, and white paper (e.g. millipore) | White paper produced by far the best result increasing the yield by a factor of 3 with respect to no wrapping. Mylar increased the yield by a factor of 2 with respect to no wrapping (see Fig. 62). |
| 7 | Electron event hit location position scans: Lateral position scan away from the light guide and transverse to the light guide. | Only small amounts light yield variations were were observed for either direction ($\sim 8\%$) |
| 8 | Electron events through the light guide. | Events that traverse the light guides contribute to the light yield seen in a detector at the fractional PE level(see Fig 61) and the relative rates are low (about 1 in 10 electron events in a guide produces a detectable event). |

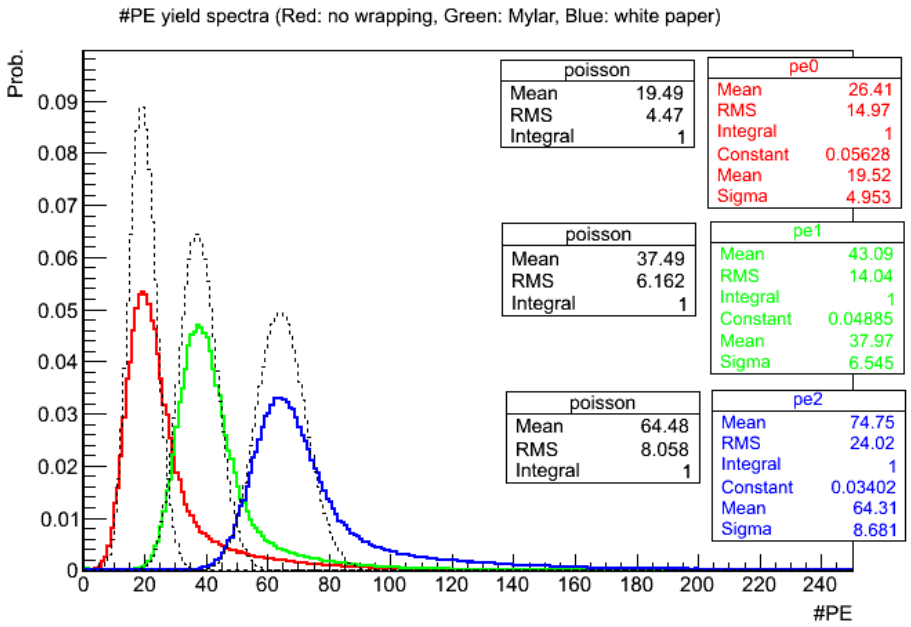


Figure 62: *Results obtained from wrapping the 2.5 cm thick quartz geometry in mylar, white paper (e.g. millpore), or leaving it unwrapped. The black dotted lines correspond to the expected Poisson distribution without excess noise, which where centered on the fitted data means. The starting point and rising edge of the Poissonian distributions fit the corresponding spectrum very well, but the falling edges are not in agreement with the spectrum due to shower tails. The mean and RMS of the whole spectrum, as well the Gaussian-fit parameters of the spectrum are also shown. The Gaussian-fit parameters are very close to the Poissonian parameters. Evidentally, white paper is the best wrapping material.*

The beam tests performed at the MAMI facility in Mainz and the comparison of the results to the simulations, prove that the current detector design is viable. As listed in Table 21, test results (1) through (4) show that the light yield is high enough and the excess noise low enough to perform the measurement with the proposed detector design. The largest difference in the light yield occurs for different quartz wrapping materials, as noted in result (5) and shown in Fig. 62. Test result (6) notes that no significant variations in light yield due to varying electron hit locations was observed. This is largely expected for small detectors like these. For most of these tests, beam was normally incident on the quartz, and the light guide was tilted 45 degrees with respect to the beam, with the PMT located upstream of the quartz. The results quoted here were taken from plots with the pedestals removed and the ADC channels converted into number of photoelectrons, using single photoelectron calibrations.

### 5.5.3 Integrating Detector Electronics Study

The design of the electronics is, of course, dictated by the properties of the signal, including the mean amplitude, the RMS width, noise sources, and expected variation as a function of helicity. For the purposes of discussing the integrating electronics, the electronic signal from a single detector $(i)$ can be written as

$$I_i^{\pm}(t) = I_{i_P}^{\pm}(t) + \sum_B I_{i_B}^{\pm}(t) + I_{i_D}(t) \quad [A]\,. \tag{9}$$

This is the current that is present at the anode of the PMT, where $I^{\pm}_{i_P}(t)$ is the contribution to the current from the physics process of interest (elastically scattered electrons and the secondaries they produce - indicated by the subscript $P$), the sum over $I^{\pm}_{i_B}(t)$ is the contribution from the various background processes (indicated by the subscript $B$), and $I_{i_D}(t)$ is the dark current (indicated by the subscript $D$). The current is converted to a voltage by an I to V amplifier with a gain of $g^{\pm}_{Amp_i}(t)$, in units of Ohms, so that the corresponding voltage yield is

$$V^{\pm}_i(t) = g^{\pm}_{Amp_i}(t) I^{\pm}_i(t) + V^{\pm}_{i_E}(t) = V^{\pm}_{i_P}(t) + \sum_B V^{\pm}_{i_B}(t) + V^{\pm}_{i_D}(t) + V^{\pm}_{i_E}(t) \quad [V]\,. \tag{10}$$

Equation 10 includes a voltage contribution from a possible amplifier offset ($V^{\pm}_{i_E}(t)$) and the voltage signal corresponding to the dark current now obtains possible helicity dependence due to possible electronic coupling of the helicity signal in the preamplifer. In the preceding expressions $g^{\pm}_{i_{P,B}}(t) = Q_{i_{P,B}}(t) g^{\pm}_{Amp_i}(t)$ is the overall gain of the detector in units of $V/Hz$, with $Q_{i_{P,B}}(t) = g_{PMT_i}(t) N_{i_{P,B}} q_i(t) e^-$ being the charge present at the anode, per incident beam electron. Here $N_{i_{P,B}}$ is the number of optical photons created per particle incident on the quartz, $q_i(t)$ is the quantum efficiency of the cathode in %, and $g_{PMT_i}(t)$ is the unitless gain of the PMT.

For integration mode measurements, counting statistics manifests itself in the root-mean-square (RMS) width of the shot noise at the PMT anode, which has contributions from all sources that generate an anode current, including background and dark current. To get the total RMS width in the signal, as it is sampled by the ADC, one has to add all sources of electronic noise $\sigma^2_{i_E}$, which includes resistive (Johnson) noise, as well as noise introduced by active components and filters. The total squared RMS noise density in the signal is then given by

$$\sigma^2_i = 2Q_{i_P} I_{i_P} + \sum_B 2Q_{i_B} I_{i_B} + 2Q_{i_D} I_{i_D} + \sigma^2_{i_E} \quad [A^2/Hz]\,. \tag{11}$$

Where $I_{i_{P,B,D}} = \langle I^{\pm}_{i_{P,B,D}}(t) \rangle$ is the mean anode current and $Q_{i_{P,B,D}} = \langle Q_{i_{P,B,D}}(t) \rangle$ is the mean quantum of charge at the anode. For the anode current this is simply a time average, but for the charge quantum the assumption is that this is the mean of a Poisson distribution and that the time integration for the current is done over a time period for which the quantum efficiency was stable. Note that, under ideal operating conditions, the dark current is dominated by thermionic emission of single electrons at the cathode, so that $Q_{i_D}(t) = g_{PMT_i}(t) e^-$ and the corresponding dark current is given by $I_{i_D}(t) = AT^2(t) e^{-(W)/kT(t)}$, where $A$ is a constant depending on the cathode material and size, $T$ is the temperature in Kelvin, $W$ is the (field modified) work function of the cathode material, and $k$ is the Boltzman constant. The mean anode current from events in the detector is given by

$$I_{i_{P,B}} = \langle I^{\pm}_{i_{P,B}}(t) \rangle = \langle R^{\pm}_{i_{P,B}}(t) Q_{i_{P,B}}(t) \rangle \quad [A]\,. \tag{12}$$

Where $R^{\pm}_{i_{P,B}}(t)$ is the instantaneous rate of electrons on a given detector. Equations 10 through 12 represent a general way of expressing the detector signal and its dependence on various experimental conditions. A possible, explicit, dependence of a given parameter on helicity state is indicated by the $\pm$ superscript, while explicit time dependence (both slow and fast), that is generally not correlated with the helicity state is indicated by the continuous time parametrization $(t)$. The primary concern of the electronics design, coupled with the data collection methodology (e.g. helicity reversal speed), is to suppress effects of random time variation or drifts and to remove helicity signal leakage into the electronics chain, the former being leading to a statistical degradation and the latter to a systematic false asymmetry.

**Integrating Electronics General Design Criteria:** Aside from the physics asymmetries, the variation of various parameters with the helicity state of the beam may be a result of either electronic coupling of the helicity signal or direct variations in the beam as a function of helicity state. Examples of the former would be the coupling of the helicity gate into the signal that comes from the detector preamplifiers $g^{\pm}_{Amp_i}(t)$ or the ADC electronics $V^{\pm}_{i_E}(t)$. Helicity correlated changes in beam conditions result in explicit changes of the rate seen in the detectors, even in the absence of any asymmetry that results from the interaction of the primary beam in the target or the rest of the experiment. Continuous time dependence in the detector signal is primarily due to variations in the beam current, target conditions, electronic drifts, temperature fluctuations, and PMT aging. A great deal of effort goes into the overall experimental design and analysis methods to remove or mitigate the dependencies on these unwanted experimental factors and many of the solutions are explicitly related to or influence the design of the integrating electronics, such as the avoidance of ground loops and the usage of optical fiber connections for the helicity gate connections to the electronics crates.

Helicity correlated changes in the beam (current, energy, position, and angle) are unavoidable, but they can be minimized to some degree (for example through feedback on the source itself,in the case of current, and other mechanism) and they can be measured using charge and position monitors. Experiments are usually designed such that it is possible to exploit symmetry to suppress some of the helicity correlated effects on one hand, and to measure the sensitivity of the detectors to these beam changes, on the other hand. The sensitivity measurements are made by measuring the correlation between the changes measured with the beam monitors to those measured with the detectors, which requires that the electronics chain used to process the measurements from the beam monitors is identical to that of the integrating detectors. This is particularly important in the case of the beam current monitors, since the integrating detector signal is normalized to (divided by) the current monitor signal to remove random drifts, fast fluctuations, and helicity correlated changes, in the beam current.

The detector signal contains random changes and systematic drifts, both fast and slow. The parametrisation in terms of continuous time $(t)$ addresses the slow drift dependence due to effects such as beam current (removed by normalization as discussed above), target conditions (target boiling and slower density changes), electronic drifts, temperature fluctuations, and PMT aging. Almost all of these can be controlled to some degree (for example by operating the PMTs at a reasonable HV bias, in a reasonably stable temperature environment, and removed from or shielded from direct radiation exposure), but the primary way to deal with possible false asymmetries due to drifts and unwanted noise above Shot noise, due to large amplitude random drifts, is to perform each asymmetry measurement on a time scale that is short compared to the timescale of the drifts. This is achieved by running the experiments with a fast helicity reversal rate. The faster the helicity reversal rate, the more the signal variation with respect to time is well approximated as constant on the time scale of an asymmetry calculation:

$$A_{i_{raw}} = \frac{V_i^+(t_+) - V_i^-(t_-)}{V_i^+(t_+) + V_i^-(t_-)} \rightarrow \frac{V_i^+ - V_i^-}{V_i^+ + V_i^-}$$

Random variations that are faster than the helicity reversal rate are dealt with and used to advantage in the electronics chain, as described in detail below. The choice of helicity reversal rate influences or determines almost every detail of the electronics design.

**Signal Structure and Sampling Scheme:** Figure 63 shows a 2 minute period of the raw and beam current normalized signals for one of the QWeak integrating detectors. This data corresponds to an integration with an equivalent bandwidth of half the helicity reversal rate (480 Hz), since the data for each helicity window is averaged to one value per helicity window, in the FPGA, after sampling. Even after normalization, drifts can be seen at time scales down to seconds, along with much longer drifts, and large non-gaussian drops in

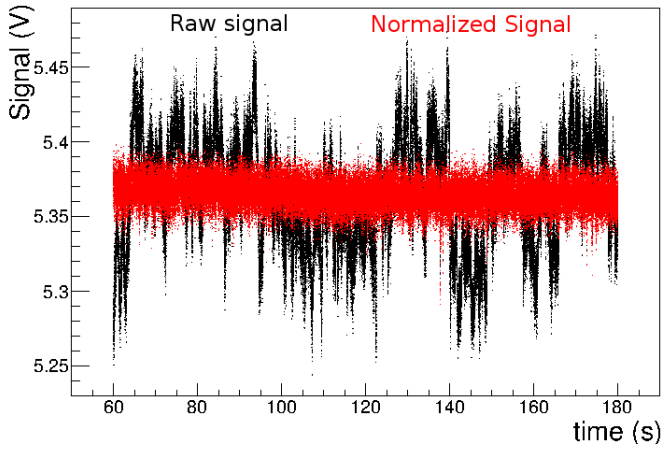


Figure 63: *Example period of a signal from one of the QWeak integrating detectors. The black data shows the raw, unnormalized yield and the red data shows the beam current normalized yield.*

yield, due to target boiling, can be seen at much shorter time scales (around $30$ ms). A high helicity reversal rate prevents these types of drifts from producing false asymmetries and reduces the contribution to the RMS width in the asymmetry signal, due these effects. For a mean signal of, say, $5$ V a physics asymmetry of $30 \times 10^{-9}$ produces a shift in the mean of about $0.15$ $\mu$V, which is much smaller than the observed RMS width of a few $\mathrm{mV}$. Since the bit resolution of even the best ADCs today is not high enough to measure a signal difference at that level, in a single sample, the combination of a suitable bandwidth selection and a high rate of oversampling is used to increase the effective bit resolution of the ADC.

Figure 64 illustrates the division of the integration mode detector signal into sampling regions. The period sampled for the physics measurement must be stable, which means that the time periods corresponding to the Pockels cell settling and ADC stability are excluded. However, it is important that the electronics be designed to allow sampling during the excluded time periods, so that the settling time can be monitored and used for systematic checks. The example in fig. 64 shows the time structure used for the QWeak experiment, with a helicity reversal rate of $960$ Hz, Pockels cell settling time of $70$ $\mu$S, and an ADC delay of $42.5$ $\mu$S. For MOLLER, the reversal rate will be $2$ kHz and the goal Pockels cell settling time is $10$ $\mu$S. This means that the integrating electronics settling should be correspondingly faster and operate at a higher sampling rate. The primary goal of the integrating electronics is to match the ADC bit resolution and sampling rate with the detector signal bandwidth needed to follow the changes in the beam (related to the helicity change and otherwise).

Figure 65 illustrates the concept behind the oversampling. The right hand side of the figure shows two simulated data sets (red and blue) for which the mean value differs (e.g. as a result of an asymmetry), as a function of sample time. The left hand side shows the samples accumulated by the ADC in histogram form. In this simulated data set, the mean difference between the two data sets is $20$ $\mathrm{mV}$, while the bin width in the histogram, which represent the resolution of the ADC, corresponds to $25$ $\mathrm{mV}$. Both of these values are exaggerated for illustrative purposes, but they show the general effect. The ADC resolution is too large to resolve the difference in the signal caused by the asymmetry during a single pair of samples, but if the signal is sampled many times within each period (i.e. the helicity window), the mean difference of the two distributions is clearly visible. This only works effectively, if the RMS width in the signal is significantly larger than the resolution of the ADC ($\Delta = V_{ref}/2^n$ for an $n$-bit ADC), which then automatically exceeds the digitization error in the ADC $\sigma_d = \Delta/\sqrt{12}$. Another benefit of the larger RMS width in the signal is that any ADC non-linearity becomes less and less significant while increasing the number of ADC channels

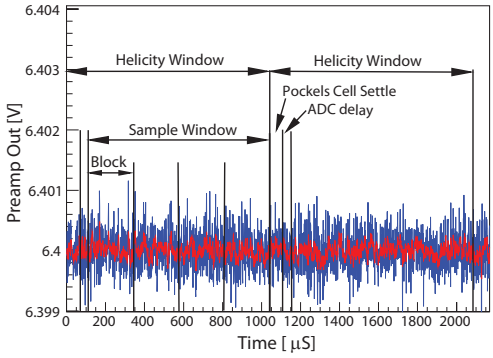


Figure 64: *Integration mode detector signal (simulated Gaussian white noise) at the preamplifier output with a* 500 kHz *bandwidth (blue) and a* 25 kHz *bandwidth(red) and how this signal is divided into helicity windows and sampling regions. A primary goal of the integrating electronics is to match the ADC bit resolution and sampling rate with the detector signal bandwidth needed to follow the changes in the beam (related to the helicity change and otherwise).*

over which the signal is spread. The experimental design and a suitable choice for the bandwidth in the preamplifiers and filters at the ADC input will ensure that this requirement is satisfied.

**Integrating Electronics Design** The design of the integrating electronics, including the preamplifiers and ADCs is based on the criteria listed below:

1. Minimization of electronics noise contribution: $\sigma^2_{i_E} \ll 2Q_{i_P} I_{i_P} + \sum_B 2Q_{i_B} I_{i_B} + 2Q_{i_D} I_{i_D}$
2. Minimization of drift effects and helicity correlated electronic pickup in the pedestal: $V^{\pm}_{i_E}(t) \rightarrow V_{i_E}$
3. Minimization of drift effects and helicity correlated electronic pickup in the amplifier: $g^{\pm}_{Amp_i}(t) \rightarrow g_{Amp_i}$
4. Bandwidth matching of all electronic components and between the various detectors that will be read out in integrating mode.
5. Optimization of ADC resolution and sampling rate with respect to a 2 kHz reversal signal and the 500 kHz input bandwidth required by the beam monitors.

Based on the success of the QWeak ADC and preamplifiers that were designed at TRIUMF, the MOLLER design will follow the QWeak design, with changes where needed. The next section discusses the main features of the QWeak design. Most of this information is available in a number of older documents on the QWeak document database and is collected here for convenience. The last section discusses the desired changes and additions for the MOLLER design.

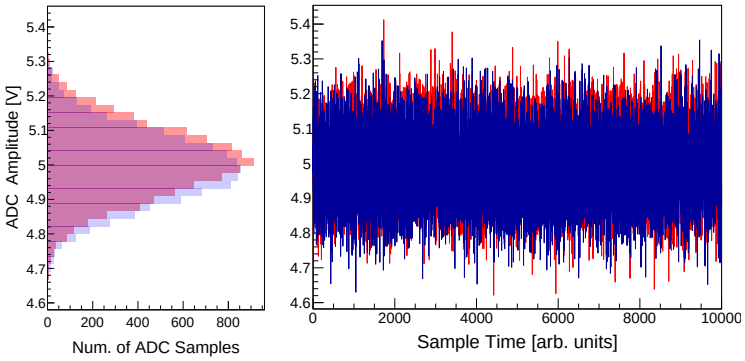


Figure 65: *Illustration of the concept behind oversampling. The right hand side of the figure shows two simulated data sets (red and blue) for which the mean value differs (e.g. as a result of an asymmetry), as a function of sample time. The left hand side shows the samples accumulated by the ADC in histogram form, where the bin width of the histogram is synonymous with the resolution of the corresponding ADC. The difference is again shown in red and blue, with the darker region being the overlap of the two distributions. The difference in the mean for the two signals is* $20\ \mathrm{mV}$*, while the bin width (ADC resolution) is* $25\ \mathrm{mV}$*, but the oversampling, together with the large RMS width in the signal, allows a high precision difference measurement within each helicity window.*

**QWeak Preamplifiers** Figure 66 shows one of the preamplifiers built for the main detectors of the Qweak experiment. The main features are:

- Gain: $\mathrm{V}_{out}/\mathrm{I}_{in}$ = 0.5, 1, 2, or 4 $M\Omega$, switch selectable.
- Output: $\pm 10$ volts. Adjustable $\pm 2$ V offset. Drives 130 m RG-213 cable.
- Input: current limit set by gain and 10 volt output limit.
- Power: +5 VDC on Lemo connector.
- Bandwidth: $\mathrm{f}_{3db} = 26$ kHz.
- Noise: 0.5 $\mu V/\sqrt{\mathrm{Hz}}$ referred to output with 1 M$\Omega$ gain setting. (Amplifier noise specification assumes the input capacitance of 5 m of RG-62.)
- Packaging: two channels per 80 mm x 70 mm x 28 mm box.

**The QWeak Integrating ADC** Figure 67 shows a TRIUMF digital integrator built for the Qweak experiment. The module has 8 channels in a single width VME module. The main features are:

- Trigger: external NIM signal or internal trigger selectable.
- Integration time: selected as a number of samples, up to 1/30 second.
- Sample rate: selectable up to 800 ksps. 18-bit ADCs.
- Clock: internal 20 MHz or external NIM selectable.

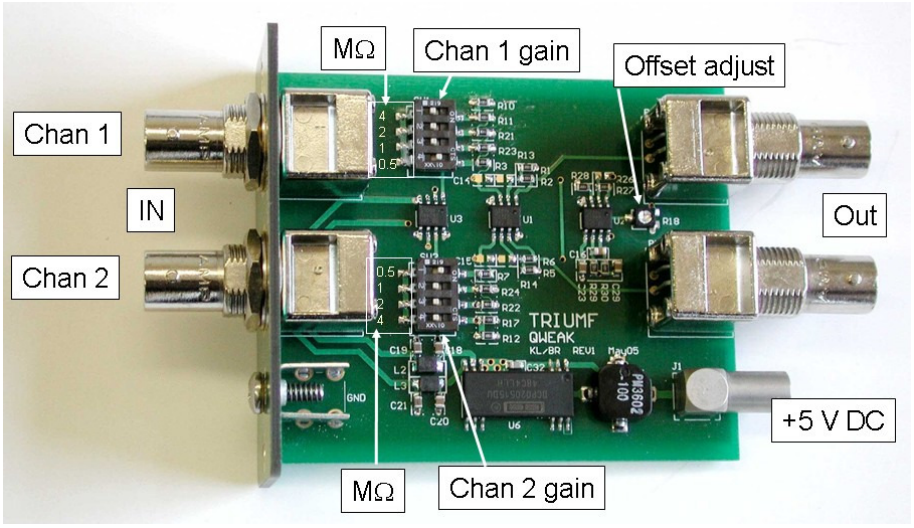


Figure 66: *TRIUMF current-to-voltage preamplifier for the Qweak experiment.*

- Input: $\pm 10$ volts. High impedance quasi-differential.
- Output: 32 bit sum. The integration period may be sub-divided into up to four blocks. No dead time between blocks.
- Anti-aliasing: 5-pole filter with 50 kHz cutoff.

Table 22: *Comparison of various sources of noise. "Beam on" shot noise is equivalent to counting statistics. The electronic noise is based on tests with TRIUMF electronics built for the Qweak experiment. The electronic noise alone is negligible compared to counting statistics. A null test with a noiseless battery could be made to* $\leq 10^{-9}$ *(one ppb) in a day.*

| Type of Noise | charge quantization (e) | Spectral density $\mu V/\sqrt{Hz}$ | RMS Noise in 500 Hz BW (1 ms integral) | RMS Noise in 50 KHz BW (VME input) |
|---|---|---|---|---|
| "beam on" shot | 6800 | 114 | 2560 $\mu V$ | 25,600 $\mu V$ |
| LED test shot | 680 | 36 | 800 $\mu V$ | 8,000 $\mu V$ |
| battery test shot | 1 | 1.4 | 31 $\mu V$ | 310 $\mu V$ |
| preamp | | 0.5 | 11 $\mu V$ | 110 $\mu V$ |
| digital integrator | | 1.3 | 29 $\mu V$ | 290 $\mu V$ |

**QWeak Performance** Table 22 shows that based on reasonable assumptions about the main detector signals of the Møller experiment, the Qweak electronics provide a suitable starting point for the MOLLER design. Noise in the table is referred to the preamp output. The total electronic noise is negligible compared to counting statistics. A null-asymmetry test with a battery-driven current source could be made in one shift at the part per billion level, or 0.1 ppb in 30 days.

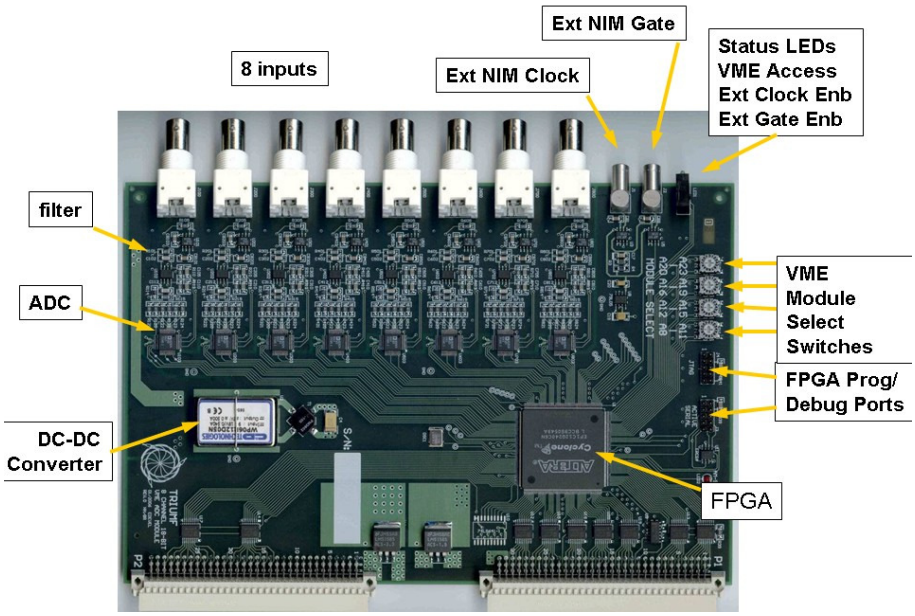


Figure 67: *TRIUMF VME-based digital integrator for the Qweak experiment.*

**MOLLER Preamplifier and ADC Design Changes** The integrating electronics development and manufacture has now been adopted as a TRIUMF project and the general design choices have been established in several recent meetings that have taken place throughout 2016, including:

1. **Bandwidth selection:** The lower limit to the system bandwidth is the need to follow the helicity flip settling time. The goal for the settling is 10 $\mu$S and if we assume the amplifier must settle to 0.01% in that time, it will take approximately 9 time constants in a single pole system. This gives us a time constant of $\sim$ 1.1 $\mu$S which is equivalent, again in a single pole system, to a rise time of $t_r \simeq 2.4$ $\mu$S or a bandwidth of $f_{3db} = 0.35/t_r \simeq 150$ kHz. The noise equivalent bandwidth is $(\pi/2)f_{3db} \simeq 240$ kHz and a factor of 2 above that ($B \simeq 500$ kHz) allows for some component variation and monitoring of additional ringing in during the helicity transition. Suitable operational amplifiers for the preamplifiers have to be selected with this criteria in mind.

2. **ADC Sample Rate:** The needed bandwidth , above, is a factor of 10 higher than the bandwidth that was used for the QWeak experiment and requires a sampling rate of at least twice the bandwidth, but preferably higher $\geq 1$ MHz, which also removes aliasing effects.

3. **Preamplifier Gain and ADC resolution:** For an event rate of 1 GHz, a PMT gain of 1000, and about 20 photoelectrons at the cathode, per event, the average current from a single detector would be about 3.2 $\mu$A. Assuming also that the background and electronic noise contributions are negligible, eqn. 11 gives an estimated RMS width in the detector signal ($\sqrt{2Q_{i_P} I_{i_P} B}$) on the order of $0.1 - 0.3\mu A$, depending on the actual event rate, which can be as high as 5 GHz in the current design. A preamplifier gain of 1 M$\Omega$ would then produce a signal at the ADC, with a mean of 3.2 V and an RMS (standard deviation) of about 100 mV, which is quite large. The preamplifier gain should be selectable, as in the QWeak module, to allow adjustment for variations in the actual event rate and detector efficiency (the number of photoelectrons per event). Another possibility for adjustment is in the PMT gain, but with limited freedom, since the gain range is restricted by PMT linearity considerations. An 18 bit

ADC with a full scale voltage range of $V_{fs} = \pm 10$ V has a resolution of $10\ \mathrm{V}/2^{17} = 0.076\ \mathrm{mV}$, which means that a signal with an RMS width of $100\ \mathrm{mV}$ would be spread over more than 1300 ADC channels, which is more than enough to average out bid noise and certainly more than enough to make the digitization noise negligible. It is more important to go to higher sampling rates, than it is to go to higher bit resolution.

4. **ADC and Filtering related - Reduce ADC delay:** Decrease the $42.5\ \mu\mathrm{S}$ distortion in the signal at short gate delay (requires a fix on the analog end of the ADC ?)

5. **FPGA programming related - Block readout phase shift:** As illustrated in Fig 64, the signal readout for QWeak included the option to split the signal into four blocks of consecutive samples, for diagnostic purposes, and this capability should be retained for the MOLLER design. In addition to this, it is desirable to implement the possibility to accumulate only every nth sample in a given block, as illustrated in Fig. 68, primarily to monitor the effects of possible phase slippage between the integrating detectors and the beam monitors.

6. **FPGA programming and VME Readout related - Read out additional helicity window / block information:** The QWeak design only allowed the readout of the sample sum for each entire helicity window and the sums for the four separate blocks within each helicity window. It is desirable to implement the read out of additional information in the data stream, such as the minimum sample value, maximum sample value, and RMS of the samples in each block.

7. **FPGA programming and VME Readout related - Waveform digitization:** For diagnostic purposes, it is often desirable to obtain the discrete fast Fourier transform of the actual signal, as it is sampled by the ADC. For this to work, it is necessary to implement the possibility of reading out every ADC sample, at a lower event rate, rather than only producing integrated numbers for each helicity window. This mode basically amounts to running the ADCs as slow waveform digitizers.

8. **FPGA accumulation start and stop times:** In the Qweak modules, information about the timing of sample accumulation by the FPGA was not available, but for the purpose of commissioning, when the DAQ is being synchronized with the rest of the experiment, it would be desirable to have front panel outputs and data stream information about when exactly the FPGA starts and stops accumulating ADC samples after the helicity gate. For the same reason, it would also be desirable to implement control of the start and stop for the accumulation period.

9. **Digital data transfer mechanism:** The QWeak modules operated at a readout speed of $600\ \mu\mathrm{S}$ per helicity readout, for a maximum of 12 boards per VME crate. This is slow, and a faster readout is necessary for the new design, especially because of the higher helicity reversal rate. Possible solutions include:

    - Gigabit ethernet connections for each module with 8b/10b IBM (timestamp) encoding, UDP, or similar.
    - implement block readout
    - explore possibility to move to the newer VMS "flavor" crates/board
    - implement possibility to switch between slow and fast readout mode

10. **Front panel real estate:** Due to additional diagnostic outputs we need to go to smaller connectors/ different layout.

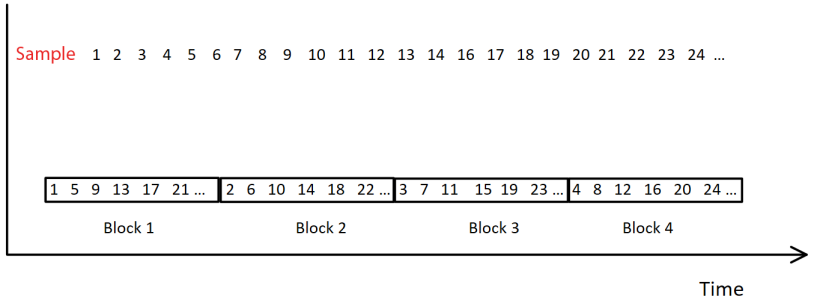


Figure 68: *Each helicity period can be separated into 4 blocks which are normally populated by samples taken in sequence. For diagnostic purposes relating to possible phase slippage in detector signals (particularly between the beam monitors and the integrating detectors), it is desirable to have only every nth sample (up to n = 4) in a given block, as illustrated in this figure.*

### 5.5.4 Mechanical Assembly

We have developed a proof-of-principle concept using a CAD program for a compact assembly of the full complement of quartz detectors and light guides. Once the light guides have been optimized with Monte Carlo simulations and benchmarked with cosmic and beam tests, the next step would be to have an engineering design of the detector assembly, which is complicated not only by the compact and dense detector array, but also the necessity to have a significant lead housing for the light detectors. This significantly increases the weight of the detector assembly and careful thought must be put into designing an assembly that can be properly aligned with respect to the rest of the apparatus. In addition, the entire assembly must be easily transportable in order to facilitate placement slightly beyond crane coverage in the Hall, and to reduce the turnaround time between interleaved projects.

### 5.5.5 Shower-Max Detectors

To guide the design process, an optical Geant4 simulation framework has been developed for the shower-max detector. Preliminary simulation studies have been performed using 10, 6, and 4 layer stack configurations. Based on these studies and the desire to balance cost and performance, a 4-layer design was chosen as the "baseline" design and is shown in Fig. 69. For this design, the four layers of tungsten are each 6 mm thick, while the four layers of quartz are each 12.5 mm thick. This corresponds to a total thickness of about 7.2 $X_o$, with 6.8 $X_o$ coming from the tungsten alone. The light guide is 25 cm long (from stack to PMT) and uses an optimized funnel-mirror to direct the Ĉerenkov light to a 3 inch diameter PMT. Simulated photo-electron (PE) distributions for the baseline design are given in Fig. 70. Further simulation studies are ongoing to determine the stack configuration and light guide geometry which optimize the PE resolution. Prototype construction and beam testing are scheduled for 2017.

### 5.5.6 Pion Background

As discussed in Secs. 2.4.3 and 3.5.4, we plan to design auxiliary detectors that will measure the relative flux of pions as well as the resultant parity-violating asymmetry directly during data collection. We have a preliminary conceptual design for these measurements. A full Monte Carlo generator for pion production including those from weak hyperon decays is being developed, and will be used to carry out more accurate simulations of pion background, which will in turn be used to optimize the "pion" detector conceptual design.

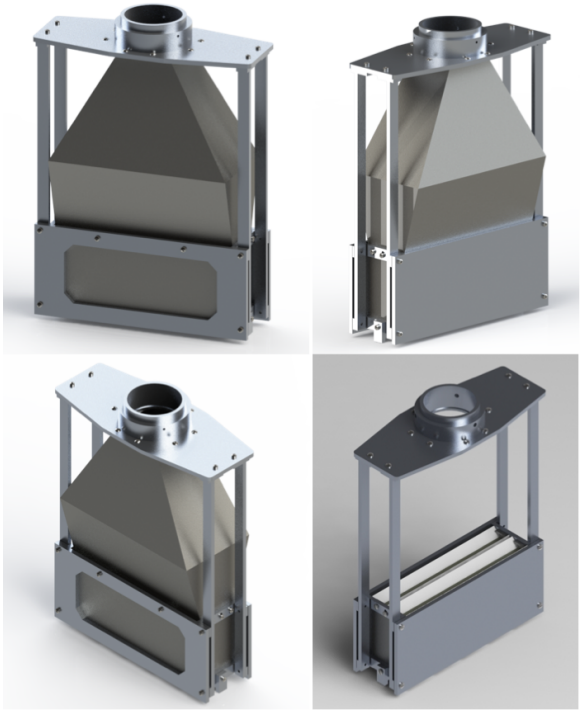

Figure 69: *CAD renders of the baseline shower-max prototype detector concept. The left two figures show the upstream face while the right two figures show the downstream end. The bottom right figure has the light guide removed to show some details of the stack.*

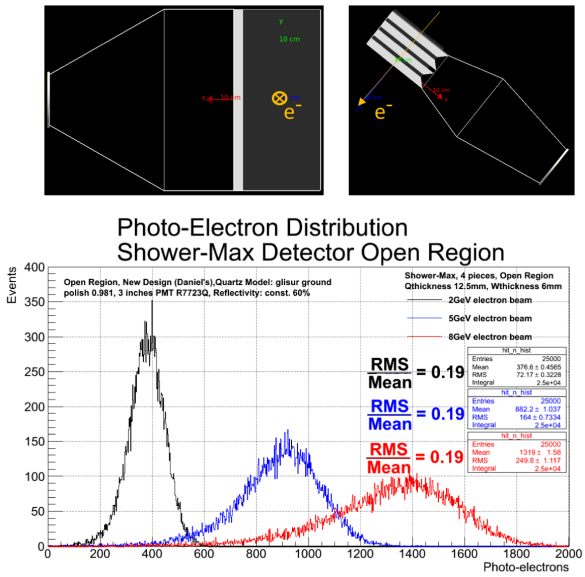


Figure 70: *G4 optical simulation results for the baseline shower-max detector. Top two figures are visualizations of the detector geometry in the simulation. Note the alternating quartz bevel design. Bottom figure shows simulated PE distributions for 2 GeV (black), 5 GeV (blue), and 8 GeV (red) electrons. These results show ample PE generation with 19% resolution for each of the energies tested.*

### 5.5.7 Alignment and Tolerances

Quantitative analysis for positioning and alignment tolerances for several subsystems as been addressed through simulations. By perturbing parameters such as target positioning, collimator apertures, and the magnetic fields, calculations of the rates and measured asymmetry provide the sensitivity on these parameters and establish tolerance limits. Due to the full azimuthal coverage and symmetry of the system, the experiment does not have particularly challenging requirements for most of these systems. The machining tolerance of the inner edge of the acceptance-defining collimator has the most stringent requirement of 200 $\mu$m.

**Target Alignment** The sensitivity of misalignments in the position of the target in z is studied via varying the target position along the nominal beam trajectory. The effect on the asymmetry was found to be less than $0.05\%$ per cm.

**Collimator Tolerance** As the collimating system is used to define the geometric acceptance of the electrons, we have studied the positioning and machining tolerances. We consider the transverse positioning of the collimators as well as changes in the inner and outer radius of their apertures. The schematic and numbering of the collimators are given in Fig. 71 and we adopt the standard Hall A right-handed coordinate system where the $z$ direction is nominally the beam direction and $y$ is against gravity. Collimator 2 is of particular importance as it is designed to be the acceptance-defining collimator.

The tolerances in the transverse alignment of collimators 2 and 4 are studied by adding small positional

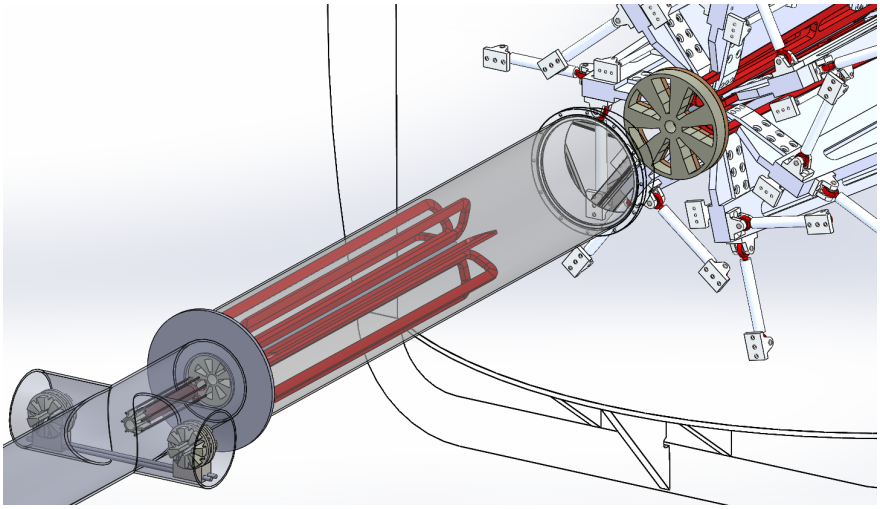

Figure 71: Overview of the collimators. Just upstream of the upstream toroids is the acceptance-defining collimator #2. Downstream of this, just upstream of the hybrid toroids is collimator #4.

| | $a$ (ppb) | $b$ (ppb/mm) | $c$ (ppb/mm$^2$) |
|---|---|---|---|
| Coll # 2, x-scan | 29.9 | $7.34\times10^{-4}$ | $3.66\times10^{-3}$ |
| Coll # 2, y-scan | 29.9 | $4.88\times10^{-4}$ | $3.98\times10^{-3}$ |
| Coll # 4, x-scan | 27.0 | $-0.58\times10^{-4}$ | $3.84\times10^{-3}$ |
| Coll # 4, x-scan | 27.0 | $1.49\times10^{-4}$ | $3.53\times10^{-3}$ |

Table 23: *Parameters of the fit equation of the form* $y = a + bx + cx^2$ *of asymmetry vs collimator position offset. The first order term* $b$ *allows for variations of* $1$ mm *with negligable perturbations.*

offsets relative to their nominal positions. The offsets are introduced independently along the transverse direction to the beam propagation direction. In all cases the dependence was found to be quadratic and the linear component to be negligably small for changes on the order of $1$ mm, Table 23.

**Collimator Apertures** The inner and outer radii of collimators 2 and 4 were varied independently within the simulation. The effects on the measured asymmetry for collimator 2 are shown in Table 24 and Fig 72. These define the machining tolerances and in particular for collimator 2, the inner radius must be machined within $200$ $\mu$m for a systematic uncertainty of 0.03 ppb on the asymmetry, or 0.1%. This is the dominant systematic.

**Magnetic Field** Changes in the magnetic field can cause changes to particle trajectory and therefore the acceptance of the quartz. A study was done by modifying a single coil position and angle and then generating a modified field map and then studying the change in measured asymmetry. Variations were done for position along the beam line, radial position, and azimuthal position. In addition rotations of a single coil about its center of mass was done about three independent axes. In all cases, the change in asymmetry was less than 0.4 ppb per cm for the position dependent cases and 0.2 ppb per degree for the rotation cases.

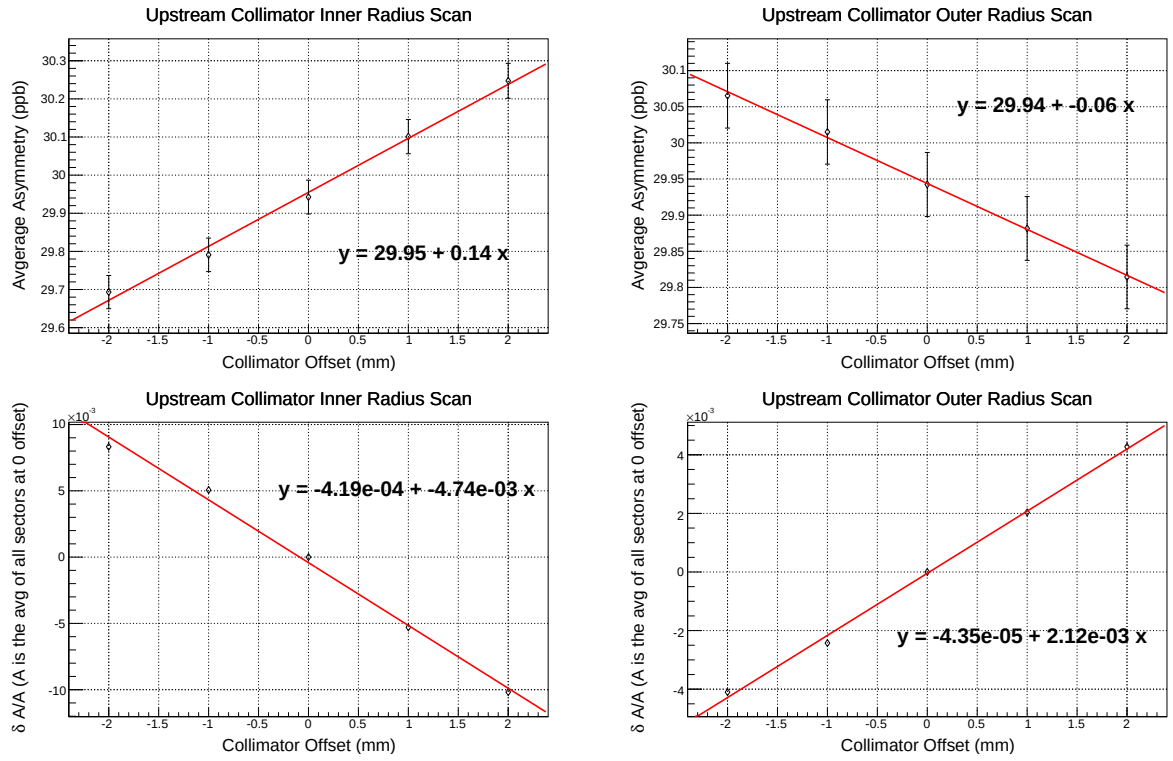


Figure 72: *Coll #2, inner/outer radii-scan*

### 5.5.8 Tracking Detectors

As described in Sec. 2.4.4, a tracking system has several critical applications to understand the apparatus and control systematic errors. The GEM technology that is being proposed is part of a significant R&D effort that is important for several other projects after the 12 GeV upgrade at JLab. MOLLER collaborators play a lead role in these initiatives. In addition, a conceptual design for the external GEM detector holders has to be developed, including the capability of remote motion of the tracking planes and a light-weight holder assembly. In the following, we provide a detailed description of design considerations and current R&D activities.

The proposed tracking system would consist of several GEM layers after the magnetic elements and immediately before the quartz. Multiple layers spaced along the beam axis provides a lever arm to reconstruct not only the positions, which we will denote with cylindrical coordinates $r$ and $\phi$, but also the directions, which we will call $r' = dr/dz$ and $\phi' = d\phi/dz$, shown in Fig. 73. These four independent variables map from the independent variables which describe the scattered particle, the lab scattering angle $\theta_{\rm lab}$, the electron momentum $p$, the lab azimuthal angle $\phi_{\rm lab}$ and the reaction vertex position $v_z$ (we neglect the $v_x$ and $v_y$ coordinates as these are known event-by-event from the raster current and represent small perturbations in the map).

**Calibration Requirements** To measure the acceptance of the apparatus, a model of the magnetic transport optics must first be obtained. Calibration of the optics over a relatively broad range can be performed by mapping out specific and identifiable points with defined polar and azimuthal angles, momentum, and target position. Using a nuclear elastic or Møller interaction with a well defined beam energy correlates the momentum and polar angle.

| Asymmetry | | |
|---|---|---|
| | $a$ (ppb) | $b$ (ppb/mm) |
| Inner-rad | 29.95 | 0.14 |
| Outer-rad | 29.94 | -0.06 |
| **Fractional change in asymmetry** | | |
| | $a$ | $b$ (1/mm) |
| Inner-rad | -4.19$\times 10^{-4}$ | -4.74$\times 10^{-3}$ |
| Outer-rad | -0.44$\times 10^{-4}$ | 2.12$\times 10^{-3}$ |

Table 24: *Parameters of the fit equation of the form $y = a + bx$ of asymmetry and fractional change in asymmetry vs inner/outer radius change of collimator 2.*

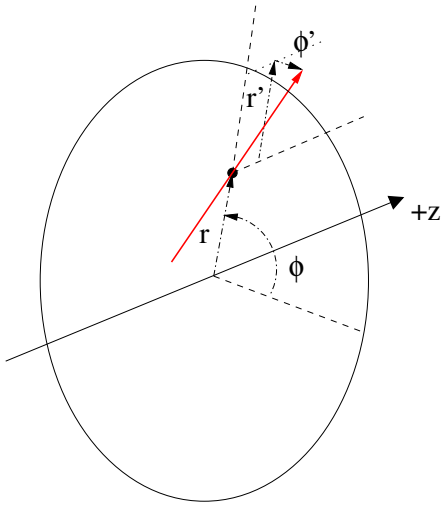


Figure 73: *Tracking coordinates system. Note that $r'$ and $\phi'$ must be taken with infintesimal change in $z$.*

With the use of foil target, known beam raster position, and a removable sieve before the magnetic elements, the remaining variables can be constrained. The sieve must be at least $\sim$ 40 $X_0$ to be able to sufficiently stop the highest energy electrons. As this sieve must be fixed relative to the acceptance-defining collimator. Absolute positioning can be done both by survey and cross-checked and adjusted by measuring and then minimizing the azimuthal modulation of rates resulting from a small transverse displacement of the acceptance defining collimator.

Figure 74 shows the amplitude of the rate modulation as a function of the collimator displacement. An array of scintillator pairs immediately behind the quartz will allow for counting mode operation with well-defined relative azimuthal efficiency. Assuming a modulation amplitude measurement to an accuracy of 2% of the average rate per sector, the positioning of the collimator can be determined to an accuracy $\sim$ 1 mm. The impact of the residual uncertainty of 1 mm on the transverse position of the acceptance-defining collimator will be less than 1% on the average analyzing power variable $\langle \mathcal{A} \rangle$, and thus negligible. Nevertheless, knowing the value of this shift is important for constraining other systematics, such as parity conserving asymmetries and helicity-correlated beam trajectory differences which could produce their own azimuthal modulations in the observed detector asymmetries.

By having a map of ($\theta_{\rm lab}$, $p$, $\phi_{\rm lab}$, $v_z$) $\rightarrow$ ($r$, $\phi$, $r'$, $\phi'$) at specific points and if this map is one-to-one, the

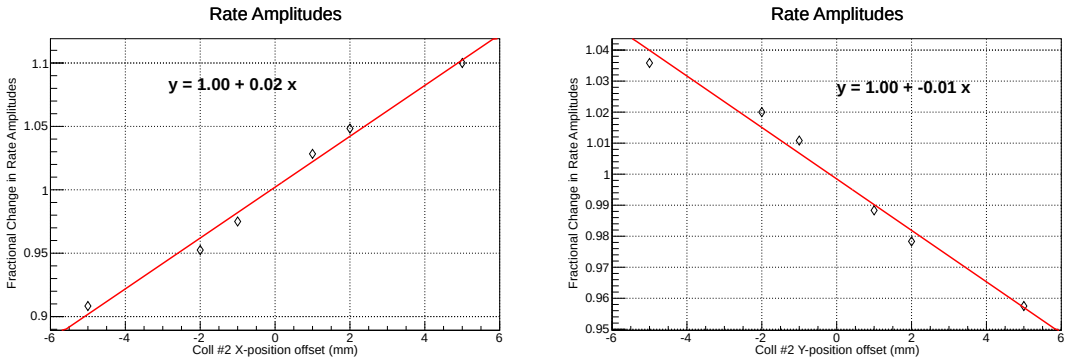


Figure 74: *A misplacement of the acceptance-defining collimator transverse to the beam produces a small azimuthal modulation in rate of about 2-3%/mm.*

problem of optics reduces to interpolating between these points. The propagated uncertainty on $\langle \mathcal{A} \rangle$ is then dependent on the number of calibration points and the functional form of the acceptance used. The form of the acceptance must rely upon simulations and perturbations on various positioning and magnetic fields which can then be used for a maximum likelihood fit. This is also critical to take into account higher order effects such as beam raster, multiple scattering, and radiative effects.

While direct measurement of the Møller acceptance over the full region of phase space is possible, this may prove to be unnecessary. There is a natural kinematic relation between the Møller-scattered, and elastic $e-p$ scattered events; see Fig. 75. By comparing the form of the $e-p$ elastic events to various simulation position and field scenarios, in addition to directly measured acceptance points and the Møller optics, additional confidence can be built in the acceptance function. Based on Monte Carlo simulations using simple models of the acceptance, such as splines which contain no actual physics or geometrical information, differences between the average analyzing power variable through various methods and the "true" value were found to be $\lesssim 0.5\%$, Fig. 76. A non-uniform spacing based on Chebyshev polynomial nodes provides a highly efficient method for numerically approximating aribtrary polynomials of a given order and would likely provide an optimal solution given the boundaries of the problem.

To obtain the relative Møller acceptance at individual points in $\theta_{\rm lab}$, which is directly related to the free variable $\theta$ in Eqn. 5, the first step is to measure judiciously chosen narrow angle bites of Møller-scattered events at the $11$ GeV beam energy. A fixed sieve where each of six sectors samples a pair of different angles is proposed, which relies on the symmetry of the magnetic field sectors. One sector will be covered by the sum of all 12 slits as a check of the symmetry. To maximize $\phi$ coverage (which is desirable to see edge effects of the phi acceptance), fixed $\phi$ coordinates can be obtained by blocking small sections through constant $\theta$ "slots".

Calibration runs at special incident beam energies of $4.4$, $6.6$ and $8.8$ GeV will help to map out variations in the momentum acceptance which must be folded in to account for radiative effects. To make relative relationships between different energies, the angles must be placed where 11 GeV Møller-scattered momenta would coincide with nuclear-elastically scattered (equivalently, the incident beam) momenta i.e. $\theta \sim 12$ and $8$ mrad respectively for $4.4$ and $6.6$ GeV.

A separation between the top row points in Fig 77 is all that is required by the GEMs for this task, meaning a few mm resolution in position with a GEM spacing of a few meters (to guarantee a resolution of $r' \sim 10^{-3}$).

Kinematically at these angles, elastic scattering from even light nuclear targets have very small recoil energies, providing scattered electrons which are practically mono-energetic. This is fortunate, because as

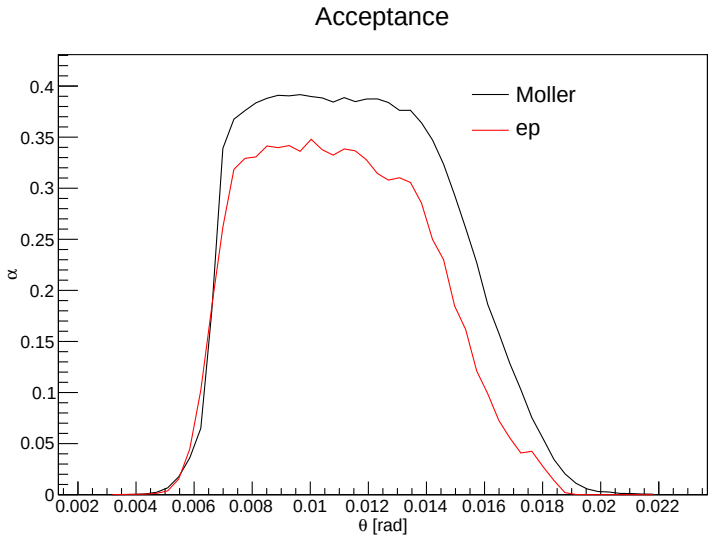


Figure 75: *Acceptance of Møller and elastic events, scaled arbitrarily, and ignoring radiative effects.*

$Z$ increases, the nuclear cross section increases as $Z^2$, whereas the Møller cross section increases as $Z$ (the bound number of electrons). A set of low-$Z$ target foils, such as $^{12}$C, will be used for the calibration runs.

**Tracking Detector Requirements** The tracking system will consist of 4 GEM planes, located downstream of the two magnets, and upstream of the main integrating quartz detectors. The primary requirement for the acceptance is to be able to separate between events from different sieve holes when we use a staggered-hole configuration. Based on Fig. 77, this can be fulfilled with $1$ mm spatial and $1$ mrad angular resolution.

As discussed above, the GEM planes will be placed in two sets of pairs in rotatable wheel assemblies, as shown in Fig. 24. The GEM planes must be insertable to intercept the charge particle flux after they exit the vacuum window, but must be out of the way during the collection of production data. In order to reduce costs, we propose to cover four septants and have them attached to a remotely controlled "wheel" with the ability to rotate in the azimuth up to one septant, providing full and redundant coverage.

The present design of GEM chambers to be used in future experiments at Jefferson Lab have roughly a $0.5\%$ radiation length for electrons incident normal to the plane. Using the standard multiple scattering formula for the central 98% of the scattered distribution of ultra-relativistic particles, the lowest momentum electrons of interest ($\sim 2$ GeV), and $x/X_0 = 2 \times 0.5\%$ for the two upstream foils, this corresponds to $\delta\theta$ of about $0.4$ mrad. This is the limiting factor on the angular resolution in the GEMs, but is still sufficient to separate the staggered peaks in the acceptance calibration.

**GEM Detectors in Simulation** Within the simulation, placeholder GEM detectors, each composed entirely of vacuum but capable of recording hits, is currently implemented in the simulation package developed for this experiment presented in Sec. 2.7. A total of 4 GEM detectors are represented within the simulation. The GEM detectors are located along the beam propagation axis in two sets of pairs. Each pair consists of GEM detectors separated by 1 m. The two pairs are separated by 4 m. Their nominal locations in simulation are 22.6, 23.6, 27.0 and 28.0 m respectively from the center of the target. (The quartz detectors are located at 28.7 m). The Monte Carlo hits recorded by the GEM detectors, $r_{\rm MC}$, $\phi_{\rm MC}$, $r'_{\rm MC}$ and $\phi'_{\rm MC}$, are used to generate "reconstructed" track variables, $r_{\rm rec}$, $\phi_{\rm rec}$, $r'_{\rm rec}$ and $\phi'_{\rm rec}$. This is done via $\chi^2$-minimization of the straight line fit through coordinates defined by $r_{\rm MC}$, $\phi_{\rm MC}$, $r'_{\rm MC}$ and $\phi'_{\rm MC}$ for each track.

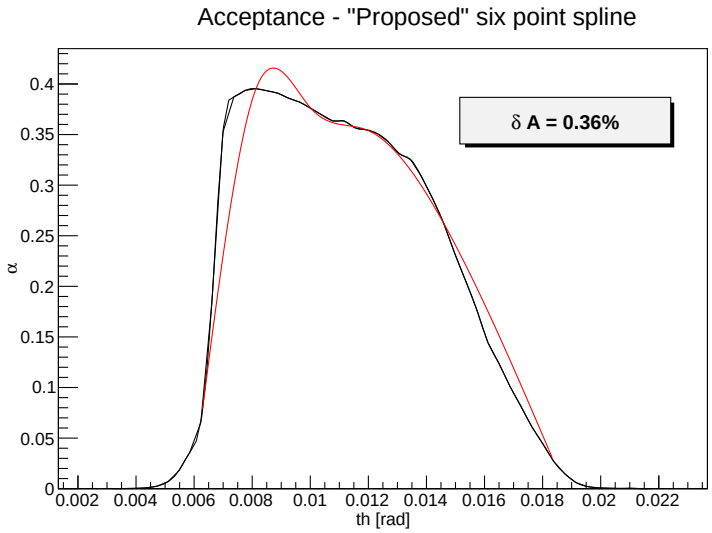


Figure 76: *Acceptance determination of Møller events based on fitting to a 6-point spline at evenly spaced fixed points. A 0.4% difference from the true acceptance is observed despite such a crude method. 12 points are proposed to be available with the sieve.*

**GEM Detector Sizes** The GEM detector sizes depend on their location along the beam propagation axis, with the detectors located further downstream requiring larger area in order to inercept the electrons in acceptance. Simulation is used to determied the GEM detector sizes. The GEM sizes necessary to intercept electrons in a given septant are determined by observing electrons that Møller scatter inside the target, and arrive at the quartz detectors. The 4 GEM detectors are located at their nominal positions of 22.6, 23.6, 27.0 and 28.0 m. The quartz detectors are located at 28.7 m.

Because strong $\phi$-defocusing results in electrons being swept across the septant boundaries by the time they arrive at the quartz detectors, the electrons that arrive at a particular septant at the nominal location of the quartz detectors are selected and tracked upstream through each of the GEM planes in order to determine the sizes of individual GEM planes. The GEM detector shapes determined from this study are trapezoidal, but with its parallel sides replaced by arcs of two different radii of a concentric center.

The GEM detector sizes determined via such analysis, and incremented by 5% in $r$ and 10% in $\phi$ is presented in Table 25. These are the sizes required to intercept electrons from any one particular septant. The proposed 4-septant GEM configuration is shown in Fig. 78 which would allow for the full azimuthal range to be covered through only one rotation to the neighboring septant. Precise placement around the azimuth at fixed septants, shown, and also half septants would be useful to test GEM efficiency across the face. Allowing a set of GEMs to have a range of motion that it can be placed across three adjacent septants would allow full cross referencing distributions in each septant by at least two GEM sets.

**GEM chamber R&D program** The University of Virginia group is currently leading an aggressive R&D program to develop large area GEM chambers for the Hall A Super Bigbite apparatus (SBS). The active area of large tracking chambers of SBS will be $60\times200$ cm$^2$. These large GEM trackers will be assembled by combining $60\times50$ cm$^2$ "chamber modules" with narrow edges. The UVa group has already constructed several $60\times50$ cm$^2$ and GEM chamber modules and is currently setting up for the production of 40 such modules for SBS. The expertise gained with these GEM modules will be applied to the design of GEM modules for SoLID.

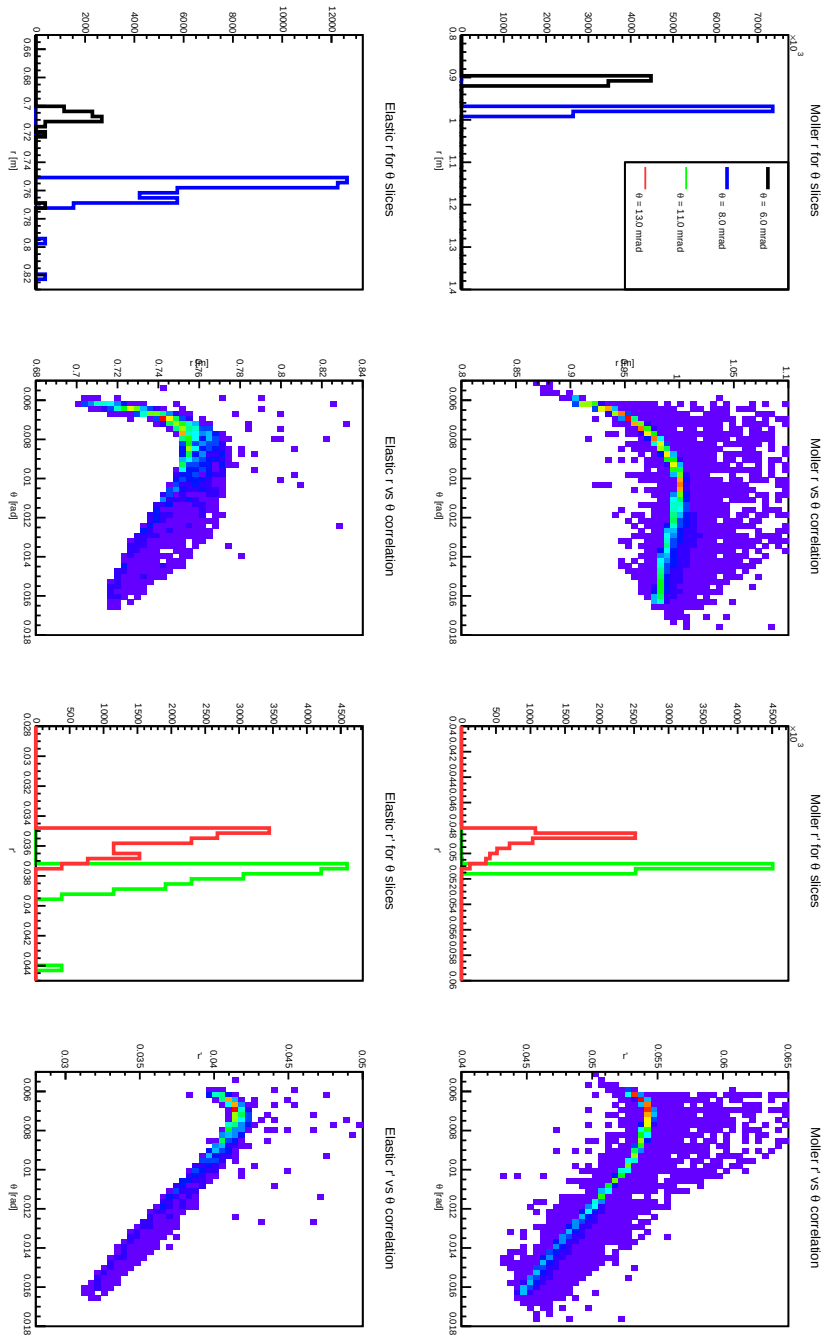


Figure 77: *The general properties of the optics reconstruction. Shown in the 1D histograms are the radius $r$ and tangent $r' = dr/dz$ for Moller (top row) and elastic (bottom row) events for two 0.2 mrad slices in $\theta$ each. Raster effects are suppressed and only thin foil target is considered. The separation between Moller events, as well as the elastic events, is clear at the* mrad *level. Small angles ($\theta_{\rm lab} < 10$ mrad) may be reconstructed with the variable $r$ while for larger angles, $r'$ can be used and is practically linear. There is a small $\phi$ dependence and a sector dependence which has been averaged over for simplicity.*

| | z(m) | Inner rad(m) | Outer rad(m) | $\pm\phi$(deg) | Area ($m^2$) |
|---|---|---|---|---|---|
| GEM #1 | 22.64 | 0.45 | 0.88 | 31.1 | 0.31 |
| GEM #2 | 23.64 | 0.49 | 0.93 | 30.5 | 0.33 |
| GEM #3 | 27.00 | 0.61 | 1.11 | 29.4 | 0.44 |
| GEM #4 | 28.00 | 0.65 | 1.17 | 29.4 | 0.49 |

Table 25: *GEM detector sizes needed to intercept electrons incident on the quartz detector of a given septant.*

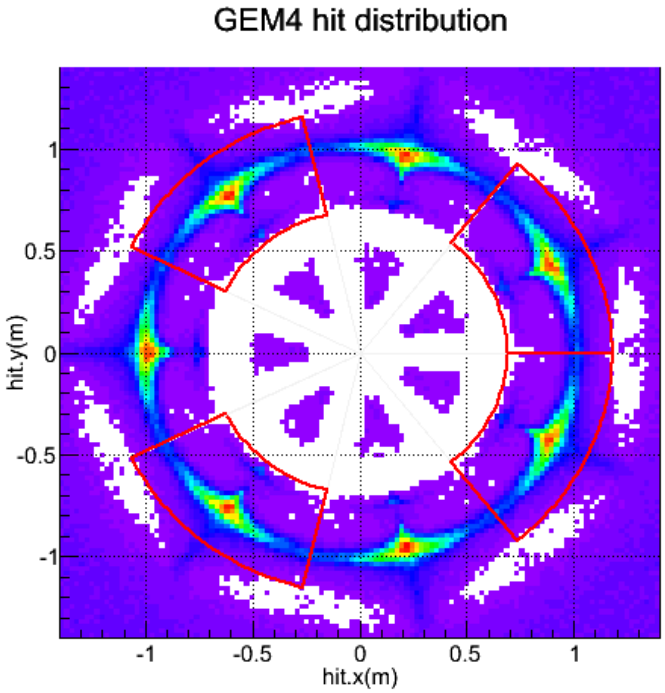


Figure 78: *The proposed GEM configuration that covers four septants. Such a configuration allows full azimuthal coverage through only one septant rotation.*

The UVa group operates a well-equipped GEM R&D facility that includes the following:

- **UVa Detector development lab:** This $10\times10$ m$^2$, well-equipped nuclear physics detector lab has been used for the development, construction and testing of many large detector systems. The detector lab consists of two $3 \times 3$ m$^2$ level 1,000 clean rooms located within a $4 \times 10$ m$^2$ semi-clean area. So far ten large area GEM chambers have been sucessfully constructed in this clean room. The specialized GEM construction equipment in the lab includes large area GEM foil stretchers, GEM foil testing high-voltage boxes, a large volume ultra-sonic cleaner for GEM frame cleaning, a Keithley 6485 picoammeter for GEM foil testing, and a GEM foil storage dry $N_2$ box.

- **GEM readout systems based on APV25-S1 electronics:** The UVa group has two APV25 based readout systems: a 10,000 channel SRS system from CERN and a 3,500 channel system developed by the INFN group. Both systems are fully operational and are used for testing prototype GEM chambers.

- **Wiener-Iseg multi-channel high voltage system** The UVa detector group owns a brand new Wiener-

Iseg multi-channel high voltage system that is especially suited to provide high voltage to sensitive tracking chambers. This system currently has 24 channels and can be expanded to 160 channels.

## 5.6 Polarimetry

### 5.6.1 Compton Polarimetry

The Compton polarimeter upgrade involves physicists from a number of collaborating institutions with prior experience with Compton polarimetry and laser development. This cohort has the necessary experience to push precision to the level of 0.4% through research and study, in preparation for and during the MOLLER experiment.

It is essential that the upgraded laser system support a 0.2% measurement of the photon polarization. Recent results from the Hall C Compton polarimeter have demonstrated this level of precision on the laser polarization using back-reflected light to tune the cavity polarization [89, 90]. This technique is now implemented in the Hall A laser system, and additional studies are planned to further refine and test the precision of this technique.

Simulations will continue for both the electron and photon systems to better refine analysis technique, and to understand possible systematic errors due to detector response, deadtime, pileup, or calibration errors. Beyond the requirement for an upgraded electron detector to achieve large acceptance and improved efficiency, the hardware of the Compton polarimeter is expected to be sufficient to reach high precision.

**Electron Detector Upgrade** The upgrade for the electron detector in the Hall A polarimeter is still under study. The previous detector was based on silicon microstrips, but had decayed with age and was replaced in 2009. The new detector system suffers from high noise and poor efficiency. If the existing readout electronics are shown to be capable of high efficiency and low noise with an increased thickness of the silicon plane, then the likely upgrade path will simply increase the detector thickness and size. If the existing Hall A electronics are not sufficient, the QWAD electronics developed to readout the Hall C Compton diamond microstrip detectors will be tried with the silicon microstrip detectors. Incorporating those electronics would require a more significant redesign of the vacuum chamber to accommodate the signal feedthrough.

Another option currently being explored is a detector based on HVMAPS technology [94] being developed for use in ATLAS, Mu3e, P2, and PANDA. These are radiation hard silicon pixel detectors, with CMOS technology used to embed readout electronics directly in the pixel. Discrimination is performed at the periphery of the detector, providing a robust signal, high efficiency, and low noise. Readout into an FPGA module allows rapid data processing. Such a system is expected to meet the requirements for radiation hardness and readout speed, and may also be cost-competitive with a silicon microstrip upgrade. A decision on which upgrade technology to pursue is expected by mid-2017.

**Control of Synchroton Radiation** At 11 GeV, significant synchrotron radiation is emitted when the electron beam is bent in a magnetic field. The total radiated power rises as $\beta^4$ for the same bend radius. At 11 GeV, this radiation load will be a significant background in the photon detector and may overwhelm the signal from Compton scattering. This was not a significant problem at lower energies, and the upgrade to 11 GeV operation required modifications to mitigate the effects of this sychrotron radiation on the electron and photon detectors.

The photon detector is illuminated by radiation from the exit of dipole 2, and the entrance of dipole 3. A few millimeters of led can be used to reduce the power of synchroton radiation, but this must be kept thin to avoid excessive distortion of the scattered photon spectrum and expected analyzing power. Figure 79 shows the energy spectrum of synchrotron light attenuated by lead shielding between 1–5 mm thick, depending on the beam energy. On the left, the spectrum for 11 GeV with unmodified magnets is compared to calculations

for the recent runs of HAPPEX-III (3 GeV) and PV-DIS (6 GeV). On the right, the energy spectrum ("Fringe 2") is shown when iron extensions, 15 cm in length, are added to the dipole magnets in order to provide an extended region of reduced field. This reduced magnetic field produces synchrotron light with lower energy range and with reduced intensity, for the portion of the electron beam trajectory that projects to the photon detector. With this modification, the bending strength of the magnet remains the same but the synchrotron light radiated into the detector is reduced by a factor of $10^4$, to a level comparable to HAPPEX-III. The magnetic field extensions were modeled using TOSCA [91]. In addition, a remotely movable collimator was placed before the photon detector, to restrict the detector acceptance for synch light to the region of reduced intensity and energy.

Initial studies with these magnet yoke extensions at 11 GeV showed that the synchrotron light, which could be ∼20 times as large as the scattered Compton signal, could be reduced by more than a factor of 10. There is an apparent mis-installation of these yoke extensions, so the system is not yet taking full advantage of the reduced bending field in line with the photon detector. When fully implemented, synchroton radiation in the photon detector will no longer be a significant problem.

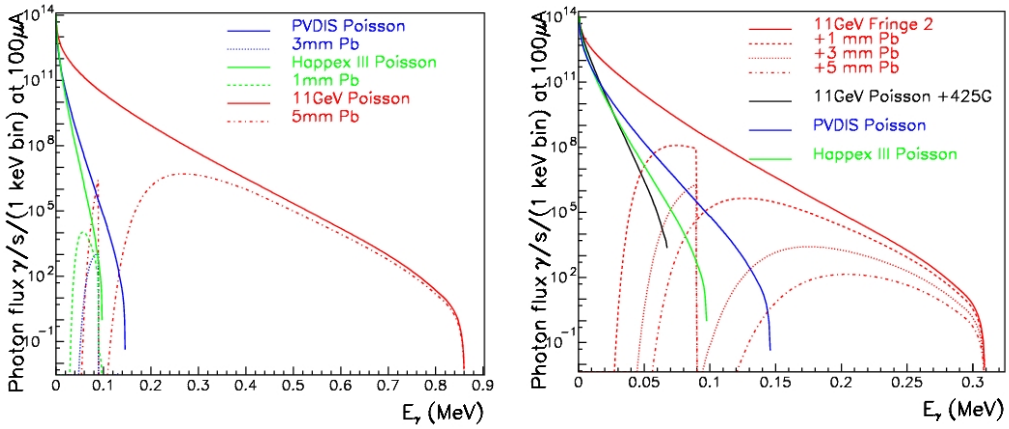


Figure 79: *Energy spectrum of synchrotron radiation penetrating lead shielding of thickness listed. Plot on left shows unmodified chicane magnets, plot on right shows energy spectrum for proposed magnetic shims which reduce the field for the bend radiating into the Compton photon detector acceptance. Note the different horizontal scales between the plots.*

The electron detector is not directly illuminated by synchrotron light from the third dipole. However, the detector is illuminated by radiation from the first bending magnet, where the primary beam is originally directed into the chicane. To correct this problem, a thick insertable shield will be installed on the straight-through beam line, to absorb this radiation and protect the electron detector.

### 5.6.2 Møller Polarimetry

As described in Sec. 3.2.2 and in more detail in Sec. 2.8.2, a Møller polarimeter using a pure iron foil target in a 5 T field will be used to cross-check the Compton polarimeter measurement with an accuracy of 0.4%. This is a significant improvement over the PREX-I measurement of beam polarization at 1 GeV in Hall A, which achieved 1.1%, but comparable to the polarimetry accuracy claimed from the Hall C Møller polarimeter. An upgrade of the target actuator for the high-field Møller apparatus in Hall A is underway which will improve its operability and systematic accuracy. Simulation studies of acceptance normalization with the Hall A spectrometer system, including Levchuk corrections, are ongoing. It is anticipated that

PREX-II (nominally running in 2018) will use this upgraded polarimeter to achieve an accuracy of better than 1%, and further studies will demonstrate the feasibility of 0.4% measurement systematic accuracy.

**Simplified Møller Scattering Target Assembly** Quite a number of small, systematic effects need to be considered in order to achieve 0.5% uncertainty on the longitudinal beam polarization. For example, Figure 38 gives an idea of the tolerance needed on iron target alignment. In order to be assured of at least 99.8% of the maximum target polarization for a field of $\sim 3$ T, the tolerance on the foil angle misalignment is $\sim 1^\circ$.

In order to interpret the target polarization to high precision, it is imperative that the foil be saturated. This can be confirmed by studying the Møller scattering asymmetry as a function of applied magnetic field. The cryogenic magnet is limited to fields less than 4 T, so according to the calculation shown in Fig. 38, we need to have the target angle precise to about $1^\circ$. It would be useful to in fact confirm the behavior suggested by the figure, by making these measurements with the target arm rotated by various angles close to $90^\circ$. As described in Sec. 2.8.2, an upgrade to the target mount and actuator will enable precision studies of saturation and target misalignment.

**Møller Spectrometer Operation at 11 GeV** The Møller scattering spectrometer needs to have a well defined acceptance in the neighborhood of $\theta = 90^\circ$, so the average analyzing power can be determined to sufficient precision. One also needs to understand uncertainties due to the Levchuk effect [112, 113], which results from the most deeply bound (and unpolarized) atomic electrons having a very different momentum distribution. When the accepted scattering angle is closely tied to the electron momentum, the Levchuk effect can be quite large, as the momentum $p_e$ of K-shell electrons in iron is $\sim 100$ keV/c and the effect goes like $p_e/m$.

Simulations of the spectrometer are underway, with some results shown in Fig. 80. The spectrometer is similar to that of the pre-upgrade Hall A Møller system [55, 100], in which the Levchuk corrections are small, estimated to be $\sim 2\%$ [55]. Originally a QQQD magnetic array, a fourth quadrupole has been added to optimize operation up to 11 GeV. We are investigating optimal settings for these elements at different beam energies, but the results are already quite promising at 11 GeV, with the acceptance maximized at the peak of the analyzing power, and a well defined region for angles not quite at $90^\circ$. For coincidence detection of both electrons, we find an acceptance region approximately $85^\circ < \theta < 95^\circ$ in center of mass scattering angle, and $-25^\circ < \phi < 25^\circ$ in azimuthal angle, relative to the horizontal plane.

Recent upgrades to the segmented detector package and data acquisition electronics will enable studies of the event distributions in energy and angle, including measurements as a function of rate. From this we will determine backgrounds and dead time corrections with precisions indicated in Table 10.

The counting rate for a 1 $\mu$m iron foil and a 10 $\mu$A beam current is $\approx 5 \times 10^4$ events per second. For a nominal target polarization of 8% and beam polarization of 80%, the raw asymmetry would be $\approx 5 \times 10^{-2}$. To measure this asymmetry to 0.25% statistical precision would therefore require about half an hour of beam time. Careful run planning will be needed to meet the statistical precision required for 0.5% beam polarization monitoring.

**Target Heating Effects** Target heating is important consideration for precision Møller polarimetry using polarized iron foils. Saturation magnetization on iron is a function of temperature, and in fact all alloys lose their ferromagnetic ability completely above some critical temperature. At high currents, the heating cannot be tolerated, so polarimeter measurements must be made at much lower currents than used for parity violation running.

These effects have been studied using the Hall C target and polarimeter. Figure 81 displays the relative magnetization of a pure iron foil, measured using the Kerr effect in laser light reflected from the foil, as the foil is heated. The desire is to operate at room temperature and keep beam heating excursions to a minimum.

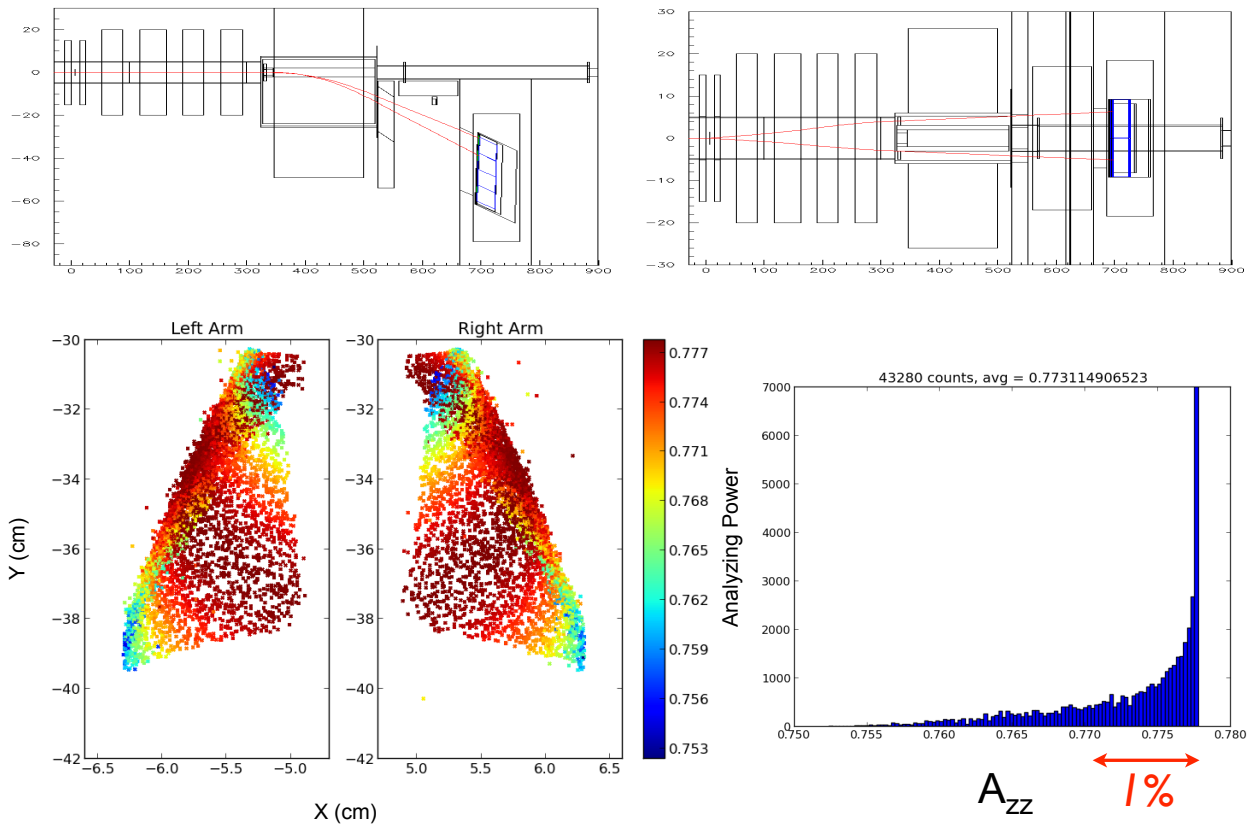


Figure 80: Simulation of the Hall A Møller polarimeter spectrometer at 11 GeV. In this QQQD design, the first two quadrupoles defocus in the horizontal plane and the second two focus before both electrons enter the dipole magnet. Two separate detector arms each detect electron. The spectrometer is optimized for center of mass scattering angle $\theta = 90°$, and the determining the effective analyzing power $\langle A_{zz} \rangle$ to a precision much smaller than 1% should be straightforward.

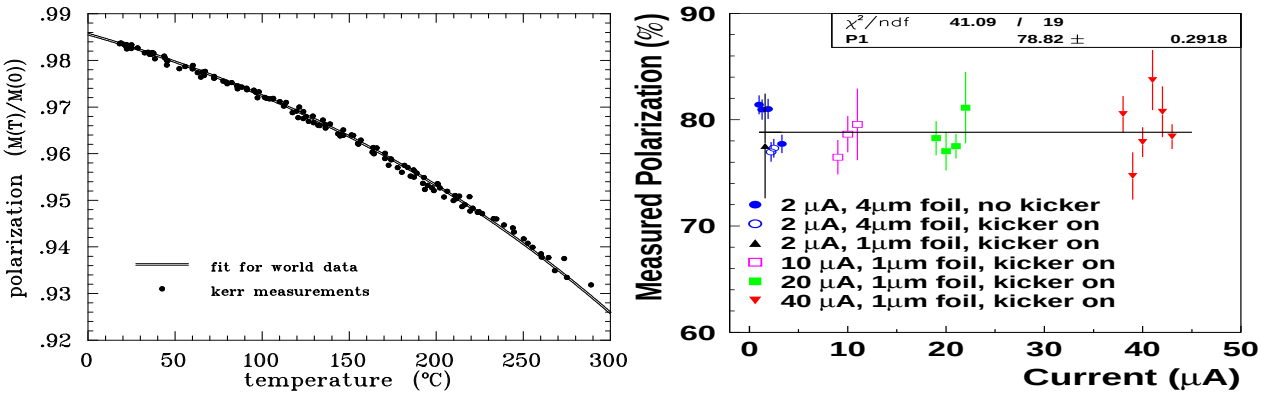


Figure 81: Measurements related to target foil heating from the Hall C/Basel group. *Left*: Relative magnetization versus temperature for a pure iron foil driven to saturation [50, 54]. The plan is to run at room temperature. *Right*: Measurements of the beam polarization at different beam currents, with and without a beam kicker to raster the beam on the foil target.

Although the direct foil measurements show several percent decrease in the magnetization for temperatures of hundreds Celsius, the beam measurements are encouraging. No clear decrease with high beam current is observed, albeit not yet at a level consistent with our precision goals.

One can attempt to mitigate foil heating effects and allow operation at higher beam current by using a fast beam kicker system combined with a thin strip or wire target. In this system, the electron beam is kicked at some low duty cycle onto or across a pure iron target. The beam is only impinging on the target for timescales on the order of $\mu$s such that the target does not have much opportunity to heat up, while the relatively long time between kicks allows the target to cool.

A series of tests have been performed in Hall C with two prototype kicker magnets and two different target configurations [114]. Initial tests were performed with 25 $\mu$m diameter iron wires replacing the iron foil at the Møller target. While these tests were moderately successful, it was found that the high instantaneous current combined with the relatively thick profile of the target lead to a high rate of random coincidences. The second generation prototype target replaced the iron wires with a 1 $\mu$m strip target, reducing the instantaneous rate.

Results from the second generation tests are also shown in Fig. 81. In this case, the duration of the beam "kick" was about 10 $\mu$s at a repetition rate between 5 and 10 kHz. Data were taken using the kicker and iron strip target up to 40 $\mu$A. In general, the results were consistent with there being no effect from target heating, albeit with relatively low precision. Problems with beam transport precluded the use of higher beam currents. Finally, it should be noted that apparent instabilities with either the source or Hall C Møller polarimeter itself (found by taking "calibration" data at 2 $\mu$A from a normal iron foil) made it difficult to conclude that target heating effects were completely avoided.

The extent to which the beam polarization at high current varies from that at lower currents is not well known. The rastered data in Fig. 81 addresses this to some extent, and no effect is evident. Another option that one can use to at least partially overcome the low current constraint imposed by the use of saturated pure iron foils is to operate the electron beam in a lower duty-cycle mode, such that the average current impinging on the target is relatively small, while the instantaneous current of a particular electron beam pulse is much larger. In particular, one can operate the polarized electron source in a so-called "beat-frequency" mode in which the source laser frequency is slightly different from that of the RF (chopper) system used to clean-up, and potentially adjust the intensity of the electron beam pulses for each hall independently. When an appropriate laser frequency is chosen, the majority of the electron pulses are out of phase with the opening of the acceptance defining slit in the chopper, and only the $N$th pulse, where $N = f_{cavity}/(f_{cavity} - f_{laser})$, is accepted.

This technique was first tested in 2006, when it was used in a variety of applications in Halls A and C [115]. A test using the Hall C Møller polarimeter was performed with the laser frequency set to 467.8125 MHz (RF cavity frequency 499 MHz) such that the nominal current of the electron beam reaching Hall C was reduced by a factor of 16 due to the loss of bunches on the aperture defining slits.

The results of the Hall C test are shown in Figure 82, where three scenarios are illustrated. The bottom plot shows the electron beam polarization as measured with the beam current being reduced using the photocathode laser power. In this case, the current from the photocathode is the same as the current arriving in Hall C. In the middle plot, high current ($\approx 60$ $\mu$A) is generated from the photocathode, but the electron beam current is reduced to a few $\mu$ A using the chopper slit. In this case, the edges of the electron beam pulse are thrown away, so one is potentially sensitive to any changes of polarization across the electron beam pulse duration. The top plot shows the polarization as measured using the beat-frequency technique. In this case, the current from the photocathode was reduced by a factor of 16, such that measurements made at an average current of $\approx 3$ $\mu$A in Hall C corresponded to a current of about 48 $\mu$A at the source. In this particular test, all measurements agreed very well, regardless of beam current, or technique used to reduce current sent to the hall.

Use of this beat-frequency mode allows measurements of the beam polarization in a mode that mimics

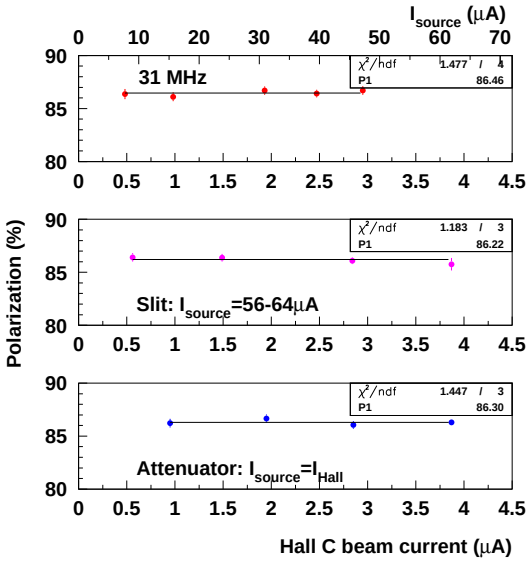


Figure 82: Results of 2006 electron source beat-frequency mode tests. The bottom plot shows the polarization measurements with the beam current controlled using the laser power directly; in the middle plot, the current was reduced using the chopper slit (high current from the photocathode); the top plot shows the current reduced using the beat-frequency technique described in the text.

high current running at the source, without any modification of the electron beam pulse itself. Use of this technique could be easily implemented for the MOLLER experiment at 11 GeV to control errors in extrapolating between Møller polarimetry measurements and the high-current MOLLER production running.

**Atomic Hydrogen Polarimetry** A separate effort will be made to develop the alternative concept of atomic hydrogen polarimetry for a continuous measurement of the JLab high intensity electron beam. A collaborative effort is in the process of being formed between the institutions interested in this project, led by MOLLER collaborators from the University of Mainz. The Institute for Nuclear Physics there has proposed a new project called MESA. It will produce up to $\sim$10 mA beams with an energy up to 200 MeV and will perform high-precision low-energy parity-violation experiments (e.g. $Q_{\rm W}^p$) as well as dark matter searches. Because of the very low beam energies, the MESA apparatus cannot use a conventional Møller polarimeter or a Compton polarimeter and will need the atomic hydrogen Møller polarimeter for sub-1% measurements. The MESA proposal has been funded, and the development of the new polarimeter concept has been launched.

It is envisioned that Mainz would become the technical lead on atomic hydrogen polarimetry, though there will be participation also from other US institutions who are part of the MOLLER collaboration. Ultimately, the Jefferson Lab target group would need to play an essential role as well. Researchers have Mainz have acquired a hydrogen cell developed some years ago by the University of Michigan. While this

cell is aged and non-functional, it is serving as a model for the construction of a prototype cell. Target cells and the electrodes for sweeping away the ions must be designed. Bench tests will be performed, and beam tests at the Mainz Microtron will be undertaken to prove that the concepts work. This practical experience and testing, along with input from refined simulations, will guide the construction of a polarimeter target for MESA and a modified target cell for JLab (should the decision be made to pursue this option).

The goal of this plan is to produce a working polarimeter based on a storage cell with 100% longitudinally electron spin-polarized hydrogen, with a thickness of at least $6 \times 10^{16}$ electrons/cm$^2$, a systematic accuracy of $\leq 0.5\%$, and that can operate in the presence of the 100 $\mu$A CEBAF beam. Once the benchmarks have all been established, the apparatus would need to be brought to Jefferson Lab for the MOLLER project. The expensive components are the solenoid and the dilution refrigerator (with its pumps), so it is presently thought that we would share these items between Mainz and Jefferson Lab. The other components of the system are relatively less expensive, and to a degree customized to the laboratory location, so they would be copied locally at each laboratory. We note that the ultimate precision of the polarimetry measurement is only required for the high-statistics Run III. Studies of the iron-foil Møller polarimeter and Compton polarimeter during Runs I and II will either confirm that polarization accuracy of 0.4% is in-hand, or else suggest the utility of this alternative, continuous polarization measurement.

# 6 Pre-Project Planning

In previous sections, we have described the MOLLER apparatus and elaborated on the technical challenges that are addressed in the conceptual design of the various subsystems. Over the past several years, as described in detail in the section on pre-R&D activities, we have carried out extensive studies in order to be able to justify and defend the technical feasibility of the proposed design to achieve the proposed statistical and systematic errors.

At the same time, we have begun to develop a detailed understanding of the steps needed to progress from the pre-conceptual design to the management structure required to design, construct, test, install and commission the various components of the experiment, if/when the Office of Nuclear Physics at DOE chooses to launch the MOLLER MIE. In this section, we build on the pre-conceptual design and define the physics requirements of the principal subsystems which will form the basis for the Level-2 structure of a potential MOLLER project. The detailed collaboration structure and the project level description of various subsystems build on the following descriptions and are captured in a separate "Pre-Project Planning" document.

**WBS 1.1: Liquid Hydrogen Target** To obtain the required $\sim 150$ GHz rate of Møller electrons between a center of mass scattering angle of $\pm 60^o$ with an incident 11 GeV beam and available beam current, more than 10 gm/cm$^2$ of target thickness is required. Liquid hydrogen ($LH_2$) is the ideal target because it provides the largest electron thickness for the least amount of radiation length. Further, using a thick $Z > 1$ nuclear target would result in beam electrons scattering off neutrons, leading to potentially large inelastic asymmetry backgrounds with poorly known electroweak couplings. The proposed $LH_2$ target is therefore specified to be 150 cm long and be capable of withstanding 5 kW from the electron beam. The target design must be also be capable of keeping relative density fluctuations well below $10^{-4}$ at the helicity flip rate of 2 kHz.

**WBS 1.2: Spectrometer** The spectrometer/collimator system downstream of the target and upstream of detectors must separate the Møller scattered electrons from backgrounds both from the target and from the surroundings over the full range of the azimuth within the avaialable space constraints in the Hall.

**WBS 1.3: Integrating Detectors** The detector system must measure the helicity asymmetry of the primary Møller-scattered electron flux of interest over the full range of the azimuth with little additional statistical degradation. Asymmetries must also be measured for electrons generated by other scattering processes in the target. Sufficient radial and azimuthal segmentation is required to unfold the various background contributions from signal. Detector response must be sufficiently linear and dead-time free, and the digitized signals must be transmitted to the data acquisition system free of any additional helicity-correlated systematic effects.

**WBS 1.4: Tracking** The tracking system must provide the diagnostic power to calibrate the primary detectors, the spectrometer optics and background processes over the full relevant radial and azimuthal ranges, and provide the capabilites of measuring the acceptance function of the primary Møller-scattered electrons so that the absolute scale of the parity-violating Møller asymmetry can be determined to better than 0.5%.

**WBS 1.5: Hall A Infrastructure and Integration** The aforementioned subsystems must be installed in the Hall within the requisite amount of positioning and alignment tolerances. Shielding must be incorporated appropriately so as to bring radiation levels in the Hall and at the site boundary to acceptable levels. Electric power and cryogenic utilities must be upgraded as required and beam diagnostic elements and polarimetry systems must be incorporated into the experimental apparatus.

**WBS 1.6: Data Acquisition** The data acquisition system must conform to JLab and industry standards and be able to operate both in counting mode for tracking runs and integration mode for the main asymmetry measurements and provide the tools for slow control and monitoring of all subsystems.

**WBS 1.7: Beam Diagnostics and Monitoring** The beam intensity and trajectory must be measured continuously with sufficient precision and accuracy to be able to make corrections to the detector response for both random and helicity-correlated jitter and the polarization flip frequency. The appropriate diagnostic tools to calibrate the detector response to beam fluctuations, and monitor target density fluctuations and false asymmetries continuously must be incorporated.

**WBS 1.8: Analysis and Data Handling** Data analysis must be carried out promptly in order to monitor data quality and beam quality to ensure sufficient systematic control and the appropriate amount of data storage to ensure redundancy and safe storage must be incorporated.

**WBS 1.9: Simulation** Progressively more sophisticated Monte Carlo simulations of the entire MOLLER apparatus will be a critical component of the experimental design and validation activities as the experiment progress from a conceptual design to construction, installation and commissioning.

**1.10: Polarized Beam** Sufficient polarized luminosity at reasonable efficiency must be made available to ensure that the data collection can be completed in the time allotted for the experiment by the Program Advisory Committee. The beam quality in terms of random and helicity-correlated jitter must conform to the requirements to achieve the proposed statistical and systematic errors.

**1.11: Polarimetry** Continuous and redundant monitors of the longitudinal beam polarization on the target are essential to achieve the proposed fractional statistical error and systematic control of the parity-violating asymmetry.

# 7 Conclusions

We have described an experimental design to measure parity-violation in electron-electron scattering to unprecedented precision using the 11 GeV electron beam in Hall A at JLab. The project represents a unique opportunity to probe physics beyond the Standard Model. The specific measurement described here would be the most sensitive low energy measurement of a flavor-conserving purely leptonic interaction at low energy and cannot be carried out in any other existing or planned facility anywhere in the world. The project would realize its full potential towards the beginning of the 2020's, which is timed well with anticipated results from high luminosity running at the LHC.

A motivated and experienced collaboration is ready to carry out the R&D, design, construction, installation, data collection and analysis. Given the evolution of related projects, the timing of the 12 GeV upgrade, and the compelling physics opportunity, we urge that the MOLLER project be given serious consideration to be reviewed to enter the Critical Decision process as promptly as possible.

# A Atomic Hydrogen Møller Polarimetry

This appendix describes the concept for a new precision Møller polarimeter.

## A.1 Potential and Prospects for a Polarized Atomic Hydrogen Target

This project has been described in detail in [116]. A summary is presented here. While this section describes a novel polarimeter scattering target which has yet to be demonstrated, R&D has started for a similar system in Mainz. That system would be used for polarimetry for high precision parity-violation experiments using an extracted beam on fixed targets at the MESA facility. The MESA facility is presently under construction, with a goal of starting the parity-violation measurements in 2018, suggesting that this development project is compatible with the schedule for the MOLLER experiment.

### A.1.1 Hydrogen Atom in Magnetic Field

The magnetic field $B_S$ and the hyperfine interaction split the ground state of hydrogen into four states with different energies. The low energy states are $|a\rangle$ = $|\downarrow\uparrow\rangle \cdot \cos\theta - |\uparrow\downarrow\rangle \cdot \sin\theta$ and $|b\rangle$=$|\downarrow\downarrow\rangle$, where the first and second (crossed) arrows in the brackets indicate the electron and proton spin projections on the magnetic field direction. As far as the electron spin is concerned, state $|b\rangle$ is pure, while state $|a\rangle$ is a superposition. The mixing angle $\theta$ depends on the magnetic field $B_S$ and temperature $T$: $tan\ 2\theta \approx 0.05\ \mathrm{T}/B_S$. At $B_S$ =8 T and $T = 0.3$ K the mixing factor is small: $\sin\theta \approx 0.003$. State $|b\rangle$ is 100% polarized. State $|a\rangle$ is polarized in the same direction as $|b\rangle$ and its polarization differs from unity by $\sim 10^{-5}$. In addition, there are high-energy states $|c\rangle$and $|d\rangle$which have the wrong polarization, but which get rapidly rejected from the field region (explained more below).

### A.1.2 Storage Cell

In a magnetic field gradient, a force $-\nabla(\vec{\mu_H} \cdot \vec{B})$, where $\mu_H$ is the atom's magnetic moment, separates the lower and the higher energy states. The lower energy states are pulled into the stronger field, while the higher energy states are repelled from the stronger field. The 0.3 K cylindrical storage cell, made usually of pure copper, is located in the bore of a superconducting ∼8 T solenoid. The polarized hydrogen, consisting of the low energy states, is confined along the cell axis by the magnetic field gradient, and laterally by the wall of the cell, as shown in Fig 83.

At the point of statistical equilibrium, the state population, $p$ follows the Boltzmann distribution:

$$p \propto \exp(\mu_e B/kT), \tag{13}$$

where $\mu_e$ is the electron's magnetic moment ($\mu_H \approx \mu_e$) and $k = k_B$ is the Boltzmann constant. The cell is mainly populated with states $|a\rangle$ and $|b\rangle$, with an admixture of states $|c\rangle$ and $|d\rangle$ of $\exp(-2\mu_e B/kT) \approx 3 \cdot 10^{-16}$. In the absence of other processes, states $|a\rangle$ and $|b\rangle$ are populated nearly equally. The gas is practically 100% polarized, a small ($\sim\ 10^{-5}$) oppositely polarized contribution comes from the $|\uparrow\downarrow\rangle$ component of state $|a\rangle$.

The atomic hydrogen density is limited mainly by the process of recombination into $H_2$ molecules (releasing ∼4.5 eV). The recombination rate is higher at lower temperatures. In gas, recombination by collisions of two atoms is kinematically forbidden but it is allowed in collisions of three atoms. On the walls, which play the role of a third body, there is no kinematic limitation for two atom recombination. At moderate gas densities only the surface recombination matters. In case of polarized atoms, the cross section for recombination is strongly suppressed, because two hydrogen atoms in the triplet electron spin state have

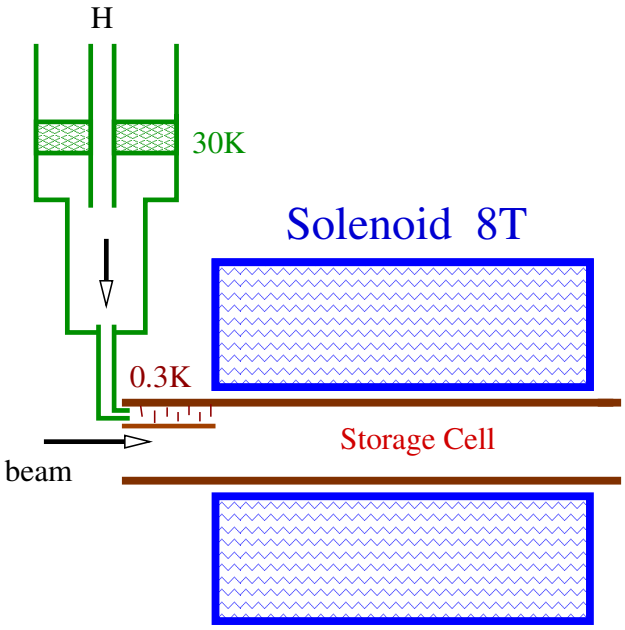


Figure 83: *A sketch of the polarized hydrogen gas storage cell, along with the holding field magnet.*

no bound states. This fact leads to the possibility of reaching relatively high gas densities for polarized atoms in the traps.

A way to reduce the surface recombination on the walls of the storage cell is coating them with a thin film ($\sim$50 nm) of superfluid $^4$He. The helium film has a very small sticking coefficient[4] for hydrogen atoms.In contrast, hydrogen molecules in thermal equilibrium with the film are absorbed after a few collisions and are frozen in clusters on the metal surface of the trap [117].

The higher energy states are repelled from the storage cell by the magnetic field gradient and leave the cell. Outside of the helium-covered cell, the atoms promptly recombine on surfaces into hydrogen molecules which are either pumped away or are frozen on the walls. Some of the higher energy states recombine within the cell and the molecules eventually are either frozen on the helium-coated wall, or leave the cell by diffusion.

The cell is filled with atomic hydrogen from an RF dissociator. Hydrogen, at 80 K, passes through a Teflon[5] pipe to a nozzle, which is kept at $\sim$30 K. From the nozzle hydrogen enters into a system of helium-coated baffles, where it is cooled down to $\sim$0.3 K. At 30 K and above, the recombination is suppressed because of the high temperature, while at 0.3 K it is suppressed by helium coating. In the input flow, the atoms and molecules are mixed in comparable amounts, but most of the molecules are frozen out in the baffles and do not enter the cell.

The gas arrives at the region of a strong field gradient, which separates very efficiently the lower and higher atomic energy states, therefore a constant feeding of the cell does not affect the average electron polarization. This technique was first successfully applied in 1980 [118], and later a density[6] as high as $3 \cdot 10^{17}$ atoms/cm$^3$ was achieved [119] in a small volume. So far, the storage cell itself has not been put in a high-intensity particle beam.

For the project being discussed a normal storage cell design can be used, with the beam passing along the

[4]The sticking coefficient defines the atom's adsorption probability per a collision with a surface.

[5]Teflon has a relatively small sticking coefficient for hydrogen atoms.

[6]This parameter is called concentration, but we will use the word density in the text; mass of the gas is not important here.

solenoid axis (Fig. 83). The double walls of the cylindrical copper cell form a dilution refrigerator mixing chamber. The cell is connected to the beam pipe with no separating windows. The tentative cell parameters are (similar to a working cell [120]): solenoid maximum field of $B_S = 8$ T , solenoid length of $L_S = 30$ cm, cell internal radius of $r_\circ = 2$ cm, cell length of $L_C = 35$ cm and temperature of $T = 0.3$ K. The effective length of such a target is about 20 cm. For the guideline, we will consider a gas density of $3 \cdot 10^{15}$ cm$^{-3}$, obtained experimentally [121], for a similar design.

### A.1.3 Gas Properties

Important parameters of the target gas are the diffusion speed. At 300 mK the RMS speed of the atoms is ∼80 m/s. For these studies we used a calculated value [122] of the hydrogen atoms cross section $\sigma = 42.3 \cdot 10^{-16}$ cm$^2$, ignoring the difference between the spin triplet and singlet cross sections. This provided the mean free path $\ell = 0.57$ mm at density of $3 \cdot 10^{15}$ cm$^{-3}$.

The average time, $\tau_d$ for a "low field seeking" atom to travel to the edge of the cell, assuming its starting point is distributed according to the gas density, is[7]: $\tau_d \approx 0.7$ s. This is the cleaning time for an atom with opposite electron spin, should it emerge in the cell and if it does not recombine before. The escape time depends on the initial position of the atom, going from $\sim 1$ s at $z = 0$ to 0.1 s at $z = 8$ cm. The average wall collision time is about 0.5 ms.

### A.1.4 Gas Lifetime in the Cell

For the moment we consider the gas behavior with no beam passing through it. Several processes lead to losses of hydrogen atoms from the cell: thermal escape through the magnetic field gradient, recombination in the volume of gas and recombination on the surface of the cell. The volume recombination can be neglected up to densities of $\sim 10^{17}$ cm$^{-3}$ [119].

The dominant process, limiting the gas density, is the surface recombination. In order to keep the gas density constant the losses have to be compensated by constantly feeding the cell with atomic hydrogen. Our calculations, based on the theory of such cells [119], show, that a very moderate feed rate of $\Phi \sim 1 \cdot 10^{15}$ atoms/s would provide a gas density of $7 \cdot 10^{15}$ cm$^{-3}$.

This can be compared with the measurement [121] of $3 \cdot 10^{15}$ cm$^{-3}$. The average lifetime of a "high field seeking" atom in the cell is ∼1 h.

### A.1.5 Unpolarized Contamination

The most important sources of unpolarized contamination in the target gas in absence of beam are:

1) hydrogen molecules: $\sim 10^{-5}$;

2) high energy atomic states $|c\rangle$ and $|d\rangle$: $\sim 10^{-5}$;

3) excited atomic states $< 10^{-10}$;

4) other gasses, like helium and the residual gas in the cell: $\sim 10^{-3}$

The contributions 1)-3) are present when the cell is filled with hydrogen. They are difficult to measure directly and we have to rely on calculations. Nevertheless, the behavior of such storage cells has been extensively studied and is well understood [119]. The general parameters, like the gas lifetime, or the gas density are predicted with an accuracy better than a factor of 3. The estimates 1)-3) are about 100 times below the level of contamination of about 0.1% which may become important for polarimetry. In contrast,

[7] This time was estimated using simulation, taking into account the gas density distribution along $z$ and the repelling force in the magnetic field gradient.

the contribution 4) can be easily measured with beam by taking an empty target measurement. Atomic hydrogen can be completely removed from the cell by heating a small bolometer inside the cell, which would remove the helium coating on this element, and catalyze a fast recombination of hydrogen on its surface. However, it is important to keep this contamination below several percent in order to reduce the systematic error associated with the background subtraction.

### A.1.6 Beam Impact on Storage Cell

We have considered various impacts the $\mathcal{I}_b = 100$ $\mu$A CEBAF beam can inflict on the storage cell [116]. The beam consists of short bunches with $\tau = \sigma_T \approx 0.5$ ps at a $\mathcal{F} = 499$ MHz repetition rate. The beam spot has a size of about $\sigma_X \approx \sigma_Y \sim 0.1$ mm. The most important depolarization effects we found are:

A) gas depolarization by the RF electromagnetic radiation of the beam: $\sim 3 \cdot 10^{-5}$;

B) contamination from free electrons and ions: $\sim 10^{-5}$;

C) gas excitation and depolarization by the ionization losses: $\sim 10^{-5}$;

D) gas heating by ionization losses: $\sim 10^{-10}$ depolarization and a $\sim$30% density reduction.

The effects A) and B) are described below.

### A.1.7 Beam RF Generated Depolarization

The electromagnetic field of the beam has a circular magnetic field component, which couples to the $|a\rangle \rightarrow |d\rangle$ and $|b\rangle \rightarrow |c\rangle$ transitions. The transition frequency depends on the value of the local magnetic field in the solenoid and for the bulk of the gas ranges from 215 to 225 GHz. The spectral density function of the magnetic field can be presented in the form of Fourier series with the characteristic frequency of $\omega_\circ = 2\pi\mathcal{F}$. The Fourier coefficients are basically the Fourier transforms of the magnetic field created by a single bunch. The bunch length is short in comparison with the typical transition frequency ($\omega_{trans}\tau \sim 0.1$). The resonance lines of the spectrum (a reflection of the 499 MHz repetition rate) populate densely the transition range (see Fig. 84). The induced transition rate depends on the gas density at a given transition frequency. This rate was calculated taking into account the beam parameters and the field map of a realistic solenoid. Provided that the field of the solenoid is fine tuned to avoid the transition resonances for the bulk of the gas in the cell (see Fig. 84), the depolarization described has the following features:

– the transition rate is proportional to $\mathcal{I}_b^2$;

– the average rate of each of the two transitions is about $0.5 \cdot 10^{-4}$ of the target density per second;

– at the center around the beam the full transition rate is about 6% of the density per second.

In order to estimate the average contamination we take into account that each resonance line presented in Fig. 84 corresponds to a certain value of the solenoid field and, therefore, affects the gas at a certain $z$. Using a realistic field map of the solenoid we obtained that the average depolarization in the beam area will be reduced to about $\sim 0.3 \cdot 10^{-4}$ by the lateral gas diffusion and by the escape of the "low field seeking" atoms from the storage cell.

In order to study experimentally the depolarization effect discussed, one can tune the solenoid magnetic field to overlap a resonance line with the transition frequency of the gas at the cell center. This would increase the transition rate by a factor of $\sim$70.

### A.1.8 Contamination by Free Electrons and Ions

The beam would ionize per second about 20% of the atoms in the cylinder around the beam spot. The charged particles would not escape the beam area due to diffusion, as the neutral atoms would do, but

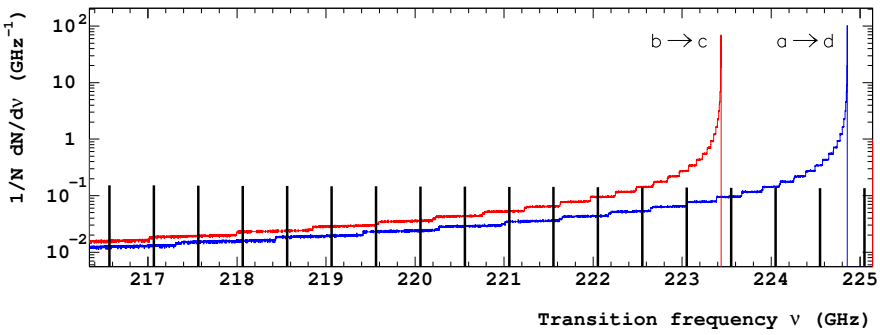


Figure 84: *Simulated spectra of the transitions on the axis of the hydrogen trap with the maximum field of 8.0 T. The density of atoms depends on the field as* $exp(-\mu_e B/kT)$. *The two curves show* $\frac{1}{N}dN/d\nu_{ad}$ *and* $\frac{1}{N}dN/d\nu_{bc}$ *- the relative number of atoms which can undergo* $|a\rangle \rightarrow |d\rangle$ *and* $|b\rangle \rightarrow |c\rangle$ *transitions at the given frequency, per one GHz. The resonant structure of the spectral function of the beam-induced electromagnetic field is shown as a set of vertical bars, 499 MHz apart.*

will follow the magnetic field lines, parallel to the beam. An elegant way to remove them is to apply a relatively weak ∼1 V/cm electric field perpendicular to the beam. The charged particles will drift at a speed of $v = \vec{E} \times \vec{B}/B^2 \sim 12$ m/s perpendicular to the beam and leave the beam area in about 20 $\mu$s. This will reduce the average contamination to a $10^{-5}$ level.

### A.1.9 Application of the Atomic Target to Møller Polarimetry

This feasibility study was done for the possible application of the target discussed to the existing Møller polarimeter in Hall A at JLab.

The beam polarization at JLab is normally about 80%, at beam currents below 100 $\mu$A. Scaling the results of the existing polarimeter to the hydrogen target discussed we estimated that at 30 $\mu$A a 1% statistical accuracy will be achieved in about 30 min. This is an acceptable time, in particular if the measurements are done in parallel with the main experiment.

There is no obvious way to measure directly the polarization of the hydrogen atoms in the beam area. The contamination from the residual gas is measurable. The rest relies on calculations. All calculations show that the polarization is nearly 100%, with a possible contamination of <0.01%, coming from several contributions. The impact of the most important of these contributions can be studied, at least their upper limits, by deliberately increasing the effect. For example, the beam RF induced transitions can be increased by a factor of ∼70, by fine tuning of the solenoid magnetic field. The contribution from the charged particles in the beam area can be varied by a factor up to $\sim 10^4$, by changing the cleaning electric field.

The systematic errors, associated with the present Hall A polarimeter, when added in quadrature give a total systematic error of about 3%. Scaling these errors to the design with the hydrogen target reduces the total error to about 0.3%. If we scale the accuracy of the Hall C polarimeter (see Table 10), the projected total error would be better than 0.2%. There is no doubt that achieving such an accuracy is a major challenge and will require re-evaluation of the error budget for including smaller effects, so far neglected. However, the technique described has a potential to deliver an accuracy of 0.4% required for the experiment proposed.

## References

[1] MOLLER Experiment Homepage:

http://http://hallaweb.jlab.org/12GeV/Moller/

[2] MOLLER Collaboration, J. Benesch at al, arXiv:1411.4088 [nucl-ex].

[3] P. L. Anthony *et al.* [SLAC E158 Collaboration], Phys. Rev. Lett. **95**, 081601 (2005) [arXiv:hep-ex/0504049].

[4] A. Czarnecki and W. J. Marciano, Phys. Rev. D **53**, 1066 (1996) [arXiv:hep-ph/9507420].

[5] A. Czarnecki and W. J. Marciano, Int. J. Mod. Phys. A **15**, 2365 (2000) [arXiv:hep-ph/0003049].

[6] J. Erler and M. J. Ramsey-Musolf, Phys. Rev. D **72**, 073003 (2005) [arXiv:hep-ph/0409169].

[7] Nuclear Science Advisory Committee Long Range Planning Document (2007):

http://hallaweb.jlab.org/12GeV/Moller/downloads/mie/nuclear_science_low_res.pdf

[8] Reaching for the Horizon: The 2015 Long Range Plan for Nuclear Science:

http://science.energy.gov/~/media/np/nsac/pdf/2015LRP/2015_LRPNS_091815.pdf

[9] Report of the Director's Review (January 2010):

http://hallaweb.jlab.org/12GeV/Moller/downloads/mie/Final_Draft_MOLLER_Review_Report.pdf

[10] Report to NSAC on Implementing the 2007 Long Range Plan (2013):

http://hallaweb.jlab.org/12GeV/Moller/downloads/mie/2013_NSAC_Implementing_the_2007_Long_Range_Plan.pdf

[11] Department of Energy Office of Nuclear Physics Report on the Science Review of the MOLLER Experiment:

http://hallaweb.jlab.org/12GeV/Moller/scirev2014/rep/MOLLER Science Review Report_2014_FINAL_revised.pdf

[12] E. Derman and W. J. Marciano, Annals Phys. **121**, 147 (1979).

[13] A. Aleksejevs, S. Barkanova, Y. Kolomensky, E. Kuraev and V. Zykunov, Phys. Rev. D **85**, 013007 (2012) [arXiv:1110.1750 [hep-ph]].

[14] A. G. Aleksejevs, S. G. Barkanova, Y. M. Bystritskiy, A. N. Ilyichev, E. A. Kuraev and V. A. Zykunov, Eur. Phys. J. C **72**, 2249 (2012).

[15] A. G. Aleksejevs, S. G. Barkanova, V. A. Zykunov and E. A. Kuraev, Phys. Atom. Nucl. **76**, 888 (2013) [Yad. Fiz. **76**, 942 (2013)].

[16] "Uncertainties in the Theoretical Calculation of the Parity-Violating Asymmetry in Møller Scattering", MOLLER Collaboration report submitted to DOE, September 15, 2016:

`http://cinder.physics.sunysb.edu/mollerdir/backup/2-loopreport_final.pdf`

[17] S. C. Bennett and C. E. Wieman, Phys. Rev. Lett. **82**, 2484 (1999) [Erratum-ibid. **83**, 889 (1999)] [hep-ex/9903022].

[18] V. A. Dzuba, J. C. Berengut, V. V. Flambaum and B. Roberts, Phys. Rev. Lett. **109**, 203003 (2012) [arXiv:1207.5864 [hep-ph]].

[19] D. Androic *et al.* [Qweak Collaboration], Phys. Rev. Lett. **111**, 141803 (2013) [arXiv:1307.5275 [nucl-ex]].

[20] C. Amsler *et al.* [Particle Data Group], Phys. Lett. B **667**, 1 (2008).

[21] G. P. Zeller *et al.* [NuTeV Collaboration], Phys. Rev. Lett. **88**, 091802 (2002) [Erratum-ibid. **90**, 239902 (2003)] [arXiv:hep-ex/0110059].

[22] [ALEPH Collaboration and DELPHI Collaboration and L3 Collaboration and OPAL Collaboration and SLD Collaboration and LEP Electroweak Working Group and SLD Electroweak Group and SLD Heavy Flavour Group ], Phys. Rept. **427**, 257 (2006) [arXiv:hep-ex/0509008].

[23] W. J. Marciano, AIP Conf. Proc. **870**, 236 (2006).

[24] T. Adams, *et al.*, Int. J. Mod. Phys. A **26**, 671 (2009).

[25] J. M. Conrad, J. M. Link, and M. H. Shaevitz, Phys. Rev. D **71**, 073013 (2005) [arXiv:hep-ex/0403048].

[26] M. Baak, *et al.*, Snomass 2013 study, arXiv:1310.6708v1 [hep-ph].

[27] K. S. Kumar, S. Mantry, W. J. Marciano and P. A. Souder, Ann. Rev. Nucl. Part. Sci. **63**, 237 (2013) [arXiv:1302.6263 [hep-ex]].

[28] V. Cirigliano and M. J. Ramsey-Musolf, Prog. Part. Nucl. Phys. **71**, 2 (2013) [arXiv:1304.0017 [hep-ph]].

[29] J. Erler and S. Su, Prog. Part. Nucl. Phys. **71**, 119 (2013) [arXiv:1303.5522 [hep-ph]].

[30] W. Chao, H. Li, M. J. Ramsey-Musolf, and S. Su, in preparation.

[31] V. Cirigliano, A. Kurylov, M. J. Ramsey-Musolf and P. Vogel, Phys. Rev. D **70**, 075007 (2004) [arXiv:hep-ph/0404233].

[32] H. Davoudiasl, H. -S. Lee and W. J. Marciano, Phys. Rev. D **85**, 115019 (2012) [arXiv:1203.2947 [hep-ph]].

[33] H. Davoudiasl, H. -S. Lee and W. J. Marciano, Phys. Rev. Lett. **109**, 031802 (2012) [arXiv:1205.2709 [hep-ph]].

[34] A. Kurylov, M. J. Ramsey-Musolf and S. Su, Phys. Rev. D **68**, 035008 (2003) [arXiv:hep-ph/0303026].

[35] M. J. Ramsey-Musolf and S. Su, Phys. Rept. **456**, 1 (2008) [arXiv:hep-ph/0612057].

[36] J. Erler, P. Langacker, S. Munir and E. Rojas, arXiv:1108.0685v1 [hep-ph].

[37] E. Eichten, K. D. Lane and M. E. Peskin, Phys. Rev. Lett. **50**, 811 (1983).

[38] A. Falkowski and K. Mimouni, JHEP **1602**, 086 (2016) [arXiv:1511.07434 [hep-ph]].

[39] Y. Li, F. Petriello and S. Quackenbush, Phys. Rev. D **80**, 055018 (2009) [arXiv:0906.4132 [hep-ph]].

[40] H. Davoudiasl, H. -S. Lee and W. J. Marciano, arXiv:1402.3620 [hep-ph].

[41] P. A. Souder *et al.*, Phys. Rev. Lett. **65**, 694 (1990).

[42] D. T. Spayde *et al.* [SAMPLE Collaboration], Phys. Lett. B **583**, 79 (2004) [arXiv:nucl-ex/0312016].

[43] A. Acha *et al.* [HAPPEX collaboration], Phys. Rev. Lett. **98**, 032301 (2007) [arXiv:nucl-ex/0609002].

[44] The Lead Radius Experiment PREX, E06002, K. Kumar, R. Michaels, P. Souder, G. Urciuoli spokespersons, http://hallaweb.jlab.org/parity/prex/ .

[45] The Qweak Experiment, http://www.jlab.org/Hall-C/Qweak/index.html, , R. Carlini Principal Investigator.

[46] C. Y. Prescott *et al.*, Phys. Lett. B **77**, 347 (1978).

[47] R.S. Hicks *et al.*, "Flux Profile Scanners for Scattered High-Energy Electrons", NIM **A553** (2005), pp 470-482.

[48] M. Gericke, "Excess Noise as a Function of Detector Thickness", September 1, 2005, a Qweak technical note available at http://qweak.jlab.org/doc-public/ShowDocument?docid=532 .

[49] T. Allison *et al.* [Qweak Collaboration], "The Qweak Experimental Apparatus, NIM **A781** (2015), pp 105-133.

[50] L. V. de Bever, J. Jourdan, M. Loppacher, S. Robinson, I. Sick and J. Zhao, "A target for precise Mller polarimetry," *Nucl. Instrum. Meth.*, vol. A400, pp. 379–386, 1997.

[51] E. Chudakov and V. Luppov, "Møller polarimetry with atomic hydrogen targets," *IEEE Trans. Nucl. Sci.*, vol. 51, pp. 1533–1540, 2004.

[52] E. Chudakov and V. Luppov, "Moeller polarimetry with atomic hydrogen targets," *Eur. Phys. J.*, vol. A24S2, pp. 123–126, 2005.

[53] M. Hauger *et al.*, "A high-precision polarimeter," *Nucl. Instrum. Meth.*, vol. A462, pp. 382–392, 2001, nucl-ex/9910013.

[54] M Loppacher, "Møller Polarimetry for CEBAF Hall C," PhD thesis, Universität Basel, April 1996.

[55] A. V. Glamazdin *et al.*, "Electron beam Moeller polarimeter at JLAB Hall A," *Fizika*, vol. B8, pp. 91–95, 1999, hep-ex/9912063.

[56] N. L. Hall, P. G. Blunden, W. Melnitchouk, A. W. Thomas and R. D. Young, Phys. Lett. B **731**, no. issue, 287 (2014) [Erratum-ibid. B **733**, 380 (2014)] [arXiv:1311.3389 [nucl-th]].

[57] D.E. Wiser, PhD thesis, University of Wisconsin-Madison, 1977.

[58] K. D. Paschke, Eur. Phys. J. A **32**, 549 (2007).

[59] B. Waidyawansa, "A 3% Measurement of the Beam Normal Single Spin Asymmetry in Forward Angle Elastic Electron-Proton Scattering using the Qweak Setup, PhD thesis, Ohio University, August 2013.

[60] J. Musson, "Functional Description of Algorithms Used in Digital Receivers, JLab Technical Report No. JLAB-TN-14-028 (2014).

[61] The MOLLER Collaboration, "Report on Aluminum and Inelastic Backgrounds", submitted to U.S. Department of Energy Office of Science Nuclear Physics Division, December 2, 2015:

`http://cinder.physics.sunysb.edu/mollerdir/backup/MOLLER_backgrounds.pdf`

[62] DOE Office of Nuclear Physics 2014 Science Review of MOLLER experiment,

`http://hallaweb.jlab.org/12GeV/Moller/scirev2014/`

[63] D. Androic *et al.* [G0 Collaboration], arXiv:1212.1637 [nucl-ex].

[64] D. Wang *et al.* [Jefferson Lab Hall A Collaboration], Phys. Rev. Lett. **111**, no. 8, 082501 (2013) [arXiv:1304.7741 [nucl-ex]].

[65] D. Wang *et al.*, Phys. Rev. C **91**, no. 4, 045506 (2015) [arXiv:1411.3200 [nucl-ex]].

[66] K. Matsui, T. Sato and T.-S. H. Lee, Phys. Rev. C **72**, 025204 (2005) [nucl-th/0504051].

[67] M. Gorchtein, C. J. Horowitz and M. J. Ramsey-Musolf, Phys. Rev. C **84**, 015502 (2011) [arXiv:1102.3910 [nucl-th]].

[68] N. L. Hall, P. G. Blunden, W. Melnitchouk, A. W. Thomas and R. D. Young, Phys. Rev. D **88**, no. 1, 013011 (2013) [arXiv:1304.7877 [nucl-th]].

[69] N. L. Hall, P. G. Blunden, W. Melnitchouk, A. W. Thomas and R. D. Young, arXiv:1504.03973 [nucl-th]. (accepted in Phys. Lett B).

[70] D. S. Armstrong *et al.*, arXiv:1202.1255 [physics.ins-det].

[71] P. E. Bosted and M. E. Christy, Phys. Rev. C P**81**:055213 (2010)

[72] C. J. Horowitz, Phys. Rev. C **89**, 045503 (2014) [arXiv:1401.6898 [nucl-th]].

[73] S. Agostinelli *et al.* [GEANT4 Collaboration], Nucl. Instrum. Meth. A **506**, 250 (2003).

[74] E. G. Brentari et al., 1965, *Boiling Heat Transfer for Oxygen, Nitrogen, Hidrogen, and Helium*, National Bureau of Standards, TN 317

[75] S. D. Covrig et al., 2005, *The cryogenic target for the G0 experiment at Jefferson Lab*, Nucl. Instr. and Meth. **A 551**, 218-235

[76] J. Gao et al., 2003, *A liquid hydrogen target for the precision measurement of the weak mixing angle in Møller scattering at SLAC*, Nucl. Instr. and Meth. **A 498**, 90-100

[77] Geant4. `http://geant4.cern.ch/`.

[78] S. Agostinelli *et al.* [GEANT4 Collaboration], Nucl. Instrum. Meth. A **506**, 250 (2003).

[79] Christy, M.E. *et al.* Phys.Rev. **C81** (2010) 055213
arXiv:0712.3731

[80] N. Falletto *et al*, "Compton scattering off polarized electrons with a high finesse Fabry-Perot cavity at JLab,", *"Nucl. Instrum. Meth."*, A459, 212-425, 2001.

[81] A. Narayan, D. Dutta, V. Tvaskis and J. W. Martin, Nuovo Cim. C **035N04**, 134 (2012).

[82] N. Vansteenkise, P. Vignolo, and A. Aspect, "Optical Reversibility Theorems for Polarization: Application to Remote Control of Polarization", J. Opt. Soc. Am. A, Vol. 10, No. 10, (1993) 2240.

[83] R.J. Loewen, "A compact light source: Design and technical feasibility study of a laser-electron storage ring X-ray source," SLAC-R-0632 (2003).

[84] S. Miyoshi *et al*., Photon generation by laser-Compton scattering at the KEK-ATF, NIM A623 (2010) 576.

[85] A. Variola *et al*., The LAL Compton Program,, NIM A608 (2009) S83.

[86] V. Brisson *et al*., High finesse Fabry-Perot cavities in the picosecond regime, NIM A608 (2009) S75.

[87] A. Denner and S. Dittmaier, "Complete $o(\alpha)$ QED cor- rections to polarized Compton scattering", Nucl. Phys. B **540** 58 (1999).

[88] M. Friend *et al*, "Upgraded photon calorimeter with integrating readout for Hall A Compton Polarimeter at Jefferson Lab", Nucl. Instrum. Methods A676, 96-105, 2012. [arXiv:1108.3116].

[89] A. Narayan *et al.*, "Precision Electron-Beam Polarimetry at 1 GeV Using Diamond Microstrip Detectors," Phys. Rev. X **6**, no. 1, 011013 (2016).

[90] D. C. Jones, Ph.D. thesis, University of Virginia, 2015 (unpublished); arXiv:1601.07172.

[91] J. Benesch, G. B. Franklin, B. P. Quinn and K. D. Paschke, "Simple modification of Compton polarimeter to redirect synchrotron radiation," Phys. Rev. ST Accel. Beams **18**, no. 11, 112401 (2015).

[92] K. Abe *et al.* [SLD Collaboration], "A High precision measurement of the left-right Z boson cross-section asymmetry," Phys. Rev. Lett. **84**, 5945 (2000).

[93] M. Woods [SLD Collaboration], "The Scanning Compton polarimeter for the SLD experiment," hep-ex/9611005.

[94] H. Augustin *et al.*, JINST **10**, no. 03, C03044 (2015). doi:10.1088/1748-0221/10/03/C03044

[95] G. W. Ford and C. J. Mullin, "Scattering of Polarized Dirac Particles on Electrons," Phys. Rev. **108**, 477 (1957); Erratum, Phys. Rev. **110**, 1485(E) (1958).

[96] A. M. Bincer, "Scattering of Longitudinally Polarized Fermions," Phys. Rev. **107**, 1434 (1957).

[97] P. Stehle, "Calculation of Electron-Electron Scattering," Phys. Rev. **110**, 1458 (1958).

[98] A. Raçzka and R. Raçzka, "Møller Scattering of Arbitrarily Polarized Electrons," Erratum, Phys. Rev. **110**, 1469 (1958).

[99] G. Alexander and I. Cohen, "Møller scattering polarimetry for high-energy $e^+e^-$ linear colliders," Nucl. Instrum. Meth. A **486**, 552 (2002) [hep-ex/0006007]. This paper contains the basic formulas for Møller polarimetry, as well as references to calculations of higher order QED corrections.

[100] E. A. Chudakov, A. V. Glamazdin, V. G. Gorbenko, L. G. Levchuk, R. I. Pomatsalyuk, P. V. Sorokin, "Electron beam Møller polarimeter at Hall A, JLab", Prob.Atom.Sci.Tech. **40**, 43 (2002)

[101] P. S. Cooper, M. J. Alguard, R. D. Ehrlich, V. W. Hughes, H. Kobayakawa, J. S. Ladish, M. S. Lubell and N. Sasao *et al.*, "Polarized electron Electron Scattering at GeV Energies," Phys. Rev. Lett. **34**, 1589 (1975).

[102] B. Wagner, H. G. Andresen, K. H. Steffens, W. Hartmann, W. Heil and E. Reichert, "A Møller polarimeter for CW and pulsed intermediate-energy electron beams," Nucl. Instrum. Meth. A **294**, 541 (1990).

[103] J. Arrington, E. J. Beise, B. W. Filippone, T. G. O'Neill, W. R. Dodge, G. W. Dodson, K. A. Dow and J. D. Zumbro, "A Variable energy Møller polarimeter at the MIT Bates Linear Accelerator Center," Nucl. Instrum. Meth. A **311**, 39 (1992).

[104] K. B. Beard, R. Madey, W. M. Zhang, D. M. Manley, B. D. Anderson, A. R. Baldwin, J. M. Cameron and C. C. Chang *et al.*, "Measurement of the polarization of a pulsed electron beam with a Møller polarimeter in the coincidence mode," Nucl. Instrum. Meth. A **361**, 46 (1995).

[105] H. R. Band, G. Mitchell, R. Prepost and T. Wright, "A Møller polarimeter for high-energy electron beams," Nucl. Instrum. Meth. A **400**, 24 (1997).

[106] P. Steiner, A. Feltham, I. Sick, M. Zeier and B. Zihlmann, "A high-rate coincidence Moller polarimeter," Nucl. Instrum. Meth. A **419**, 105 (1998).

[107] G. G. Scott and H. W. Sturner, "Magnetomechanical Ratios for Fe-Co Alloys," Phys. Rev. **184**, 490 (1969).

[108] J. Crangle and G. M. Goodman, "The Magnetization of Pure Iron and Nickel," Proceedings of the Royal Society of London, Series A, **321**, 477 (1971).

[109] C. D. Graham, Jr., "Iron and Nickel as Magnetization Standards," J. Appl. Phys. **53**, 2032 (1982).

[110] G. G. Scott, "Review of gyromagnetic ratio experiments," *Rev. Mod. Phys.*, vol. 34, pp. 102–109, Jan 1962.

[111] E. C. Stoner and E. P. Wohlfarth, "A Mechanism of Magnetic Hystersis in Heterogeneous Alloys," Phil. Trans. Royal Soc. London, Series A **240**, 599 (1948).

[112] L. G. Levchuk, "The Intraatomic motion of bound electrons as a possible source of a systematic error in electron beam polarization measurements by means of a Møller polarimeter," *Nucl. Instrum. Meth.*, vol. A345, pp. 496–499, 1994.

[113] M. Swartz, H. R. Band, F. J. Decker, P. Emma, M. J. Fero, R. Frey, R. King and A. Lath *et al.*, "Observation of target electron momentum effects in single arm Møoller polarimetry," Nucl. Instrum. Meth. A **363**, 526 (1995) [hep-ex/9412006].

[114] D. Gaskell, D. G. Meekins, and C. Yan, "New methods for precision Møller polarimetry," *Eur. Phys. J.*, vol. A32, pp. 561–564, 2007.

[115] M. Poelker, J. Grames, J. Hansknecht, R. Kazimi, J. Musson, Phys. Rev. ST Accel. Beams **10**, 053502 (2007).

[116] E. Chudakov and V. Luppov, "Møller polarimetry with atomic hydrogen targets," tech. rep., JLab, 2005. `http://www.jlab.org/~gen/hyd/loi_3.pdf`.

[117] I. F. Silvera, "Ultimate fate of a gas of atomic hydrogen in a liquid-helium chamber: Recombination and burial," *Phys. Rev. B*, vol. 29, pp. 3899–3904, Apr 1984.

[118] I. F. Silvera and J. T. M. Walraven, "Stabilization of atomic hydrogen at low temperature," *Phys. Rev. Lett.*, vol. 44, pp. 164–168, Jan 1980.

[119] I. F. Silvera and J. T. M. Walraven, "Spin polarized atomic hydrogen," *Progress in Low Temperature Physics, vol. X*, pp. 139–370, 1986.

[120] T. Roser *et al.*, "Microwave driven extraction of stabilized spin polarized atomic hydrogen," *Nucl. Instrum. Meth.*, vol. A301, pp. 42–46, 1991.

[121] M. Mertig, V. G. Luppov, T. Roser, and B. Vuaridel, "Continuous density measurement of atomic hydrogen by means of a bolometer," *Rev. Sci. Instrum.*, vol. 62, pp. 251–252, 1991.

[122] M. D. Miller and L. H. Nosanow, "Possible "new" quantum systems. ii. properties of the isotopes of spin-aligned hydrogen," *Phys. Rev. B*, vol. 15, pp. 4376–4385, May 1977.